

Prediction of peri-implant bone adaptation to mechanical environments: theoretical developments and experimental validation

THÈSE N° 6273 (2014)

PRÉSENTÉE LE 22 AOÛT 2014

À LA FACULTÉ DES SCIENCES ET TECHNIQUES DE L'INGÉNIEUR
LABORATOIRE DE MÉCANIQUE APPLIQUÉE ET D'ANALYSE DE FIABILITÉ
PROGRAMME DOCTORAL EN MÉCANIQUE

ÉCOLE POLYTECHNIQUE FÉDÉRALE DE LAUSANNE

POUR L'OBTENTION DU GRADE DE DOCTEUR ÈS SCIENCES

PAR

Marco PICCININI

acceptée sur proposition du jury:

Prof. J.-F. Molinari, président du jury
Prof. I. Botsis, Dr J. Cugnoni, directeurs de thèse
Prof. P. Ammann, rapporteur
Prof. D. Pioletti, rapporteur
Dr V. Stadelmann, rapporteur



ÉCOLE POLYTECHNIQUE
FÉDÉRALE DE LAUSANNE

Suisse
2014

*A mio padre, l'esempio
a mia madre, la forza
ai miei fratelli, parte di me
e a mia moglie, perché per me è tutto.*

Abstract

Dental and orthopedic prostheses are complex devices designed to restore compromised functionalities such as chewing or walking. The working conditions of these implants entail a direct contact with bone, which is a biological tissue characterized by astonishing adaptation capabilities. Indeed bone grows and preserves the body equilibrium by adapting to processes driven by various stimuli: mechanical, chemical and hormonal among others. In particular, the mechanical stimuli drive the skeleton development during growth and keep influencing bone adaptation during the whole life. In presence of prostheses, the mechanical environment that occurs in bone can be significantly different from healthy conditions, and this can lead to strong structural adaptation of the tissue. Since this mechanism is not fully understood, the study of bone adaptation to the presence of an implant, as well as the identification of validated rules for the prediction of this phenomenon, are crucial to optimize rehabilitation therapies, extend the prostheses operation and promote innovative designs.

This thesis aims at explaining the dependence of implants integration on mechanical stimulations, through a coupled experimental-numerical investigation of implanted rats' tibiae. Three main goals are addressed: the systematic identification of mechanics-related bone adaptation phenomena, the quantification of their causes and effects and the establishment of prediction strategies validated experimentally.

The *in-vivo* experiments are based on the 'loaded implant' model, which allows studying the dependence of implants fixation on the mechanical stimulation, through the activation of cylindrical implants housed in the proximal part of rats' tibiae. A combination of morphologic analyses and mechanical tests highlight three main outcomes. Firstly, the rat locomotion causes a peri-implant cortical loss that has harmful influences on the implants stability and can lead to the complete bone-implant detachment. Nevertheless, implants stability of well integrated specimens is improved through the external loading. Indeed, the ultimate strength of well integrated specimens subjected to external stimulation is improved due to the peri-implant tissue adaptation to the imposed exercise. Finally, the results highlight biodiversity (i.e. differences between individuals) as a key factor influencing the implants state of integration.

These experimental findings are investigated through a novel protocol to generate high fidelity, specimen-specific finite element models of implanted rat tibiae from high-resolution computed tomography images. This verified and validated procedure allows preserving the characteristics of the individual bones and satisfactorily captures their mechanical response.

Furthermore, the detrimental effects of the animal's activity are correlated to the mechanical environment through the analysis of the musculoskeletal forces occurring during gait. This investigation is performed to quantify the deformations occurring in a rat tibia during locomotion and to analyze the peri-implant stresses generated by different integration states. The results lead to a detailed representation of the stress and strain fields that develop in the tibia during gait, which enhance the knowledge of the biomechanics of rat tibiae under physiological loading conditions. Moreover, this study identifies the causes of the peri-implant cortical loss observed experimentally. This detrimental adaptation process is initiated by a loss of bone-implant adhesion, and the consequent detachment-resorption process eventually goes on driven by the cyclic loadings on the interface due to gait.

Finally, reliable predictions of peri-implant bone adaptation to different loading conditions are achieved through a phenomenological algorithm inspired by the 'Mechanostat', which updates the bone mechanical properties depending on the stimulation. An optimized strategy, based on stimuli's thresholds derived from the physiological deformation of the rat tibia, provides predictions of both bone density variations and implants lateral stability that are in close agreement with the observed phenomena. This analysis is characterized by a comparison of existing approaches, a systematic validation through comparison with experiments and sensitivity studies, which quantify the dependence of the results on the main assumptions. The influence of both the physical activity and the implant loading on the bone structure are quantified separately, then combined on a single model representative of the mechanical homeostasis characterizing the 'loaded implant' experiment.

In conclusion, the findings presented in this thesis are obtained through validated numerical approaches and lead to interesting clinical perspectives concerning the development of therapies for bone growth through controlled mechanical stimulation and the understanding of peri-implant bone defects due to disuse or overloading.

Keywords: in~vivo stimulation, bone augmentation, bone loss, implant, specimen-specific, finite element, adaptation algorithm, disuse, overloading, homeostasis, mechanical stimulation, musculoskeletal loads.

Résumé

Les prothèses dentaires et orthopédiques sont des dispositifs complexes visant à restaurer des fonctionnalités compromises comme la mastication ou la déambulation. Les conditions de travail de ces implants impliquent un contact direct avec l'os, qui est un tissu biologique caractérisé par d'étonnantes capacités d'adaptation. En effet, l'os se développe et préserve l'équilibre du corps en s'adaptant à des processus concaténés et entraînés par différentes stimulations: mécaniques, chimiques et hormonaux entre autres. En particulier, la stimulation mécanique conduit au développement du squelette durant la croissance et préserve son influence sur l'adaptation de l'os pendant toute la vie. En présence de prothèses, l'environnement mécanique qui se produit dans l'os peut être significativement différent de conditions saines, et cela peut conduire à une forte adaptation structurelle du tissu. Etant donné que ce mécanisme n'est pas totalement compris, l'étude de l'adaptation osseuse à la présence d'un implant ainsi que l'identification des modèles validés pour la prédiction de ce phénomène sont indispensables pour optimiser les thérapies de réhabilitation, prolonger le fonctionnement des prothèses et favoriser des conceptions innovantes.

Cette thèse vise à expliquer la dépendance de l'intégration des implants par la stimulation mécanique grâce à une étude expérimentale-numérique des tibias de rats implantés. Trois objectifs principaux sont abordés: l'identification systématique des phénomènes d'adaptation osseuse dépendant des stimulations mécaniques, la quantification de leurs causes et effets et l'établissement de stratégies de prédiction validées expérimentalement.

Les expériences *in-vivo* sont basées sur le modèle 'loaded implant', ce qui permet l'étude de la dépendance de l'intégration des implants par la stimulation mécanique au moyen de l'activation d'implants logés dans la partie proximale du tibia des rats. Une combinaison d'analyses morphologiques et des tests mécaniques met en évidence trois résultats principaux. Tout d'abord, la locomotion entraîne une perte d'os corticale autour des implants, qui a des influences néfastes sur la stabilité des implants et peut conduire au détachement complet de la prothèse. Néanmoins, la stabilité des implants dans les échantillons bien intégrés est améliorée grâce à la charge externe. En effet, la résistance à la rupture des spécimens bien intégrés et soumis à la stimulation externe est améliorée grâce à l'adaptation osseuse du tissu autour des implants. Enfin, les résultats mettent en

évidence la biodiversité (c.-à-d. les différences entre les individus) comme un facteur clé qui influence l'état d'intégration des implants. Ces résultats expérimentaux sont étudiés à travers un nouveau protocole pour générer des modèles d'éléments finis de tibias de rat implanté à partir des images de tomодensitométrie à haute résolution. Cette procédure vérifiée et validée permet de préserver les caractéristiques de chaque individu et capture leur réponse mécanique de façon satisfaisante.

En outre, les effets néfastes de l'activité de l'animal sont corrélés à l'environnement mécanique par l'analyse des forces musculosquelettiques qui se produisent pendant la marche. Cette analyse est adoptée pour quantifier les déformations qui se produisent dans un tibia de rat pendant la locomotion et qui permet d'analyser les contraintes autour des implants au cours de différents états d'intégration. Les résultats conduisent à une représentation détaillée des champs de déformation et de contrainte qui se développent dans le tibia lors de la marche, ce qui améliore la connaissance de la biomécanique du tibia de rats dans les conditions physiologiques. De plus, cette étude identifie les causes de la perte corticale observée expérimentalement autour des implants. Ce processus d'adaptation néfaste est déclenché par une perte d'adhérence entre l'os et l'implant et aggravée par les charges cycliques à l'interface dues à la locomotion.

Enfin, des prévisions fiables de l'adaptation osseuse à différentes conditions de chargement sont atteintes grâce à un algorithme phénoménologique inspiré par le 'Mechanostat', qui met à jour les propriétés mécaniques de l'os en fonction de la stimulation. Une stratégie optimisée, basée sur les seuils de stimulation provenant de la déformation physiologique du tibia de rat, fournit des prévisions des variations de la densité osseuse et de la stabilité latérale des implants qui sont en accord avec les phénomènes observés. Cette analyse est caractérisée par une comparaison des approches existantes, une validation systématique par comparaison avec les expériences et des études de sensibilité qui quantifient la dépendance des résultats aux hypothèses principales. L'influence de l'activité physique et celle de la charge de l'implant sur la structure osseuse sont quantifiées séparément, puis fusionnées dans un modèle unique entièrement représentatif de l'homéostasie mécanique caractérisant l'expérience 'loaded implant'.

En conclusion, les résultats présentés dans cette thèse sont obtenus par des approches numériques validées et ouvrent des perspectives cliniques intéressantes concernant le développement de thérapies pour la croissance osseuse grâce à une stimulation mécanique contrôlée et la compréhension de défauts osseux autour des implants dus à l'inactivité ou à la surcharge.

Mots clés: stimulation in vivo, augmentation osseuse, perte osseuse, implant, spécimens spécifiques, éléments finis, algorithme d'adaptation, inactivité, surcharge, homéostasie, stimulation mécanique, charges musculosquelettiques.

Sommario

Le protesi dentarie ed ortopediche sono strumenti complessi progettati per ripristinare funzionalità compromesse come la masticazione o la deambulazione. Le condizioni di lavoro di questi impianti prevedono un contatto diretto con l'osso, che è un tessuto organico caratterizzato da incredibili capacità di adattamento. Il tessuto osseo, infatti, cresce e preserva l'equilibrio corporeo adattandosi a processi concatenati dovuti a vari stimoli: meccanici, chimici e ormonali fra gli altri. In particolare, gli stimoli meccanici guidano lo sviluppo dello scheletro durante la crescita ed esercitano la loro influenza sull'adattamento osseo durante tutta la vita. In presenza di protesi, gli stimoli meccanici possono essere molto diversi da quelli percepiti in condizioni normali, e questo può indurre un adattamento della struttura ossea. Dato che questo meccanismo non è chiaro, lo studio dell'adattamento osseo alla presenza di un impianto e l'identificazione di modelli predittivi convalidati sono argomenti di ricerca cruciali per ottimizzare terapie di riabilitazione, migliorare il funzionamento delle protesi e promuovere design innovativi.

Questa tesi aspira a spiegare la dipendenza dell'integrazione di impianti dalla stimolazione meccanica, attraverso uno studio numerico-sperimentale relativo a tibie di ratto impiantate. Gli obiettivi principali sono tre: l'identificazione sistematica dei fenomeni di adattamento osseo legati alla stimolazione meccanica, la quantificazione delle loro cause ed effetti e la definizione di strategie di previsione convalidate sperimentalmente.

Gli esperimenti in-vivo si basano sul modello 'loaded implant', che consente di studiare la dipendenza dell'integrazione di impianti dalla stimolazione meccanica attraverso l'attivazione di perni inseriti nella parte prossimale della tibia degli animali. Una combinazione di analisi morfologiche e test meccanici evidenzia tre risultati principali. Per prima cosa, la deambulazione dell'animale causa una riduzione del tessuto osseo intorno agli impianti che ne influenza negativamente la stabilità e può condurli al distacco completo. Nonostante ciò, la stabilità degli impianti ben integrati migliora grazie alla stimolazione esterna. I provini stimolati, infatti, sono più resistenti alla rottura grazie al potenziamento causato dall'adattamento osseo. Infine, i risultati evidenziano la biodiversità (cioè la differenza fra gli individui) come un fattore di grande influenza sull'integrazione degli impianti.

Queste scoperte sperimentali sono studiate attraverso un protocollo innovativo che consente di generare dettagliati modelli agli elementi finiti di ossa impiantate, a partire da scansioni tomografiche computerizzate ad alta risoluzione. Questa procedura verificata e convalidata consente di preservare le caratteristiche dei singoli provini e di rappresentarne correttamente il comportamento meccanico.

Gli effetti negativi dell'attività fisica dell'animale sono correlati alla stimolazione meccanica attraverso lo studio delle forze muscolari che si esercitano durante il movimento, le quali sono utilizzate per quantificare le deformazioni che caratterizzano la tibia durante la deambulazione, e per analizzare gli stati di tensione che si verificano intorno agli impianti con diverse condizioni di integrazione. I risultati conducono ad una rappresentazione dettagliata delle deformazioni che si sviluppano nella tibia durante la deambulazione, consentendo di migliorare le conoscenze biomeccaniche di questo organo in condizione fisiologiche. Questo studio consente, inoltre, di identificare le cause dell'indebolimento del tessuto osseo osservato sperimentalmente intorno agli impianti. Questo fenomeno indesiderato è dovuto ad una perdita di adesione tra il tessuto osseo e l'impianto, alimentata dagli sforzi ciclici causati dalla deambulazione.

Infine, previsioni affidabili dell'adattamento osseo a differenti condizioni di carico sono ottenute tramite un algoritmo fenomenologico ispirato al 'Mechanostat', che consente di aggiornare le proprietà meccaniche del tessuto in funzione della stimolazione. Una strategia ottimizzata, basata sugli stimoli percepiti dall'animale in condizioni fisiologiche, fornisce previsioni delle variazioni di densità ossea e della stabilità degli impianti che combaciano con i risultati sperimentali. Quest'analisi è caratterizzata dal confronto fra approcci esistenti, da una sistematica validazione su base sperimentale e da studi di sensibilità che quantificano la dipendenza dei risultati ottenuti dalle ipotesi principali. L'influenza dell'attività fisica e della stimolazione esterna sono considerate separatamente ed in seguito combinate in un unico modello globalmente rappresentativo della omeostasi meccanica che caratterizza il sistema vivente analizzato.

In conclusione, le scoperte presentate in questa tesi, ottenute attraverso metodologie numeriche convalidate, conducono ad interessanti prospettive cliniche relative allo sviluppo di terapie per il potenziamento osseo attraverso una stimolazione meccanica controllata, e alla comprensione dei difetti ossei che si presentano intorno agli impianti in caso di disuso o sovraccarico.

Parole chiave: potenziamento osseo, riduzione ossea, impianto, specimen-specific, elementi finiti, algoritmo di adattamento, inattività, sovraccarico, omeostasi, stimolazione meccanica, forze musculo-scheletriche, in~vivo.

Acknowledgements

First of all, I would like to thank my supervisors, Prof. John Botsis and Dr. Joël Cugnoni, for giving me this great opportunity and trusting me throughout the whole project. Prof. Botsis always supported me, in particular when obstacles and setbacks occurred. Dr. Cugnoni provided an immeasurable scientific support and an intense willingness to share ideas which have been crucial for my work.

Thanks to the project partners of the University of Geneva, in particular Prof. Anselm Wiskott and Prof. Patrick Ammann, who fulfilled my doubts on ‘living stuff’ and provided an incredibly wide set of experimental data. Through their experience, I had the chance to investigate different phenomena while being always in touch with reality, which is often a privilege in biomechanics. A special thanks to Miss Severine Clement for her attention and technical expertise. None of the experiments could have been performed without her precious competence.

Thanks to Dr. Vincent Stadelmann and his research team at AO Foundation for the extremely fruitful collaboration and for their willingness and technical competence.

I also would like to express my gratitude to the Swiss National Science Foundation for founding the initial part of this project (FNS grants n. 315200-116853/1 and n. 315230-127612/1).

I would like to thank all the colleagues met at LMAF. It has been extremely interesting to share doubts and ideas with such a variety of people involved in different fields of research. But mostly, thanks for every discussion we had around a coffee (or beers). These relaxing moments have been really important to me.

During these four years I had the chance to enjoy the company of several people. I thank them all for sharing their time with me. A really special thanks goes to all the friends met along the way, there are no words to express how much I feel lucky for your friendship. A special mention for Matteo, Alice, Angelo, Marco, Milad and Sahar.

I’m really grateful to my family for their support during these years: they are my landmarks and inspirations.

Finally, I’m extremely grateful to my wife Giulia: her vitality, concreteness and patience are my mainstays. Nothing of what I did was possible without her, grazie!

Contents

Contents	xi
List of Tables	xv
List of Figures	xvii
List of Symbols	xxi
List of Abbreviations	xxv
1 Introduction	1
1.1 Aims	1
1.2 Implants biomechanics	2
1.2.1 Orthopedics	2
1.2.2 Dentistry	3
1.2.3 Complications of osseointegrated implants	4
1.2.4 Implants in research	5
1.3 Bone tissue	7
1.3.1 Cortical and trabecular bone	7
1.3.2 Bone cells	8
1.3.3 Modeling and Remodeling	9
1.4 Bone mechanical adaptation	10
1.4.1 Experimental approaches	12
1.4.2 Theoretical approaches	16
1.4.3 Numerical approaches	19
1.5 Motivations of the thesis	21
1.6 Objectives of the thesis	22
1.7 Contributions and methodology	23
1.8 Thesis structure	25

2	Experimental approach	27
2.1	Aim	27
2.2	Animal model	28
2.2.1	Principle	28
2.2.2	Surgery and animal care	28
2.2.3	Implants and loading device	30
2.2.4	Experiments	31
2.3	Methodology	33
2.3.1	Computed tomography analyses	33
2.3.1.1	Morphometric analysis	34
2.3.1.2	Morphologic analysis	34
2.3.2	Ex~vivo mechanical tests	36
2.3.2.1	Pull-out	36
2.3.2.2	Indentation	36
2.3.2.3	Stiffness tests	36
2.4	Results and Discussion	38
2.4.1	Series 1. Mild overloading	38
2.4.2	Series 2. Daily activity	42
2.4.3	Series 3. Overloading	45
2.4.3.1	Implant rejections	45
2.4.3.2	Bone augmentation	47
2.5	Summary	51
2.6	Conclusions	52
3	Specimen-specific numerical modeling	55
3.1	Aim	55
3.2	Introduction	56
3.3	Materials and Methods	58
3.3.1	Segmentation	58
3.3.1.1	BMD histogram generation	58
3.3.1.2	Bone and Titanium density levels	60
3.3.1.3	Generation of a closed volume of bone	61
3.3.2	Finite Element model generation	61
3.4	Results and Discussion	64
3.4.1	Validation tests	64
3.4.2	Imaging	64
3.4.3	Segmentation	67
3.4.4	Finite Element discretization	68

3.4.5	Density-Elasticity relationship	69
3.4.6	Measured and simulated specimen stiffness	69
3.4.7	Simulated strain field	73
3.5	Summary	74
3.6	Conclusions	77
4	Physiological deformation of the rat tibia	79
4.1	Aim	79
4.2	Introduction	80
4.3	Gait-based analysis	81
4.3.1	Loading condition	81
4.3.2	Finite Element models	83
4.3.3	Validation	84
4.3.4	Results and Discussion	86
4.4	Signals of bone adaptation	92
4.4.1	Mechanical stimuli	92
4.4.2	Comparison settings	94
4.4.3	Results and Discussion	97
4.5	Conclusions	100
5	Bone adaptation	101
5.1	Aim	101
5.2	Introduction	102
5.3	Numerical framework of bone adaptation	103
5.3.1	Theory of bone adaptation	104
5.3.2	Algorithm of bone adaptation	105
5.3.3	Signal blending and Zone of Influence	106
5.3.4	Convergence criteria and output representation	108
5.4	External loading	109
5.4.1	Comparison of existing approaches	109
5.4.1.1	Models formulation	110
5.4.1.2	Results and discussion	111
5.4.2	Optimized approach	114
5.4.2.1	Formulation and parameters	114
5.4.2.2	Validation	116
5.4.3	Sensitivity studies	121
5.4.3.1	Attractor states	121
5.4.3.2	Law formulation	123
5.4.3.3	Zone of Influence	123

5.4.3.4	Load level	126
5.4.3.5	Summary	129
5.5	Musculoskeletal loading	131
5.5.1	Methods	131
5.5.2	Bare tibia	132
5.5.3	Cortical bone loss	132
5.6	Multi-load model	135
5.7	Conclusions	139
6	Longitudinal study: proof of concept	141
6.1	Aim	141
6.2	Introduction	142
6.3	Methods	142
6.4	Results	143
6.5	Discussion	145
6.6	Conclusions	151
7	Conclusions and perspectives	153
7.1	Aim	153
7.2	Summary and conclusions	154
7.3	Proposed methodologies	156
7.4	Perspectives	157
7.4.1	Multi-scale adaptation	159
A	Implants drawings	161
B	Computed Tomography image	165
	Bibliography	167
	Curriculum Vitæ	183

List of Tables

1.1	Features of animal models described in literature.	15
2.1	Details of the <i>in~vivo</i> experiments.	32
2.2	Results of the morphometric analysis (Zacchetti et al., 2013), Series 1.	39
2.3	Results of the Indentation and pull-out tests (Zacchetti et al., 2013), Series 1.	40
2.4	Results of the morphologic analysis, Series 1.	40
2.5	Results of the morphologic analysis, Series 2.	43
2.6	Implant loss, Series 3.	46
2.7	Inter-Implant mechanical properties, Series 3.	48
3.1	Comparison of segmentation techniques.	67
3.2	FE models volume and density reproduction.	68
3.3	Comparison of density-elasticity relationships.	70
3.4	Comparison of strain measurements.	74
3.5	Influence of the modeling parameters.	76
4.1	Loads acting on the tibia during gait, calculated with respect to the reference system in Figure 4.2b.	83
4.2	Details of the boundary conditions adopted in the FE models.	84
5.1	Adaptation parameters from the literature.	111
5.2	Adaptation parameters of the optimized approach.	115
5.3	Adaptation parameters for the comparison of formulations.	124

List of Figures

1.1	X-ray images and trends of joint replacement surgeries	3
1.2	Tooth anatomy and dental implants	4
1.3	Bone structure and composition	7
1.4	Bone modeling and remodeling	9
1.5	Bone mechanical adaptation	11
1.6	Overview of animal models for studies on bone mechanical adaptation . . .	13
1.7	The Mechanostat	17
1.8	Research methodology	24
2.1	Set-up for <i>in~vivo</i> implants loading	29
2.2	Implant positioning and loading	30
2.3	Implants shape and usage	31
2.4	Regions of interest for the morphometric analysis	34
2.5	Morphologic features	35
2.6	Set-up for <i>ex~vivo</i> mechanical tests	37
2.7	Indexes of integration	41
2.8	Conic depth at different integration periods	44
2.9	Implant rejections in Series 3	46
2.10	Inter-implant failure: implants orientation and load-displacement trends. .	48
2.11	Bone Mineral Density measured in Series 3	50
2.12	X-ray images of (a) non-stimulated and (b) stimulated (5 N) specimens. . .	50
2.13	Experiments recap	51
3.1	Segmentation steps	59
3.2	Bone mineral density Histogram	60
3.3	3D representations of segmented specimens	62
3.4	Force-displacement trends of validation tests	65
3.5	X-ray artifacts in mCT images	66
3.6	Stiffness' variation as function of the resolution of Young's modulus range.	70
3.7	Correlation between the normalized experimental and simulated stiffness. .	71

3.8	Density-elasticity relationships adopted in this study.	72
3.9	Equivalent strain field of a specimen subjected to 1 N of inter-implant loading.	75
4.1	Musculoskeletal model of the rat hindlimb	81
4.2	Rat hindlimb equilibrium systems	82
4.3	Mapping of the longitudinal strains in the bare tibia subjected to gait loads	85
4.4	Finite Element analysis of the rat tibia with in~silico implants.	86
4.5	Contact analysis in case of no bone-implant adhesion.	88
4.6	Simplified representation of the mechanisms leading to the cortical bone loss.	88
4.7	Longitudinal stresses in case of partial cortical loss of adhesion.	90
4.8	Conic depth at different integration periods	91
4.9	Comparison of mechanical signals: regions of interest and tissue differentiation	96
4.10	Distribution of mechanical signals during physiological activity	98
4.11	P-P plots of mechanical signals	99
5.1	Bone adaptive modeling as a function of the mechanical stimulus	103
5.2	Block diagram representation of the algorithm of bone adaptation.	107
5.3	Boundary conditions of the FE models for iterative computation.	110
5.4	Li et al. (2007) and Crupi et al. (2004) adaptation models.	111
5.5	Example of Inter-implant BMD field variation calculated through (a) Li et al. (2007) and (b) Crupi et al. (2004).	112
5.6	Inter-implant strain and BMD variations in ROIs predicted by Crupi et al. (2004) and Li et al. (2007).	113
5.7	ψ_ϵ -based approach: formulation and parameters.	115
5.8	Inter-implant BMD field variation predicted with the ψ_ϵ -based approach.	117
5.9	BMD variations in ROIs and inter-implant strain variation predicted with the ψ_ϵ -based approach.	117
5.10	Comparison of BMD distributions between mCT scans and FE models.	120
5.11	Results sensitivity to the apposition ψ_a and damage ψ_d attractor states.	122
5.12	Formulations of adaptation rate versus ψ_ϵ	124
5.13	Results sensitivity to the law formulation.	124
5.14	Results sensitivity to the Zone of Influence.	126
5.15	Inter-implant strain sensitivity to the external load magnitude.	127
5.16	BMD field variation with respect to the external load magnitude.	127
5.17	Density in ROIs sensitivity to the external load magnitude.	128
5.18	Summary of the parametric study	130
5.19	Ranking of the effects of perturbations on the numerical predictions	130
5.20	BMD field variation on a whole tibia subjected to gait-loads and processed with the ψ_ϵ -based adaptation algorithm.	133

5.21	Prediction of cortical bone loss due to disuse	134
5.22	BMD field predicted with the multi-load approach	137
6.1	Loading and scanning schedule adopted in longitudinal mCT analysis.	143
6.2	Time-lapsed in~vivo mCT scans of Specimen 1	144
6.3	Time-lapsed in~vivo mCT scans of Specimen 2	145
6.4	Time-lapsed in~vivo mCT scans of Specimen 3	146
6.5	BMD in ROIs monitored in longitudinal studies.	146
6.6	in~vivo mCT analysis: BMD variation in ROIs.	147
6.7	in~vivo mCT analysis	147
6.8	Specimen-specific BMD field variation: FE analysis and longitudinal mCT scans.	149
6.9	in~vivo mCT analysis: ROI comparison with FEM.	149
7.1	Proposed methodologies	157
7.2	Perspectives on multi-scale adaptation approaches	159
A.1	Proximal implant draft.	162
A.2	Distal implant draft.	163
B.1	Computed tomography image of a stimulated specimen	166

List of Symbols

A_j	ankle joint reaction
Al	aluminum
B_f	bicep femoris
BV/TV	relative bone volume
C_l	lateral condylar reaction
C_m	medial condylar reaction
$Ct.Th$	cortical thickness
D_{ji}	distance between nodes i and j
d	inter-implant displacement
d_U	inter-implant ultimate displacement
dr/dt	adaptation velocity
E	Young's modulus
e	error of adaptive modeling
F_i	internal forces
F_P	pull-out ultimate force
F_U	inter-implant ultimate force
f	weight function inside the Zone Of Influence (ZOI)
G_l	lateral gastrocnemius
G_m	medial gastrocnemius
H	indentation hardness
I_A	percentage of specimens showing periosteal reaction
I_C	percentage of specimens showing cortical bone loss
I_D	integration index of the distal implant
I_F	percentage of specimens showing perfect cortical adhesion
I_P	integration index of the proximal implant
I_S	percentage of specimens with the distal implant surrounded by alveolar bone
I_U	percentage of specimens with homogeneous alveolar bone around the proximal implant
II_K	inter-implant stiffness

II_S	inter-implant strain
i	node number
K	adaptation rate constant
K_a	apposition rate constant
K_d	damage rate constant
K_r	resorption rate constant
k	iteration number
L	left (i.e. non-stimulated) tibia
L_1	lower segmentation threshold for bare specimens
L_2	lower segmentation threshold for implanted specimens
L_h	inter-implant heads distance
l	length
M_i	internal moments
m	constant to weight stress and number of cycles
N	total number of loading conditions
n	loading cycles
P_i	patellar load
R	right (i.e. stimulated) tibia
R_X	percentage of right tibiae (i.e. stimulated) prematurely lost
R_f	rectus femoris
S_v	surface density of bone tissue
T_{Ad}	tibialis anterior distal
T_{Ap}	tibialis anterior proximal
T_{imp}	threshold for titanium
$Tb.N$	trabecular number
$Tb.Sp$	trabecular spacing
$Tb.Th$	trabecular thickness
U	strain energy density
u	strain energy
U_U	inter-implant ultimate energy
U_1	upper segmentation threshold for bare specimens
U_{imp}	upper segmentation threshold for implanted specimens
V	volume
V_l	vastus lateralis
V_m	vastus medialis
W	indentation energy
Δt	iteration time step
ϵ	unit of strain ($\Delta l/l$)

$\bar{\epsilon}$	strain tensor
ϵ_{long}	longitudinal strain
ϵ_{oct}	octahedral shear strain
Φ_{bmd}	field of Bone Mineral Density (BMD) at nodes
Φ_E	field of elastic modulus at nodes
μ_1	mean of the segmentation density histogram (bare specimens)
μ_2	mean of the segmentation density histogram (implanted specimens)
ν	Poisson's ratio
ρ	apparent density
ρ_{bmd}	Bone Mineral Density (BMD)
$\rho_{bmd,c}$	Bone Mineral Density (BMD) of mineralized bone
ρ_c	apparent density of mineralized bone
σ	continuum effective stress
$\bar{\sigma}$	stress tensor
σ_1	standard deviation of the segmentation density histogram (bare specimens)
σ_2	standard deviation of the segmentation density histogram (implanted specimens)
σ_b	stress at bone tissue level
σ_{radial}	radial tension
Ψ	field of stimulus of bone adaptation at nodes
ψ	stimulus of bone adaptation
ψ_a	apposition attractor state stimulus of bone adaptation
ψ_d	damage attractor state stimulus of bone adaptation
ψ_r	resorption attractor state stimulus of bone adaptation
ψ_{ref}	attractor state stimulus of bone adaptation
ψ_U	energy-based stimulus of bone adaptation
ψ_ϵ	strain-based stimulus of bone adaptation
ψ_σ	stress-based stimulus of bone adaptation

List of Abbreviations

3D	three-dimensional
BA	Basal group of specimens
BH	Beam Hardening
BIC	Bone-Implant Contact
BMD	Bone Mineral Density
BMU	Bone Multicellular Unit
CGAL	Computational Geometry Algorithms Library
CT	Computed Tomography
CY	Cylindrical
FE	Finite Element
HA	Hydroxyapatite
II	Inter-Implant
LMAF	Laboratory of Applied Mechanics and Reliability Analysis
LZ	Lazy Zone
mCT	micro Computed Tomography
NS	Non-stimulated group of specimens
P-P	Percent-Percent
ROI	Region of Interest
RVE	Representative Volume Element
SD	Standard Deviation
SEM	Standard Error of the Mean
SLA	Sandblasted, Large-grit, Acid-etched
SNFS	Swiss National Science Foundation
ZOI	Zone Of Influence

Chapter 1

Introduction

1.1 Aims

Orthopedic and dental implants are complex devices designed to support dysfunctional tissue (e.g. osteoporotic or fractured bone) and restore compromised functionalities (i.e. walking or chewing). These prostheses work directly in contact with the living tissues of the human body that are characterized by astonishing abilities to adapt to environmental variables and maintain the homeostasis (i.e. body equilibrium). In particular, the bone tissue grows, is maintained and evolves in relation to physiological feedback processes driven by various stimuli: chemical, hormonal and mechanical among others.

Although the complexity of this mechanism is far from being fully understood, the study of bone adaptation in presence of an implant is fundamental to the efforts of improving and extending the prosthesis operation, to promote innovative designs and to optimize rehabilitation therapies.

This is the context in which this work has been developed. In this chapter, the motivations, objectives and structure of this thesis follow an introduction concerning:

- Implant biomechanics and related problems in orthopedics, dentistry and research.
- Osseous tissue anatomy and homeostasis.
- Experimental, theoretical and numerical approaches that concern the study of peri-implant bone adaptation to the mechanical environment.

1.2 Implants biomechanics

An implant is a medical device conceived to be surgically inserted in living tissues to support or replace an existing organ. The complexity of these devices depends on the application, and ranges from biocompatible objects with structural functions to complex electronic devices. Indeed, the scope of these devices are various: they allow recovering weakened senses (e.g. intraocular lens and cochlear implants to treat cataracts or hearing impairment, respectively), to control vital processes (e.g. pacemakers) and to restore structural, load-bearing functions.

The latter scope involves the *osseointegration* process, that is “the formation of a direct interface between an implant and bone, without intervening soft tissue” (Miller et al., 2003). The success of this process influences firstly the patient safety, secondly the actual recovery of the function set as goal, and finally the short and long term post-operation assistance. The human and economic impact of surgical procedures involving implants housed in bone directly depends on the understanding of the osseointegration process. Although this theme concerns consolidated orthopedic and dentistry procedures, it is still an important issue of scientific research and discussion.

1.2.1 Orthopedics

Implants are widely adopted in orthopedics, with a variety of designs, materials and functionalities. The main applications concern the support of damaged bone and the replacement of joints.

Bone fractures consist in loss of continuity in bone tissue due to severe injury or diseases. The large variability of damage sizes and configurations lead to several healing strategies. Non-invasive methods, such as immobilization or external fixtures, may be ineffective in case of serious bone fractures, which are treated through surgical procedures involving nails, screws and plates. These components are employed to align the detached bone compartments and share the load with the injured tissue, and in some cases their function is permanent Figure 1.1a.

Joint prostheses are designed to replace damaged or dysfunctional articulations, as knee, hip and shoulder joints. Although this treatment consists in an invasive solution to painful diseases, often not resolvable with less invasive medical care, it is characterized by high rates of success and long term reliability. Nowadays, hip and knee replacements are considered as standard orthopedic procedures and their occurrence is monotonically increasing (Figure 1.1d). As a matter of fact, the indications for joint replacement in case of osteoarthritis or rheumatoid arthritis are correlated with the growing aging of the population, which implies an increasing occurrence of these diseases. Depending on the surgical techniques adopted to perform joint replacements, part of bone tissue is removed

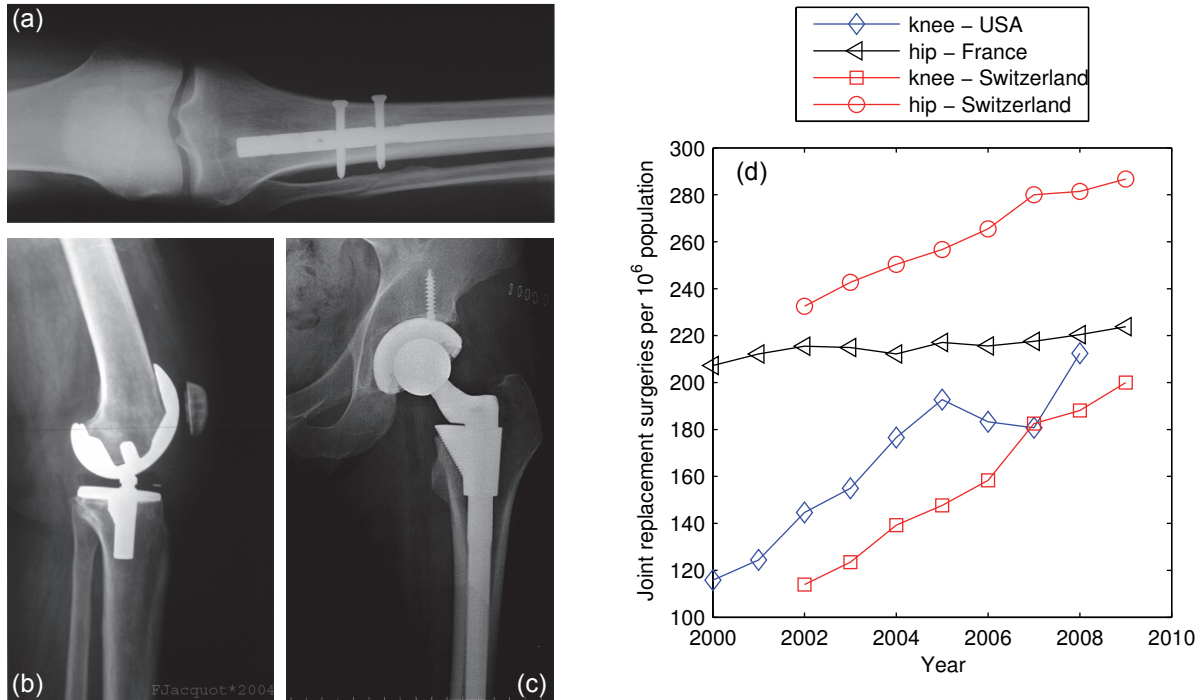


Figure 1.1: X-ray images showing (a) titan nail and screws in human tibia, (b) total knee replacement and (c) total hip replacement. (d) trend of joint replacement surgeries¹.

to allow placing the prosthesis. For example, in total knee replacement the distal end of the femur and the proximal end of the tibia are cut to fit the implants shape, previously adapted to the patient anatomy (Figure 1.1b). In total hip replacement, bone tissue is removed on both pelvis and femoral head, to create the place for the acetabular cup and the femoral stem (Figure 1.1c). The implant stability is consolidated through cements or obtained without intermediary materials, namely through osseointegration.

1.2.2 Dentistry

Dental implants have been adopted since several decades to replace missing teeth, and are also employed as orthodontic anchors or support for dentures and bridges (i.e. multiple tooth prosthesis, Figure 1.2a). Nowadays, orthodontic procedures involving dental implants are performed with good success rates. Their function is granted by an assembly of different components, as shown in Figure 1.2b. Indeed, an implant is inserted in the jaw bone and acts as replacing root, while the abutment allows fixing the external crown or bridge to the osseointegrated component.

¹(a), (b), (c) are adapted from en.wikipedia.org; (d) is adapted from www.oecd-ilibrary.org.

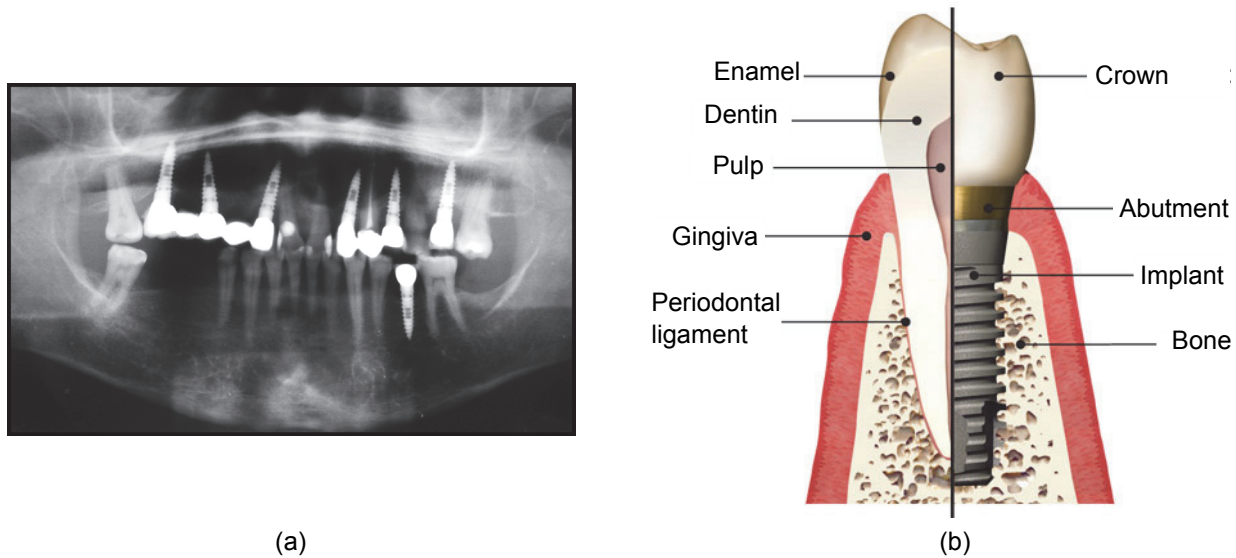


Figure 1.2: (a) X-ray image of a mouth with several implants. (b) Tooth anatomy and dental implant comparison².

The implants are inserted through one- or two-stage surgical techniques, depending on the clinical case. In the one-stage procedure, the implant is inserted in the jaw cavity, carved through a slow-speed driller, and connected to a healing cup protruding from the gingiva. Abutment and crown are placed after 3-6 months of healing. In the two-stage procedure, the gingiva is sutured over the implant for the whole healing period and a new incision is needed to place the healing cup. Abutment and crown are placed only after the full recover of the gingiva. This technique is preferred when the bone quality of the implantation site is not optimal. As a matter of fact the success of dental implants depends on both the bone structure of the patient and the strength of the osseointegration.

1.2.3 Complications of osseointegrated implants

In both orthopedics and dentistry, the implant life span and its performance are affected by several factors: human, procedural and biomechanical among others. Certainly, the human factor (e.g. the surgeon experience and the patient respect of the prescribed therapy) has a strong influence on the result. Furthermore, short- and long- term complications are often related to infections initiated by contamination during surgery. However, the occurrence of these complications continuously decreases thanks to the definition of rigorous procedures and practices (Witjes et al., 2007). Finally, the long-term success of implants depends on

²(a) is adapted from en.wikipedia.org; (b) is adapted from misch.com

the biomechanical interaction with the surrounding tissue. As a matter of fact, both dental and orthopedic implants are conceived to restore structural functions by sharing loads with the bone tissue.

Dental implants restore the patient's biting ability without reproducing the whole tooth structure. Indeed, the pressure-sensitivity granted by the periodontal ligament is not preserved (Figure 1.2b) and bone is directly in contact with the implant (Ramfjord and Ash, 1979). Thus, the patient may unconsciously expose the surrounding bone tissue to high stresses while eating or grinding (Brånemark et al., 1985). An unfavorable mechanical environment may lead to the implant failure or the gradual loss of adjacent bone, with negative effects on the crown stability. Certainly, the strength of the osseous tissue is a key factor to achieve a good implant fixation (Palacci, 1995), as well as the primary stability, which is the immediate mechanical engagement between the implant and the bone tissue. With a loose coupling the chances to obtain a satisfactory stability are definitely reduced (Javed and Romanos, 2010).

A good primary stability is required also in orthopedic surgery. Indeed, screws, nails and cement-less femoral stems are inserted without intermediary adhesive material, and their osseointegration depends on the initial engagement with bone. However, the short-term success of integration does not prevent the occurrence of long-term complications. Usually, the life-span of orthopedic prosthesis is not expected to cover the entire patient's life. After about 10-15 years, implant failures or bone weakness can cause pain and a mobility reduction, imposing a surgical revision. Both success rate and reliability of this operation are lower compared to the initial one. Moreover, the costs for the hospitalization, surgery and patient care notably increase considering that the operation concerns the same initial problem. The principal reason of these problems is loosening: implants lose their adhesion with bone and move within their houses, potentially provoking pain and bone fractures. From the mechanical point of view, this phenomenon occurs because part of the bone tissue surrounding the implant is resorbed (Huiskes et al., 1987), depriving the prosthesis of the needed support. Moreover the increasing relative movement between the implant and the bone tissue may rise up to deleterious levels (Jasty et al., 1997). Nowadays, this state is not reversible and the revision surgery can be delayed but not avoided.

1.2.4 Implants in research

The improved design of implants and the optimization of healing therapies are key factors of the increasing reliability of orthopedic and dentistry procedures. Improvements and problems that concern osseointegrated implants interest research groups worldwide (Goodacre et al., 1999). The quality of implants integration is investigated since years through pre-clinical animal models (Stadlinger et al., 2012). The goal is to highlight the

optimal conditions granting the implantation success, by investigating the pre-requisites for bone formation: material, design, surface, status of bone, surgical technique and loading condition (Albrektsson, 2008). An overview of the fields of research is reported hereafter:

Diseases. Bone health is important to grant a good integration. As a consequence, systemic diseases and metabolic disturbances may interfere with the tissue recovering ability, compromising the implant stability. Several studies report the implants integration in presence of diseases as diabetes and osteoporosis (Fiorellini et al., 1999, Glosel et al., 2010, Viera-Negrón et al., 2008) and systemic treatments (Ammann et al., 2007, Dayer et al., 2006).

Drug delivery. The early implant integration is improved by systemic treatments promoting the osteogenesis (Ammann et al., 2007, Dayer et al., 2006). Moreover, recent studies on local treatments involve the drug delivery only in the peri-implant area (Peter et al., 2005, Pioletti et al., 2008, Stadelmann et al., 2008), reducing the drawbacks related to systemic therapies (Dannemann et al., 2007).

Secondary stability. While the primary stability depends on the immediate mechanical engagement between the implant and the bone seat, the secondary stability requires the establishment of a resistant bone-implant adhesion. To this goal, the implant's surface is determinant. Several investigations have been performed to evaluate the performance of surface morphologies (Cochran et al., 1996, Gross et al., 1987) and osteogenic coatings (Durual et al., 2013, Hara et al., 1999, Jaatinen et al., 2011)

Fracture healing. The healing process of fractures requires optimized components to preserve the alignment of the bone fragments and promote the tissue regeneration (Mirhadi et al., 2013). This theme is investigated through studies on bone defects involving fixations, such as locking plates and intra-medullary rods, which require osseointegration to work (Histing et al., 2011).

These research efforts pursue a clear goal: improve the implants' efficiency in working conditions, i.e. as structural supports subjected to stress due to the living host activity. As a matter of fact, both clinical and research applications require implants to be subjected to mechanical environments generated during the everyday activities (e.g. walking, stair climbing and biting). These are the conditions in which the bone-implant 'assembly' must grant stability and reliability. Since several individual-based factors affect the success of implantations (e.g. age, bone structure and diseases), challenging issues concern the definition of implants' designs and post-surgery treatments that can be adapted to the patient's needs.

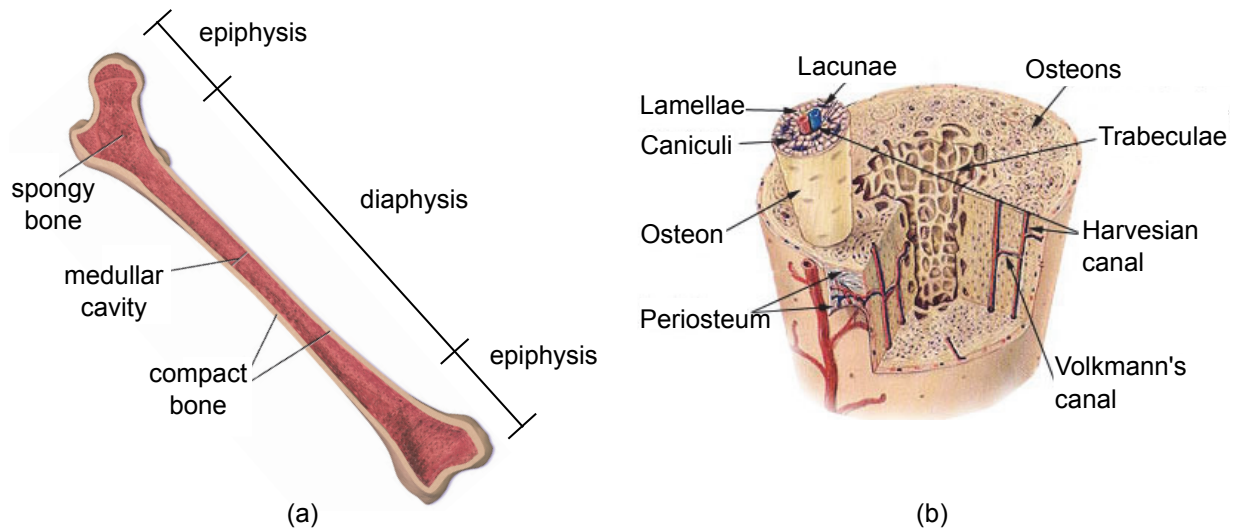


Figure 1.3: (a) long bone structure. (b) bone composition. Adapted from *en.wikipedia.org*.

1.3 Bone tissue

The osseous (i.e. bone) tissue is the most important connective tissue of the human body and represents the rigid part of bones framing the skeleton. This tissue is composed of different types of cells embedded in a collagen matrix impregnated by mineral phases, mostly hydroxyapatite, which lends mechanical strength and robustness to bones.

Four main functions are directly attributable to the bone tissue: (i) protection of vital organs (e.g. heart and lungs), (ii) support of the body, (iii) leverage for muscle activation and movements, (iv) mineral reserve (e.g. calcium phosphate). Moreover, the production and regulation of blood cells depends on the red marrow stored inside bones. These functions are the outcome of the macro- and micro-structural differentiation of the osseous tissue, briefly presented in the following sections.

1.3.1 Cortical and trabecular bone

As shown in Figure 1.3a, bone can be classified in two tissues: cortical (i.e. compact) and trabecular (i.e. spongy).

Cortical tissue constitutes the outer cortex of bones and represents the 80 % of the total skeleton's weight. In diaphyses (i.e. central part of long bones) the mechanical strength of cortical bone provides the appropriate resistance to torsion and bending occurring during movements (Figure 1.3b). The cortex is covered externally and internally by two collagen membranes, the periosteum and the endosteum, which regulate the bone interchange with the outer body elements. The cortical bone is composed by functional units aligned

along the longitudinal direction and named osteons: concentric layers of lamellae, spaced by canaliculi and surrounding the Haversian canal. The osteons are interconnected by Volkmann's canals along the transverse plane. Despite the macroscopically uniform appearance, the cortical tissue can be compared to a complex multiscale, poroelastic material where solid and fluid phases have equivalent relevance.

Trabecular bone represents only 20 % of the skeleton weight, nevertheless it performs important tasks. Its structure is comparable to a complex reticulum composed by structural units, the trabeculae, which are characterized by different shapes, sizes and orientations depending on bones. The main structural role of this scaffold is to distribute compressive loads occurring in epiphyses of long bones composing joints and in vertebrae. Moreover, the inter-trabecular cavities host the red marrow, which has the function of producing blood cellular components.

From the mechanical point of view, both tissues show an inhomogeneous anisotropic elastic behavior at low frequencies ($\sim 1 - 3$ Hz, compatible with most of the everyday activity as walking or biting), with properties dependent on the bone volume fraction and on the orientation and mineralization of their structural units (i.e. osteons and trabeculae). This dependence implies a wide spectrum of mechanical responses depending on the location within the skeleton, on the differences between individuals and species (Cvetkovic et al., 2013).

1.3.2 Bone cells

The cellular activity in bones is driven by complex bio-chemical phenomena involving hormones, proteins and growth factors. Bone cells are classified in four main families:

Osteoblasts. These mono-nucleated cells produce new bone synthesizing a dense extracellular reticulum of collagen fibers, named osteoid. Mineralization of osteoid provides the bone tissue with stiffness. Osteoblasts work in groups and some of them remain embedded in the bone matrix becoming osteocytes.

Osteocytes. These cells are embedded in the bone matrix, housed in lacunae between layers of lamellae and connected by canaliculi. This cellular reticulum is indicated as the sensorial network driving the bone tissue growth and maintenance by cellular processes transmitted through canaliculi and captured by osteons.

Osteoclasts. These multi-nucleated cells destroy both organic and inorganic bone components. Osteoclasts attack the bone surface by sealing the tissue underneath and releasing acid to dissolve it.

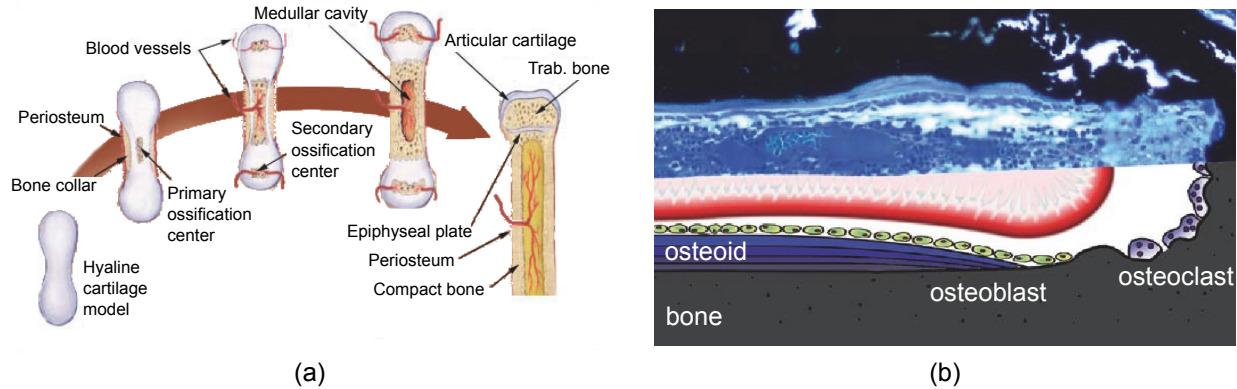


Figure 1.4: (a) bone modeling during growth (adapted from *en.wikipedia.org*). (b) Bone Multicellular Unit (adapted from Robling et al. (2006)).

Lining cells. These cells cover the bone surfaces. In case of osteoclasts' activity, lining cells retract from the tissue surface to leave osteoclasts attack bone. Highly interconnected to the osteocytes through the canalicular network, lining cells are indicated as quiescent osteoblasts.

1.3.3 Modeling and Remodeling

The formation and maintenance of the skeletal structure are performed through two distinct processes: bone modeling and remodeling (Frost, 1990a,b). Although both are the result of the cellular activity previously described and grant the osseous tissue's functions, modeling and remodeling are characterized by different working principles.

Bone modeling takes place especially during the growth age and allows the skeleton structure to adapt to the increasing mechanical demand characterizing the organism development (Figure 1.4a). As a matter of fact the increasing body mass, volume and muscles activity require a solid and optimized framework to correctly perform the daily activities. Thus, bone modeling involves a perceptible skeleton variation (i.e. concerning both size and shape) obtained through the combination of tissue apposition and resorption on free surfaces. For example, in long bones this process occurs along the longitudinal direction through the lengthening of the diaphysis. At the cellular level, bone modeling involves both osteoclasts and osteoblasts but not at the same location. This process nearly stops when the growth age ends and the skeleton reaches its complete maturity. Nevertheless, bone modeling may be reactivated during the whole life if the skeleton requires structural adaptation (e.g. because of injuries, diseases or hard workout).

Bone remodeling is the process in charge of the skeleton maintenance and repair. Different from modeling, this process involves a precise sequence of resorption and apposition at

the same location, which provides the replacement of old tissue with new one, without significant variations of the net mass balance. Remodeling is carried on by Bone Multicellular Units (BMUs): groups of cells ‘traveling’ along the bone structure (Figure 1.4b). These units dig canals within the cortical bone or replace the trabecular surfaces with the same mechanism, structured in three phases: resorption, reversal and apposition. Osteoclasts are charged of the first phase, generating the resorption cavity that is successfully lined by mononuclear cells during the reversal period. Even if the cellular dynamics of these cells has not been clarified, they precede the bone apposition phase in which osteoblasts deposit layers of osteoid concentrically. In cortical bone, the center of the hole is left empty and becomes a Haversian canal. The balance between bone resorption and apposition are important to preserve the skeleton structure. Several diseases provoke an unbalanced bone deposition, i.e. a discrepancy between the replaced and added amount of bone, that can lead to bone fractures (e.g. osteoporosis).

1.4 Bone mechanical adaptation

The mechanical environment drives the skeleton development during growth and preserves its influence on bone adaptation during the whole life. Several phenomena related to particular mechanical environments highlight the persistence of this dependence. An evident case is the loss of mineral content characterizing bones of astronauts during space flights (Sibonga et al., 2007). The absence of gravity eliminates the deformation normally occurring on bone because of body weight and muscular activity, and the organism reacts by weakening the unloaded tissue. Notably, the loss of bone mineral content occurs also in ordinary conditions, such as limb immobilization (Sato et al., 1998) or bed rest (Figure 1.5a). Similarly, bones subjected to an intense mechanical environment adapt by increasing their strength, as it happens to runners and soccer players (Fredericson et al., 2007) (Figure 1.5b).

Implanted bones are not exempted from this logic. Actually, the insertion of an orthopedic or dental prosthesis radically changes the stress state of the surrounding osseous tissue, often initiating an adaptation process that can be detrimental to the implant stability on the long term. Indeed, implants are designed as compact and rigid elements (e.g. stems, pins, screws) made of stiff materials (e.g. titanium alloys) to provide reliability and resistance. Notably, from the mechanical point of view this design highly differs from that of the osseous tissue, which is flexible, porous and adjustable. As a consequence, the deformation occurring on implanted bones is really different from healthy ones. Clinically, the identification of validated rules and models for the prediction of bone adaptation is crucial to improve the implants design and healing therapies.

Since Roux (1895) and Wolff (1986) postulated the existence of mathematical laws

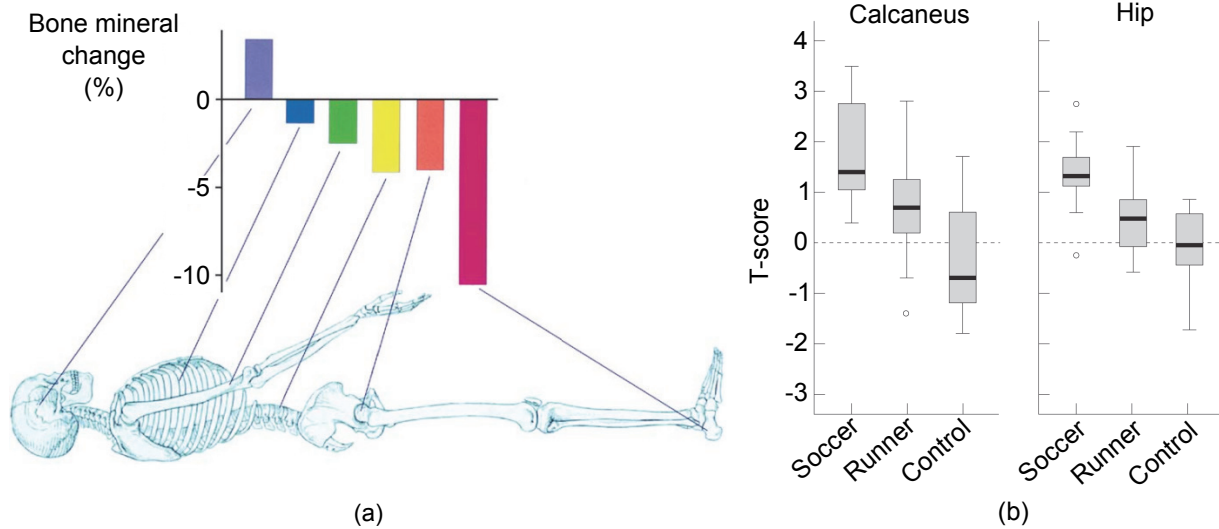


Figure 1.5: (a) bone mineral change after 17 weeks of bed rest (adapted from Robling et al. (2006)). (b) T-score of calcaneus and hip in runners and soccer players compared to controls (adapted from Fredericson et al. (2007)).

driving the bone biological adaptation as a function of the mechanical environment, many efforts have been addressed to understand the numerous processes involved in this phenomenon.

Several investigations show that dynamic deformations lead to bone formation while nearly no effects are generated by static loads (Lanyon and Rubin, 1984, Lisková and Hert, 1971). Indeed, bone tissue reacts to the external stimulation in case of high strain applied at physiological frequencies (e.g. 2000-3000 microstrain at 1-3 Hz, Rubin and Lanyon, 1984, Turner et al., 1994a), but also to low strains applied at high frequencies (e.g. ≤ 5 microstrain at 10-50 Hz, Ozcivici et al., 2010).

The number of loading cycles also affects the results. Bone response tends to decrease with an increasing duration of the stimulation because of the saturation of the cells mechanosensitivity (Robling et al., 2001). Thus, an efficient stimulation must account for the alternation of loading and rest sessions, to allow the cells to recover. Notably, inserting the rest period between the load cycles, not only at the end of the stimulation, greatly enhanced osteogenesis (Srinivasan et al., 2002). These findings are perfectly summarized through the three rules proposed by Turner (1998):

1. “Bone adaptation is driven by dynamic, rather than static, loading.”
2. “Only a short duration of mechanical loading is necessary to initiate an adaptive response. Extending the loading duration has a diminishing effect on further bone

adaptation.”

3. *“Bone cells accommodate to a customary mechanical loading environment, making them less responsive to routine loading signals.”*

These rules are actually descriptive of the everyday mechanical environment to which the bone tissue is subjected to. As a matter of fact, the daily activities involving a cyclic stimulation, such as walking and biting, are limited to short time periods and alternated with rest.

Moreover, investigations on overloading environments highlight the detrimental effects of stimulations overcoming certain thresholds. This theme is widely investigated on dental implants: these prostheses are often subjected to conscious and unconscious high loads that may provoke marginal bone loss (Isidor, 1997). Indeed, an intense axial loading of the prosthesis provokes peri-implant bone loss (Hoshaw et al., 1994) and the rejection is observed in case of excessive premature occlusal contacts (Isidor, 1996).

These results highlight an ample spectrum of possibilities to perturb the bone structure through the modulation of load level, frequency and number of cycles experienced by the osseous tissue. This is reflected in the large number of experimental, theoretical and numerical methods developed to investigate these relevant issues.

1.4.1 Experimental approaches

Experiments conceived to study bone adaptation are based on in~vivo animal models characterized by modified mechanical environments, obtained through movement’s prevention, physical activity, implants or external loading. Small animals as mice, rats and rabbits are preferred due to several reasons: they ensure the study of large populations, possibly with controllable genetic backgrounds, and they allow easy handling and feeding with limited costs. The features of the animal models commonly adopted in literature are summarized in Table 1.1 and described here:

Suspended-tail model. Rats are suspended by their tail, preventing the hindlimbs’ contact with the ground and unloading the animal’s hindquarters (Figure 1.6a, Globus et al., 1984). This model is adopted for studies on the effects of weightlessness and disuse on bone metabolism (Barbosa et al., 2011, David et al., 2003, Machwate et al., 1993).

Limb overload model. One rat hind limb is immobilized and secured to the rat abdomen, while the animal locomotion is not constrained. Thus, the full bodyweight is charged on the free limb. The former limb evolves because of disuse while the latter because of overloading (Jee and Li, 1990).

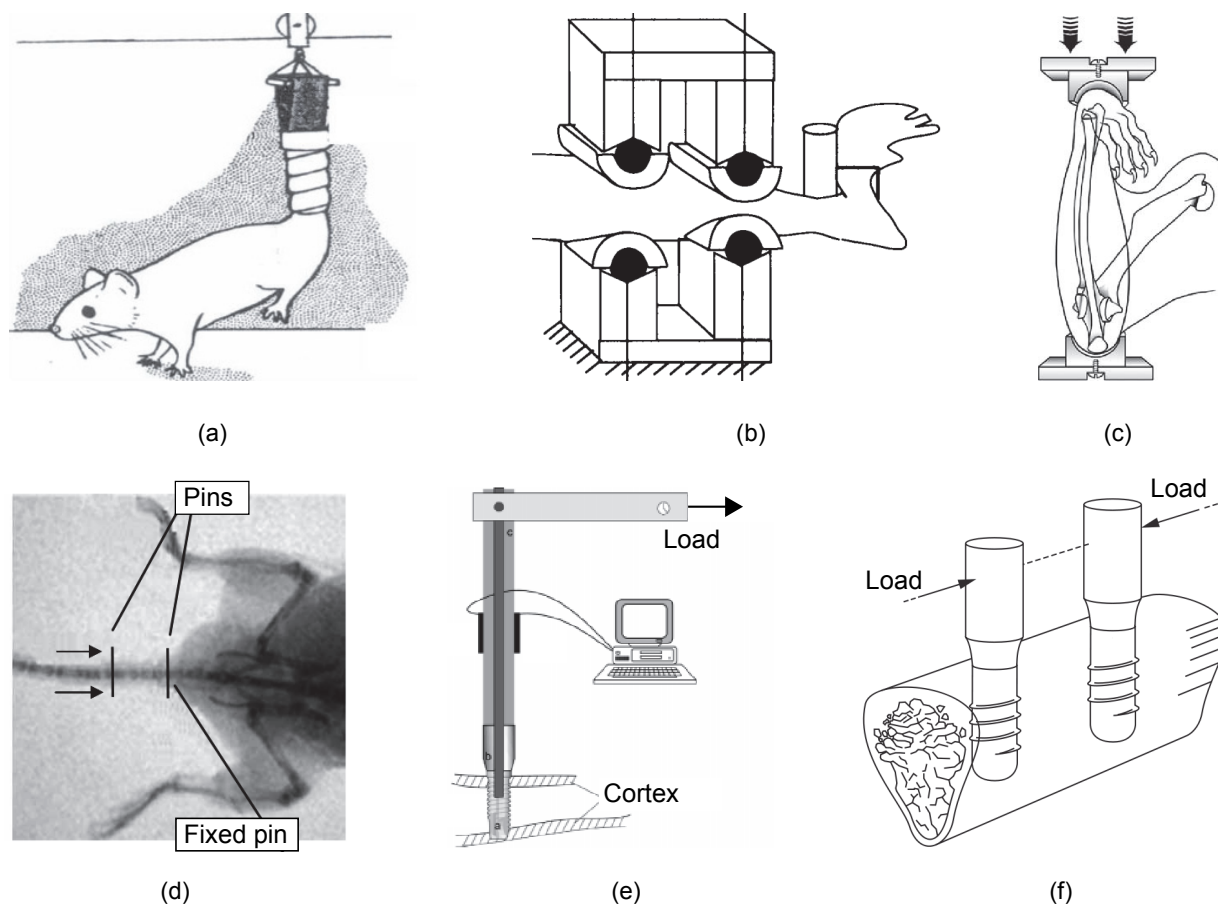


Figure 1.6: Overview of animal models for studies on bone mechanical adaptation: (a) suspended tail (Barbosa et al., 2011), (b) four point bending (Turner et al., 1991), (c) compressed ulna (Robling et al., 2002), (d) compressed vertebra (Webster et al., 2008), (e) activated implant (Duyck et al., 2001) and (f) loaded implants (Wiskott et al., 2008).

Jumping model. Rats are electrically stimulated to jump at different heights and frequencies. This model provides data on the bone mass evolution because of intense physical activity (Ooi et al., 2009, Umemura et al., 1997).

Running model. Rats or mice are trained to run on treadmills. Once they tolerate the exercise, different training programs are applied, with variable duration, running speed and weekly cadence. The effects of running activities and post-training sedentarism are analyzed (Fujie et al., 2004).

Four-point bending model. A tibia of mouse or rat is subjected to loading cycles provided through a four point bending set-up (Figure 1.6b, Akhter et al., 1992, Turner et al., 1991). The animal is anesthetized during stimulation and free to move in

its cage otherwise. These models allow the quantitative monitoring of the external stimulation and an individual-based comparison (i.e. one tibia is stimulated and the other is kept as control).

Compressed ulna. The rat ulna is compressed along its longitudinal direction through loading machines which allow controlling the force, frequency and loading cycles (Figure 1.6c, Robling et al., 2002). A similar stimulation is adopted for the mouse's tibia (Stadelmann et al., 2011). Similarly to the previous model, the animal is anesthetized during stimulation and left unconstrained otherwise.

Compressed vertebra. Two pins are inserted into the rat's caudal vertebrae, by leaving a bare one in the middle. The pins are pulled each other and the intermediate vertebra is subjected to compression (Chambers et al., 1993). Recently this model has been adapted for mice (Figure 1.6d, Webster et al., 2008). This test allows the quantitative monitoring of the external stimulation and a reduced influence of the daily activity (i.e. the tail is mostly employed to maintain the equilibrium and has no weight-bearing function). Only the intermediate vertebra is analyzed.

Activated implant. Single dental implants are inserted in tibiae of dogs (Hoshaw et al., 1994), rabbits (Figure 1.6e, Duyck et al., 2001) or guinea pigs (De Smet et al., 2005), and controlled loads are applied directly to the prosthesis, which transfer the stress to the bone tissue. Implants are subjected to axial loads (Leucht et al., 2007), torsion (Van der Meulen et al., 2006) or bending (De Smet et al., 2006). A similar approach is adopted in the 'loaded implant' model: two implants are screwed mono- and bi-cortically into the tibia of rabbits or rats and a controlled external stimulation forces the implant's heads together (Figure 1.6f, Wiskott et al., 2008, 2012).

These animal models are employed on individual- or group-base. The former entails the treatment of single animals at one time, thus producing results highly dependent on the subject characteristics and without statistical relevance. This strategy is chosen in case of high costs (e.g. genetically modified animals) or when the planned analysis is too much demanding for several subjects (e.g. *in-vivo* X-ray longitudinal follow-up). The latter involves multiple animals at one time, often divided in groups subjected to different treatments. These analyses provide results with statistical relevance and are employed to estimate the effects of the therapy on the selected population.

Table 1.1: Features of animal models described in literature.

Model	Settings				Stimulation			Output	
	Animal	Implants	Daily activity	External load	on bones	on implants	Bone adaptation	Implant integration	
Suspended-tail ¹	rat	×	×	×	×	×	✓	×	
Limb overload ²	rat	×	✓	×	✓	×	✓	×	
Jumping ³	rat	×	✓	×	✓	×	✓	×	
Running ⁴	rat	×	✓	×	✓	×	✓	×	
4-point bending ⁵	rat, mouse	×	✓	✓	✓	×	✓	×	
Compressed ulna ⁶	rat, mouse	×	✓	✓	✓	×	✓	×	
Compressed vertebra ⁷	rat, mouse	✓	✓	✓	×	✓	✓	×	
Activated implant ⁸	various ^a	✓	✓	✓	✓	✓	✓	✓	

^a mouse, rat, guinea pig, rabbit, dog.

¹ David et al. (2003), Globus et al. (1984), Machwate et al. (1993).

² Jee and Li (1990).

³ Ooi et al. (2009), Umemura et al. (1997).

⁴ Fujie et al. (2004).

⁵ Akhter et al. (1992), Turner et al. (1991).

⁶ Robling et al. (2002), Stadelmann et al. (2011).

⁷ Chambers et al. (1993), Webster et al. (2008).

⁸ De Smet et al. (2005), Duyck et al. (2001), Hoshaw et al. (1994), Leucht et al. (2007), Van der Meulen et al. (2006).
Wiskott et al. (2008, 2012).

The design strategy of the presented animal models is justified by the complexity of the observed phenomena and the necessity to reduce the dependence of results on uncontrolled factors. Each test is conceived to perturb the bone homeostasis internally or externally (i.e. through musculoskeletal or external loads) provoking a selected mechanical environment (i.e. disuse, physical exercise or overloading) and reporting a specific output (i.e. bone volume and mineral content, histological structure or osseointegration), with consequent limitations.

The models based on the animal's physical exercise produce effects dependent on the training protocol, but they are difficultly correlated to the local deformation experienced by the osseous tissue. This drawback is overcome through designs involving the stimulation of selected organs through appropriate setups delivering controlled loads. This strategy allows investigating the effects of the external stimulation without conditioning the animal daily activity. However, these experiments involve limitations in studies on implants integration. Although implanted bones may be studied, the absence of direct loads applied to the implants limits their role to stress concentrators. The pertinence of these analyses is unquestionable, but the load-bearing function of dental and orthopedic implants is not represented.

The compressed vertebra model involves the direct loading of implants, but the effects of the daily activity are limited because the tail is not directly involved during gait. Moreover, only the intermediate (i.e. bare) vertebra is investigated while the effects of the mechanical stimulation on the implanted vertebrae are not documented.

The animal models involving loaded implants inserted in limb bones are less affected by limitations. The implant transfers monitored loads to the osseous tissue, which is also stimulated by the musculoskeletal loads acting on the limb during the animal daily activity, thus involving a different stress distribution with respect to bare organs. These features actually mimic the working condition of orthopedic and dental implant, but they also involve relevant difficulties to analyze and discriminate the effects of all the factors. Indeed, the outputs of these studies are often limited to the positive or negative effects of the external loading condition on the osseointegration and the biomechanical system is not entirely investigated.

1.4.2 Theoretical approaches

The complexity and multiplicity of processes characterizing bone mechanical adaptation stimulated the researcher inventiveness. In the last decades, several attempts to theoretically describe this phenomenon have been formalized and discussed within a diversified community, composed by biologists, medical doctors, dentists and engineers. Two main approaches can be identified: mechanistic and phenomenological.

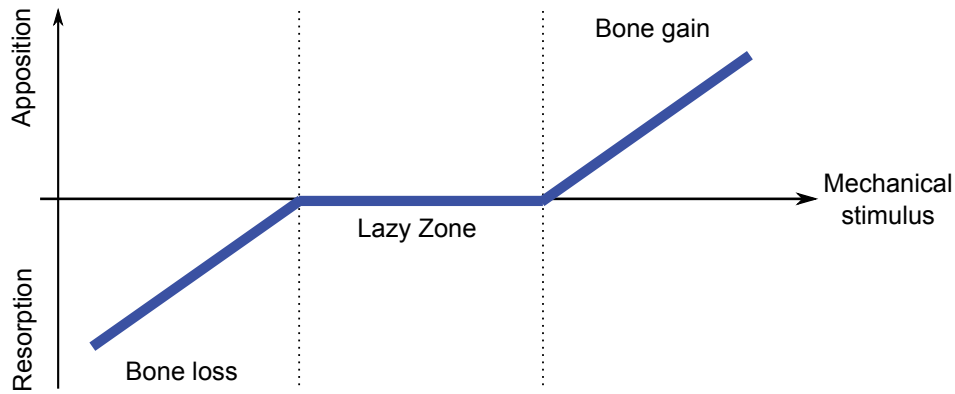


Figure 1.7: *The Mechanostat: a biological response (i.e. bone apposition or resorption) is generated depending on the mechanical stimulus. If the stimulus falls within the Lazy Zone, apposition and resorption are in equilibrium.*

The mechanistic approach aims at clarifying the detailed physiology of the phenomenon, from the molecular and cellular scale to the macroscopic bone structure. This is the most difficult way to proceed, because each step of the process needs to be investigated, understood and linked to the others. At the present state, research groups are mainly focused on single sub-processes (i.e. metabolic pathways and cellular regulation) while their multiscale interconnection is not established yet. However, several mechanistic theories have been proposed (e.g. Hambli and Rieger, 2012, Paoletti et al., 2012, Peterson and Riggs, 2010).

The phenomenological approach aims at explaining the bone adaptation as a result of experimental observations, even if their intrinsic working principles have not been clarified. Theories belonging to this category are of easier implementation with respect to the former one, because they generally require the identification of fewer parameters. For this reason these models are applicable to single-scale problems (i.e. macro, micro or cellular) without considering the complete hierarchy.

Among other phenomenological approaches, the research community mostly agrees upon the Mechanostat theory (Figure 1.7). Formulated by Frost (1987), this theory relies on two main working hypotheses. First, under normal conditions the mechanical stimulus occurring in bone falls within a certain range, named Lazy Zone (LZ). In this situation, the bone tissue is sustained by the remodeling: apposition and resorption are balanced and the total rate of bone mass does not change. Second, if the mechanical stimulus is beyond or below the lazy zone, the system triggers a biological response to recover the mechanical homeostasis by unbalancing the bone turnover in favor of apposition or resorption, respectively.

This theory is compatible with the majority of the experimental results on bone mechanical adaptation retrieved in literature and is considered as a milestone of the phenomenological approaches in this field of research. Moreover, its generic formulation permits different interpretations and implementation strategies, classifiable in three main categories depending on the available inputs and the desired output (Zadpoor, 2013):

I. Parameter identification. Studies belonging to this category focus on the estimation of parameters necessary for the implementation of adaptation models. Usually, this procedure requires on-purpose experiments providing accurate results, that are processed for the identification of the model's parameters (Lambers et al., 2011, Terrier et al., 2005). This strategy is accurate but expensive and time consuming, thus it is often eluded by adapting parameters available in the literature or performing trial and error estimations. Both choices involve a lack of experimental validation that may affect the results.

II. Load estimation. This category includes analysis for the estimation of loading conditions mimicking daily activities. The working principle is the following: considering that the mechanical environment affects the bone structure, the density and structure of bones provide information about their loading history (Bona et al., 2006, Campoli et al., 2012, Kenneth et al., 1995). This approach provides quantifications of musculoskeletal loads otherwise retrievable from inverse dynamic analysis.

III. Tissue response prediction. This category is the most explored and involves the investigation of the tissue adaptation to the mechanical environment. The loading condition, the parameters and the initial bone structure constitute the input of the analysis, while the tissue evolution is the output. Both physiological (Beaupré et al., 1990b) and external (Chennimalai Kumar et al., 2010) loads can be considered. Several models adopt an initial condition not representative of the bone real structure and investigate the model capability to produce a result consistent with reality (Mullender and Huiskes, 1995). Other approaches are focused on the influence of therapies (Stadelmann et al., 2009) or prosthesis (Terrier et al., 1997).

Despite their versatility, phenomenological approaches such as the Mechanostat often rely on strong assumptions. Moreover, the robustness of their predictions is rarely verified, because studies concerning the dependence of results on key hypotheses are scarce (Cox et al., 2011). An important open question concerns the mechanical variable chosen as triggering signal. Several investigation on magnitudes such as strain (Frost, 1983, Weinans et al., 1992), strain energy density (Huiskes et al., 1989), stress (Beaupré et al., 1990a, Carter et al., 1989), fluid flow (Lacroix and Prendergast, 2002a, Weinbaum et al., 1994) and micro-damage (Doblaré and García, 2002, McNamara and Prendergast, 2007) lead to

interesting results in specific applications, but there is no agreement on which one provides a better performance. Furthermore, the spectrum of mechanical stimulation is often limited and the harmful effects of overloading are neglected. Only few works consider the damage provoked by high levels of stimulation, which is crucial in particular to predict the bone adaptation around dental implants (Crupi et al., 2004, Li et al., 2007, McNamara and Prendergast, 2007, Van Oosterwyck et al., 1998).

1.4.3 Numerical approaches

From the numerical point of view, the phenomenon of bone mechanical adaptation can be approximated by an iterative, structural optimization process that follows the Mechanostat principle. As a consequence, the implemented frameworks rely on feedback loops where structural variables are updated in relation to a mechanical signal, monitored through convergence criteria. The criteria are based either on the mechanical signal (e.g. the convergence is reached when the signal achieves a certain value) or on structural variables (i.e. the convergence is achieved when the bone adaptation ends).

Bone reaction to stimulation is expressed in terms of mass modifications or structural realignment. In ‘external’ adaptation models the bone density is fixed while its geometry is variable, thus the volume of tissue is modified to fit the defined criteria while bone material properties are preserved (Helgason et al., 2008). This technique is implemented to predict periosteal bone apposition (Chennimalai Kumar et al., 2010, Martínez et al., 2006). In ‘internal’ adaptation models the geometry is invariant and the bone density is updated in relation to the mechanical environment. This implementation is preferred when dealing with implants integration at the macroscopic scale (Pioletti and Rakotomanana, 2004, Skinner et al., 1994, Terrier et al., 1997). Bone anisotropy may be accounted through fabric tensors (Cowin, 1985), also realigned depending on the mechanical environment.

Finite Element (FE) models are usually adopted as a numerical tool for the calculation of the mechanical signals, such as strain and stress, because of their ability in reproducing complex geometries. However, the bone complexity and multiscale heterogeneity imply relevant computational costs. As a consequence, several simplified approaches are proposed, focusing the interest to different length scales:

Continuum-level. This strategy assumes bone to be a continuous medium. Usually employed for studies on whole bones, these models assure consistent results with relatively low computational costs, but the output is limited to the organ macro-scale. Indeed the trabecular reticulum is not resolved, but represented by local mechanical properties depending on the tissue density or texture. These models are often adopted as a reference for ‘internal’ adaptation analysis (e.g. Beaupré et al., 1990b), where bone modeling is performed by varying the local density field.

Micro-structural. This approach geometrically resolves the complete trabecular structure, with no simplifications. The material properties of the tissue are preserved while the ‘external’ adaptation modifies the problem geometry by updating the FE mesh. The advantage of these models is the high detail level (e.g. Schulte et al., 2013). However, they require such a high computational time that whole bones micro-structural models are still beyond the capability of present-day computers.

Multi-scale. Multi-scale models attempts to solve problems that have important connections with different spatial scales. Sub-modeling techniques are adopted to transfer field of deformation from a macroscopic, general model to a microscopic, detailed region (Be’ery-Lipperman and Gefen, 2006). Homogenization methods are widely used to predict homogeneous responses of trabecular bone by studying its intricate micro-architecture (Verhulp et al., 2008).

Numerical approaches allow exploring a wide spectrum of phenomena concerning cells, tissues and whole bones. As a matter of fact, numerical models are often the only solution to estimate bone deformation in locations where it is nearly impossible to plan experimental investigations. Their potential grows with advancements concerning specimen-specific procedures, where models are generated by reconstruction from imaging data (e.g. X-ray scans). From the clinical point of view, specimen-specific FE models may improve the diagnoses and treatments of several pathologies. However, the interest for these techniques is associated to criticism about the accuracy of the predictions they provide. As a consequence, results obtained through numerical models are considered only if supported by a detailed analysis of their accuracy, reliability and sensitivity, obtained through three procedures: verification, validation and sensitivity study (Anderson et al., 2007, Viceconti et al., 2005).

The verification allows determining if the theoretical model is correctly implemented. Usually, simplified problems of known solution and critical tests are adopted as benchmarks to highlight the implementation weaknesses. This step provides the errors due to numerical approximations, model discretization (e.g. mesh size) and computational limits.

The validation defines the accuracy of the model’s prediction with respect to a gold standard, which is the experimental data. The quantification of the discrepancy between calculated and real data clarifies the reliability of the implemented approach and its degree of usefulness. Thus, the validation of a numerical approach entails the planning of on-purpose experiments representative of the phenomenon of interest. The comparison of numerical results with experimental data from the literature is also an option, despite it is limited by differences in experimental approaches and lack of raw data.

The sensitivity study quantifies the dependence of results on the inputs, providing information on the parameters mostly affecting the results. The dependency of results on

variations of material properties, geometry and loading conditions is a key factor for the quantification of the effects of biodiversity. As a matter of fact, specimen-specific models supply accurate results representative of an individual, but this individual is not necessarily representative of an entire population. The sensitivity studies focus on this theme, thus exploring the robustness of specific results.

Finally, it is worth noticing that even if numerical models have been proposed and discussed by the research community in biomechanics for years, the publication of results along with verification, validation and sensitivity studies is scarce, in particular for studies focusing on *in-vivo* phenomena.

1.5 Motivations of the thesis

Despite decades of investigations and the unquestionable relevance of the achieved results, the acquired knowledge is nowadays not sufficient to accurately predict the dependence of implants integration on the bone mechanical adaptation. This research field is in continuous evolution and still characterized by open problems.

Several studies focus on specific mechanical environments and their consequences on bone adaptation, while there is a lack of studies exploring the whole range of mechanical stimulation (i.e. disuse, homeostasis, overloading and damage) on the same experimental and numerical framework. As a consequence, a comprehensive overview of this phenomenon can be obtained only by pulling together results of different studies retrieved in literature, which are hardly comparable due to biodiversity and uncontrolled factors. Therefore, a complete benchmark would be required to produce sound results and reduce these uncertainties.

The investigations are addressed to a specific scientific sector, specialized on detailed outputs (i.e. gene expression, histology, prosthesis design), while the global vision is secondary. Several studies adopt mechanical stimulations and report the induced tissue adaptation, but there is no feedback on the influence of these variations on the bone mechanical properties or implants' stability. On the contrary, approaches that provide widespread outputs would promote the employment of these results in orthopedics and dentistry.

There is a lack of studies concerning the contribution of the daily activity to the integration of implants in bone. The unconstrained locomotion is commonly adopted in animal models involving implants, and its effects influence the tissue adaptation to the foreign body. However, the obtained state of integration is only considered as baseline (i.e. control) for the comparison with perturbed conditions. Although the quantitative analysis of physiological activities is successfully adopted for humans, its influence on the implants integration in animal models is neglected. Because of this lack, bone adaptation phenomena that depend on the animal's activities cannot be identified, and the obtained

results are bound to a comparison (e.g treatment versus control groups). Investigations of the effects of physiological activities would help going beyond the logic of comparisons by reaching ‘stand-alone’ results.

A number of specimen-specific approaches to generate individual-based numerical models have been recently proposed. Animal models are often investigated through single specimen-specific models, thus assuming that an individual is representative of entire populations. This approach neglects the effects of biodiversity and reduces the results efficiency. Systematic numerical approaches that account for several individuals would provide the statistical relevance of the obtained results, that is otherwise limited to the experiments.

Finally, there is a lack of quantitative correlations between experimental results and numerical predictions of bone mechanical adaptation. Qualitative comparisons are helpful indicators, but they do not provide the basis to determine the accuracy of the estimated results. A reliable validation of calculated predictions is required to promote numerical tools towards clinical applications.

1.6 Objectives of the thesis

This thesis aims at explaining the dependence of implants integration on bone mechanical adaptation, by focusing on the physiological loading environment characterizing dental prosthesis (i.e. when subjected to high loads at functional frequencies).

To achieve this objective, a solid framework based on the ‘loaded implant’ model is built by blending *in-vivo* experiments, *ex-vivo* mechanical tests and specimen-specific FE analyses. Three relevant questions are addressed:

- Q1.** Is it possible to define a numerical framework to investigate the specimens’ mechanical behaviour preserving the bio-variability? The differences between individuals affect the success of the implantation. Thus, an approach that preserves the bio-variability is needed to obtain statistically relevant results.
- Q2.** Is the peri-implant cortical loss mechanically driven? This phenomenon is correlated to the animal’s daily activity and occurs even if the implants are not activated. It provokes a reduction of the bone-implant contact area and compromises the implants stability.
- Q3.** Can the density variation generated by the implants activation be predicted through an adaptation algorithm? The bone adaptation to the external loading improves the implants fixation. If reliable predictions can be calculated, this approach opens new perspectives on osteogenic post-surgery treatments.

1.7 Contributions and methodology

The research proposed in this thesis is based on *in-vivo* and *ex-vivo* experiments that are adopted as reference for the comparison with numerical analyses. The contributions to this work are reported hereafter:

***In-vivo* test campaigns.** Investigations concern the *in-vivo* stimulation of implanted rat tibiae. Experiments were conducted at the University of Geneva Hospital and at AO Research Institute of Davos. Surgery, animal care, specimens' ablation and computed tomography analyses were performed by experts (i.e. Severine Clement³, Isabelle Badoud³, Vincent Stadelmann⁴).

***Ex-vivo* experimental analysis.** Morphometric analyses, pullout and indentation tests were conducted at the University of Geneva Hospital by Giovanna Zacchetti³. Morphologic analyses, definition of integration indices, analysis of conic defects as well as tests on the specimens' stiffness and deformation were conducted at the Laboratory of applied mechanics and reliability analysis by the author.

These experiments highlight three main results: the effects of biodiversity, a cortical bone loss due to the animal daily activity and bone per-implant augmentation due to the controlled stimulation. The author used these results to develop and validate the numerical analyses proposed in this thesis:

Numerical procedure. The mechanical stimulus occurring on the rat tibia is investigated through a numerical approach that generates individual-based FE models from mCT scans. The results of these models are verified and validated.

Daily activity. The effects of the animal's daily activity on the implants integration are quantified through a novel loading condition, which is representative of the musculoskeletal loads that occur in the rat tibia during gait.

Prediction of bone adaptation Predictions of bone adaptation to the mechanical environment are estimated through an optimized phenomenological approach, based on the physiological deformation of the rat tibia. Several specimens are processed to obtain statistically relevant numerical predictions. The robustness and accuracy of the results are investigated through sensitivity studies and comparison with experiments, respectively.

The research methodology adopted in this thesis is presented in Figure 1.8.

³Department of Internal Medicine Specialities, Geneva University Hospitals and Faculty of Medicine, Geneva, Switzerland.

⁴CT imaging, Biomedical Services, Clavadelerstrasse 8, 7270 Davos, Switzerland.

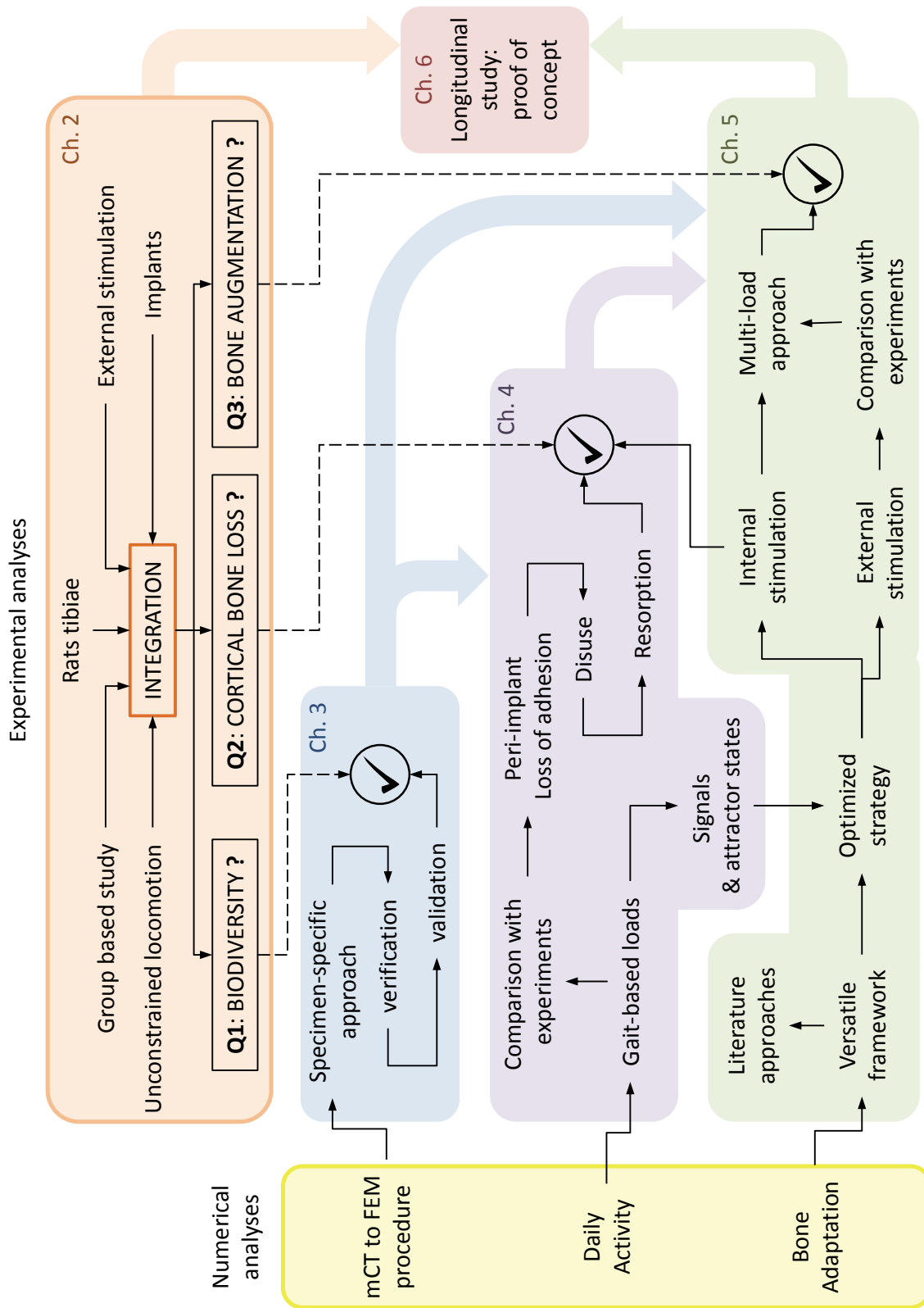


Figure 1.8: Research methodology.

1.8 Thesis structure

Including the present introduction (focused on (i) the implants biomechanics and related problems, (ii) the osseous tissue anatomy and (iii) the dependency of bone on the mechanical environment) this thesis is structured in seven chapters:

Chapter 2 illustrates the performed experimental analysis by describing the in~vivo and ex~vivo protocols and discussing the results of the ‘loaded implant’ model in terms of tissue adaptation and implants’ stability.

Chapter 3 is dedicated to the development of a methodology to generate specimen-specific FE models of implanted rat tibiae from mCT scans. The procedure is accurately verified, the results are validated through on-purpose tests and the sensitivity to biodiversity is estimated by processing several specimens.

Chapter 4 deals with the analysis of the deformations occurring in a rat tibia during locomotion. An original gait-based loading condition is presented and adopted to investigate the peri-implant stresses characterizing the chosen animal model. The numerical results are correlated with experimental observations.

Chapter 5 addresses the predictive capabilities of bone adaptation models. Approaches inspired by existent theories are implemented on the same numerical framework and compared. An optimized approach is defined and compared to the results of in~vivo experiments. The influence of both the animal physical activity and the implant loading on the bone structure is quantified separately, then merged on a single benchmark involving the entire spectrum of mechanical stimulation.

Chapter 6 describes the upgrade of the ‘loaded implant’ model to perform longitudinal computed tomography analyses and reconstruct specimen-specific integration histories.

Chapter 7 contains a summary of the obtained results and a discussion on further developments.

Chapter 2

Experimental approach

2.1 Aim

The complexity of the research themes approached in this thesis requires the establishment of a solid experimental background, which allows highlighting the phenomenon of interest with accuracy and completeness.

The goal of this chapter is to present the results of *in-vivo* experiments focused on the identification and quantification of the effects of mechanical stimulations on the stability of implants integrated in bone. The adopted animal model, involving different implantation strategies, is based on the rat tibia and allows one to investigate both the effects of controlled external loads and the influence of the animal daily activity. As a matter of fact, both the external stimulation and the animal unconstrained locomotion affect the strength of the integration.

Several analyses are performed to provide a complete description of the observed phenomena: quantifications of bone structural parameters through 3D micro Computed Tomography (morphometric analysis), classification of the peri-implant tissue through pre-defined features (morphologic analysis) and mechanical tests to identify the elastic and ultimate properties of the bone tissue.

The topics addressed in this chapter are summarized under three main themes:

1. Analyze the behavior of group of animals subjected to different mechanical environments in order to highlight the effects of biodiversity.
2. Investigate the dependency of implants integration on the animal unconstrained locomotion.
3. Quantify the bone structural optimization when subjected to controlled external loads and monitor its influence on the implant integration strength.

2.2 Animal model

The ‘loaded implant’ model allows investigating the bone reaction to a mechanical stimulation transmitted through integrated implants. Controlled loads are applied daily to the implants protruding from the animal skin, triggering a biological reaction to the imposed mechanical environment.

Initially developed for rabbits (Wiskott et al., 2008), this model is now optimized for rats (Wiskott et al., 2012, Zacchetti et al., 2013), which permits studies involving larger populations and establish the experimental reference for this thesis. The *in-vivo* experiments are conducted at the University of Geneva Hospital and approved by the medical faculty’s animal rights committee. The details of this animal model are discussed in the following.

2.2.1 Principle

The principle of the ‘loaded implant’ model is represented in Figure 2.1. Two titanium implants are inserted into the rat’s tibia with their heads protruding from the skin. The distal implant is anchored bicortically while the proximal implant penetrates the medulla by ~ 2 mm. The external load is applied through a cable, activated by the loading machine and sliding inside a sheath. This force generates a combined compression-bending environment in the bone tissue, with high stress concentrations around the implants. Moreover, the load is transmitted to the trabecular bone by the floating proximal implant.

The interest of this setup is that it represents two important implantation strategies that are widely adopted in dentistry and orthopedics (e.g. vertebral screws or external fixations).

2.2.2 Surgery and animal care

This study is performed on female Sprague Dawley rats, an albino breed of rat, calm and easy to handle. All the animals are implanted at an age of 27 weeks (weight ~ 280 g). The rats are pair-fed for two weeks before surgery to obtain an initial acclimatization. Prior to implantation, the animals are sedate with Ketarom 40 mg/kg (1.2 ml ketamine hydrochloride, 0.8 ml 2 % xylazine, 8 ml isotonic saline). A schematic representation of the implant placement is represented in Figure 2.2a. A standardized surgery procedure is established to ensure reproducibility. After exposing the bone surface, the proximal implant location is identified 4 mm far from the growth line in the caudal direction. The distal location is then fixed 7.5 mm far from the first one. Surgical drills (diameter 1 mm, speed 1500 – 2500 rpm) are employed to create the implants seats under saline irrigation. The proximal hole stops before the second cortex, while the distal one is drilled bi-cortically.

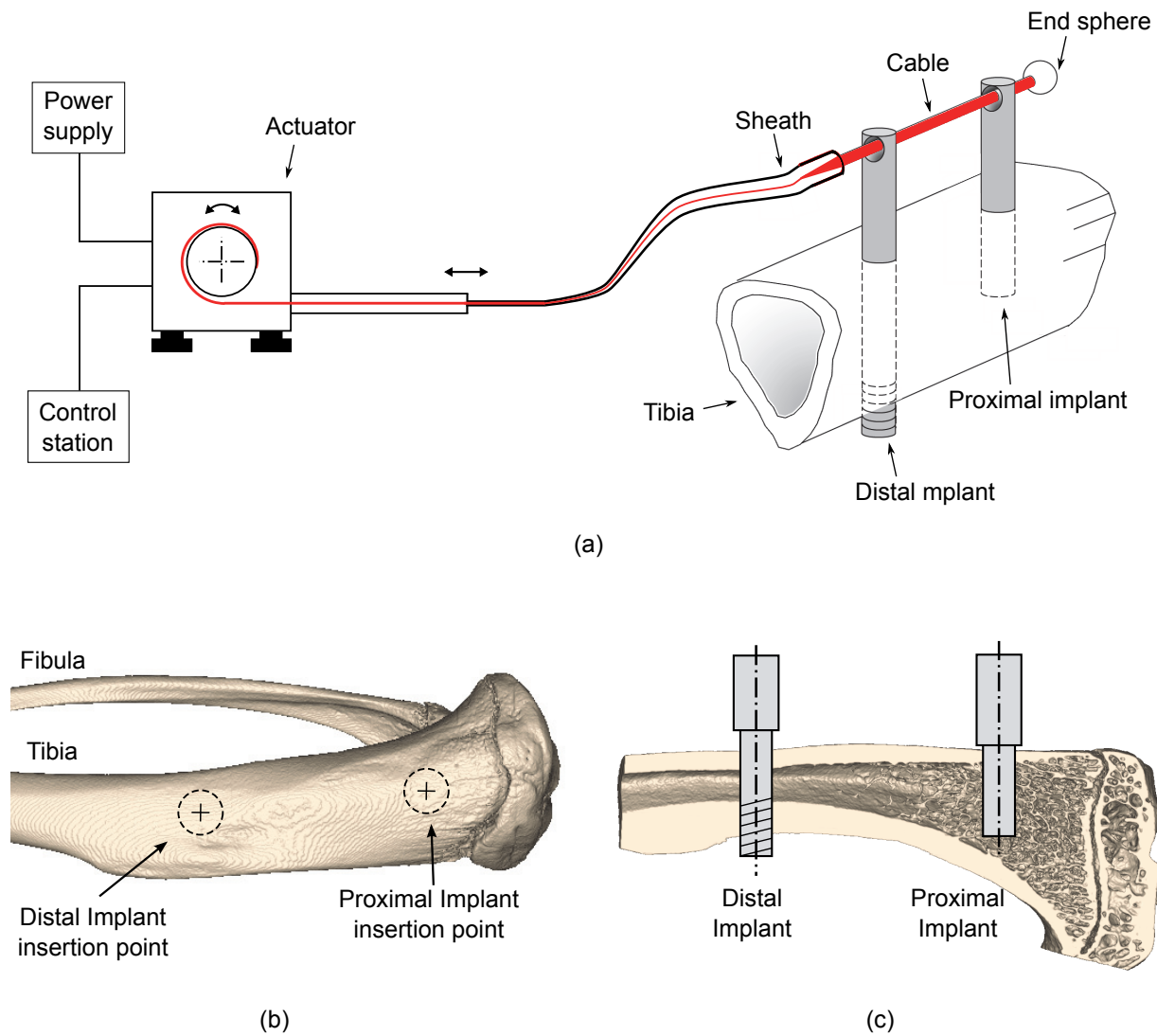


Figure 2.1: (a) Set-up for *in-vivo* implant loading. The actuator moves the cable within the sheath. The implants heads are designed to transmit the loads to the bone tissue. (b) Location of the implants. (c) the distal implant is screwed bicortically, while the proximal one floats inside the trabecular bone.

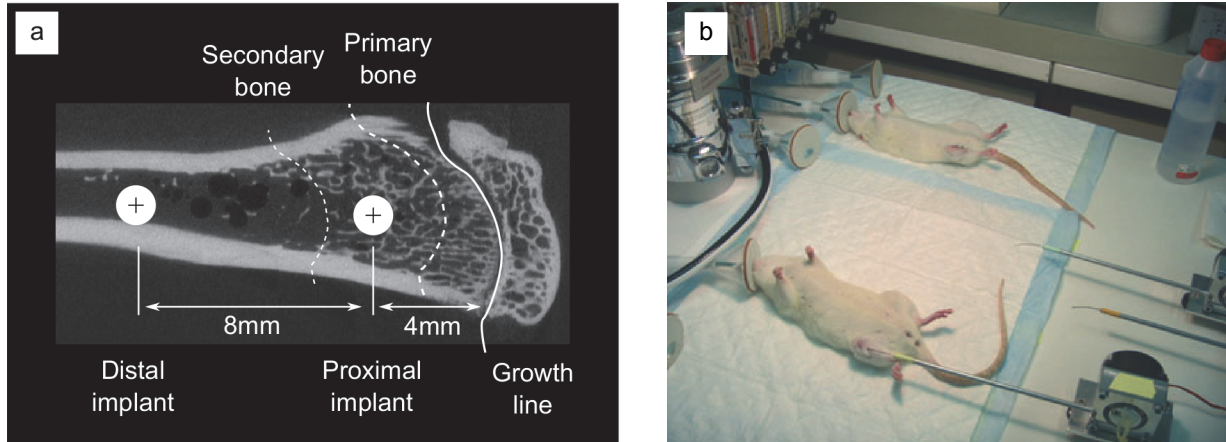


Figure 2.2: (c) During surgery, the proximal implant is placed first and serves as reference for the placement of the distal pin. (b) Animals undergoing stimulation.

The proximal implant is press fitted into the first bore (radial interference 0.01 mm), while the distal one is screwed into the second. Finally the skin is sutured leaving the implants heads protruding by ~ 2 mm.

After surgery, the rats are caged individually at 25°C with free access to food and water. Analgesic is administered for two days (Temgesic 0.83 ml/kg SC, Reckitt Benckiser, Slough, UK) and no antibiotic is employed. A healing period of two weeks is considered to grant a good initial integration of the implants. During stimulation the animals are anesthetized with isoflurane-oxygen delivered through snout masks (Figure 2.2b). At the end of the experiments the rats are euthanized. The tibiae are ablated, cleared of the soft tissue coverage, individually wrapped in saline-soaked gauze and frozen to -22°C . Prior to scanning and mechanical testing, the specimens are maintained at 4°C for 24 h in a 0.9 % solution of NaCl and then brought to room temperature.

2.2.3 Implants and loading device

The overall dimensions and geometry of the implants adopted in this study are shown in Figure 2.3a. A highly biocompatible material, Titanium grade IV, is chosen to support the desired mechanical loads. The insertion depth of the proximal implant is controlled through the diameter variation, which acts as a geometrical landmark. The threaded tip allows the distal implant to be anchored to the cortex. A thin slit with a spherical cavity is carved on both implants heads to allow placing the activation cable and the load transmission. The implants' surfaces expected to be in contact with bone are sandblasted with a $250\ \mu\text{m}$ powder of Al_3O_3 and acid-etched in a mixture of one volume of 37 % HCl and four volumes

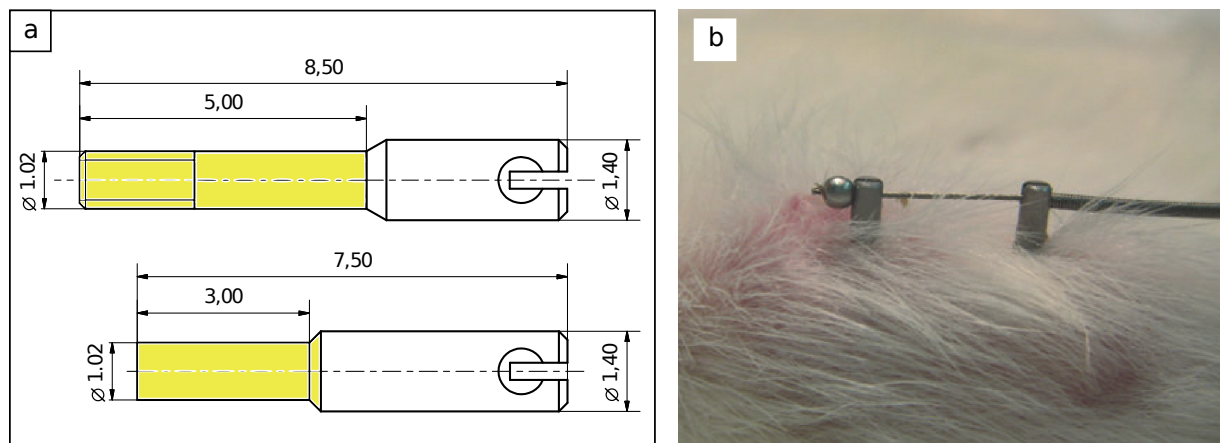


Figure 2.3: (a) Distal (top) and proximal (bottom) implant overall dimensions (detailed drawings are reported in Appendix). The yellow areas indicate the SLA-etched surfaces. (b) Load transmission during *in-vivo* tests.

of 100 % H_2SO_4 at 100° C. This treatment generates a surface roughness $R_a \sim 3$. Before surgery, the implants are processed in phosphate-free cleaning solution (Deconex 15PF-x, Borer Chemie AG, Zuchwil, Switzerland), rinsed in pure water in an ultrasonic bath and sterilized with ethylene oxide.

The external load is applied 5 days/week through a calibrated rotary coil actuator, which activates the movement of the cable inside the sheath. The sphere placed at the end of the cable and the sheath fit the seats carved on the implants heads, allowing the force transmission (Figure 2.3b). At the beginning of the stimulation period, the external load is increased by 1 N/day until the defined level is reached. Load, frequency and number of cycles are controlled by an external command station. The external stimulation is modulated through different load amplitudes, while frequency and number of cycles are fixed (i.e. 1 Hz and 900 cycles/day, corresponding to 15 min/day of stimulation).

2.2.4 Experiments

All the experiments last 8 weeks: two weeks of acclimation, two weeks of post surgery healing, and four weeks of external stimulation. These settings are based on the results of previous studies that establish the adequate healing and stimulation period (Wiskott et al., 2012).

Three series of experiments are conducted to gather a maximum of knowledge on the implant integration in this animal model. The details are summarized in Table 2.1. Each series is planned with a precise goal:

Table 2.1: *Details of the in-vivo experiments.*

Series	Group Name	Number of units	Implanted tibia	Healing period (weeks)	Stimulation period (weeks)	Load (N)
SERIES 1	BA	10	right	2	-	-
	NS	10	right	6	-	-
	1N	10	right	2	4	1
	2N	10	right	2	4	2
	3N	10	right	2	4	3
SERIES 2	BA	10	right	2	-	-
	NS 1	10	right	4	-	-
	NS 2	10	right	6	-	-
SERIES 3	BA	8	bilateral	2	-	-
	2N	8	bilateral	2	4	2
	3N	8	bilateral	2	4	3
	4N	8	bilateral	2	4	4
	5N	8	bilateral	2	4	5

BA: basal; NS: non-stimulated

SERIES 1: Mild overloading. The goal of this series is to analyze the effects of an external load on the implant integration, limiting the bone stimulation to mild overloading. Five groups of 10 individuals are allotted for this series. The implants are placed only on the right tibia. Two control groups are euthanized after two and six weeks of implantation respectively, without implants activation. The remaining three groups undergo two weeks of integration followed by four weeks of external stimulation at 1, 2, and 3 N, respectively (1 Hz sinusoidal cycle, 900 cycles/day, 5 days/week).

SERIES 2: Daily activity. The goal of this series is to investigate the influence of the rats' daily activity on the implant integration. Three groups of 10 individuals are allotted for this series. The implants are placed only on the right tibia. The groups are euthanized after two, four and six weeks of integration, respectively. No implant activation is delivered.

SERIES 3: Overloading. The goal of this series is to investigate the implants integration when subjected to a critical mechanical environment. Five groups of 8 individuals are allotted for this series. The implants are placed on both tibiae and only the right one is stimulated. One control group is euthanized after two weeks of integration. The remaining four groups undergo two weeks of integration followed by four

weeks of external stimulation at 2, 3, 4 and 5 N, respectively (1 Hz sinusoidal cycle, 900 cycles/day, 5 days/week).

2.3 Methodology

Standard morphometric analyses performed on micro Computed Tomography (mCT) images are coupled with mechanical tests and morphologic inspection of the peri-implant bone shape. The goal is to quantify the implants stability and correlate the bone adaptation to the mechanical environment. Significant differences (level set to $p \leq 0.05$) are identified by analyses of variance (ANOVA) and Fisher post hoc test, for normally distributed data, or Mann-Whitney-U test.

Tests and analyses presented in the following sections are performed at the Geneva University Hospitals and Faculty of Medicine and at the École Polytechnique Fédérale de Lausanne. In details, the mCT scanning, the morphometric analyses, the pull-out and indentation tests are performed at the Division of Bone Diseases, Department of Internal Medicine Specialties in Geneva, while the morphologic analysis, the tests on the specimens' stiffness and ultimate strength are performed at the Laboratory of Applied Mechanics and Reliability Analysis, in Lausanne.

2.3.1 Computed tomography analyses

The specimens are processed using a high-resolution CT imaging system (mCT-40, Scanco Medical AG, Brüttisellen, Switzerland). The images, stored in DICOM format, are obtained with the following settings:

- Slices \times rotation: $1022 \times 360^\circ$.
- Isotropic voxel size: 20 μm .
- Source potential: 70 kVp.
- Tube current: 114 mA.
- Field of view: 20×26.5 mm.

A 1200 mgHA/cm³ hydroxyapatite beam hardening (BH) correction is applied prior to reconstruction (Kazakia et al. 2008). The same procedure is applied to scan a phantom provided by the manufacturer. The phantom comprised four hydroxyapatite cylinders of known density embedded in a resin matrix (i.e. 100, 200, 400, 800 mgHA/cm³). The analysis of the phantom provides a linear regression correlating the X-ray attenuation coefficient with the density.

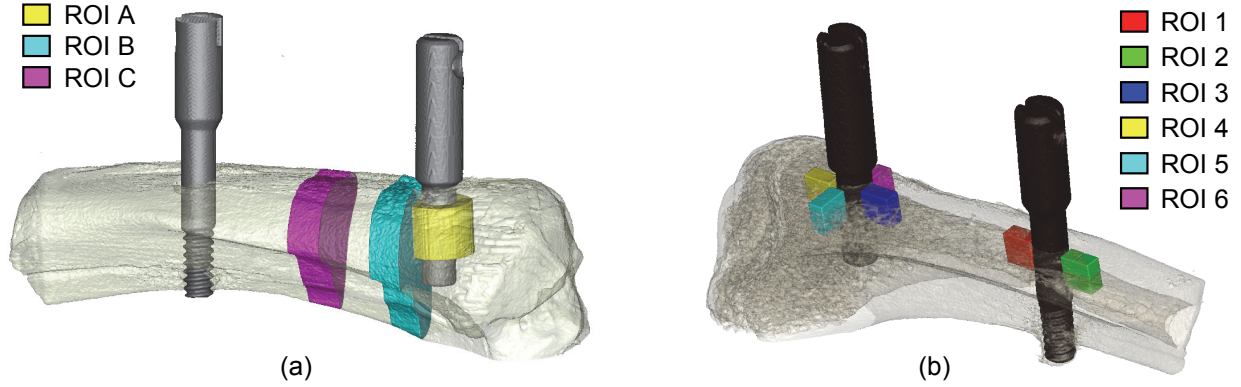


Figure 2.4: Regions of interest for the morphometric analysis: (a) Series 1 and (b) Series 3.

2.3.1.1 Morphometric analysis

Relative bone volume (BV/TV), trabecular number ($Tb.N$), trabecular thickness ($Tb.Th$), trabecular spacing ($Tb.Sp$), Bone-Implant Contact (BIC), cortical thickness ($Ct.Th$) and Bone Mineral Density (BMD) are assessed from the scans through the SCANCO post-processing software and ITK-snap (Yushkevich et al., 2005). The investigated Regions Of Interest (ROIs) are represented in Figure 2.4. Three discrete ROIs are investigated in Series 1: a cylinder of trabecular bone 0.5 mm thick around the proximal implant, a 1 mm section including cortical and trabecular bone in the immediate proximity of the proximal implant and a 2 mm section including cortical and trabecular bone between the implants. Six ROIs are investigated in Series 3: $1 \times 1 \times 0.6$ mm parallelepipeds including cortical and trabecular bone placed along the longitudinal and medio-lateral directions with respect to the implants.

2.3.1.2 Morphologic analysis

The morphology of the peri-implants bone is inspected and classified through a pre-defined set of features (Figure 2.5). The features are defined in order to qualitatively describe the bone-implant integration and the tissue morphology with respect to an ideal state of integration, shown in Figure 2.5a. For each group, indexes of integration are calculated as the percentage of specimens characterized by the following features:

- I_F . Cortical fit. Identifies the percentage of specimens showing perfect implant's integration in cortical bone (Figure 2.5a represents a perfect cortical fit, on the contrary of Figure 2.5b).

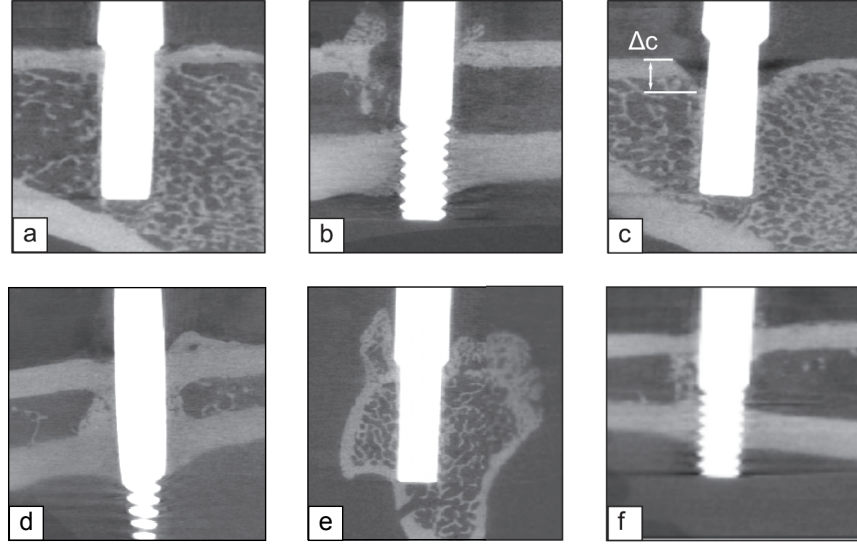


Figure 2.5: Examples of peri-implant features identified around both implants. (a) perfect cortical fit, (b) imperfect cortical fit, (c) cortical loss and conic depth Δc , (d) bone shell, (e) periosteal reaction and (f) not uniform alveolar bone.

I_C . Cortical loss. Highlights the percentage of specimens showing good implant integration (i.e. no detachment) but characterized by a cortical bone loss (Figure 2.5c).

I_S . Bone shell. Highlights the the percentage of specimens showing a thick layer of bone tissue surrounding the distal implant within the medullar canal (Figure 2.5d).

I_A . Periosteal reaction. Identifies the the percentage of specimens showing bone periosteal apposition near the implant (Figure 2.5e).

I_U . Alveolar uniformity. Highlights the percentage of specimens showing a uniform distribution of trabecular bone around the implant (not uniform alveolar bone is shown in Figure 2.5f).

These indicators are then combined to obtain implant-based indexes of integration, I_P and I_D for the proximal and distal implant respectively (Equations 2.1 and 2.2). Indexes I_A and I_C are both considered as undesired bone reactions, thus their contribution is negative.

$$I_P = I_{F_s} I_U (1 - I_C) (1 - I_A) \quad (2.1)$$

$$I_D = I_{F_s} I_{F_t} I_S (1 - I_C) (1 - I_A) \quad (2.2)$$

where I_{F_s} and I_{F_t} refers to the smooth and threaded part of the implants in contact with cortical bone, respectively.

2.3.2 Ex~vivo mechanical tests

The adopted mechanical tests aim at investigating the implant stability, the quality of the integration and the strength of the bone tissue. The implants pull-out strength and lateral stability are addresses with dedicated tests. Three-point bending and indentation tests are performed to investigate the bone mechanical properties.

Prior to testing, the specimens are maintained at 4°C for 24 h in a 0.9 % solution of NaCl and then brought to room temperature. These tests also provide the experimental reference to validate the numerical approach presented in Chapter 3.

2.3.2.1 Pull-out

The pull-out test is performed on the proximal implant through a servo-controlled electromechanical system (Instron 1114; Instron Corp., High Wycombe, UK). A metal clasp is fixed to the implant's head and clamped to the machine while the tibia lies on a metal jig. The actuator displacement is set to 1 mm/min, and the pull-out strength is determined as the peak force F_P applied to provoke the implant detachment. Further details on this test are described by Maïmoun et al. (2010).

2.3.2.2 Indentation

The indentation test is performed through a nano-hardness tester (NHT, CSM Instruments, Peseux, Switzerland). The tibiae are embedded in resin, sectioned midway the implants and polished. A pyramidal diamond indenter is driven into the trabecular bone surface exposed by the cut, up to 900 nm depth at a strain rate of 76 mN/mm. After 5 s in this position, the indenter is withdrawn at the same strain rate. Tests are performed on wet bone. The generated force-displacement curve is processed to quantify the tissue Young modulus E , hardness H and working energy W developed during indentation, following the Oliver and Pharr's method (Oliver and Pharr, 1992).

2.3.2.3 Stiffness tests

Bare and implanted specimens are tested to provide the three point bending stiffness and the inter-implant mechanical properties, respectively (i.e. stiffness, strain, ultimate displacement, ultimate force and ultimate energy). The tests are carried out using an electromechanical system (5848 Microtester, Instron Corp., High Wycombe, UK).

The set-up for the three point bending is shown in Figure 2.6a. The specimen rests on two steel supports with the tibial crest facing up. The position is chosen to avoid any contact between the supports and the epiphyseal plate. The distance between the supports is fixed at 10.6 mm. A small notch (depth ~ 0.1 mm) is carved on the tibia's anterior

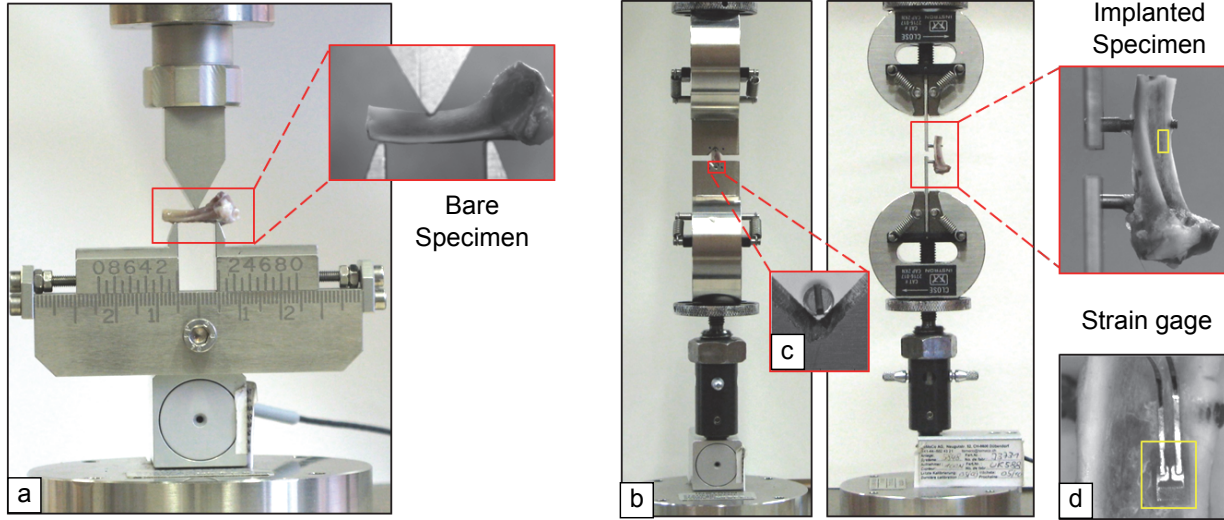


Figure 2.6: (a) Three-point bending set-up¹. (b) Inter-implant stiffness set-up. (c) V-shaped notch to align the implants. (d) strain gauge aligned with the longitudinal axis.

crest to stabilize the actuator and prevent lateral sliding during loading. The specimens are subjected to five load cycles in the range of 2 – 16 N at a speed of 0.01 mm/min.

The Inter-implant properties are evaluated by measuring the machine crosshead displacement, while loading the implant heads (Figure 2.6b). The implants' heads are vertically aligned through sharpened, V-shaped notches, machined on two 1.5 mm thick steel plates. Upon activation, a bending moment is thus generated on the bone tissue. A single element strain gauge (LY11-0.3/120, Hottinger Baldwin Messtechnik GmbH, Darmstadt, Germany) is bonded to the bone surface of a batch of specimens (5 units) along the distal-proximal direction to measure the surface deformation (Figure 2.6d). Each sample is subjected to five cycles ranging from 1 to 5 N at a rate of 0.01 mm/min to determine the inter-implant stiffness II_K and strain II_S (calculated as d/L_h , where d and L_h are the inter-implant heads displacement and distance, respectively). On a second batch of specimens (15 units), the ultimate force F_U and displacement d_U are measured by loading up to failure at 0.01 mm/min. The ultimate energy U_U is calculated through Equation 2.3 by considering the loading part only.

$$U_U = \int_0^{d_U} F_U(x) dx \quad (2.3)$$

The inherent elasticity of both experimental set-ups is evaluated through on-purpose tests performed on known metallic samples, and used to correct the measured machine crosshead displacement (stiffness in series with specimens).

¹courtesy of the Laboratory of Biomechanical Orthopedics, EPFL, Lausanne.

2.4 Results and Discussion

The results of the experiments highlight different responses to the mechanical stimulation. Being aware that the implants integration depends on several factors and it is only partially driven by the adaptation to the mechanical environment, the results are presented and discussed to highlight the impact of the external loading and the animal daily activity on the implants stability.

Generally, the animals respond well to surgery and stimulation. Concerning Series 1 and 2, few animals developed erythematous inflammatory reactions around the protruding implants, which have been regularly disinfected. However, these reactions are not correlated with abnormal bone growth. In Series 1, two animals died during snout mask anesthesia and one implant was rejected during the very initial activation period. None of the implants were lost in Series 2. These phenomena are considered irrelevant with respect to the observed population (totally 80 units for Series 1 and 2). On the contrary, Series 3 is characterized by several implant loss and inflammatory states compatible with the overloading environment of this series: a dedicated discussion of these data is reported in Section 2.4.3.1. To facilitate the reading, the results of each series are presented and discussed separately.

2.4.1 Series 1. Mild overloading

This test campaign focuses on the effects of the external loading on the implants integration. The implant stimulation ranges from 1 to 3N (i.e. corresponding to peak equivalent strains from ~ 660 to $1980 \mu\epsilon$, see Section 3.4.7). This external loading modifies the mechanical environment of the tibia in the proximity of the implants by reaching levels of deformation known to be osteogenic for rats (Robling et al., 2002, Turner et al., 1994b).

The results of the morphometric analysis are reported in Table 2.2. The bone architecture around the proximal implant (ROI A, Figure 2.4a) is not significantly altered by the mechanical loading. Compared to the Non-Stimulated group, *NS*, a moderate increase of all the parameters characterizes the stimulated groups, in particular *1N*. The bone section near the proximal implant (ROI B) highlights a significant increases of *BV/TV* and *Tb.Th* in the *1N* group with respect to *NS* and *3N* groups. The cortical bone shows a significant increase of thickness in the *3N* group with respect to the *1N*. Similar results are obtained in ROI C: significantly higher *BV/TV* is shown in the *1N* group with respect to *3N*, while the cortical thickness slightly increases in the *3N* group with respect to the other groups, but this variation is not statistically relevant.

These results highlight a tissue-dependent adaptation to the implant's activation: trabecular and cortical tissues react differently. The trabecular bone reacts positively to low loads (1 N) while deleterious effects are observed for higher forces (2 N, 3 N).

Table 2.2: Results of the morphometric analysis (Zacchetti et al., 2013), Series 1.

Region of Interest	Group Name	BV/TV (%)	Tb.N (1/mm)	Tb.Th (mm)	Tb.Sp (mm ³)	BIC (%)	Ct.Th (mm)
ROI 1	BA	50.3 ± 2.5	6.44 ± 0.16	0.150 ± 0.004	0.156 ± 0.007	82.07 ± 2.36	-
	NS	44.2 ± 3.1	6.23 ± 0.18	0.142 ± 0.003	0.169 ± 0.008	76.02 ± 2.66	-
	1N	50.5 ± 2.3	6.53 ± 0.20	0.153 ± 0.006	0.160 ± 0.012	78.73 ± 2.25	-
	2N	48.5 ± 1.9	6.02 ± 0.23	0.145 ± 0.003	0.174 ± 0.010	78.35 ± 2.19	-
	3N	48.0 ± 3.9	6.27 ± 0.29	0.149 ± 0.005	0.168 ± 0.015	76.85 ± 3.70	-
ROI 2	BA	18.0 ± 2.0	4.03 ± 0.24	0.076 ± 0.003	0.25 ± 0.02	-	0.41 ± 0.01
	NS	14.6 ± 2.2 ^a	3.74 ± 0.27	0.074 ± 0.002	0.28 ± 0.03	-	0.44 ± 0.01
	1N	20.1 ± 2.2	4.26 ± 0.29	0.080 ± 0.003	0.24 ± 0.02	-	0.43 ± 0.01
	2N	16.9 ± 2.1	4.03 ± 0.23	0.074 ± 0.003	0.25 ± 0.02	-	0.43 ± 0.01
	3N	13.8 ± 2.2	3.67 ± 0.14	0.071 ± 0.004	0.28 ± 0.01	-	0.46 ± 0.01 ^b
ROI 3	BA	9.2 ± 1.0	2.59 ± 0.21	0.072 ± 0.001	0.42 ± 0.04	-	0.46 ± 0.02
	NS	8.3 ± 1.4	2.77 ± 0.22	0.071 ± 0.002	0.38 ± 0.03	-	0.49 ± 0.02
	1N	11.5 ± 1.2 ^c	3.20 ± 0.22 ^c	0.071 ± 0.002	0.33 ± 0.03	-	0.48 ± 0.02
	2N	8.2 ± 1.3	2.58 ± 0.29	0.071 ± 0.002	0.47 ± 0.12	-	0.48 ± 0.03
	3N	6.1 ± 1.1	2.19 ± 0.17	0.071 ± 0.005	0.48 ± 0.03	-	0.51 ± 0.02

Mean ± SEM.

BA: basal; NS: non-stimulated.

^a p < 0.05 vs 3N^b p < 0.05 vs 1N^c p < 0.01 vs 3N

Table 2.3: Results of the Indentation and pull-out tests (Zacchetti et al., 2013), Series 1.

Group	Indentation			Pull-out
	E (GPa)	H (MPa)	W (pJ)	F_P (N)
BA	-	-	-	29.40 ± 4.44
NS	14.2 ± 0.5	552 ± 20	3491 ± 115	39.57 ± 2.23
1N	14.5 ± 0.4	578 ± 17	4014 ± 97 ^b	40.82 ± 3.12
2N	16.3 ± 0.4 ^{b,c,d}	604 ± 17 ^{a,d}	3785 ± 135	46.63 ± 2.21 ^a
3N	14.4 ± 0.4	528 ± 14	4024 ± 92	43.81 ± 3.41

Mean ± SEM; BA: basal; NS: non-stimulated.

E: Elastic modulus; H: hardness; W: energy; F_P : ultimate force.

^a p < 0.05 vs NS; ^b p < 0.001 vs NS; ^c p < 0.01 vs 1N; ^d p < 0.01 vs 3N

Table 2.4: Results of the morphologic analysis, Series 1.

Implant	Group	I_{Fs} (%)	I_C (%)	I_A (%)	I_S (%)	I_U (%)	I_{Ft} (%)
Distal	BA	76.7	0.0	10.0	66.7	-	83.3
	NS	76.7	7.7	16.7	77.8	-	100.0
	1N	51.8	5.8	22.2	63.0	-	100.0
	2N	37.5	4.7	45.6	50.0	-	87.5
	3N	50.0	0.0	25.0	62.5	-	87.5
Proximal	BA	90.0	0.0	0.0	-	90.0	-
	NS	83.3	37.5	3.3	-	100.0	-
	1N	77.8	8.6	7.4	-	77.8	-
	2N	100.0	12.5	14.8	-	100.0	-
	3N	79.2	4.9	0.0	-	87.5	-

The cortical bone is unaffected by all stimulation but the 3 N loading, which generate a positive response in the close vicinity of the proximal implant.

These results confirm the different tissue-dependent reaction documented in literature: modulated with respect to a range of stimuli for the trabecular bone, instantaneously triggered and disorganized for the cortical bone (Turner et al., 1994b). On the contrary, the absence of significant trabecular bone variations around the implant (ROI A) disagree with the results of animal models involving guinea pigs and comparable stimulation ranges (De Smet et al., 2006). The results of the indentation and pull-out tests are reported in

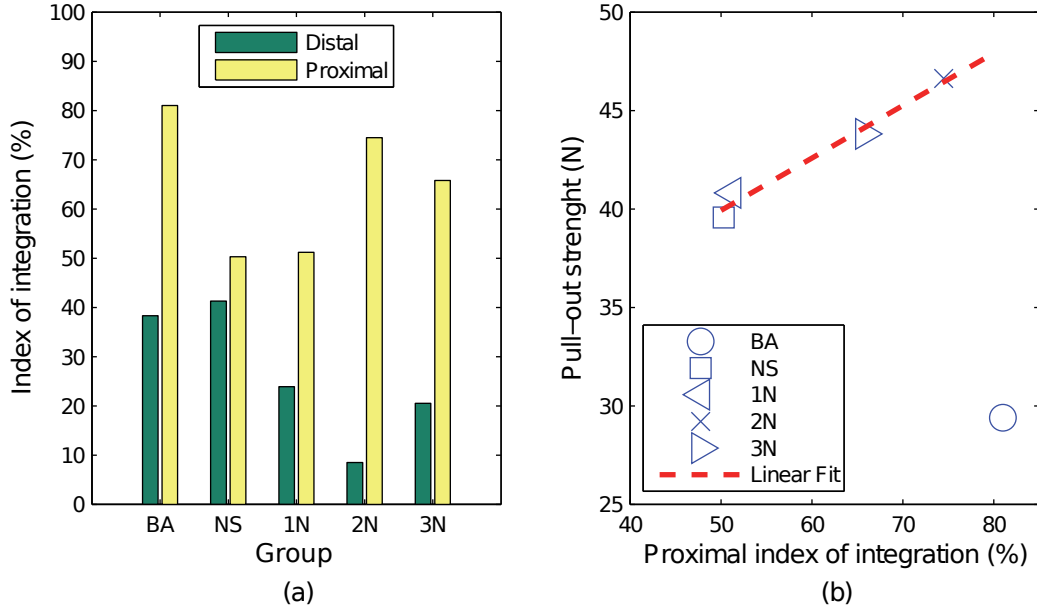


Figure 2.7: (a) Distal and Proximal indexes of integration calculated through the morphologic analysis. (b) Correlation between the pull-out strength and the proximal index of integration. The basal group is not included because subjected to two weeks of integration.

Table 2.3. The stimulation significantly increased the modulus of elasticity and hardness of trabecular bone in the $2N$ group (+15% vs. NS; +12% vs. 1N; +13% vs. 3N). A similar trend is observed for the indentation energy, which is significantly higher in the 3N group. The section of bone where these measurements are done is comparable with ROI C in the morphometric analysis. Interestingly, in this region the 2 N stimulation produces a reduction of the morphometric parameters but also an improvement of the local mechanical properties of the trabecular bone.

The implant activation improved also the pull-out strength in all the stimulated groups, with higher values in the $2N$ group that shows +17.8% increase in strength. Several factors affect the results of this test, e.g. the bone material properties, the tissue adhesion to the implant surface and the trabecular micro-architecture. However, the morphometric analysis of ROI A highlights no variation of the trabecular micro-structure, limiting the main causes to two factors: the bone-implant interface and the peri-implant morphology. Concerning the first one, the adopted sand-blasting and acid-etching treatments generate optimal implant surfaces, characterized by a roughness which improves the osteogenesis (Cochran et al., 1996). The bone cells growth into the irregularities of the implants surfaces improves the implant stability and increases the resistance to pull-out. The improvement is already relevant without external stimulation (NS group +34% vs BA), and

can be modulated through the implant activation. This shows that there is an influence of mechanical loading on bone formation immediately around implants. However, this area is affected by metal artifacts (Kataoka et al., 2010) and cannot be investigated with the proposed mCT procedure. Due to this drawback, the reliability of measurements concerning the bone to implant contact (BIC in Table 2.2) is still on debate. Nevertheless, previous studies underline the correlation between BIC and the implant pullout resistance (Dayer et al., 2006). Unfortunately, other types of analysis of the bone-implant interfaces, e.g. histology, hamper the pull-out test, and thus are not performed on these specimens.

The results of the morphological analysis are reported in Table 2.4. The external load worsens the quality of the distal implant integration. The occurrences of perfect fit around the smooth part of the implant (I_{Fs}) decrease, as well as the presence of a cortical shell within the medullar canal (I_S). Moreover, an increase of specimens characterized by cortical loss and extra-cortical apposition is noticed. The threaded part of the implant is less affected and preserves its integration (I_{Ft}). A similar trend characterizes the proximal implant, although the quality of the integration is superior. The difference between the implantation strategies is clearly highlighted by the indexes I_D and I_P reported in Figure 2.7a. After 2 weeks of integration (group BA) the proximal peri-implant tissue presents fewer anomalies than the distal one. After 6 weeks of integration and no external load (group NS) the implants indexes reach similar values mostly because of a degradation of the proximal implant state of integration. Finally, if an external load is applied a diverging trend is observed: the quality of the integration for the proximal implants is increased while it decreases for the distal one.

The qualitative nature of this analysis, comparable to existing classifications of peri-implant bone defects (Vanden Bogaerde, 2004) and morphology (Zhang et al., 2013), allows drawing interesting conclusions. The effects of the *in-vivo* activation depends on both the implantation site and strategy (i.e. mono- or bi-cortical). Although the morphology of the distal peri-implant bone indicates worsening features, the threaded part is well integrated avoiding the implant rejection and granting its anchoring function. On the contrary, the proximal implant integration slightly improves thanks to the external activation. Moreover, the integration index of the proximal implant, I_P , shows a clear correlation with the measured average pull-out force ($R^2 = 0.97$, Figure 2.7b). This correlation confirms that the pull-out strength depends also on the peri-implant morphology, and highlights the validity of the proposed qualitative analysis as indicator of the integration strength.

2.4.2 Series 2. Daily activity

This series focus on the effect of the animals' daily activity on the implants integration. Three groups of animals undergo different integration periods (i.e. 2, 4 and 6 weeks)

without external stimulation. The rats are caged individually and cannot interact with each other. Moreover, cone collars are introduced to prevent the animal to gnaw the implants during the early post-surgery days, when the animal may show restlessness or wound heal difficultly. With these precautions, the influence of uncontrolled factors (e.g. biting or scratching) on the implant integration is limited and the bone response mainly depends on the animal unconstrained locomotion in the cage. The morphologic inspection of the peri-implant cortical bone is mainly focused on the monitoring of the cortical fit and cortical loss. Moreover, if a cortical loss is present, the conic depth Δ_C is recorded (Figure 2.5c). The results concerning the peri-implant features are reported in Table 2.5. After 2 weeks of integration, 14% and 20% of distal and proximal peri-implant regions are characterized by cortical loss, respectively. After 6 weeks the frequency of this feature increases up to the 41% and 45% respectively. The complete opening of the bone-implant interface characterizes only the distal implant, with a maximum frequency of 17%, while the loss of bone-implant contact is not observed around the proximal one. The distal threaded tip is perfectly integrated in all the specimens and none of the implants was rejected. The measurements of the conic depth for the three groups of specimens are represented in Figure 2.8. The conic depth increases with time reaching values comparable to the diaphysis cortical thickness (~ 0.5 mm) around the distal implant, with a significant difference between 2 to 6 weeks for both implants.

These results confirm that the influence of the animal daily activity on the implants integration is not negligible. The loss of cortical fit and the increase of conic depth highlight a peri-implant bone adaptation to the modified mechanical environment. Indeed, the presence of the implants compromises the homeostatic equilibrium of the bone tissue inducing an adaptation to the new configuration. This theme is widely investigated for humans and improves the understanding of clinically relevant issues (e.g. the stress shielding (Huiskes et al., 1992)), but is not documented for rats. The observed phenomena, arising after two weeks of integration, do not affect the early post surgery stability, confirming the adopted

Table 2.5: Results of the morphologic analysis, Series 2.

Implant	Feature	Integration period (weeks)		
		2	4	6
Distal	I_F	93.3	83.3	83.3
	I_C	14.0	33.3	41.7
Proximal	I_F	100.0	100.0	100.0
	I_C	20.0	35.0	45.0

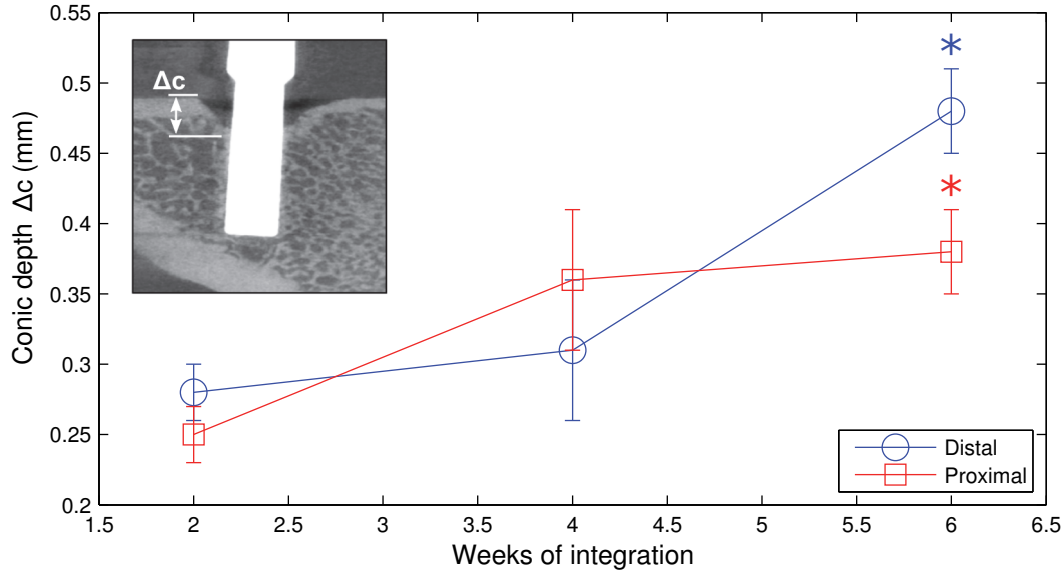


Figure 2.8: Conic depth, Δ_C , measured at different integration periods around the implants (mean \pm SEM). * $p < 0.05$ with respect to two weeks.

implant design which includes a press fit. As a matter of fact, the generated interference fit grants the implants primary stability, avoids harmful micro-motions and facilitates the initial integration (Abdul-Kadir et al., 2008). Unfortunately the effect of the press fit ends 3-4 days after the surgery because of the tissue adaptation (Dhert et al., 1998), and the bone peri-implant morphology evolves depending on several factors: the quality and thickness of the bone-implant adhesion, the shape and strength of the tissue, but also the rat daily activity during recovery. Indeed, the animal may lame or prevent to charge the implanted leg with its own weight due to pain or post-operation stress. Interestingly, the complete opening of the bone-implant interface is observed only in few cases during the considered time period, but the dominant feature is a cortical loss with monotonically increasing depth in time.

Thus, this progressive adaptation of the bone tissue depends on the mechanical environment generated by the rat daily activity. In several studies the influence of the daily activity is accounted through control groups of individuals. This approach is often sufficient because the daily activity plays a secondary role with respect to other factors (e.g. diseases or medicaments, Ammann et al. (2007), Glosel et al. (2010)) and the main output of the analysis is based on the comparison between test and control groups. On the contrary, in this animal model the external activation introduced through the loaded implants interacts with the daily activity to define the implants integration state. To optimize the

stimulation and reduce the spread of the results, the implants stability is desired to change only because of the external load. The results of this series show that this condition is not achieved, because the daily activity clearly affects the implants integration and influences the efficiency of the implants activation. Indeed, if the implants insertion depth changes because of a cortical loss, the lever arm through which the external load is transmitted to the bone tissue becomes variable and the bone stimulation loses controllability. For these reasons the daily activity cannot be considered as a negligible loading condition and the comprehension of its correlation with the bone adaptations is a crucial step toward the development of the ‘loaded implant’ model.

2.4.3 Series 3. Overloading

This series describes the reaction to a critical mechanical environment involving both the external loading and the daily activity. In this test campaign, both tibiae are implanted and only the right one is stimulated with external loads reaching 5 N (i.e. corresponding to peak equivalent strains of $\sim 3300 \mu\epsilon$, see Section 3.4.7). In terms of daily activity, the double leg implantation prevents the rat to unload the operated limb, amplifying the effects of the animal locomotion on the implants state of integration. Concerning the external stimulation, the 5 N load ensure the achievement of a peri-implant deformation definitely above the physiological limit measured in rat tibiae during gait (Rabkin et al., 2001).

These settings produced conflicting results, involving both implant rejections and improved integration. For the sake of clarity, the results of this series are presented and discussed in separate sections.

2.4.3.1 Implant rejections

Some animals hardly adapt to the adopted settings. Unlike the previous series, inflammatory states and implants rejections characterize all the groups of animals. Table 2.6 reports a summary of the observed phenomena. Five proximal implants are rejected during the integration period. Eighteen implants (11 right and 7 left) are rejected during the stimulation period. Two right proximal implants are integrated but rotated by $\sim 90^\circ$ with respect to their axis, thus hampering the stimulation. All the rejections are associated to inflammation and swelling, and in two animals the skin fully covered the implants heads. Totally 15 rats have been prematurely sacrificed because of rejections and infections (38 % of total). In Figure 2.9a are reported the implant loss with respect to the integration period for both loaded and control groups. With the bi-lateral implantation both legs are engaged in carrying the animal weight during locomotion and the absence of rest negatively influence the implants stability. As a consequence, even if the primary stability is granted by the initial press-fit, the implants integration after two weeks is not stable enough to

Table 2.6: *Implant loss, Series 3.*

	Limb		Implants loss						R_X %
	swelling		Integration period		Stimulation period				
	R	L	week 1	week 2	week 3	week 4	week 5	week 6	
BS	2	1	-	1 Lp	-	-	-	-	12
2N	3	3	1 Lp	1 Lp 1 Rp	1 Lp 1 Rp	1 Rp	1 Lp 1 Rp	-	62
3N	4	4	-	-	3 Rp	1 Rd	1 Lp	-	50
4N	3	2	-	1 Rp	1 Rp	2 Rp 2 Lp	-	1 Lp	50
5N	3	2	-	-	1 Lp 1 Rp	-	-	-	12

L: left tibia, R: Right tibia; p: proximal implant; d: distal implant; R_X percentage of right tibiae (i.e. stimulated) prematurely lost.

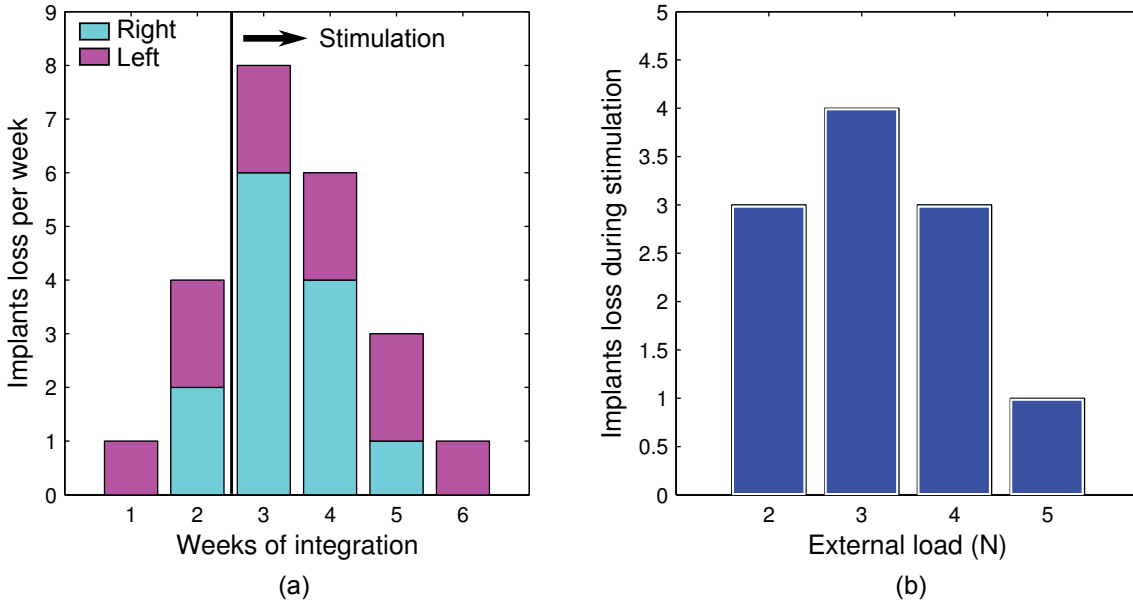


Figure 2.9: (a) *implant rejections per week with respect to the duration. Both right and left implant losses are reported (total = 23).* (b) *implant rejections after 6 weeks with respect to the external load (left implants are excluded).*

handle the external loading (i.e. five implants rejected before stimulation, Figure 2.9a).

The stimulation applied to unstable implants deteriorates the state of integration and drastically increases the implant losses. As shown in Figure 2.9a, the peak of loss is reached during weeks 3-4 (i.e. the first and second weeks of stimulation), and mostly concerns loaded implants.

Interestingly, the load level and the implants loss are not linearly correlated, as shown in Figure 2.9b. Indeed, the stimulation that provokes mild overloading (i.e. 2 N, 3 N and 4 N) deteriorates the integration more than the maximum force (i.e. 5 N). The latter one balances the harmful effects of the daily activity and reduces the occurrence of implant loss. These results are different from the ones obtained in Series 1 (Section 2.4.1), where specimens subjected to mild overloading (1-3 N) show an improved integration, in particular concerning the pull-out force (Table 2.3). Since the difference between these test campaigns is the bilateral implantation, it can be postulated that implanting both legs changes the interplay between daily activity and external stimulation, and this provokes different integration states (see the experiments' recap in Figure 2.13).

These data confirm the strong sensitivity of this animal model to the mechanical environment generated by the rat locomotion (highlighted in Series 2), as well as a relevant interaction with implant loading. Note that the bilateral implantation is successfully adopted in animal models involving rodents, for example to investigate bone scaffolds (Roshan-Ghias et al., 2011), without integration problems comparable to the ones presented here. Among several factors affecting the implants integration (e.g. animals sex and age, materials, surgery protocols), the implant shapes is an important feature of this study. Indeed, the choice to preserve cylindrical surface in contact with bone produces several drawbacks: they offer less anchorage to the bone tissue with respect to screws and may reach critical level of stability in physiological conditions. Nevertheless, these features make this animal model more sensitive to the mechanical stimulation, producing interesting results. As a matter of fact, the specimens that resisted the overloading imposed by the daily activity adapted well to the 5 N stimulation, showing definitively improved mechanical properties as described in the following section.

2.4.3.2 Bone augmentation

As discussed in the previous section, the groups that underwent mild stimulations are characterized by several premature sacrifices (2N, 3N and 4N groups, Table 2.6). Since in this experiment a negative effect on integration is attributed to mild overloading (Figure 2.9b), the remaining stimulated specimens that belong to these groups are not considered. Moreover, the specimens affected by cortical bone loss cannot be compared to the others, due to the uncontrolled variation of the implant integration depth that alters the effects of the external stimulation (Section 2.4.2). Thus, the attention is focused on the specimens char-

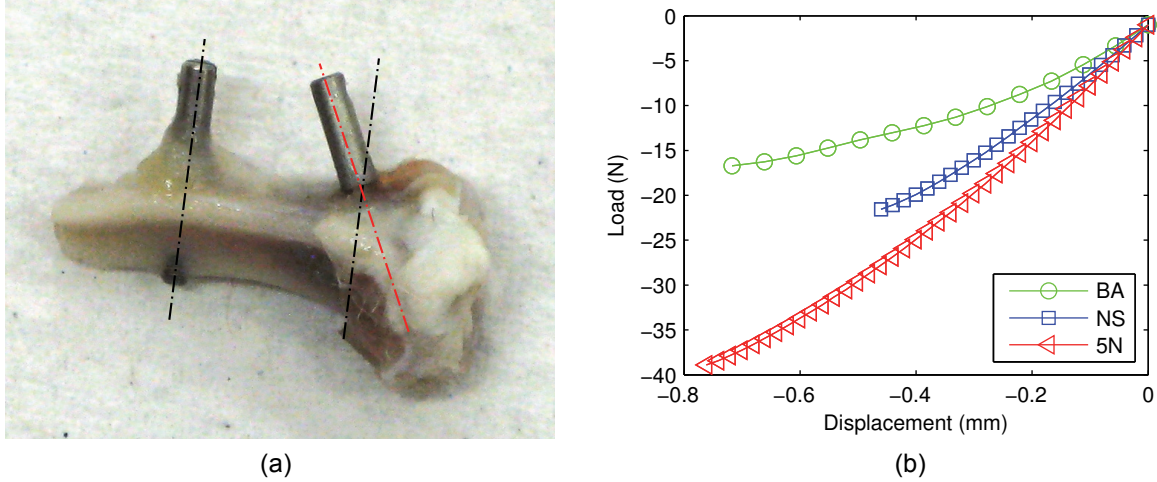


Figure 2.10: (a) Implants orientation before (black) and after (red) inter-implant failure. (b) examples of load-displacement trends of specimens from Series 3: the stimulated specimen (5N) shows improved ultimate load and displacement with respect to the basal (BA) and non-stimulated (NS) ones.

acterized by a good implant integration: five Basal specimens, five specimens stimulated at 5 N and five Non-Stimulated specimens randomly chosen among the left tibiae (total = 15 specimens).

As described in Section 2.3.2.3, the specimens are tested to determine the inter-implant strain II_S (estimated on 5 loading-unloading cycles), and the ultimate force F_U , displacement d_U and energy U_U measured by loading up to failure (Table 2.7). The failure always takes place around the proximal implant provoking its collapse (Figure 2.10a). An example of the representative force-displacement trend of specimens belonging to the three groups is shown in Figure 2.10b. The comparison between the basal and non-stimulated spec-

Table 2.7: Inter-Implant mechanical properties, Series 3.

Group ($n = 5$)	II_S ($\cdot 10^{-3}$)	F_U (N)	d_U (mm)	U_U (mJ)
BA	-4.24 ± 0.14	-20.93 ± 0.52	-0.61 ± 0.02	8.02 ± 0.11
NS	-4.23 ± 0.05	-23.25 ± 1.11	-0.48 ± 0.01^a	6.87 ± 0.47
5N	-3.98 ± 0.13	-40.25 ± 0.75^b	-0.72 ± 0.01^c	17.41 ± 0.11^b

Mean \pm SEM; BA: basal; NS: non-stimulated

^a $p < 0.05$ vs BS; ^b $p < 0.01$ vs NS; ^c $p < 0.05$ vs NS.

imens highlights the brittle behavior of the latter ones, which implies a higher strength but lower displacement. This phenomenon is attributed to the higher mineralization of the non-stimulated specimens due to the animal aging (Turner, 2006). On the contrary, the implant activation definitively improves the strength of the stimulated specimens, resulting in a significant increase of the ultimate strength (+73 %), displacement (+50 %) and energy (+153 %) with respect to the non-stimulated ones (Table 2.7). Thus, the bone adaptation to the external loading improves both ultimate strength and displacement, as opposed to the brittling trend characterizing non-stimulated specimens. Interestingly, the inter-implant strain reduction measured in the stimulated specimens (-6 %) is not statistically relevant, highlighting that the improvement of the bone strength is significant for the ultimate mechanical properties but does not affect as much the inter-implant stiffness. This result agrees with studies on the rat fibulae subjected to mechanical loading (Robling et al., 2002).

The effects of the external loading are quantified also in terms of BMD variation in the ROIs represented in Figure 2.11: a significant increase of density is measured between the implants, in ROI1 and ROI3, with respect to basal and non-stimulated specimens. The medio-lateral ROIs and the bone tissue outside the implants (i.e. ROI4 and ROI5) are not affected by significant density variations.

These results clearly highlight that the bone tissue adapts to the external load by increasing the peri-implant density. Interestingly, both implants are characterized by this adaptation despite the different implantation strategies. The density variation is localized along the tibia longitudinal direction (i.e. the loading direction) and does not involve the medio-lateral tissue. Moreover, a significant increase of density is measured only between the implants, where the bone tissue is subjected to compression during the implant activation, but not in the tensile regions. The mCT images of representative stimulated and control specimens are shown in Figure 2.12. This peri-implant bone adaptation provokes a notable improvement of the ultimate mechanical strength, making the implants more resistant to critical loading conditions with respect to non-stimulated specimens.

It is worth underlining that these specimens represent only the part of the observed population characterized by good integration, and not affected by the harmful influence of the daily activity (i.e. implant rejections or cortical bone loss). Therefore they are probably more resistant with respect to the average. However these specimens represent the outcome of a successful implantation under critical mechanical conditions.

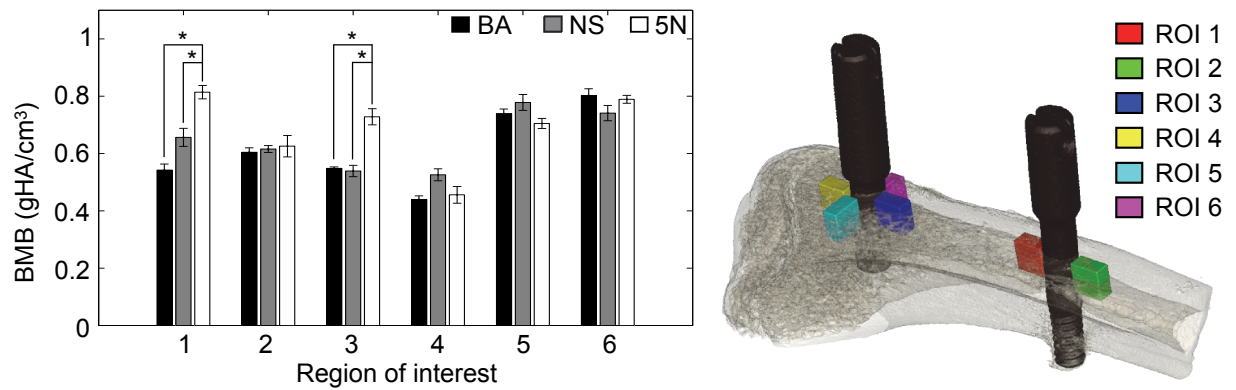


Figure 2.11: Bone Mineral Density (mean \pm SEM) measured in ROIs of specimens from Series 3. * $p < 0.05$.

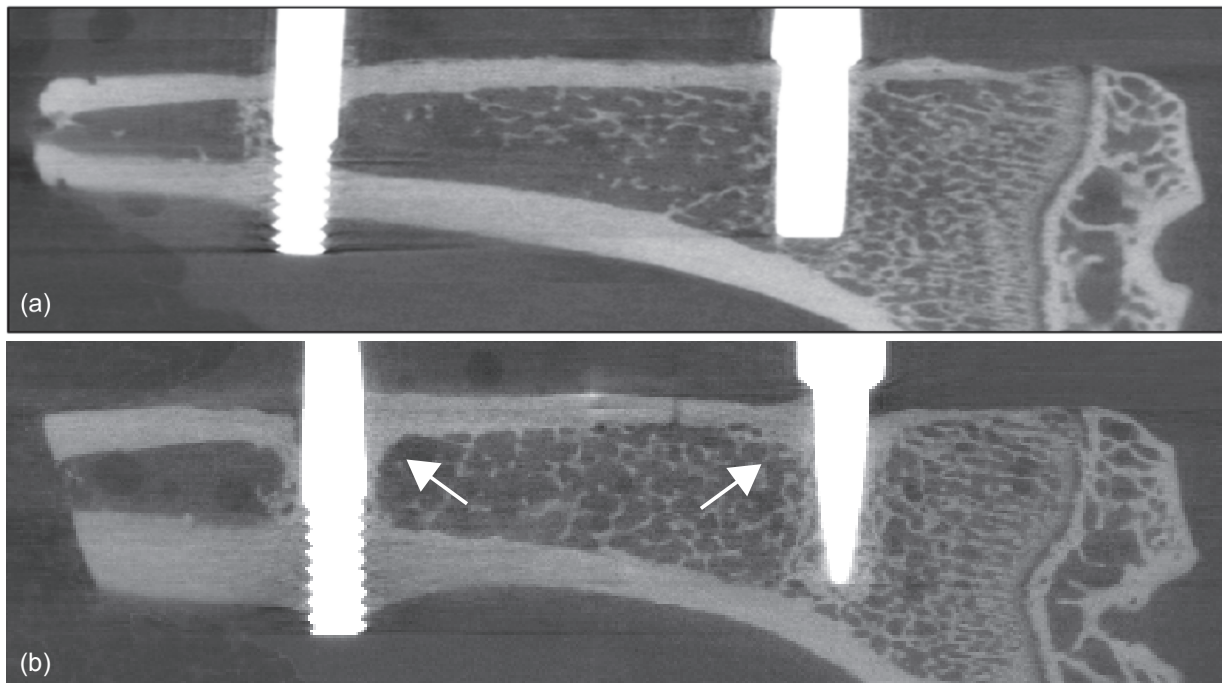


Figure 2.12: Inter-implant sections of mCT scans from (a) a non-stimulated and (b) a stimulated (5 N) specimen. The arrows highlight the peri-implant increase of density between the implants.

2.5 Summary

A summary of the tests campaigns presented in this Chapter is shown in Figure 2.13. This flowchart highlights the variability of results generated by the factors that mostly influence the implants integration in the ‘loaded implant’ model. The interplay between mechanical stimulations (i.e. daily activity and external stimulation) and biodiversity changes in relation to the adopted implantation strategy. In case of monolateral implantation, the implants’ integration is stable. Although peri-implant defects (i.e. openings or cortical bone loss) may appear (Section 2.4.2), none of the implants is rejected and the integration is improved by mild implant stimulation (Section 2.4.1). In case of bilateral implantation, the mechanical environment generated by the daily activity is critical due to the impossibility to unload the implanted leg. The implants’ integration state is unstable and degenerates if mild stimulations are applied (Section 2.4.3.1). On the contrary, high stimulations counterbalance the harmful effects of the daily activity and, if applied to well integrated specimens, cause a significant improvement of integration (Section 2.4.3.2).

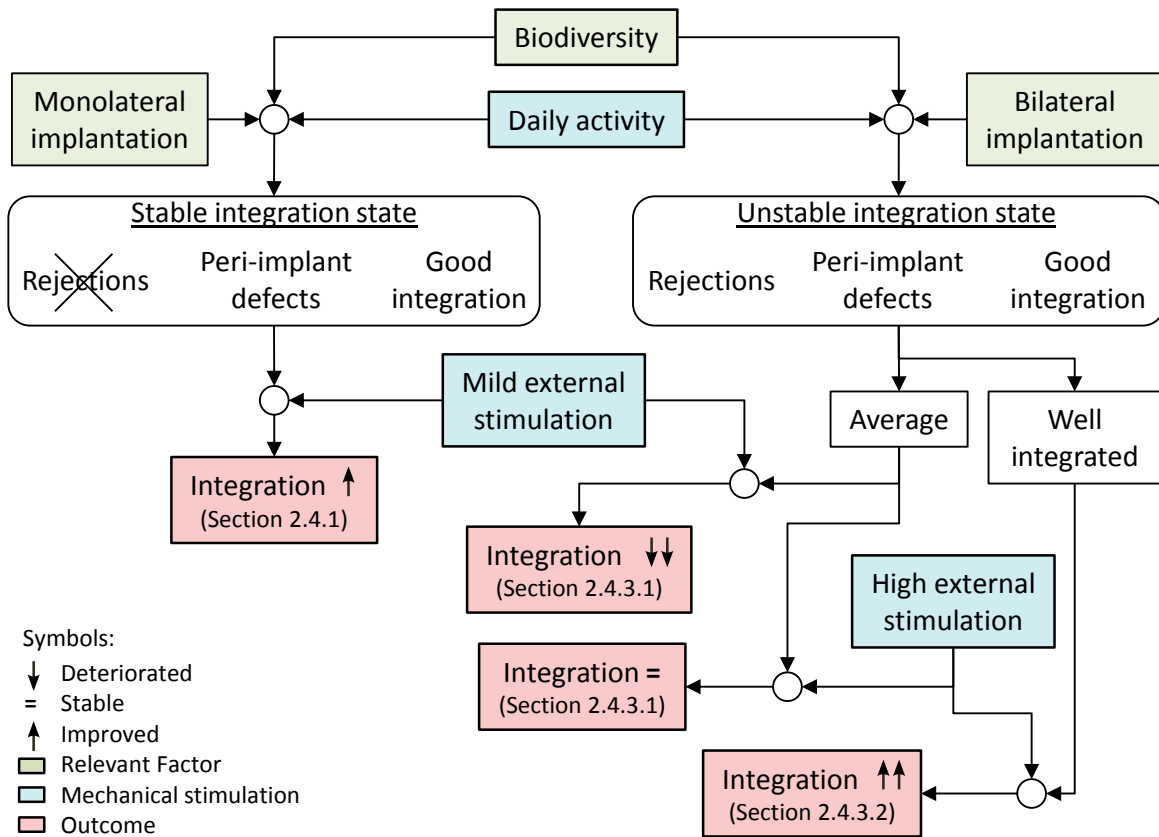


Figure 2.13: Experiments recap.

2.6 Conclusions

The ‘loaded implant’ model allows studying the dependency of implants integration on the mechanical stimulation, through the activation of implants housed in the proximal part of rats tibiae. The peculiarity of this animal model consists in the direct application of the external load to the implants, locally stimulating a small area of bone tissue instead of the whole tibia. Moreover, two different implantation strategies are considered, mono- and bi-cortical, involving a bone-implant contact mainly based on cylindrical surfaces (i.e. not threaded). In addition to a controlled external stimulation based on a wide range of load levels, these features contribute to an increase of knowledge concerning the integration of implants in rat tibiae and its dependence on the mechanical environment. The obtained results allow drawing relevant conclusions, summarized as follow.

1. The rat locomotion has a harmful influence on the implants stability.
 - The rat daily activity provokes a peri-implant cortical loss with a conic shape. Both implants are concerned. The depth of this feature monotonically increases within the observed time (i.e. 6 weeks) and sometimes leads to the complete bone-implant detachment. Moreover, this phenomenon provokes irreparable effects in case of bilateral implantation. Thus, the daily activity cannot be considered as a negligible loading condition and its investigation can lead to the reasons of the observed bone adaptation (see Chapter 4).
 - The implants state of integration changes due to the animal daily activity. This fact, combined with biodiversity, influences the outcome of the external loading and increases the results’ spread. As a matter of fact, a variable depth of bone-implant contact modifies the transmission of a constant external load to the bone tissue.
2. The implants stability is improved through the external loading.
 - The proximal implant pull-out strength is improved in case of mild overloading and monolateral implantation. Although this strength mostly depends on the bone cell proliferation within the implants surface cavities, it can also be modulated through the external loading.
 - The ultimate inter-implant strength of well integrated specimens subjected to overloading is improved with respect to the non-stimulated ones (force +73 %, displacement +50 % and energy +153 %). Indeed, the peri-implant tissue adapts to the imposed exercise producing a significant improvement of the resistance to failure.

3. Cortical and trabecular bone react differently to the external mechanical stimulation.
 - The cortical thickness increases and the mechanical properties are improved in case of mild overloading while a slight decrease of the morphometric parameters affects the trabecular bone.
 - The cortical peri-implant density around the implants increases with overloading, while no effects are seen in trabecular bone. Moreover, the bone apposition is manifested only in the area between the implants, where the cortical tissue is under compression.

4. Both implantation strategies offer advantages and drawbacks.
 - The bi-cortical implantation, characterizing the distal implant, often shows integration problems around the cylindrical part in contact with the cortex. On the contrary, this implantation strategy provides a higher resistance to the ultimate loads. Indeed no failure takes place around the distal implant during *ex vivo* tests.
 - The mono-cortical implantation of the proximal implant, floating in the trabecular bone, provides a better integration despite the absence of thread. On the contrary, it grants less resistance to the ultimate loads. As a matter of fact, all the *ex vivo* specimen failures, obtained through inter-implant compression, occur because of the proximal implant collapse.

From the engineering point of view, the correlation between the mechanical stimulation and the bone adaptation, highlighted by these conclusions, leads to three interesting questions:

1. Is it possible to define a numerical framework to investigate the specimens' mechanical behavior preserving the bio-variability? The differences between the animals contribute to an increase of the results' spread, and affect the success of the implantation. Thus, the generalization of the whole animal population through a single numerical model can lead to ambiguous conclusions, while an approach based on the preservation of the bio-variability allows reaching more representative results (see Chapter 3).

2. Is the peri-implant cortical loss mechanically driven? The investigation of the rat locomotion can clarify if this bone loss is the result of the tissue adaptation to the tibia deformation during gait, and highlight the dominating causes, e.g. overloading, disuse, damage (see Chapter 4).

3. Can the density variation generated by external overloading be predicted through an adaptation algorithm? This investigation can quantitatively describe the correlation between the tissue reaction and the implant loading, allowing a comparison with different animal models. Moreover, this approach can be used to investigate different ranges of simulation, in order to optimize the animal model's settings and efficiently plan further test campaigns (see Chapter 5 and 6).

These questions are deeply investigated in the following chapters, integrating the presented experimental findings with detailed engineering considerations.

Chapter 3

Specimen-specific numerical modeling

3.1 Aim

A protocol to derive Finite Element (FE) models from micro computer tomography scans of implanted rat bone is presented (Piccinini et al., 2012). A detailed sensitivity study highlights the coherence of the generated models and quantifies the influence of the modeling parameters on the results. The stiffness and deformation of bare and implanted rat tibiae are predicted by simulating three-point bending and inter-implant displacement, respectively. The results are validated through comparison with experiments. This numerical modeling provides precise features that highlight the phenomena observed in *in-vivo* experiments:

- FE models allow investigating the bone deformation and its correlation with the tissue structure.
- The specimen-specific approach preserves the differences between specimens, allowing one to study several subjects instead of selecting a single individual, representative of a population.
- The protocol is optimized and validated for different loading conditions and both implanted and bare specimens, which allow investigating the mechanical environment of both test and control tibiae.

3.2 Introduction

Due to its importance in clinical and research applications, subject-specific FE modeling of bone is a fast growing domain. A number of specimen-specific modeling procedures were proposed in the past decade (Anderson et al., 2005, Guan et al., 2011, Weinans et al., 2000, Wullschlegel et al., 2010). However, the assessment of the reliability of the mechanical predictions obtained using such models remains a challenging issue as it depends on both the methods applied and the research discipline.

A growing body of evidence supports numerical methods in modeling the response of bone to mechanical stimuli. Bone is treated either as a macroscopic continuum (Silva et al., 1998, Stülpner et al., 1997) or discretized into its micro-architecture (Kowalczyk, 2003, Yeh and Keaveny, 1999). The osseous tissue's intricate morphology may be approximated either via simplified geometries (Smit and Burger, 2000) or taken from medical images of the specimens or subjects under investigation. Computed tomography (CT) is a common imaging technique employed for this purpose (Ritman, 2004). FE models built on these data preserve the characteristics of each subject. Moreover, when taken as groups, subject-specific FE models permit assessments of the structural and physiological biovariability which, among others, assist in increasing the efficiency of statistical validations. However, the procedures by which subject-specific FE models are derived from CT images are laborious and characterized by systematic errors, user-dependent decisions or random inaccuracies that ultimately affect the results.

An important source of errors depends on the specifications of the CT imaging device. Obviously, the resolution of the CT images greatly influences the accuracy of the FE mesh. Ex vivo high-resolution images yield a detailed description of the bone tissue, trabecular reticulum included. Conversely, for in vivo imaging, the amount of X-ray exposure must be limited and, therefore, the images do not reach the same level of detail (Frush and Applegate, 2004). In addition, the CT scans are affected by artifacts (Al-Shakhrah and Al-Obaidi, 2003). These graphic discrepancies are magnified when structures with large density contrasts (e.g. metal prostheses and bone tissue) are to be imaged (Kataoka et al., 2010). Although their influence can be lessened by corrective measures (Barrett and Keat, 2004), artifacts will affect the FE models derived from the scans.

Another source of error is related to segmentation, that is the process by which different objects can be identified and differentiated in a sequence of CT images (Pal and Pal, 1993). Current methods for segmenting bone tissue are based on (i) geometrical parameters (i.e. objects are outlined by identifying regions and edges, Cufi et al. (2003)), (ii) grey level thresholding or (iii) hybrid methods (Pham et al., 2000). On the whole, the user must combine different segmentation methods and fine tune the parameters of numerous filters to optimize the segmentation of each object, thereby introducing various levels of user-

dependence on the final results.

The FE mesh generated from segmented CT images is yet another source of error as most automated meshing algorithms are appropriate for specific applications only (Ulrich et al., 1998, Viceconti and Taddei, 2003). For instance, voxel-based hexahedral meshes are recognized as computationally stable and suited to micro-scale models (Van Rietbergen et al., 1995). On the downside, the elements' size follows the image's resolution and thus may require large computational time when macroscopic structures are treated. Conversely, high-quality tetrahedral meshes are typically applicable to macro-scale continua as they are less dependent on image resolution (Frey et al., 1994). Still, their geometric accuracy strongly depends on the surface extraction method and notably on mesh decimation and smoothing filters (Taubin, 1995, Vollmer et al., 1999).

The characterization of osseous tissue and its implementation into numerical models is a challenging endeavor due to the bone's multi-scale structure, anisotropy, heterogeneity and biovariability. A number of FE approaches were proposed to model bone structure. High-density FE models can be derived from high resolution CT images and are applicable to the analysis of the osseous microstructure (Verhulp et al., 2008). Intrinsic bone properties are assigned to the osseous tissue as constants and the anisotropy of the system solely depends on trabecular geometry. Alternatively, macroscopic models are often continuum based. The bone is treated as an elastic, continuous but inhomogeneous medium whose local mechanical properties are derived from the grey levels of the corresponding CT voxels. Anisotropy may be added to the structure by implementing Cowin's fabric tensor (Cowin, 1985). Typically, the elastic response is modeled using empirical relationships that relate the CT grey levels to an apparent density of bone mineral, which in turn is converted into a modulus of elasticity (Helgason et al., 2008). However, the scatter of the experimental measurements from which these relationships are derived introduces an error that is critical for specimen-specific studies.

CT-based FE models are widely used, yet only a few reports (Chui et al., 2009, Pahr and Zysset, 2009) provide sufficient details regarding the medical images elaboration, the segmentation protocol and the meshing strategy, to ensure reproducibility of results. Sensitivity studies or experimental validations of FE models generated from *in vivo* or *ex vivo* data-sets are scarce (Taddei et al., 2006). Yet verification and validation of an FE model are cardinal indicators of its reliability (Anderson et al., 2007).

To address these issues, this chapter presents a novel semi-automatic procedure to generate subject-specific, continuum-based FE models from mCT images of rat bone specimens. The essential features of the procedure are as follows:

- Semi-automated segmentation using specimen-specific thresholding.
- Automated quality tetrahedral meshing of the domain based on a direct surface

extraction algorithm.

- Adaptive integration of the density and modulus fields in each element.
- High-intensity artifacts filtering.
- Segmentation-based group definition for boundary conditions.

The procedure is applied to predict the stiffness of bare and implant-fitted specimens in two different loading conditions: inter-implant loading and three-point bending. A comparative experimental-numerical analysis is carried out to verify each step of the procedure and to quantify the influence of the sources of error on the resulting data.

3.3 Materials and Methods

3.3.1 Segmentation

The procedural steps for the semi-automated segmentation are detailed below and presented in Figure 3.1.

3.3.1.1 BMD histogram generation

The specimens scans obtained with the protocol described in Section 2.3.1 were imported into the software ITK-SNAP¹ (Yushkevich et al., 2005). The intensity level of each pixel was converted to BMD using the correlation obtained from the calibration phantom and stored in *Analyze* format (Figure 3.1a,e). The cortical bone was segregated from the background (low-density voxels and saline solution) through the analysis of the BMD histogram (Russ, 2002). Such histogram expresses the distribution of the voxels intensity after conversion to BMD. Four peaks were observable in the histogram of the implant-fitted tibiae, although their location varied between specimens (Figure 3.2 from the left)

- the spongy material used to hold the sample.
- the saline solution.
- the bone tissue.
- the titanium implant.

The last peak was not present in bare specimens.

¹www.itksnap.org

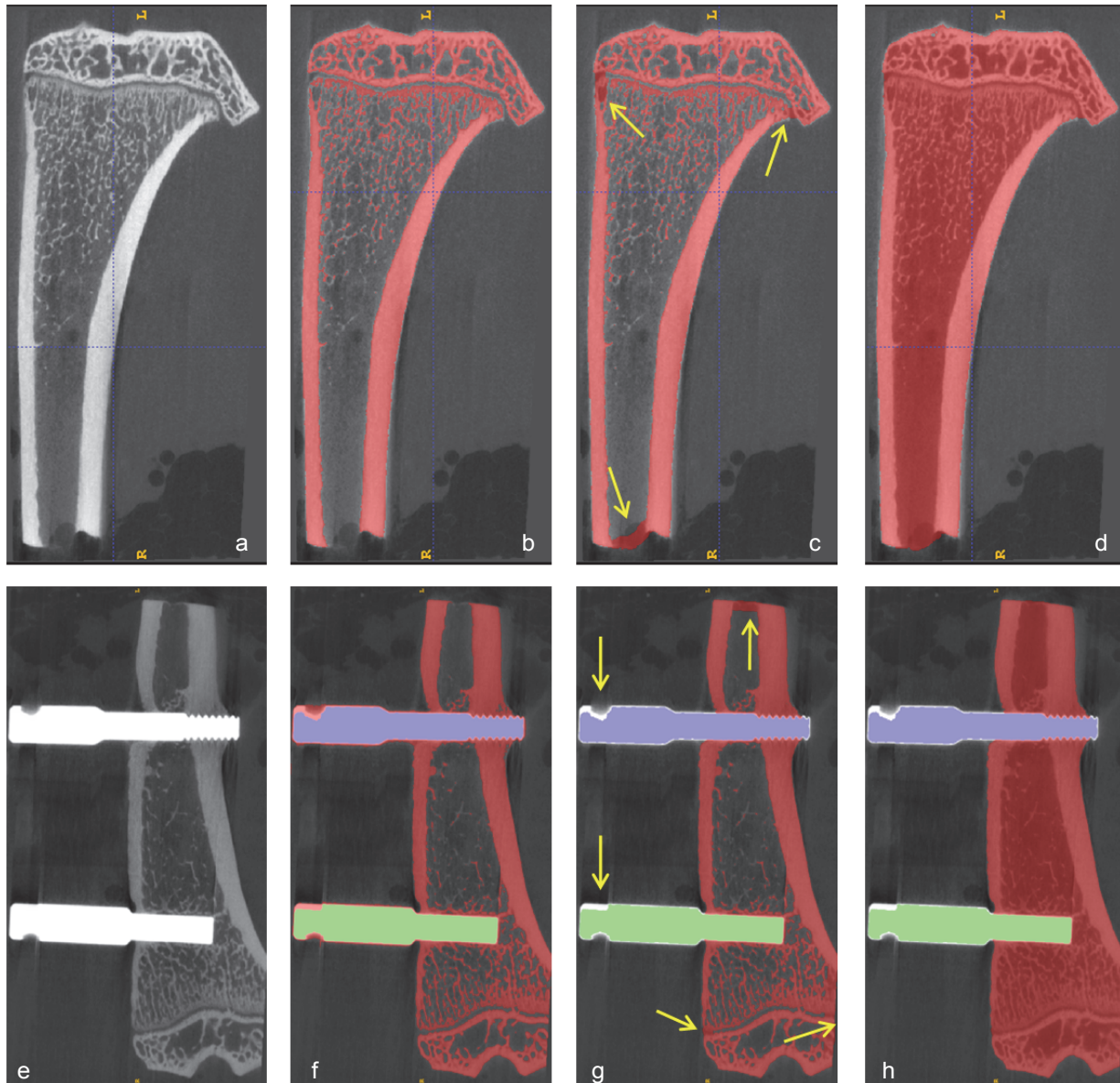


Figure 3.1: Segmentation steps for a bare and an implanted tibia (first and second row respectively). First column: grayscale images. Second column: histogram based threshold segmentations. Third column: manual adjustments to generate closed volumes (yellow arrows). Fourth column: final segmentations. The dark zones on the background correspond to a low-density spongy material used to hold the sample during the scanning process.

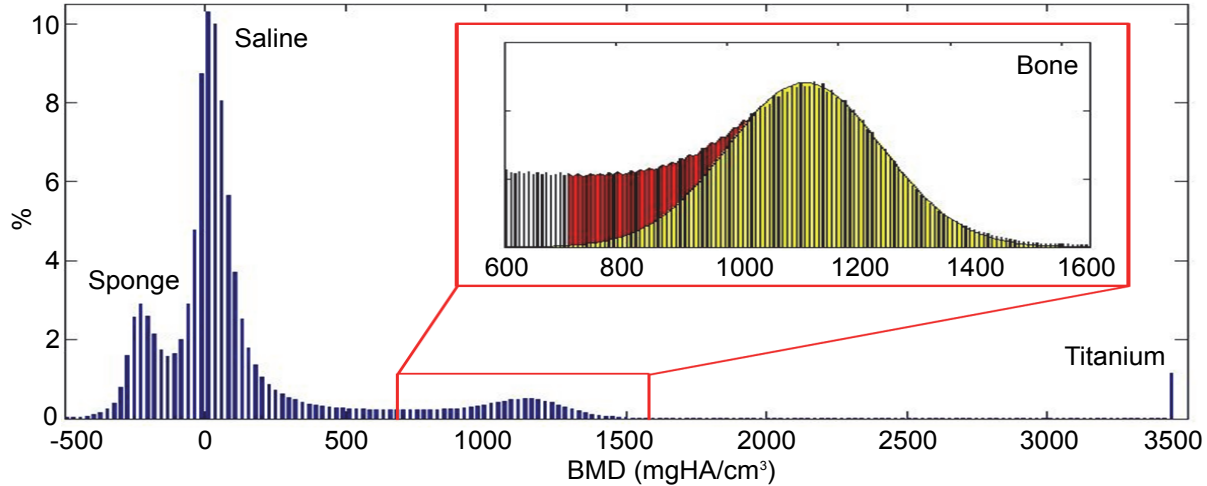


Figure 3.2: BMD histogram of a specimen fitted with implants. From low-to-high BMD values the peaks correspond to: the spongy holder, the saline solution, the bone tissue and the titanium. The enlargement shows the Gaussian fitting (yellow area) and the partial bone voxels included into the bone label (red area).

3.3.1.2 Bone and Titanium density levels

In bare specimens, bone voxels were identified by first fitting the right (i.e. the unambiguous) part of the bone peak with a Gaussian distribution (Figure 3.2). Then the lower, L_1 , and the upper, U_1 , bone thresholds were set as

$$L_1 = \mu_1 - 2.5\sigma_1 \quad (3.1)$$

$$U_1 = \mu_1 + 2.5\sigma_1 \quad (3.2)$$

where μ_1 and σ_1 are the mean and the Standard Deviation (SD) of the Gaussian distribution. All voxels with $L_1 < BMD < U_1$ were grouped under a single label (Figure 3.1b,f). It is worth noticing that these thresholds included a number of ‘partial’ bone voxels (the red area in Figure 3.2) whose brightness was an average between bone and marrow levels. These ‘partial’ voxels mainly affected the trabecular reticulum due to its lower volume-to-surface ratio as compared to that of cortical bone. Considering that all voxels enclosed inside the cortical shell were included into the ‘bone’ label in the last step of the segmentation, there was no need of corrections.

In specimens fitted with implants, two additional labels were identified, both related to the presence of titanium. First the metal was segmented. The metal was segmented by thresholding so it corresponded to a single BMD value, T_{imp} . Voxels with a BMD equal to T_{imp} were thus classified as ‘titanium’. The proximal implant was differentiated from the

distal implant by region-growing filtering. Concerning the bone tissue, the lower threshold, L_2 , was taken as shown in Equation 3.1. However, to account for the metal artifacts, the upper threshold U_2 was set to Equation 3.4

$$L_2 = \mu_2 - 2.5\sigma_2 \quad (3.3)$$

$$U_2 = T_{imp} - 1 \quad (3.4)$$

where μ_2 and σ_2 are the mean and SD of the Gaussian distribution fitted on the scans of implant-fitted specimens. This treatment prevented geometric discontinuities between the bone and titanium domains.

An example of a multi-label segmented image is provided in Figure 3.1f. Note that the segmentation thresholds were derived from each sample's density histogram and thus accounted for the biovariability, precluding the interpretation by the operator.

3.3.1.3 Generation of a closed volume of bone

The images were adjusted as shown in Figure 3.1c,g. The gaps at the end of the diaphysis and at the periphery of the epiphyseal plates were closed by manual 3D brush segmentation to obtain a 'water-tight' volume. An algorithm was applied to fill the volumes delimited by a specific label. The final results of the semi-automated segmentation are shown in Figure 3.1d,h, in which the bare and the implant-fitted specimens are now entirely individualized relative to the background. The voxels labeled as 'bone' (in red) include the bone tissue and the marrow. Finally, the segmented bone volume was subjected to minor refinements to simplify the definition of boundary conditions. For three-point bending analyses three further labels were generated by manual 3D brush painting, thus overwriting the original bone label in the regions of the cortical surface where the supports contact the bone during the test (Figure 3.3a). For inter-implant stiffness, the implants' heads were differentiated (Figure 3.3b).

3.3.2 Finite Element model generation

A versatile FE mesh generator called *VoxelMesher* was developed to automatically generate a tetrahedral mesh from segmented multi-label images. *VoxelMesher* combines a quality surface meshing algorithm, an octree domain decomposition technique and a Delaunay tetrahedral meshing algorithm. More specifically, each label is extracted as a binary image and its boundary is discretized using a triangle meshing algorithm for 3D implicit surfaces (Boissonnat and Oudot, 2005), available in the Computational Geometry Algorithms Library CGAL². To generate a quality tetrahedral mesh, the surface meshes are merged

²www.cgal.org

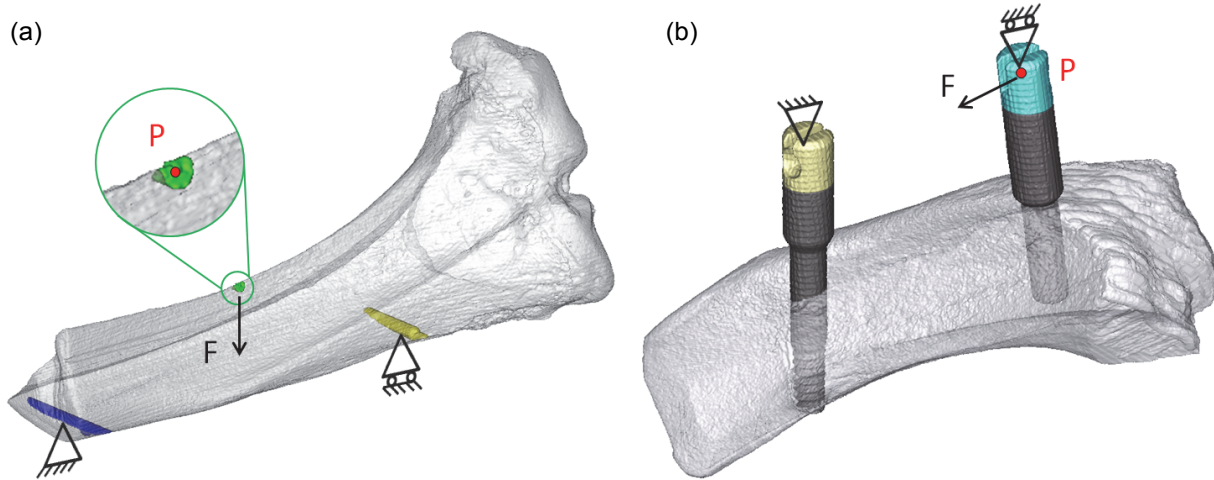


Figure 3.3: 3D representations of specimens segmented to simulate (a) three-point bending and (b) inter-implant stiffness. The colored regions were adopted to apply the boundary conditions by kinematic coupling with reference points. The force F was applied to the reference point P (red color) to calculate the specimen stiffness.

in a non-manifold triangulation and embedded in a bounding box, where seed nodes are generated using a recursive octree decomposition of the domain. For each octree cell, if the cell does not contain a node of the surface, a seed node is inserted at its centre, otherwise the octree cell is split into eight smaller cells. The octree decomposition continues until the octree cell size is smaller than three times the characteristic size of the surface mesh. Using the bounding box, the surface mesh and the seed nodes as input, an initial constrained Delaunay tetrahedral mesh is generated using TetGen³ (Si, 2002) with relaxed quality criteria. Each tetrahedral element of the mesh is labeled using the multi-label segmentation image as reference. After deleting the undesired domains, a high-quality tetrahedral mesh is calculated by refining the initial one using a local element size map. By default, elements are grouped as belonging either to the surface or to the volume of their respective label. The user may create additional groups by processing a supplemental segmentation image, hence facilitating the implementation of pertinent boundary conditions. Finally, the linear triangles and tetrahedra are converted to quadratic elements by adding mid-side nodes.

Each element belonging to the label ‘bone’ was assigned a modulus of elasticity in accordance with a previously generated 3D map of elastic modulus (Taddei et al., 2007). This 3D image of Young’s moduli was obtained by converting the BMD value of each voxel into a corresponding modulus of elasticity using the relationship developed by Cory et al. (Cory et al., 2010) (Equation 3.5), originally derived using bone specimens extracted

³tetgen.berlios.de

from the cortical and trabecular bone of Sprague-Dawley rat femurs. This relationship was compared to that proposed by Hodgkinson and Currey (Hodgkinson and Currey, 1992) (Equation 3.6) with the goal to evaluate the FE model’s sensitivity to the material characterization. Hodgkinson and Currey’s relationship, though, is derived from human bone specimens and thus might be less applicable to characterize the intrinsic bone properties of rats. The densitometric measures were homogenized to BMD using the relations of Keyak et al. (Key) and Burghardt et al. (Burghardt et al., 2008).

$$E = 8.36\rho_{bmd}^{2.56} \quad (3.5)$$

$$E = 3.98\rho_{dry}^{1.78} \quad (3.6)$$

where E is Young’s modulus, ρ_{bmd} is the BMD and ρ_{dry} is the dry density. As the FE size and the resolution of the field image may be radically different, *VoxelMesher* handles an adaptive integration scheme inspired from Taddei et al. (Taddei et al., 2007). If the volume of a tetrahedron is larger than 15 voxels, the average of the field is computed by summation of the discrete voxel values enclosed within the element. Otherwise, the average is computed through a four-point quadrature formula (Yu, 1984) using interpolated voxel values. For computational purposes, the user must discretize the range of E to a finite number of intervals. All the titanium elements were assigned a constant elastic modulus of 110 GPa and Poisson’s ratio $\nu = 0.3$.

To limit the effect of metal artifacts which would translate into unrealistically stiff bone elements, the BMD-modulus relationship was modified by introducing a maximum BMD threshold. The piecewise conversion for the implanted tibiae was set to

$$E = \begin{cases} E(\rho_{bmd}) & \text{if } \rho_{bmd} \leq U_{imp}; \\ E(U_{imp}) & \text{if } U_{imp} < \rho_{bmd} < T_{imp}. \end{cases} \quad (3.7)$$

where U_{imp} is the upper BMD threshold of the cortical bone in the implant-fitted tibia computed as

$$U_{imp} = \mu_2 + 2.5\sigma_2 \quad (3.8)$$

Capping Young’s modulus prevented the assignment of aberrant material properties to elements affected by high-intensity artifacts.

VoxelMesher exported the models as ABAQUS-Standard^{®4} input files appending the user-defined boundary conditions for computation. As shown in Figure 3.3, the boundary conditions were assigned by kinematic coupling of reference points to user-defined regions. The contact compliance between the sample and the set-up was verified to be negligible to estimate the specimen stiffness. In both analyses, a 1 N force was applied to the point P, whose displacement was monitored to calculate the stiffness. Linear computations were carried out by the implicit ABAQUS-Standard[®] solver.

⁴6.10, Dassault Systèmes, Vélizy-Villacoublay, France.

3.4 Results and Discussion

The presented protocol leads to the generation of specimen-specific FE models of a large variety of bone samples. In the following sections, the sensitivity to the input parameters and the reliability of the protocol are discussed. First, the models' performance and the dependency of the final results on the modeling assumptions were investigated. Several benchmarks were implemented, reflecting key aspects of the protocol and identifying potential causes of error. Second, the capability of the generated models is compared with the experiments.

3.4.1 Validation tests

In light of the small dimensions of rat tibiae, three-point bending tests were deemed most suitable for short specimens in full awareness that the stiffness essentially depends on the mechanical properties and geometry of the cortical bone. The length-to-thickness ratio of the tibiae is not a limiting factor in this case as the bones are compared with a full 3D simulation under the same experimental conditions. Each tibia was subjected to five load-unload cycles and the first two were not included into the analysis to permit the samples adjustments on the supports. The force-displacement plots of the four samples under three-point bending are shown in Figure 3.4a. As shown, the specimens responded linearly and elastically ($R^2 > 0.95$). Furthermore, the coincidence of the loading and unloading paths indicated the absence of hysteresis, faulty displacements of the samples on their supports or cracks propagation.

In implant-fitted specimens, the tip of the proximal implant is entirely surrounded by trabecular bone, thus the stiffness depends on the mechanical properties of both cortical and cancellous bone. The force-displacement plots of the inter-implant test are displayed in Figure 3.4b. As the V-shaped notches were sharpened, their position on the implant heads was fully reproducible. Moreover, the low load levels applied exclude any noticeable indentation of the steel blades on the titanium. In this test as well, the specimens responded linearly and elastically. In both experiments, the measurements were repeated twice to verify the method. Both the loading and the unloading paths were included into the linear regression fits when stiffness was computed.

3.4.2 Imaging

The settings of the mCT system were chosen to obtain a reliable representation of the specimen geometry and density (Nazarian et al., 2008). The $20 \mu m$ voxel size and the 0.358 angular step ensured a good representation of the bone morphology (Cha, Yeni et al., 2005).

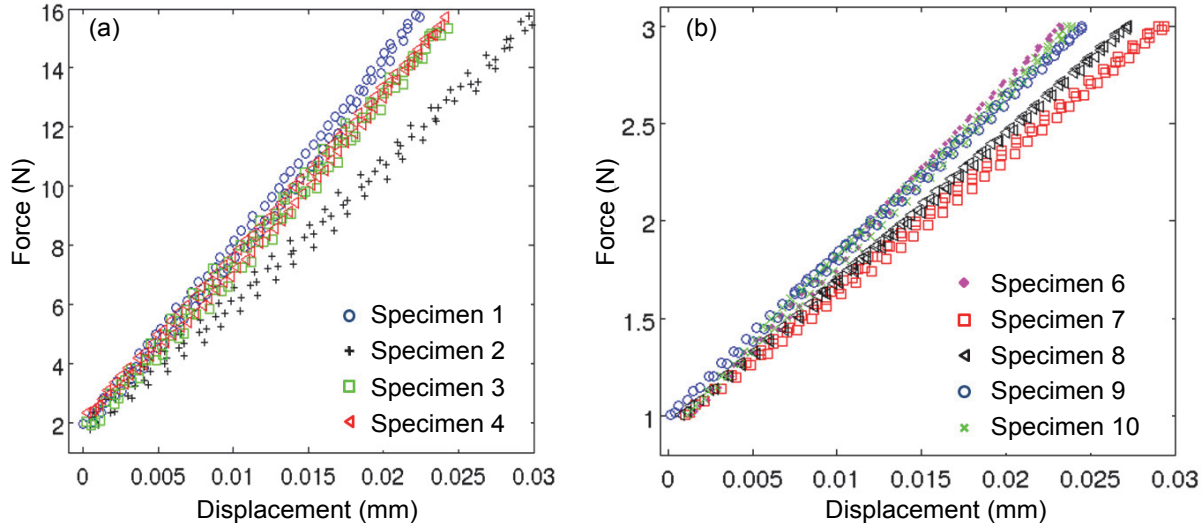


Figure 3.4: Force-displacement trends of the specimens under (a) three-point bending and (b) inter-implant stiffness. Two load-unload cycles are shown. The displacement values account for the respective set-up stiffness

The *SCANCO*[®] system generates a polychromatic cone-shaped X-ray beam which is subjected to Beam Hardening (BH), a phenomenon that is caused by the absorption of low-energy photons by the material under scrutiny and may result in BH artifacts (Fajardo et al., 2009). Two levels of BH correction were evaluated (200 and 1200 mgHA/cm³), resulting in less than 3 % variation in the stiffness predicted by the FE models. A 200 mgHA/cm³ BH correction was finally adopted because recommended for the imaging of long bones of small animals (Burghardt et al., 2008).

The images are also marred by strike artifacts caused by the titanium. These artifacts appear as bright or dark non-uniform stripes whose intensity and direction depend on the orientation of the implants relative to the X-ray beam (Barrett and Keat, 2004). To limit these artifacts, two specimen orientations were considered: with the implant axes parallel or perpendicular to the scanner's rotation axis *Z* (Figure 3.5a,b respectively). The latter orientation was affected by discontinuities between bone and implants (red circles), so the former was preferred as it caused notably less distortion. The influence of the artifacts on the final results was limited by the bounded conversion law in Equation 3.7, calculated with specimen-specific density thresholds. The imposed maximum density value prevented the overestimation of material properties in regions affected by such artifacts. To evaluate the influence of this upper density threshold, several models were generated both with and without correction. The difference in terms of inter-implant stiffness was in the range

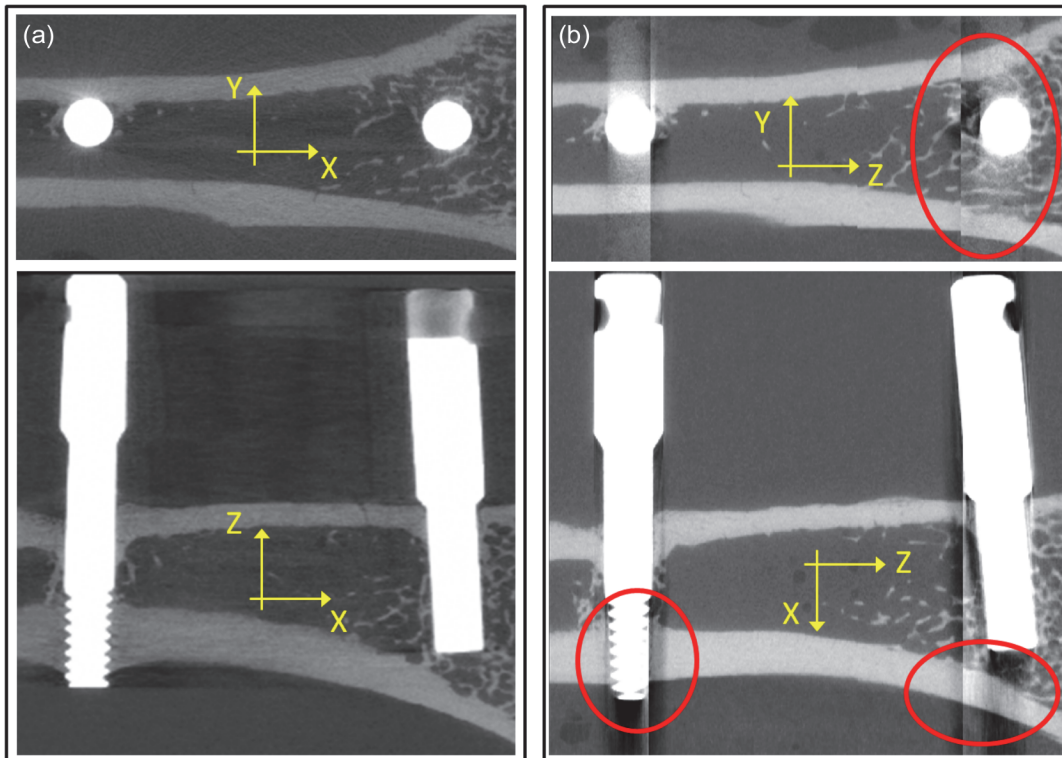


Figure 3.5: Comparison of the artifacts in mCT images of an implant-fitted tibia with regard to the orientation of the implant axes: (a) parallel and (b) perpendicular to the rotation axis Z . The second image is affected by non-negligible discrepancies (red circles)

of 2.5-3 %. Most of the voxels affected by this correction were located in the immediate vicinity of the titanium-bone interface and thus only affected local stiffness values close to the implant. Although the present artifact limitation strategy is not comparable to metal artifact correction algorithms (Boas and Fleischmann, 2011), it provided a reliable prediction of the specimen’s stiffness.

3.4.3 Segmentation

The specimen-specific segmentation method was verified by analyzing its capability to reproduce the volume and density of an elementary specimen. Two HA cylinders, 400 and 800 mgHA/cm³ density, a volume of 104 mm³ and embedded in resin, were imaged with the mCT system and segmented using three different techniques:

- Manual 3D brush segmentation.
- Trial-and-error threshold identification.
- Histogram-based segmentation, described above.

All three techniques were carried out by an experienced ITK-SNAP user and the results are compared in Table 3.1. Note here the accuracy in volume and density, but also the time spent by the user to complete the segmentation.

With all three methods, the absolute error was less than 5 % in volume and density. The higher density cylinder, whose mineral content is comparable to cortical bone, yielded errors of less than 2 % and 1 % for volume and density. For the lower density cylinder, the automated and trial-and-error thresholding methods lacked definition as the contrast with the surrounding environment was reduced. Still, the two manual techniques are affected

Table 3.1: Comparison of segmentation techniques.

Method	Cylinder Density (mgHA/cm ³)	Segmentation				
		Volume (mm ³)	Volume error (%)	Density (mgHA/cm ³)	Density error (%)	Time (min)
Manual brushing	400	103.86	-0.1	420 ± 66	5	~ 25
	800	102.65	-1.3	801 ± 72	0.1	
Trial-and-error thresholding	400	107.27	3.1	413 ± 57	3.25	~ 10
	800	105.64	1.6	795 ± 77	-0.6	
Histogram-based thresholds	400	109.04	4.8	418 ± 91	4.5	~ 2
	800	103.74	-0.2	803 ± 92	0.4	

by a variety of drawbacks. The accuracy of manual 3D brush segmentation dramatically decreases when handling complex geometries. Moreover, the results of the manual and trial-and-error threshold segmentation are affected by the user’s experience, hence their repeatability is lousy. The latter factor was tested in a repeatability study involving three different operators. For each operator, two 3D segmentations of implanted bone specimens were generated at one-day intervals using the trial-and-error threshold method. The variability recorded in this simple test was 6 % for bone volume and 3 % for density.

Overall, the proposed histogram-based method provided an adequate level of accuracy in a short processing time while minimizing the influence of the operator. All three aspects are essential whenever large groups of specimens are to be segmented. In the present research line this method has proven robust for single- or multi-label segmentations provided that the various elements were reflected as well-differentiated grey levels in the brightness histogram. It is worth noticing, though, that the efficiency of this segmentation method has been verified only for specimens with a high volume-to-surface ratio (i.e. filled cylinders and rat long bones mainly composed by cortical tissue) and not for trabecular bone samples.

3.4.4 Finite Element discretization

A mesh-convergence study was conducted to assess whether the FE mesh generator adequately reproduced the volumes and mean densities of the segmented labels. Three models with fine, medium and coarse mesh were generated after segmenting specimen number 7. Table 3.2 reports the data obtained directly from segmentation as compared to those derived from each FE model.

The fine mesh reproduced the segmented volume and mean density with errors less than 1 %, while the SD was underestimated by 8.5 %. The medium-size mesh was in close

Table 3.2: *FE models volume and density reproduction. In parenthesis is reported the difference with respect to the segmentation.*

	Mesh details		Property		
	Number of nodes	Voxels per element	Volume (mm^3)	Density mean ($mgHA/cm^3$)	Density SD ($mgHA/cm^3$)
Segmentation	–	–	225.84	873.28	270.17
Fine mesh	626176	51	225.67(−0.07)	877.04(0.43)	247.25(−8.48)
Medium mesh	86158	326	225.00(−0.37)	889.39(1.84)	234.26(−13.29)
Coarse mesh	2209	12323	217.77(−3.57)	935.80(7.16)	171.49(−36.52)

range in terms of volume. The mean density error increased to 1.8 % and the SD was underestimated by 13 %. The coarse mesh was less efficient: the segmented volume was underestimated by 3.6 %, the mean density error increased to 7.2 % and SD was 36 % lower.

In view of these data, a mesh density of at least 300 voxels per element is required to properly capture the density field. Finally, the cortical and trabecular bone compartments are modeled as continua of which each element is fitted with an average of the elastic moduli of its constitutive voxels. Therefore, the reduction in SD observed for medium and coarse meshes merely denotes the spatial averaging that follows the conversion from a microstructural, voxel-based, density field to its more macroscopic, element-based, counterpart. Hence, the above mentioned variations in the SD of the density field do not cause significant errors in the resulting stiffness computations.

3.4.5 Density-Elasticity relationship

The user must specify the number of intervals that make up the range of pertinent elastic moduli. These parameters, coupled with the voxel/element size ratio, determines the accuracy of the material property field. To test the effects of both factors, a convergence study was conducted taking the inter-implant stiffness as reference. The number of intervals was varied from 16 to 65536 possible values (i.e. the shades of 4- and 16-bit greyscale images). As shown in Figure 3.6, the medium mesh demonstrated an irregular behavior when increasing the number of intervals while the fine mesh shows a smooth convergence. Nevertheless, with both mesh sizes and a number of intervals greater than 256, the variations in the computed stiffness is lower than 1.2 %.

In light of these findings, the FE models in this research were established with fine meshes (51 voxels per element) and 256 intervals in the range of Elastic modulus. For adaptive modeling analyses (i.e. involving iterative processes) the models were established with the medium mesh to limit the computational time.

3.4.6 Measured and simulated specimen stiffness

The measured stiffness was taken as the reference to compute the error affecting each specimen-specific FE model. The BMD-elasticity relationship by (Cory et al., 2010) yields models (FEM_C) in good agreement with the experimental inter-implant stiffness. The accuracy of the three point bending models was inferior as they underestimated the stiffness by 9.8 % on average. In spite of the differences between specimens, a high correlation was found between experimental values and computed stiffness, with R^2 of 0.91 and 0.83 for three-point bending and inter-implant stiffness respectively (Figure 3.7). These lev-

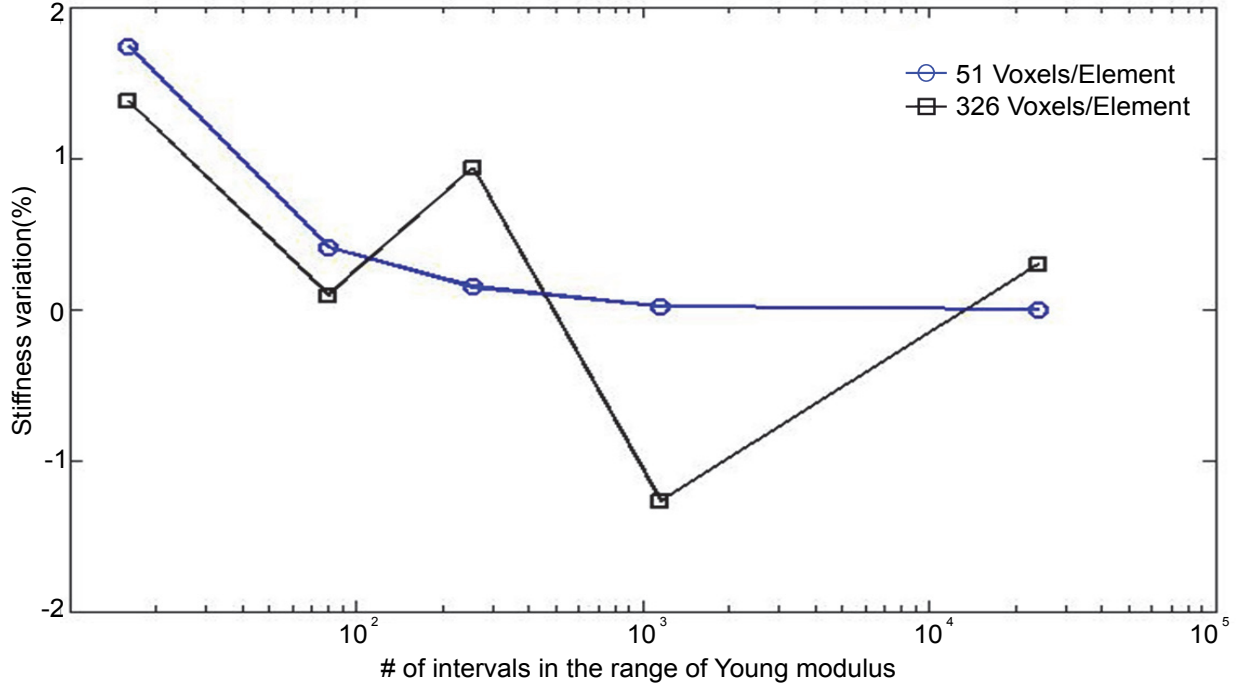


Figure 3.6: Stiffness' variation as function of the resolution of Young's modulus range.

Table 3.3: Comparison of density-elasticity relationships.

	Sample number	Stiffness (N/mm)	FEM_C error (%)	FEM_H error (%)	$FEM_C - \sigma$ error (%)	$FEM_C + \sigma$ error (%)
Three point bending	1	1275.0	-6.5	12.7	-41.3	51.7
	2	818.3	-19.5	4.1	-50.2	28.7
	3	978.2	-2.3	15.4	-37.2	62.0
	4	1020.7	-22.4	8.4	-47.7	45.9
	Average	-	-9.8	10.1	-44.1	47.1
Inter-implant stiffness	6	101.4	-5.4	3.4	-26.8	18.1
	7	78.2	-1.1	6.6	-20.1	18.3
	8	90.2	-9.3	-1.8	-29.7	12.7
	9	83.5	-1.3	5.5	-19.1	16.3
	10	98.1	1.9	9.6	-18.9	24.0
	Average	-	-3.0	4.7	-22.9	17.9

FEM_C and FEM_H with $E(\rho_{bmd})$ based on (Cory et al., 2010) and (Hodgkinson and Currey, 1992). $FEM_C - \sigma$ and $FEM_C + \sigma$ with $E(\rho_{bmd})$ based on the lower and upper bounds of the relationship by (Cory et al., 2010).

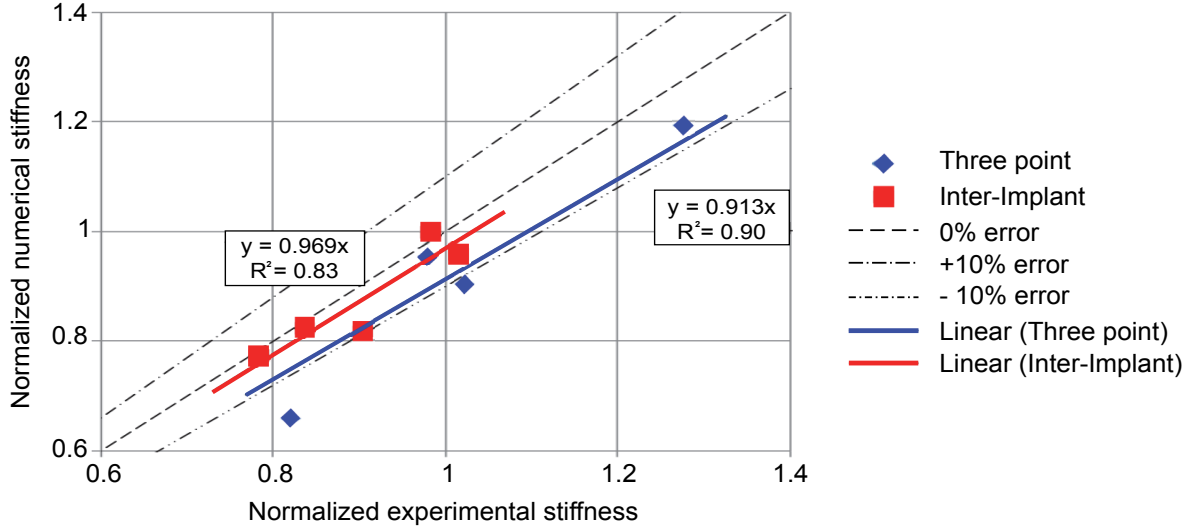


Figure 3.7: Correlation between the normalized experimental and simulated stiffness values for each specimen. Normalized stiffness is defined as stiffness/1000 for three-point bending and stiffness/100 for inter-implant.

els of correlation demonstrate that the protocol accounts for the variability between the specimens.

Cory et al.'s and Hodgkinson-Currey's models (FEM_H) were compared for all the specimens. As shown in Table 3.3, Cory et al.'s relationship systematically underestimates the stiffness while Hodgkinson-Currey's law does the opposite. As shown in Figure 3.8, above 700 mgHA/cm³, Hodgkinson-Currey's relationship yields higher Young moduli with respect to Cory et al. This range is precisely that of cortical bone hence explaining the 10 % FEM_H stiffness overestimation. The mean error incurred in inter-implant stiffness is only 4.7 % as this load case involves both cortical and trabecular bone and thus depends on a wider range of BMD values.

This comparison highlights the strong dependency of the results on the density-modulus relationship and the important differences obtained using such relationships derived for various species, loading conditions and length scales. The results in Table 3.3 do not indicate a clear superiority of either Cory et al.'s or Hodgkinson-Currey's relationship. Still, for the present research, Cory et al. was selected because it was originally derived from Sprague-Dawley rat bone tissue under compression and thus ensures some coherence with the present experimental conditions.

In general, the following recommendations are made to minimize the risk of errors due to density-elasticity relationships. In the absence of prior experimental knowledge regarding a specific application, the density-modulus relationship should be coherent with

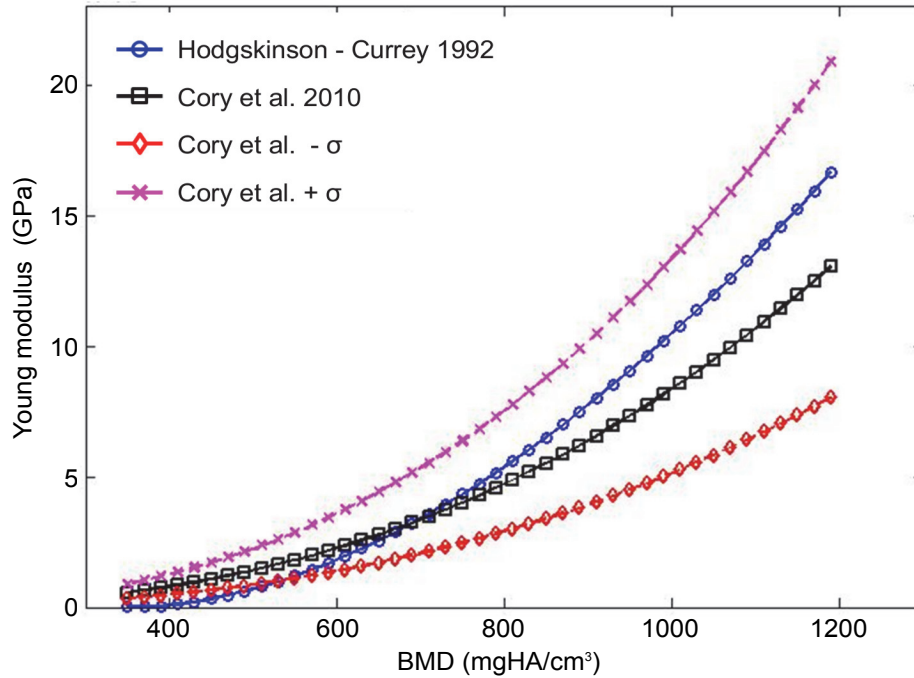


Figure 3.8: *Density-elasticity relationships adopted in this study.*

- the species under investigation.
- the type of bone tissue (range of BMD and specimen size).
- the loading condition (stress level, tension/compression).

Even if a matching elasticity relationship can be found in the literature (as in this study), it is still recommended to validate the numerical predictions with experiments.

In a further investigation, the confidence interval of the density-modulus relationship by Cory et al. was assessed (Figure 3.8). The upper and lower bounds were estimated by assuming a normal distribution of the experimental points representing Young's moduli with respect to BMD. The confidence interval accounts for the scatter due to the experimental procedure, the intra-specimen biovariability (caused by natural gradients within a specimen) and the biovariability between individuals (Sema Issever et al., 2002). The quantification of the influence of these three factors is complex, therefore, density-elasticity relationships should not be taken as deterministic but only as denoting the mean (\pm SD) of a group of specimens. Using the estimated confidence bounds of the density-modulus relationship, a corresponding confidence interval of stiffness values representative of 68 % of the specimen population can be calculated. The simulated range of variation of the three-point bending and inter-implant stiffness is about 45 % and 20 % of the mean value,

respectively Table 3.3. These very wide confidence intervals demonstrate that the uncertainty related to density-modulus relationship is the factor that potentially has the most influence on the simulation results. In principle, with such variability, it would only be possible to obtain a correct estimation of the average specimen behavior on a fairly large number of samples, and the predictive capabilities of a single specimen-specific FE model would be limited. However, we observe here that when using the average density-modulus relationship, the errors are much smaller than the confidence interval would suggest and that the correlation between the experimental and simulated stiffness remains high. Even though the number of experiments presented here is not statistically representative, the relatively small errors obtained using the mean relationship suggests that a significant part of the scatter of the density-elasticity relationship vanishes when simulating the whole bone stiffness. This fact may be explained by the following points:

- The global stiffness is a homogenized measure of the local moduli, so the random local stiffness variations (i.e. intra specimen variability, e.g. related to bone structure) do not significantly influence the final stiffness results.
- the scatter due to experimental characterization procedures used to determine the modulus-density relationship is in principle not correlated with the BMD and thus should have a limited influence on the final simulation results.
- in the present situation, the inter specimen variability in terms of stiffness seems to be mostly related to bone geometry.

However, if local properties are considered (e.g. stress or strain), it is expected that the intra-specimen variability and inter- specimen variability will develop a much larger effect. To mitigate the influence of inter-specimen variability, specimen-specific intrinsic bone properties could be determined (e.g. through indentation tests) to correct the average density-elasticity relationship for each subject.

3.4.7 Simulated strain field

Several attempts to place the strain gauge between the implants were made. Unfortunately, the reduced space and the surface roughness were critical obstacles. The zone where the strain gauges were glued provides enough space to operate and experiences enough deformation to be interrogated. Nevertheless it is narrow and curved: both features should be avoided to obtain a correct measurement. Because of these problems two strain gauges were not well bounded to the bone surface and could not be interrogated. The comparison between the measured and numerically predicted surface strains is reported in Table 3.4.

Table 3.4: Comparison of strain measurements.

Test	Sample number	Longitudinal strain ($\mu\epsilon$)	FEM ¹ error (%)
Inter-Implant stiffness	6	355	-14
	8	201	-12
	9	298	-6
	Average	-	-11

¹ Cory et al.

The well glued sensors confirmed the prediction of the FE models with a maximum under-estimation of 14 %. This validation permits quantitative considerations on the adaptive modeling signals investigated in this thesis.

To illustrate the results obtained with the present protocol, the equivalent strain field of specimen number 9 subjected to 1 N of inter-implant force is depicted in Figure 3.9. The inhomogeneous field of elastic moduli generates a deformation pattern which is indicative of the structural differences of the bone tissue. Views (a) and (c) identify those regions that are most affected by bending, whereas the zones shown in views (b) and (d) are nearly undeformed. Strains are distributed in the inter-implant cortical tissue and the trabecular reticulum surrounding the implants, hence supporting the concept that inter-implant stiffness depends on the mechanical behavior of both the cancellous and the cortical bone. Note that the bone-implant interface is sharply delineated and the threads are accurately defined, a finding which is considered as a confirmation of the accuracy of the segmentation and meshing protocol.

3.5 Summary

The proposed protocol is suitable for generating subject-specific mCT-based FE models capable of predicting the stiffness of implant-fitted and bare rat tibiae while preserving the individual geometry and the bone's density field of each specimen. Segmenting one image requires about 30 min of which most of the time is due to the manual adjustments required to adapt the segmented images to the user's needs (e.g. the additional labels for the three-point bending). The histogram-based thresholding technique provides a user-independent segmentation and the volumes and densities of the specimens are preserved with errors less than 2 % and 1 %, respectively. With an optimized element-voxel volume ratio (maximum 300) and an 8-bit interval discretization of the range of Young's moduli (256 values), the geometry and the mean density of the specimens are reproduced in the FE mesh with less

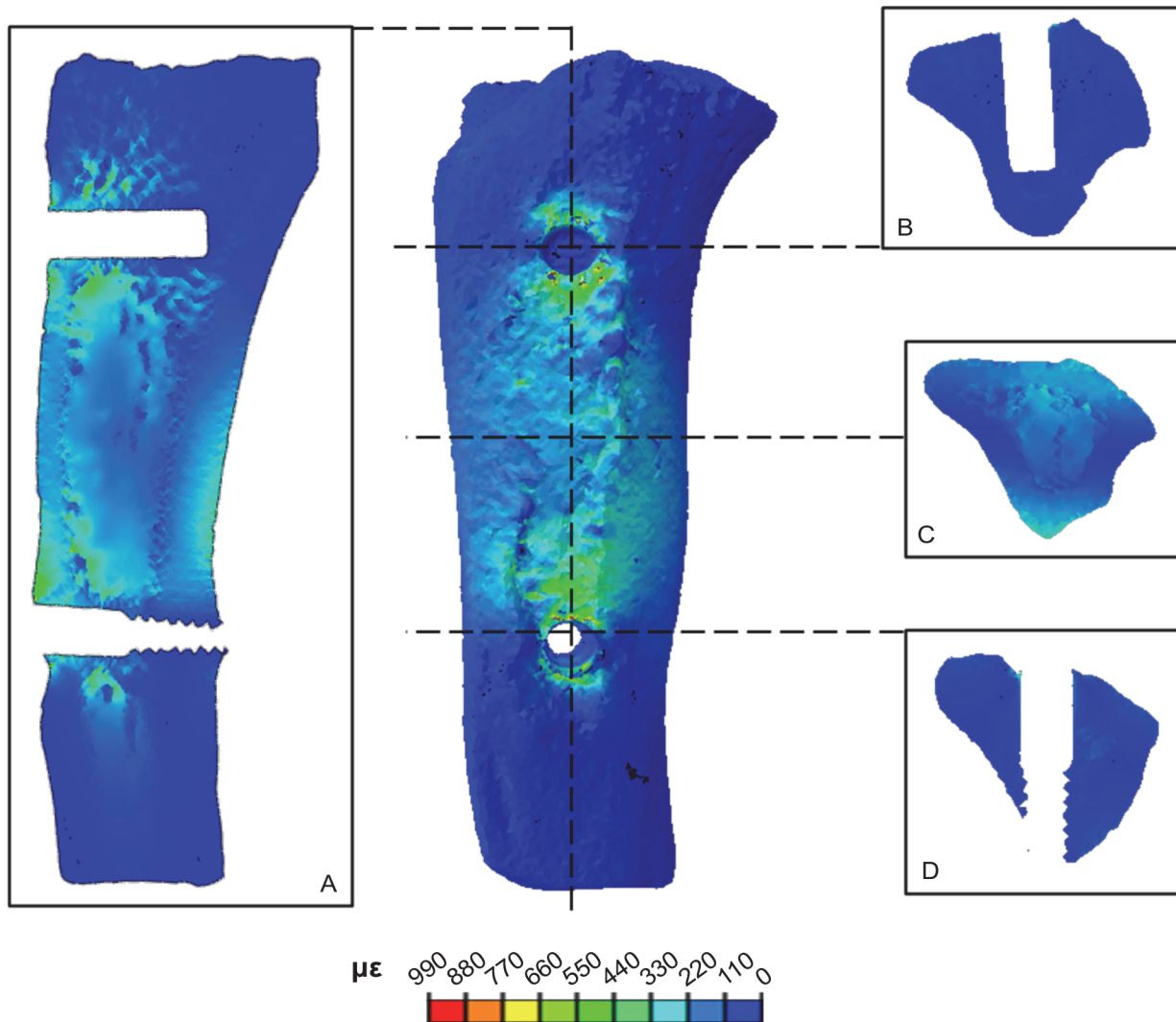


Figure 3.9: Equivalent strain field of the specimen number 9 subjected to 1 N of inter-implant loading. The elements belonging to the implants are omitted. The views (a) and (c) highlight the deformation caused by bending. The views (b) and (d) show undeformed bone tissue. The deformation is distributed by the cortical tissue between the prosthesis and the trabecular tissue surrounding the proximal implant.

Table 3.5: *Influence of the modeling parameters.*

Parameter	Affects	Relative error (%)
Artifact correction	Stiffness	< 3
BH	Stiffness	< 3
Semi-automatic segmentation	Volume	1
Manual threshold segmentation repeatability	Volume	6
Material property intervals	Stiffness	1
FE size (medium to fine)	Volume	0.5
	Density	2
	Stiffness	1
Density modulus relationship:		
Same species (total error wrt experiments)	Stiffness	10
Different species (% change)	Stiffness	20
Biovariability (worst-case confidence interval)	Stiffness	20 – 45

than 1.4 % errors. The elastic properties of the bone tissue are derived from empirical relationships converting the density into Young’s modulus. The laws are modified to avoid the presence of overestimated material properties, due to metal artifacts. The proposed meshing tool, *VoxelMesher*, generates coherent discretizations (0.1 % repeatability error) that are not affected by low-quality elements. The model with the maximum number of nodes (ca. 620000 nodes) was meshed in less than 2 min and solved in 24 min on a 6 × 3 GHz station. Starting from the mCT images, a complete analysis can be done in a short time (ca. 1 h, computational time included). Overall, the magnitudes of the sources of error affecting the results of the FE models are summarized in Table 3.5.

3.6 Conclusions

A new protocol to generate high fidelity, specimen-specific FE models of bare and implant-fitted rat tibiae from high-resolution CT images is presented. The protocol reliability was investigated by conducting a series of benchmarking procedures that related the stiffness and deformation of bare- and implant-fitted bones as measured experimentally to values computed by FE modeling. The protocol satisfactorily held up to all comparisons demonstrating good correlations for both the implanted and the non-implanted tibiae. By combining techniques such as semi-automated threshold segmentation, a direct image-based meshing tool with adaptive density field integration and a simple strike artifacts limitation strategy, the proposed protocol demonstrated an excellent repeatability, user independence and robustness in all the application benchmarks. The characteristics of the individual bone specimens such as geometry and material property field were preserved and the differences between the individual bones could definitely be captured. Each step of the protocol was evaluated to quantify associated errors. It was concluded that the relationship that links bone mineral densities to Young's moduli and the associated confidence intervals were the dominant parameters.

The systematic investigation of the protocol confirmed its applicability to studies that account for biovariability when assessing the mechanics of implant-fitted and bare rat bones.

Chapter 4

Physiological deformation of the rat tibia

4.1 Aim

Among other factors, the implants integration in the ‘loaded implant’ model depends on the animal daily activity and musculoskeletal loads, which affect the bone deformation. As a matter of fact, the range of deformations experienced by the bone tissue in physiological conditions represents the stimulus gold standard, i.e. the reference signal which allows maintaining the bone structure. When bone experiences non-physiological deformations, the mechanisms of resorption or apposition are activated to modify the tissue structure and force the signal within the limits. As a consequence, the physiological deformation represents an important reference point for studies based on the adaptation to mechanical stimuli.

This chapter aims at establishing an original loading condition of the rat tibia, through which the bone physiological deformation during gait is quantified, and investigate its effects on the ‘loaded implant’ model. In details, the tibia deformation, when subjected to this boundary condition, is adopted to pursue the following goals:

1. Investigate the correlation between the peri-implant deformation and the cortical bone loss described in Section 2.4.2. Clarify if this phenomenon depends on the mechanical environment generated during gait.
2. Perform specimen-specific FE analysis to compare the pattern of different mechanical stimuli of bone adaptation. The tibia deformation during gait is adopted as benchmark to investigate the distribution of different signals at different locations and tissues (i.e. cortical and trabecular).

4.2 Introduction

To optimize biological resource allocation, bones are maintained in a state of structural balance between applied loads and mechanical resistance. Under this premise, reduced mobility (Globus et al., 1984, Maïmoun et al., 2010) or strong exercise (Fujie et al., 2004) alter a skeleton’s muscular environment and the bones adapt to the newly established stress fields. After a period of structural modeling, a new equilibrium is established (Frost, 1990b). Similarly, endosseous implants modify the stress field within the bone bed. This induces a tissue adaption that may detrimentally affect the osseous casing, such as highlighted by the results of Series 2, where a peri-implant cortical defect characterizes both implants of the ‘loaded implant’ model (Section 2.4.2).

Problematically though, the histological process of integration always proceeds within the environment of mechanical stimuli generated during the animals’ daily activity. Indeed, when the implants are placed on limbs and the animals are left unconstrained, locomotion will affect peri-implant bone healing and adaptation. Typically, these sways are accounted for by establishing test and control groups that account for both the animals’ genetic bio-variability and their everyday musculoskeletal activation. In most instances, this approach suffices because the analyses are based on comparisons between large groups so that the effects on the outcome parameters can be extracted.

Concerning the ‘loaded implant’ model though, the rats’ daily activity strongly interferes with the implants’ experimental loading and thus precludes a pertinent analysis of the research issue under scrutiny. To extract relevant information from such data sets, these situations require a thorough assessment of the stress systems developed during normal, daily life. In humans, this theme is approached through inverse dynamics analysis and FE models accounting for musculoskeletal loads (Ramaniraka et al., 2005, Terrier et al., 2008). Concerning rats, some evidence was provided in studies on rat stride lengths, frequencies and ground reaction forces (Clarke and Parker, 1986, Clarke, 1991, Muir and Whishaw, 1999). But still, there is a considerable research deficit regarding the quantification of the forces developed by the musculature and the loads generated on the joints during the rat gait. Few works partially address this issue dealing with the internal moments and forces acting on the femur (Wehner et al., 2010) or the ankle motion (Blum et al., 2007).

The establishment of a framework representative of the musculoskeletal loads acting on rat tibiae can fill this research gap by disclosing the bone mechanical behavior in physiological conditions and assessing the interplay between the animal daily activity and the bone’s reactions around the implants.

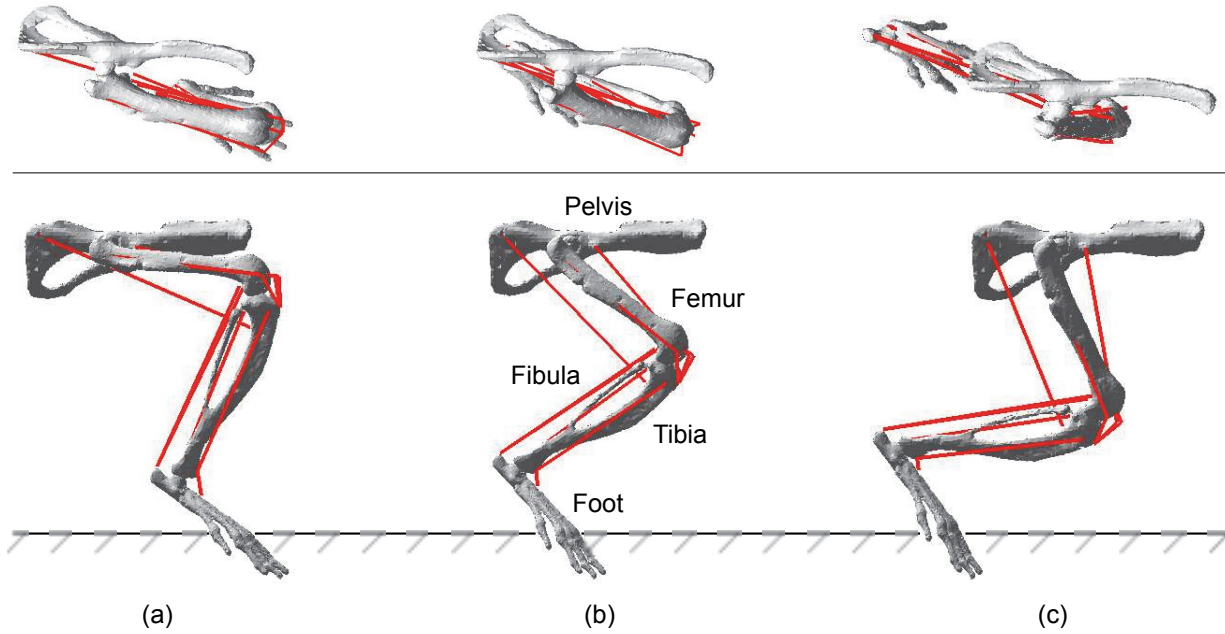


Figure 4.1: Simplified musculoskeletal system of the rat's hindlimb. Muscles are represented as lines connecting their origin-via-insertion (Johnson et al., 2008). (a) initial contact, (b) mid-stance and (c) pre-swing.

4.3 Gait-based analysis

The performed analysis of the forces acting on the rat tibia during gait is based on the musculoskeletal geometry presented by Johnson et al. (2008) and the kinematic analysis discussed by Wehner et al. (2010). The former introduced an accurate 3D model of the rat hindlimb¹, comprehensive of muscle attachment and joint center coordinates (Figure 4.1). The latter quantified some of the forces belonging to the hindlimb muscular compartment through an inverse-dynamic model, to investigate the internal loads and moments acting on the femur during gait.

In the following sections, these data are combined to establish a loading condition on the tibia that is based on the rat movements during gait.

4.3.1 Loading condition

The joints and muscle loads acting on the rat tibia during gait are estimated through the equilibrium of the femur and tibia rigid body models, performed with the software

¹Available at simtk.org

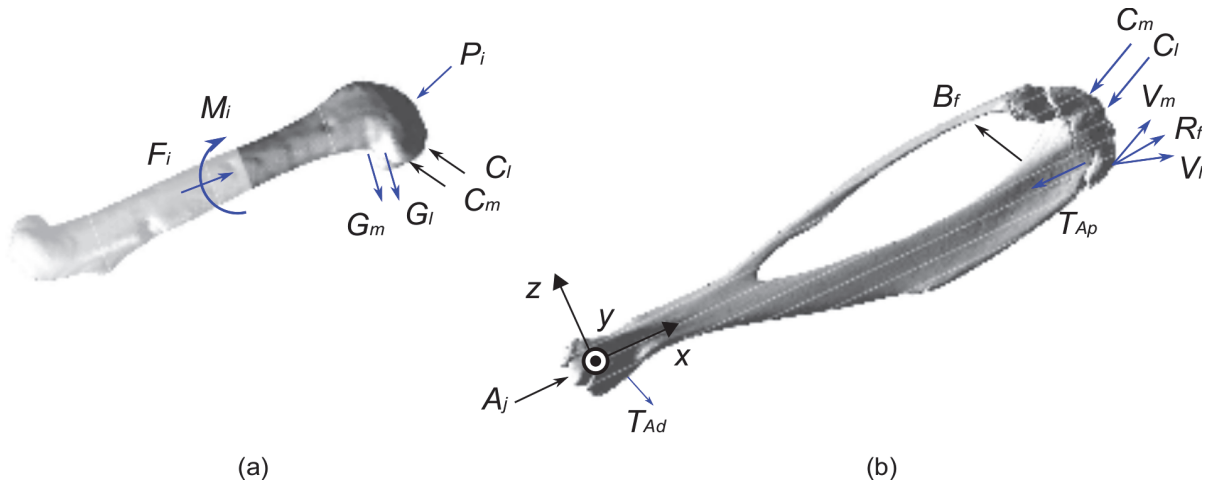


Figure 4.2: (a) Equilibrium of the femur. Symbols: medial and lateral condylar reactions, C_m and C_l , internal forces F_i and moments M_i , patellar load P_i , lateral and medial gastrocnemius, G_l and G_m . (b) Equilibrium of the tibia. Symbols: ankle joint reaction A_j , biceps femoris B_f , vastus medialis V_m and lateralis V_l , rectus femoris R_f , tibialis anterior proximal T_{Ap} and distal T_{Ad} .

Mathematica^{®2}. The static equilibrium is calculated at a time-step corresponding to the 35 % of the gait cycle (Figure 4.1b), i.e. at the half of the stance phase when most of the muscles reach their maximum force (Wehner et al., 2010).

First, the condylar reactions acting on the femur are calculated by equilibrating a system that includes (i) the femur's internal forces and moments, (ii) the lateral and medial gastrocnemius and (iii) the loads developed in the patella taken as the resultant of pulls by the m. vastus lateralis, the m. vastus medialis and the m. rectus femoris, all acting along the bisector lines of their origin-via-insertion coordinates (Figure 4.2a). The coordinates of the condylar joint reactions are compatible with the contact areas on the femur's condyles (Dao et al., 2011). Then the tibial equation system is established. It comprises the calculated condylar reactions and the forces developed by the m. vastus lateralis and medialis, the m. rectus femoris and the m. tibialis anterior. The m. biceps femoris is treated separately. Indeed, although it has been demonstrated as being active during the stance phase (Gillis and Biewener, 2001), there is a lack of information regarding the force generated by this muscle during gait. Hence, the tibial equation system is solved while treating the m. biceps femoris and a single ankle reaction acting on the inter-malleolar point as unknowns (Figure 4.2b). The coordinates of the muscular attachments and the calculated loads are listed in Table 4.1.

²version 9, Wolfram Research, Oxfordshire, UK.

Table 4.1: Loads acting on the tibia during gait, calculated with respect to the reference system in Figure 4.2b.

Structure	Coordinates (mm)			Forces (N)		
	x	y	z	x	y	z
Rectus femoris ^{1,2}	39.70	0.00	-2.00	5.45	-0.22	3.94
Vastus lateralis ^{1,2}	39.70	0.00	-2.00	2.33	-2.27	2.37
Vastus medialis ^{1,2}	39.70	0.00	-2.00	1.95	0.88	1.41
Tibialis anterior proximal ^{1,2}	39.00	-2.29	-1.50	-2.83	0.24	0.01
Tibialis anterior distal ^{1,2}	4.27	0.00	-0.86	1.61	-0.33	-2.57
Biceps femoris ²	33.00	-0.50	-0.20	0.00	3.63	5.98
Lateral condylar reaction	40.10	-2.00	1.90	-12.75	-0.38	-7.56
Medial condylar reaction	39.90	2.00	1.10	0.03	-0.38	-5.84
Ankle joint reaction ²	0.00	0.00	0.00	4.20	-1.17	2.26

¹ Loads magnitudes from (Wehner et al., 2010). The x-, y- and z-components are calculated as the projection to the insertion-origin direction.

² Coordinates from (Johnson et al., 2008).

4.3.2 Finite Element models

Four FE models characterized by different structure and boundary conditions are adopted for this analysis, their essentials are summarized in Table 4.2. A continuum FE model of a whole tibia is generated from available micro-CT data through the procedure described in Chapter 3. This model represents the reference of a not implanted tibia subjected to gait loads, and is compared to in~vivo strain measurements to highlight the pertinence of the proposed strategy.

In a second FE model the implants are inserted in~silico into the tibia proximal segment whereby the distal implant's threaded end is reduced to a cylinder with tie contact to the cortical bone. As integration progresses during the healing period, the mechanics of the implant-bone interface evolve from a press-fit condition to a simple adhesion. To simulate this phenomenon, three boundary conditions were analyzed. Initially, the implants were "press-fitted" into their bone bed a condition which is modeled as a homogeneous radial displacement field of 0.01 mm, applied to the cylindrical surfaces of the implants (Natali et al., 2009). In a further FE model, bone is tied to the implant surfaces, while in the last one the opening of the bone-implant interface is allowed. All the models are subjected to the gait-based loading condition previously defined.

Table 4.2: *Details of the boundary conditions adopted in the FE models.*

FE model	Implants	Bone-Implant adhesion	Press fit	Gait loads
Bare	No	-	-	Yes
Press fit	Yes	Yes	Yes	Yes
Adhesion	Yes	Yes	No	Yes
Opening	Yes	No*	No	Yes

*Frictionless hard contact.

4.3.3 Validation

The validation of models aiming at reproducing the deformation occurring on bone during movements is a challenging issue. Briefly, it is worth recalling the main hypothesis through which the problem has been simplified, to understand the intrinsic limits of the obtained results.

Firstly, the dynamic phenomenon of gait is represented through a unique static equilibrium. As the stride length and frequency change in relation to the animal speed and travelled distance, the musculoskeletal forces are also subjected to a high variability, not accounted in this study. Nevertheless, the muscular forces coming from the inverse-dynamic model by Wehner et al. account for the inertia of the hindlimb system, and the propagation of dynamic effects on the tissue deformation can be assumed negligible considering that the stride frequency hardly overcome 4 Hz (Clarke and Parker, 1986).

Moreover, the forces accounted in this study are not comprehensive of the whole hindlimb muscular system. At the moment, the scarcity of literature data on this field of research limits further improvements, and some assumptions are necessary to face this lack (e.g. concerning the contribution of the Bicep femoris).

Finally, the proposed modeling strategy involves the representation of the joints' contacts through punctual forces. In reality, knees and ankles allow the hindlimb to move through large contact areas on the cartilaginous tissue characterizing the joints. Thus, the load transmission takes places trough a distributed pressure instead of punctual forces. As a consequence, the pattern of deformation characterizing the epiphysis of the presented FE model is probably affected by discrepancies. For the same reason, the results close to the muscle attachment points are imprecise. Indeed, skeletal muscles are anchored by tendons to the bone tissue through extended attachment surfaces. The influence of this simplification, quantified for the human femur and pelvis (Phillips, 2009, Phillips et al., 2007), is still not available for rats.

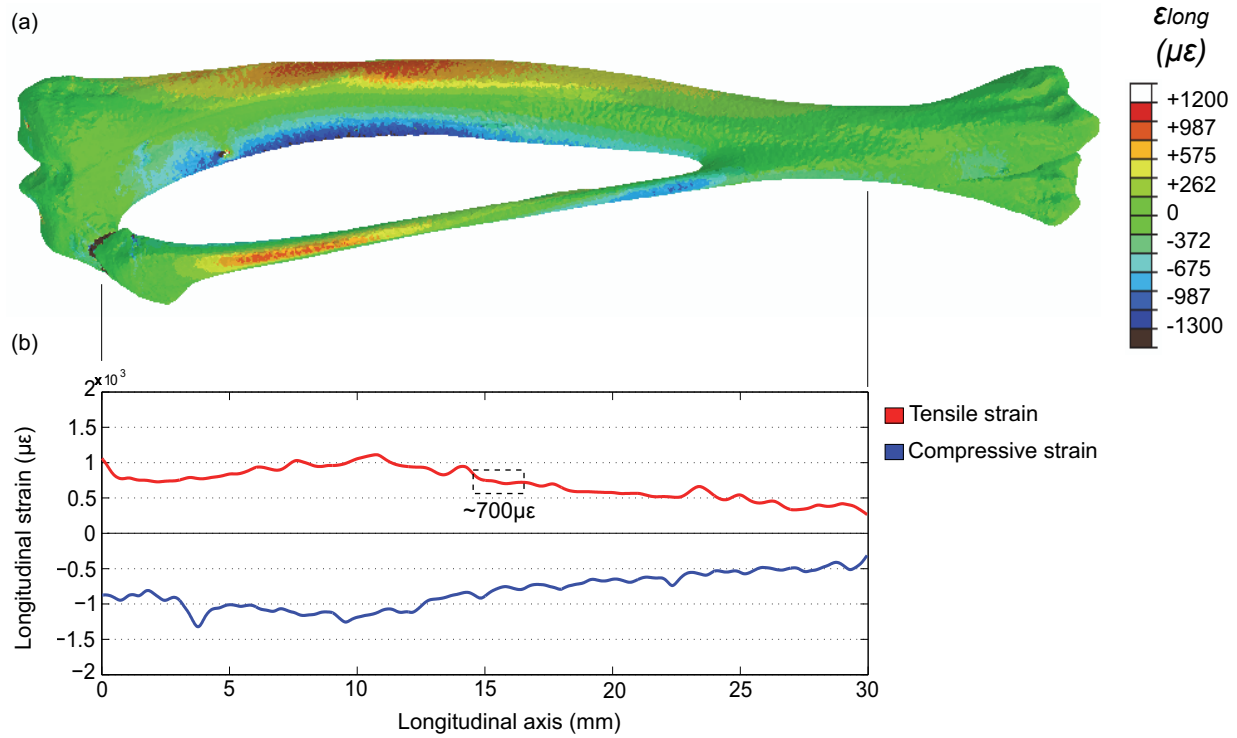


Figure 4.3: (a) mapping of the longitudinal strains in the bare tibia subjected to gait loads. (b) maximum and minimum longitudinal strains along the tibial midshaft. The fibula is not considered. The value in the dotted box agrees with *in-vivo* measurements (Rabkin et al., 2001).

Despite these drawbacks, the results of the model shown in Figure 4.3 are satisfactory. When the bare tibia model is subjected to nominal gait loads, the deformation pattern occurring on the diaphysis is not affected by discontinuities due to numerical hypothesis. The strain pattern develops as a coupling of bending and compression typical of long bones. The tensile and compressive longitudinal strains in the midshaft reach $1112 \mu\epsilon$ and $-1318 \mu\epsilon$ respectively. The pertinence of the numerical model is verified by matching previously published values to comparable locations in the model. For instance, the strains on the tibia's midshaft are in close agreement with those generated in rat long bones during locomotion, $600\text{-}1200 \mu\epsilon$ (Hillam and Skerry, 1995, Mosley et al., 1997, Turner et al., 1994b). Similarly, the longitudinal strain illustrated in Figure 4.3b agrees with *in-vivo* measurements on the same location ($\sim 700 \mu\epsilon$ vs $740 \pm 190 \mu\epsilon$, Rabkin et al., 2001).

4.3.4 Results and Discussion

As described in Section 2.4.2, the cortical bone surrounding the straight cylindrical surfaces of both implants shows a funnel-shaped defect, with increasing depth with respect to the integration period. The complete opening of the bone-implant interface is observed only around the distal implant. The hypothesis that this phenomenon is correlated to the animal daily activity is supported by the increase of implant loss characterizing Series 3 (Section 2.4.3.1) where both legs were implanted to maximize the effects of the animal movements.

The numerical analysis discussed in this chapter aim at relating the cortical bone defects observed in Series 2 and 3 to local stress and strain patterns and to the ensuing osseous adaptation. Indeed, the FE models concerning the implanted tibia include different boundary conditions replicating potential integration states.

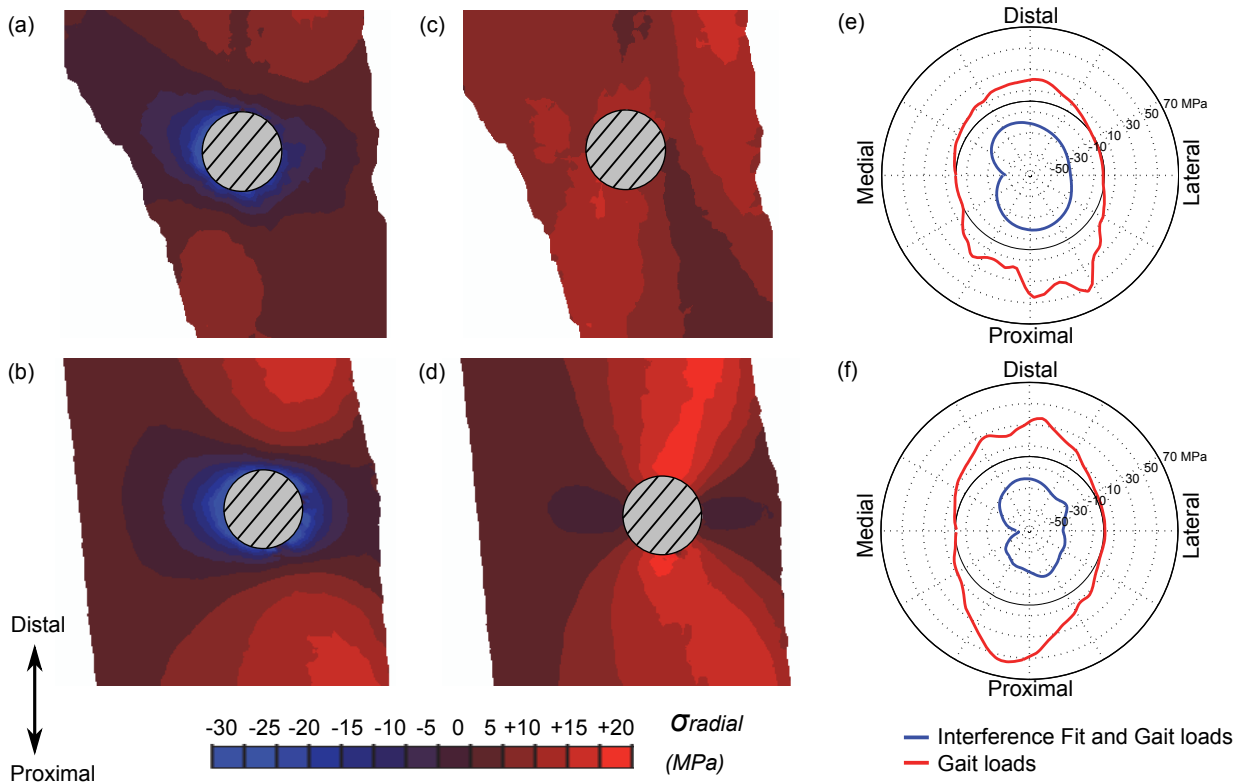


Figure 4.4: Cortical radial stress assuming a perfect bone-implant adhesion. Considering both the gait loads and the press fit: (a) proximal and (b) distal implant. Considering only the gait loads: (c) proximal and (d) distal implant. Stresses along the implant circumference considering both press fit and gait loads (blue) and only gait loads (red): (e) proximal and (f) distal implant.

During the early days after surgery, the deformation state occurring in the FE model with *in-silico* implants combines the effects of the gait loads and the initial press fit, generating the peri-implant radial stress represented in Figures 4.4a and b, concerning the cortical tissue. The radial compression pattern generated by the press-fit surpasses the tensions developed during gait loading in the vicinity of the implants. As the first one is predominant, the compressive forces impart their stability to the implants, prevent harmful micro-motions and thus facilitate the initial integration (Abdul-Kadir et al., 2008).

In the next phase of integration, the effects of press-fitting are released and only the gait loads act on the implanted tibia. Indeed, the stabilizing effect comes to an end 3-4 days after implant placement due to the resilience and adaptation of the surrounding osseous tissue (Dhert et al., 1998). Now the peri-implant bone's evolution depends on the rats' physical activity and the adhesive strength of the bone-implant interface. As shown in Figures 4.4c and d, the interface is subjected to severe radial tensile stresses in the distal-proximal direction, reaching peak values of 50 MPa. Problematically, these values exceed the adhesive strength between the implant and the surrounding bone (~ 4 MPa) (Gross et al., 1987, Takatsuka et al., 1995). It follows that the loss of bone-to-implant contact as observed experimentally may well be initiated by a loss of adhesion due to the excess tensile stresses generated at each gait cycle.

Figure 4.5 depicts the response of non-adhesive (i.e. hard frictionless contact) bone-to-implant interfaces in terms of contact pressures and openings that develop at the implant surface. Under this condition, gait loads result in compressive radial stresses on the implants' circumference with exception of the superficial zones in which tension develops and the bone detaches from the implant. This phenomenon was observed around both distal and proximal implants but was more pronounced in the former one. Around the proximal implant no clear-cut distinction between zones of pressure and opening was possible due to irregularities in thickness of the cortical bone and its partial entanglement with trabecular tissue. These distributions of contact pressure and opening suggest that the loss of adhesion may not be recovered.

Indeed, these results allow postulating a mechanism driving cortical bone loss (Figure 4.6). The detached bone is pulled back from the titanium at each gait cycle, thus losing its stimulation. Without mechanical stimulation, bone enters in a resorption state and the debonding-resorption process may continue by migrating in apical direction. Clinically, this phenomenon is similar to the marginal bone loss observed around dental implants (Qian et al., 2012) and which has been attributed either to disease (Bodic et al., 2005) or to overload (Isidor, 1996). Yet none of these factors was active in the present study.

According to the present FE analysis, permanent gaps may develop at the implant-bone interface. If this occurs, an irreversible process is initiated as the bone tissue that is separated from the implant is in a condition of stress shielding and it is resorbed because

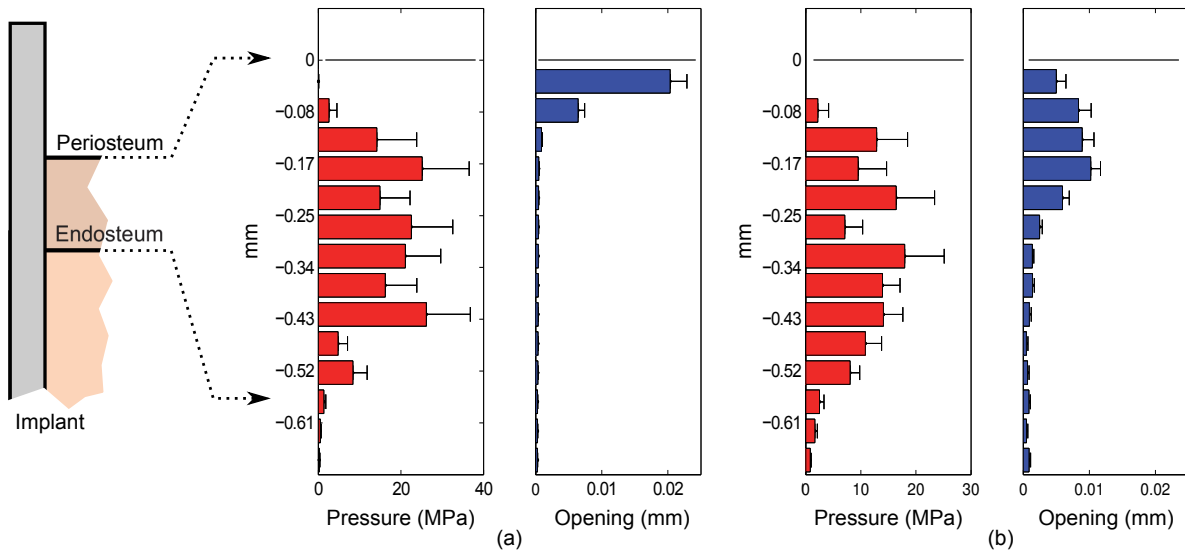


Figure 4.5: Contact analysis in case of no bone-implant adhesion. Contact pressure and opening around (a) the distal and (b) the proximal implant. Mean and standard deviation are calculated on the implant circumference.

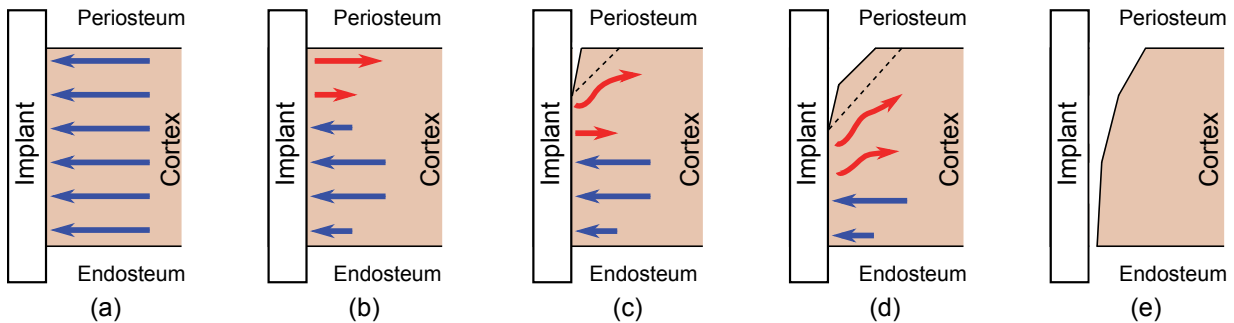


Figure 4.6: Simplified representation of the mechanisms leading to the cortical bone loss. (a) During early post surgery days the implant is stable because of the compressive stress field due to the press fit. (b) When the press fit is released, part of the interface is subjected to traction. (c) The cyclic loading provokes a loss of bone-implant adhesion in the periosteal area. The stress distribution changes and part of the tissue is unloaded (i.e. above the dotted line). (d) The unloaded tissue is resorbed and the opening propagates along the implant axis. (e) If no stable configurations exist, the opening reaches the endosteum and the bone-implant contact is totally lost.

of disuse (Engh et al., 1987, Huiskes et al., 1992). As a matter of fact, Figure 4.7 shows the stresses occurring in the longitudinal plane in case of opening depths corresponding to the 30 and 60 % of the cortical thickness and with perfectly adherent implant-bone interface elsewhere. The bone tissue in the proximity of the open contact is clearly unloaded and shows the observed funnel-shaped distribution.

Moreover, once the process of gap formation is initiated, the stresses generated during each gait cycle are relocated further down the implant and a new zone of the bone-implant interface is subjected to tensile forces. As shown in Figure 4.7, high tensile stresses characterize the area immediately below the opening zone. The stress concentrations affecting the distal implant overcome 20 MPa and are relatively independent on the opening depth. On the contrary, the stress concentration is less pronounced around the proximal implant and show sign of a progressive reduction with the increase of the conic depth.

The stability of this progressive process is controlled at least partially by the evolution of the peak tensile stresses occurring at the bone-implant interface, and thus depends on the implantation strategy and local bone structure. Indeed, this mechanism was observed in both ROIs but the differing bony environment led to different defect morphologies.

The tip of the distal implant is screwed-tightened into the opposing cortex while the upper part is inserted in a thick layer of cortical bone without trabecular bone in between. Due to an extended contact area, this configuration yielded an excellent initial resistance to the loss of adhesion (lower initial stresses). Clinically, it took 4 weeks for the funnel in ROI d to start to increase (Figure 4.8, from Section 2.4.2), thus indicating a high initial resistance of the interface. However, once debonding occurred, this configuration demonstrated a fast development of a funnel shape between 4 and 6 weeks. The high stress concentrations seen in the FE simulations (Figure 4.7a and b) and the fact that their magnitude does not decrease when debonding propagates explains the high rate of development of conic depth and the presence of an open gap in 17 % of the distal implants after 6 weeks (Table 2.5).

By contrast, the proximal implant was inserted into a thin layer of cortical bone and large amounts of trabecular bone underneath. As shown by the conic depth evolution reported in Figure 4.8 and the relatively high percentage of conic features between 2 and 4 weeks (Table 2.5), this environment seems to offer less initial resistance to periosteal tension and promotes early debonding at the outer cortical surface. However, this implantation strategy demonstrated a better adaptation to the mechanical environment after the early stages, as the rate of evolution of the conic features was much less than around the distal implant after 4 weeks and no open gaps were observed around the proximal implants after 6 weeks. Indeed, as shown in Figure 4.7c and d, the smooth gradient of stiffness offered by the underlying trabecular bone helped to progressively decrease the interfacial stress concentration with increasing conic depth, and thus lead to an arrest of the gap formation process. Thus, the absence of trabecular bone around the distal implant could be seen as a

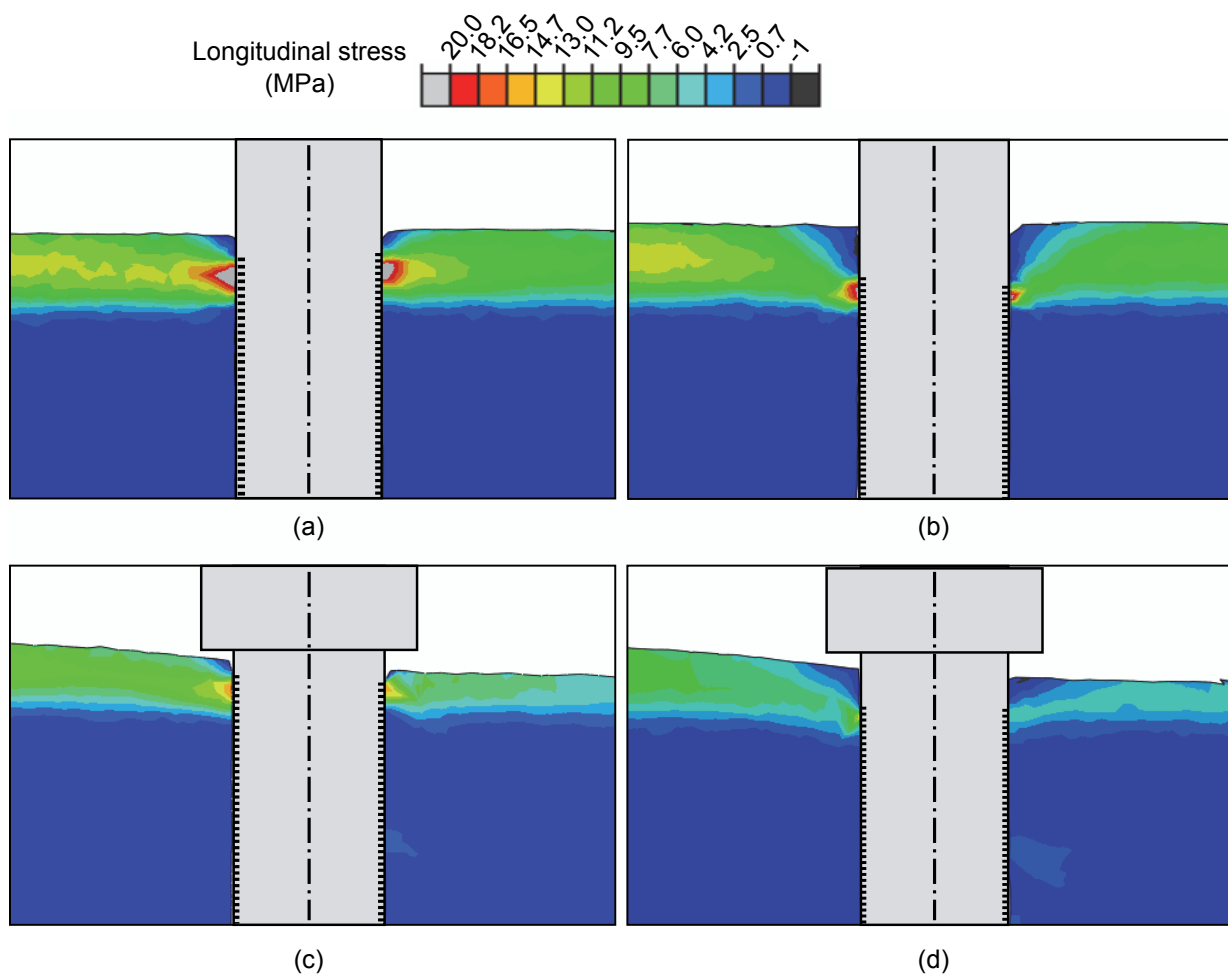


Figure 4.7: Longitudinal stresses in case of partial cortical loss of adhesion. Distal implant with loss depth equal to (a) 30 % of cortical thickness and (b) 60 % of cortical thickness. Proximal implant with loss depth equal to (c) 30 % of cortical thickness and (d) 60 % of cortical thickness.

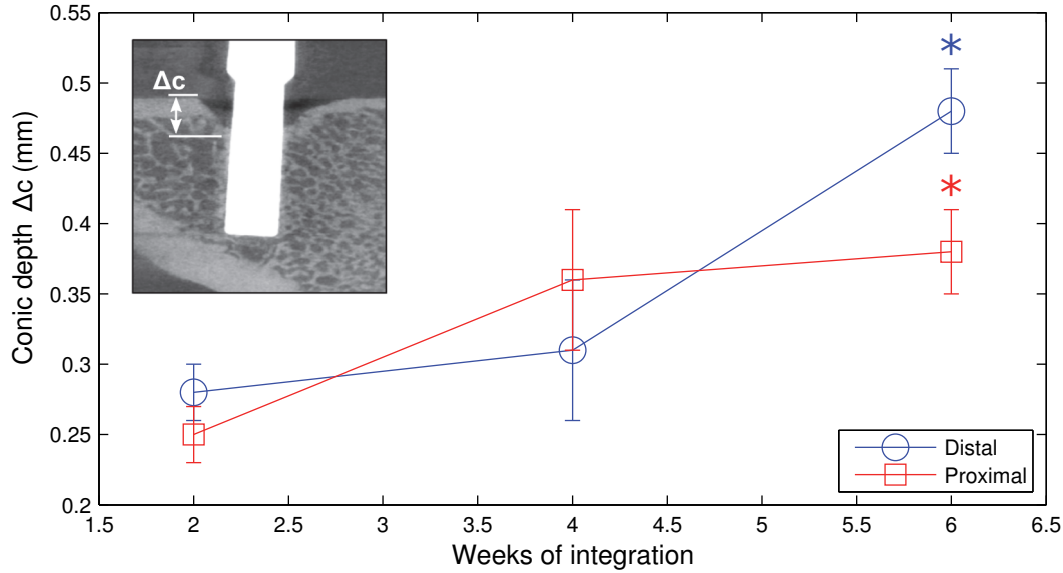


Figure 4.8: Conic depth, Δ_C , measured at different integration periods around the implants (mean \pm SEM). * $p < 0.05$ with respect to two weeks. Figure from Section 2.4.2.

factor limiting the adaptation capacity and facilitating the formation of a fully open gap.

To summarize, it appears that locomotion causes the inward propagation of a gap along the implant surface with the ancillary effect of resorption of unloaded bone and the eventual formation of a funnel-shaped defect in the cortical bone. The large contacts zones in the cortical bone reduce the stress concentrations, delaying the opening of a gap, while the trabecular bone hampers the propagation of the gap and prevents the complete failure of the interface.

Still, whether an animal will demonstrate peri-implant bone loss cannot be predicted. Indeed a number of individual factors are contributive: the adhesive strength and the size of the bone-implant contact, the morphology and material properties of the surrounding bone tissue as well as the rats' activity during the post-surgical period. As a matter of fact, different levels of pain might prevent the animal to use the implanted leg and thus reduce the number and levels of load applications, condition not possible if a bilateral implantation is adopted. This result explains the significant implant losses observed in Series 3 (Section 2.4.3.1), where both legs are implanted, and confirms that the outcome of implant's integration strongly depends on both animal's daily activity and biodiversity (Figure 2.13).

4.4 Signals of bone adaptation

As described in Section 1.4.2, the Mechanostat theory implies the existence of a physiological range of mechanical stimulus that occurs in bone during the daily activity (i.e. the Lazy Zone). The stimulation falling within this range continuously activates the remodeling process. Although no macroscopic changes are perceived, bone is maintained and the skeleton preserves its load-bearing function. On the contrary, relevant bone resorption or apposition are activated if the stimulation is below or above the LZ, respectively.

The implementation of this theory depends on the identification of a mechanics-related stimulus that is representative of the deformation under certain loading conditions. Different approaches are currently adopted with success in studies involving whole bones (Chennimalai Kumar et al., 2010, Prendergast and Taylor, 1994), trabecular structures (Schulte et al., 2013, Van Der Linden et al., 2001) or even bone multicellular units (Smit and Burger, 2000, Van Oers et al., 2008). Nevertheless, the signal selection is not frequently discussed, and comparisons of different magnitudes are rare (Mellal et al., 2004, Terrier et al., 1997).

The presented gait-based set of loads offers the opportunity to investigate the deformation occurring in the rat tibia during gait, that is in physiological condition, and identify the more suitable signal. As a matter of fact, a general interpretation of the Mechanostat entails the existence of a LZ neither dependent on the location within bone, nor on the tissue type (i.e. cortical or trabecular). With these hypotheses, under physiological conditions an adequate stimulus should respect these criteria:

Location invariance. The signal distribution is location-independent. Different regions of bone are subjected to the same range of stimulus.

Tissue invariance. The signal distribution is tissue-independent. Cortical and trabecular bone undergo the same range of stimulus.

Three stimuli are compared in the following sections by highlighting their compatibility with the proposed criteria, on the benchmark of whole tibiae subjected to physiological deformations.

4.4.1 Mechanical stimuli

The three mechanical stimuli compared in this analysis are based on different mechanical magnitudes: energy, stress and strain. Moreover, they are all chosen to be scalar (i.e. not dependent on a direction, vectorial magnitudes are excluded a priori) and non negative (i.e. exhaustively represent the deformation state without differentiation of sign).

The three signals are described in the following.

Elastic energy per unit of mass. The elastic energy per unit of mass is adopted in remodeling algorithms for orthopedic (Weinans et al., 1992) and dentistry studies (Li et al., 2007) As defined in equation 4.1, the energy-based stimulus ψ_U depends on the strain energy density U_i that occurs during the loading condition i , on the local bone apparent density ρ , and on the number of loading conditions N .

$$\psi_U = \frac{1}{N} \sum_{i=1}^N \frac{U_i}{\rho} \quad (4.1)$$

where U is calculated as the strain energy, u , per unit of volume, V

$$U = \frac{u}{V} = \frac{1}{2} \bar{\sigma} \cdot \bar{\epsilon} \quad (4.2)$$

where $\bar{\sigma}$ and $\bar{\epsilon}$ are the stress and strain tensor. Equation 4.1 accounts for several loading conditions, and their mean define the signal of bone adaptation.

Daily stress. The stress-based stimulus presented by Carter, Beaupré and co-workers (Beaupré et al., 1990a,b, Carter et al., 1989) introduces the concept that the bone adapts with respect to the daily stress history. The signal ψ_σ is formulated as shown in Equation 4.3, and depends on multiple loading types N , on the loading cycles n_i and on the stress at the tissue level σ_{bi} (i.e. evaluated on mineralized bone tissue).

$$\psi_\sigma = \left(\sum_{i=1}^N n_i \sigma_{bi}^m \right)^{1/m} \quad (4.3)$$

where m is an empirical constant adopted to weight the number of cycles and the stress depending on the physical activity.

In applications involving whole bones, the trabecular tissue is often modeled as a continuum replicating the tissue macroscopic stiffness, without resolving the singular trabeculae. In this case, the stress-based stimulus ψ_σ can be written as a function of the continuum effective stress σ_i .

$$\psi_\sigma = \left(\frac{\rho_c}{\rho} \right)^2 \left(\sum_{i=1}^N n_i \sigma_i^m \right)^{1/m} \quad (4.4)$$

where ρ_c is the apparent density of mineralized bone and ρ is the local apparent density. The continuum effective stress σ (Fyhrie and Carter, 1986) is calculated by Equation 4.5.

$$\sigma = \sqrt{2EU} \quad (4.5)$$

where E is the elastic modulus and U is the strain energy density evaluated for a continuum material. From Equation 4.4 results that if $\rho = \rho_c$ then the stimulus at continuum or tissue level are equivalent.

Octahedral Shear strain. Frost introduced the hypothesis that the Mechanostat is driven by the peak daily strains that occur on bone tissue (Frost, 1983, 1987, 2000). The stain-based stimulus ψ_ϵ can be expressed as shown in Equation 4.6.

$$\psi_\epsilon = \max(\overline{\epsilon}_1, \overline{\epsilon}_2, \dots, \overline{\epsilon}_N) \quad (4.6)$$

where N is the number of loading conditions and $\overline{\epsilon}_i$ is the strain tensor generated during the loading condition i . Unfortunately, the tensorial formulation presented in Equation 4.6 implies a dependency on directions that is not compatible with the criteria previously fixed. Thus, the strain-based stimulus is formulated as a function of the octahedral shear strain, as shown in Equation 4.7.

$$\psi_\epsilon = \max(\epsilon_{oct,1}, \epsilon_{oct,2}, \dots, \epsilon_{oct,N}) \quad (4.7)$$

where ϵ_{oct} is the octahedral shear strain, calculated as

$$\epsilon_{oct} = \frac{2}{3} \sqrt{(\epsilon_{xx} - \epsilon_{yy})^2 + (\epsilon_{xx} - \epsilon_{zz})^2 + (\epsilon_{yy} - \epsilon_{zz})^2 + 6(\epsilon_{xy}^2 + \epsilon_{xz}^2 + \epsilon_{yz}^2)} \quad (4.8)$$

The choice of the octahedral shear strain is inspired by the results of several investigations that highlight the influence of shear on the tissue differentiation (Lacroix and Prendergast, 2002b, Prendergast et al., 1997).

In the following, these signals are investigated through a single loading condition ($i = 1$), based on the musculoskeletal loads previously derived. Moreover, the number of loading cycles characterizing the daily stress is fixed to $n = 1$. As a consequence, the considered energy-, stress- and strain-based stimuli are formulated as shown in Equation 4.9, 4.10 and 4.11, respectively.

$$\psi_U = \frac{U}{\rho_{bmd}} \quad (4.9)$$

$$\psi_\sigma = \left(\frac{\rho_{bmd,c}}{\rho_{bmd}} \right)^2 \sigma \quad (4.10)$$

$$\psi_\epsilon = \epsilon_{oct} \quad (4.11)$$

where ρ_{bmd} and $\rho_{bmd,c}$ are the local BMD, averaged in FE models, and the fully mineralized BMD, respectively.

4.4.2 Comparison settings

The signals comparison is performed on five specimen-specific FE models of rat tibiae. The mCT images of whole tibiae are processed to obtain FE models through the procedure

described in Chapter 3 (element size ratio: 51 voxels/element, average model size: 1.2 M nodes). The tibial equilibrium system presented in Section 4.3.1 is solved for each rat, with small adjustments of the loads coordinates and magnitudes based on the morphology and bodyweight of each animal. Thus, specimen-specific boundary conditions are applied to the respective FE model to generate the desired physiological pattern of deformation. The stimuli comparison is limited to the proximal part of the tibia, where the deformation well correlates with *in-vivo* strain measurements and shows results compatible with experiments (Section 4.3.4). In details, the stimuli distribution is investigated in two regions of interest fixed with respect to the ideal location of the implants, as shown in Figure 4.9a. Firstly, the implant insertion coordinates are identified through the surgical procedure described in Figure 2.2a. Secondly, the Inter-Implant region of interest ROI_{II} is obtained by dilatation of the plane where both implant axes lie. Finally the region of interest ROI_{CY} is defined as a cylinder surrounding the proximal implant location. The ROIs overall dimensions are shown in Figure 4.9b and c. The definition of these regions allows comparing the mechanical stimuli where it is most interesting with respect to the ‘loaded implant’ model. As a matter of fact, ROI_{II} represents the region where the external stimulation is more effective, and ROI_{CY} provides an estimation of the signals all around the implant floating inside the trabecular bone.

The signals comparison also accounts for the differentiation between cortex, trabecular tissue and marrow. Indeed, these elements are present in both regions of interest. A BMD threshold is fixed to discriminate these tissue, modeled in the FE analysis through local, BMD-dependent material properties (Figure 4.9d). In details, signals are classified as cortical if $BMD > 0.8 \text{ gHA/cm}^3$ and trabecular if $0.3 < BMD \leq 0.8 \text{ gHA/cm}^3$. These thresholds are based on the experimental results fitted to derive the adopted density-elasticity relationship (Cory et al., 2010). A view cut of a tibia with the proposed tissue differentiation is shown in Figure 4.9e. although it does not account for the specimen’s geometry, the proposed partitioning permits a coherent tissue subdivision throughout the whole specimen.

The results belonging to the marrow, that is $BMD \leq 0.3 \text{ gHA/cm}^3$, are neglected. This exclusion depends on the type of signals compared in this study. Indeed, the three of them are based on the hypothesis that the elastic deformation is the key and only factor driving the bone adaptation. This hypothesis is valid if the signals belong to tissues characterized by enough stiffness to be considered an elastic material. The elements of the FE models with $BMD \leq 0.3 \text{ gHA/cm}^3$ belongs to regions composed by little bone, marrow and blood vessels, which are characterized by a non-linear, poro-elastic mechanical behavior. Thus, in these regions the linear and elastic magnitudes may not correctly represent the reference signals for the Mechanostat, and for this reason they are excluded from the analysis.

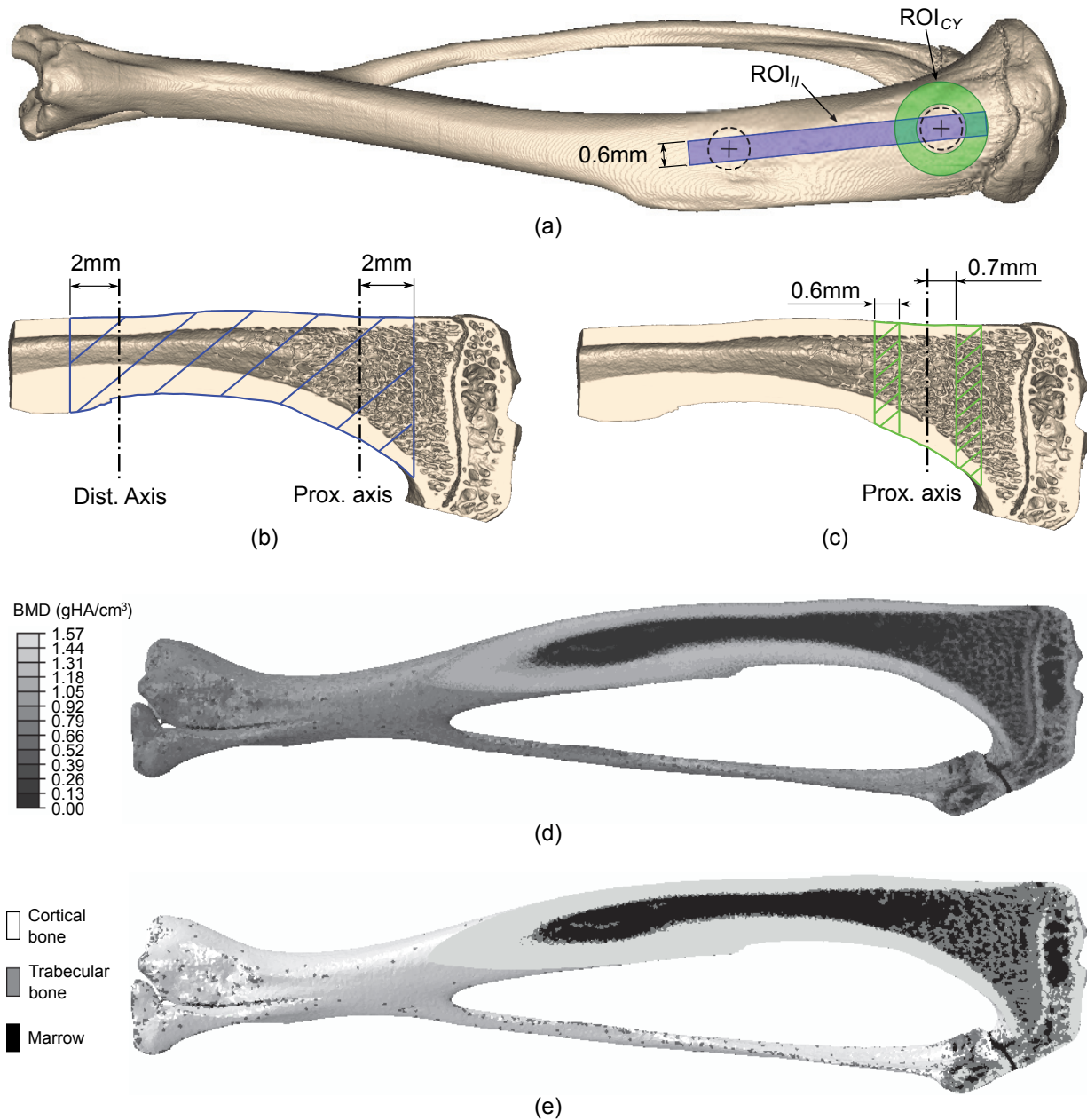


Figure 4.9: Regions of interest for the comparison of mechanical signals. (a) positioning of the Inter-Implant and Cylindrical regions of interest with respect to the implants insertion coordinates (ROI_{II} and ROI_{CY} , respectively). View cuts of the tibia: overall dimensions of (b) ROI_{II} and (c) ROI_{CY} . (d) view cut of the BMD pattern characterizing the FE model of a tibia. (e) BMD-based tissue differentiation: cortical (white, $BMD \geq 0.8 \text{ gHA/cm}^3$), trabecular (grey, $0.3 < BMD \leq 0.8 \text{ gHA/cm}^3$) and marrow (black, $BMD \leq 0.3 \text{ gHA/cm}^3$).

4.4.3 Results and Discussion

The distributions of the signals belonging to different ROIs and tissues are shown in Figure 4.10. These distributions represent the mean \pm SEM calculated on the five specimen-specific FE models of whole tibiae subjected to the gait-based loading condition.

Considering the energy-based stimulus ψ_U , a large amount of cortical bone in ROI_{II} ($\sim 40\%$ of the total) shows levels of strain energy not comparable to the ones measured in ROI_{CY} (black arrows in Figure 4.10a). Even though, the distributions on the trabecular bone are comparable between ROIs (i.e. the histograms are nearly superimposed, Figure 4.10b). However, the spectrum of stimulus that occurs in trabecular bone falls between 0 and 2×10^{-3} J/g, and is different from the one that characterizes the cortical tissue (between 0 and 8×10^{-3} J/g). As a consequence, the energy-based signal ψ_U does not satisfy the tissue-invariance criterion. Interestingly, the signal distributions in cortical bone of ROI_{CY} and trabecular bone of both ROIs show a not negligible amount of bone characterized by $\psi_U = 0$, which indicates that part of the tissue is undeformed when the tibia is subjected to the proposed gait loads.

The stress based stimulus ψ_σ shows location-invariant distributions, indeed the differences between ROIs are minimal (Figure 4.10c and d, respectively). Nevertheless, the trends characterizing the cortical and trabecular bone are not comparable either in terms of shape, or in terms of range. Indeed, the stress in trabecular and cortical bone reaches 100 and 50 MPa respectively. As a consequence, the stress-based signal ψ_σ does not satisfy the tissue-invariance criterion. However, there is no unstressed tissue in the explored regions, independently on the tissue type.

Finally, the distributions of the strain based stimulus ψ_ϵ are shown in Figure 4.10e and f. The shape of the distributions is similar in both ROIs and tissues, as well as the explored ranges of stimulus (200 – 1500 $\mu\epsilon$). Similarly to ψ_σ , there is no undeformed bone within the explored volumes. These results highlight the strain based stimulus ψ_ϵ as the only one that respects both tissue- and location-invariance criteria.

A qualitative confirmation of these results is provided through the Percent-Percent plots (P-P plots) reported in Figure 4.11. The P-P plot is a graphical technique adopted to compare two set of cumulative distributions. In details, the cumulative distribution under investigation is plotted against a reference one and the resulting trend determines their correlation. Indeed, two overlapping distributions produce a P-P plot perfectly aligned with the diagonal of the graph, while different distributions generate non linear trends. In Figure 4.11, the cumulative distribution characterizing the cortical bone of ROI_{II} is selected as reference and compared to the others. The signal ψ_ϵ shows trends comparable with the diagonal for all the ROIs and tissues, unlike the energy- and stress-based stimuli.

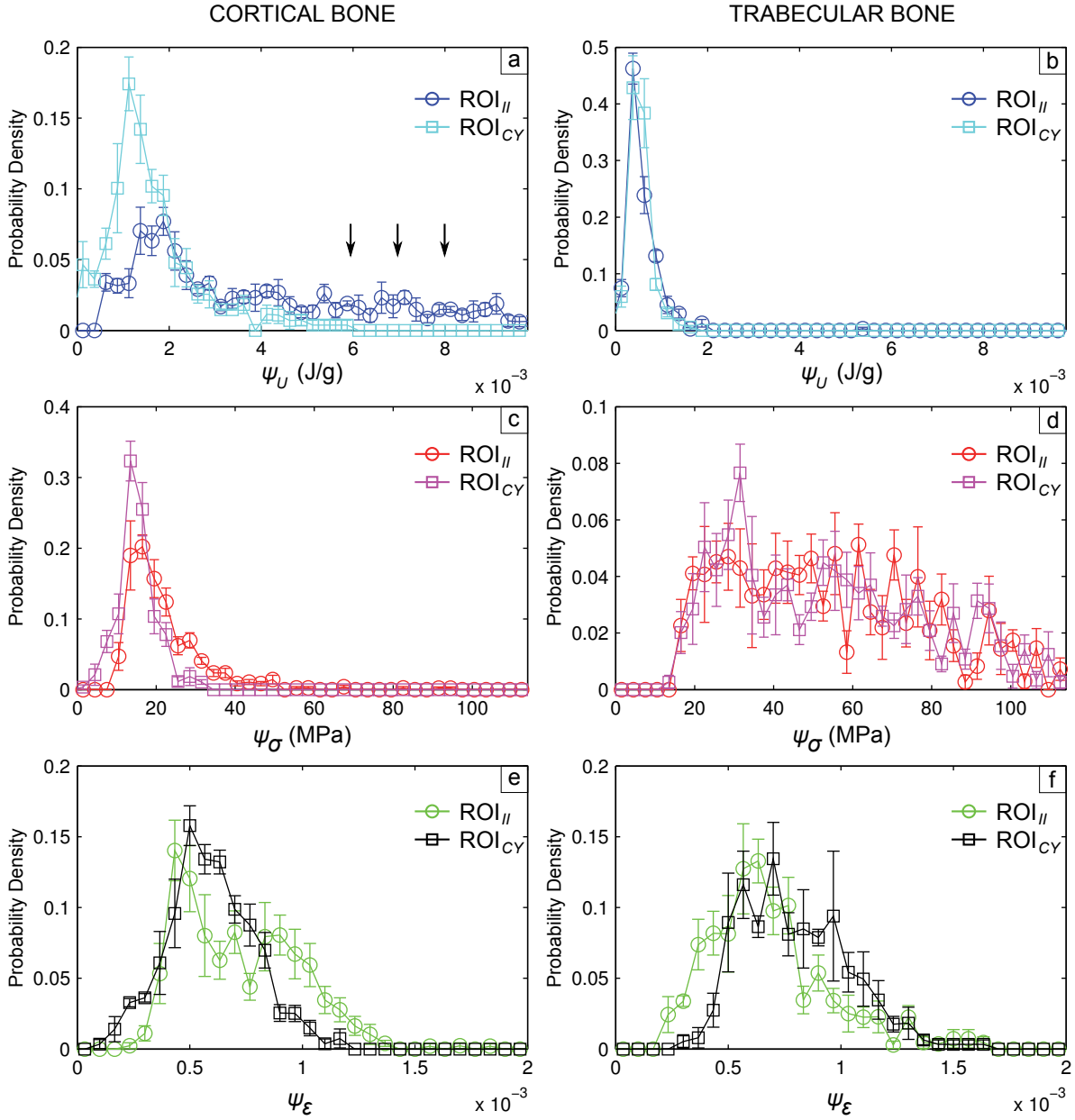


Figure 4.10: Distribution of signals (rows) with respect to the tissue type (columns) and the regions of interest ROI_{II} and ROI_{Cy} (legend). In details: energy-based signal ψ_U in cortical (a) and trabecular (b) tissue, stress-based signal ψ_σ in cortical (c) and trabecular (d) tissue, and strain-based signal ψ_ϵ in cortical (e) and trabecular (f) tissue.

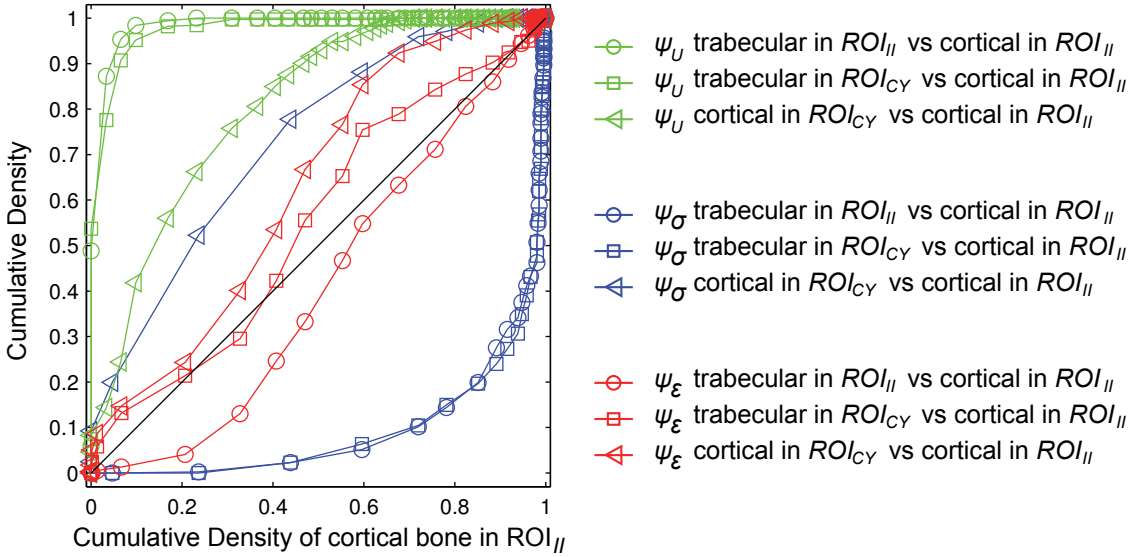


Figure 4.11: Percent-Percent plot of the probability distributions characterizing the signals ψ_U , ψ_σ and ψ_ϵ in both ROIs with respect to the one observed in the cortical bone of the inter-implant region of interest.

These results highlight that the octahedral shear strain is the stimulus with less dependency on the position and tissue type, and better fitting the imposed criteria of location- and tissue-invariance. Thus, octahedral shear strain seems the ideal mechanical variable to develop a Mechanostat model at the continuum level.

These results depend on the hypothesis that the proposed gait-based loading condition is fully representative of the animal daily activity. The rats perform other movements during the day (i.e. spins, jumps and transitions from quadrupedalism to bipedalism while eating), which induce different deformations on the bone tissue. Although these movements are not accounted in this analysis, the proposed set of loads allows describing the physiological deformation experimentally measured *in-vivo*, and the proposed signal comparison is considered pertinent.

4.5 Conclusions

An original model of a rat's tibia subjected to musculoskeletal loads is constructed, yielding a realistic representation of the deformation fields that develop in the tibia during gait. This model enhances the knowledge of the biomechanics of rat tibiae under physiological conditions and sets the baseline according to which implantation studies on tibiae are to be evaluated.

Within the framework of the 'loaded implant' model, the proposed methodology allows achieving three relevant goals:

1. It appears that normal locomotion may tear the adhesive interface between the implant and the bone to the extent that a gap opens or at least the contact area is drastically reduced. The peri-implant cortical loss observed experimentally is caused by bone disuse atrophy, which is initiated by a loss of bone-implant adhesion and kept ongoing by the cyclic loadings on the interface due to gait cycles. Thus, rat locomotion detrimentally affects the implant integration. This result explains the significant implant losses observed in case of bilateral implantations (Section 2.4.3.1).
2. Within the observed time period, three configurations are possible: (1) no implant-bone debonding occurs because press fit is retained sufficiently long to allow bone in-growth and stability of the implant, (2) a local debonding is initiated on the outer cortical surface which finally stops at a certain depth (3) an unstable evolution of debonding and bone resorption which leads to an open gap between implant and bone. Thus, the outcome of the external stimulation depends on the interaction of the external load with these states of integration (see Figure 2.13, Section 2.5).
3. The analysis of the stimuli of bone adaptation performed on the bare tibia highlights the octahedral shear strain as the better candidate for the implementation of the Mechanostat theory at continuum scale. When gait-based loads are applied, this signal shows location- and tissue-independent distributions. This result confirms the existence of a unique range of stimuli corresponding to physiological conditions, which drives the bone macroscopic structural adaptation to mechanical stimulations.

Chapter 5

Bone adaptation

5.1 Aim

This chapter addresses the predictive capabilities of bone adaptation models. A robust and versatile algorithm allows comparing existent theories of bone adaptation to an optimized approach based on the analysis of stimuli presented in Chapter 4. The predicted implant lateral stability, as well as the overall and local density variations, are validated through comparison with the experiments presented in Chapter 2. In addition, sensitivity studies are performed to highlight the dependency of the results on the proposed settings.

The following themes are addressed:

- The peri-implant bone adaptation to the ‘external’ stimulation (i.e. the implant loading) of well integrated implants.
- The adaptation of the whole tibia to the ‘internal’ stimulation (i.e. the gait-based loading condition presented in Section 4.3.1) and its correlation with the observed peri-implant cortical bone loss.
- The combination of both loading environments in a multi-load framework representative of the ‘loaded implant’ model.

5.2 Introduction

The phenomenological bone adaptation models currently adopted in literature can be grouped in three main categories: models based on homeostasis, models based on damage repair and models based on optimality criteria (Zadpoor, 2013).

The models based on homeostasis assume the maintenance of a reference signal within fixed limits through the variation of the bone mass (e.g. Huiskes et al., 1987, Mullender, 1994, Weinans and Prendergast, 1996). This theory often implies a homeostatic range of signal, the Lazy Zone (LZ), within which only bone maintenance occurs, without macroscopic changes (i.e. remodeling). In these models, the bone mass variation plotted against the reference signal assumes the trend of the Mechanostat, as shown in Figure 5.1a, where three phenomena are represented: mass resorption due to disuse, the homeostasis and mass apposition because of overloading. Several parameters are adopted as stimuli of bone adaptation, for example the strain energy density (Huiskes et al., 1989), strains (Frost, 1983, Weinans et al., 1992), or stresses (Beaupré et al., 1990a, Carter et al., 1989).

The models based on damage repair belong to the observation of microcracks in bone. Small cracks are always present, even in healthy tissue, and suggest that the working condition of bone involve a certain level of physiological damage (Taylor et al., 2007). If the damage due to the mechanical environment does not overcome a limit, the tissue remains in a remodeling equilibrium where no macroscopic structural changes are visible. On the contrary, if the tissue accumulates too many microcracks the repairing mechanism is activated to adapt the bone structure and reduce the accumulated damage (e.g. Doblaré and García, 2002, Prendergast and Taylor, 1994, Ramtani et al., 2004, Vahdati and Rouhi, 2009).

The models based on optimality criterion require the definition of optimization functions and constraints (e.g. Harrigan and Hamilton, 1992a,b, Payten and Law, 1998). In models assuming mass conservation, the tissue adapts to the external loading by maximizing its stiffness while preserving the total mass (Bagge, 2000). This constraint is not imposed if bone is considered an open system, exchanging mass with the environment (Fernandes et al., 1999).

It is worth noticing that the application of bone adaptation models is mainly focused on orthopedic biomechanics, while relatively few investigations address the integration of dental implants (Chou et al., 2008, Lin et al., 2009, Mellal et al., 2004, Reina et al., 2007). The analysis of bone adaptation in dentistry requires the study of an extended range of mechanical stimulus that includes the resorption because of overloading (Figure 5.1). This phenomenon is one of the most frequently reported causes of peri-implant marginal loss and seriously affects the long term stability of dental implants (Hoshaw et al., 1994, Qian et al., 2012). For this purpose, bone adaptation algorithms including resorption

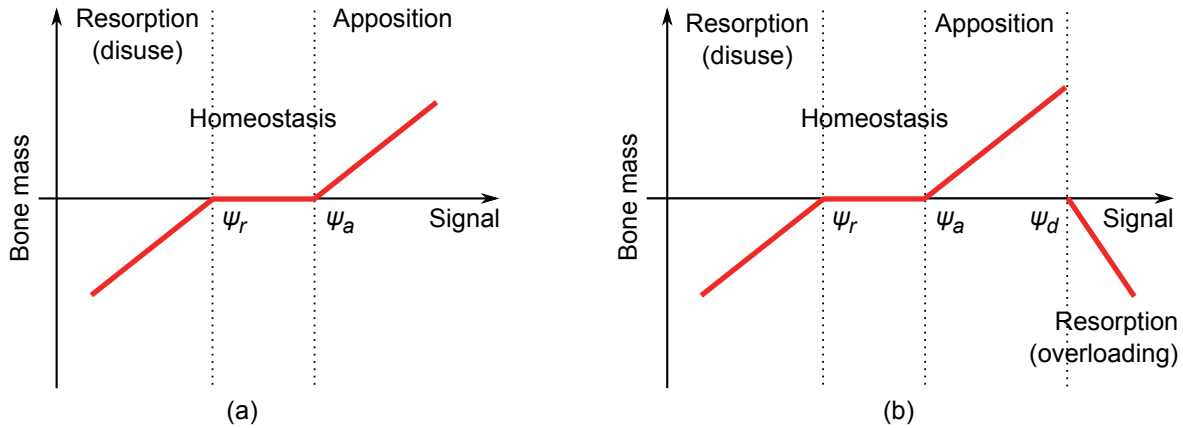


Figure 5.1: Bone adaptive modeling as a function of the mechanical signal: (a) without resorption because of overloading and (b) with resorption because of overloading.

due to overloading have been proposed (Crupi et al., 2004, Li et al., 2007, McNamara and Prendergast, 2007, Van Oosterwyck et al., 1998). These models do not explain the mechanistic nature of the resorption due to overloading, but they allow studying bone adaptation by fixing an upper limit of deformation, as shown in Figure 5.1b.

Although this field of research has been widely explored, none of the described approaches have shown sufficient reliability to be recognized as gold standard by the research community. Indeed, the choice of the appropriate model depends on the investigated theme, on the available inputs and on the desired outputs. Concerning the ‘loaded implant’ model, the focus is on the implant stability and on macroscopic peri-implant bone adaptation to the mechanical stimulation induced by the animal daily activity and the implant loading. As shown in the analysis of mechanical stimuli (Section 4.4), the physiological activity leads to a bounded range of strain (i.e. the Lazy Zone). Thus, in this work predictions of internal bone adaptation are addressed through Mechanostat-based models involving resorption because of overloading.

5.3 Numerical framework of bone adaptation

The peri-implant bone adaptation characterizing the ‘loaded implant’ model is investigated through a versatile numerical modeling. Specimen-specific FE models are processed through a feedback algorithm that updates the bone material properties in relation to the mechanical environment until a converged solution is achieved. Then, the results are post processed to highlight the variation of implant stability and bone density distribution between the initial and final configuration. The adopted theory, the implemented algorithm

and analyses settings are discussed in the following sections.

5.3.1 Theory of bone adaptation

The simulations of bone adaptation to mechanical stimuli are based on a site- and tissue-independent formulation: it is assumed that any tissue (e.g. cortical or trabecular) in any location of the tibia attempts to equalize its mechanical stimulus to a constant reference value (or range of values), named attractor state (Beaupré et al., 1990a), by reducing or increasing the bone local mechanical properties. In details, the difference between the local signal ψ and the attractor state ψ_{ref} defines the error of adaptive modeling e , driving the variation of bone density as described in Equation 5.1.

$$\frac{d\rho_{bmd}}{dt} = Ke = K(\psi - \psi_{ref}) \quad (5.1)$$

where $d\rho_{bmd}/dt$ is the rate of BMD turnover and K is an adaptation rate constant. As described in Section 3.3.2, a BMD variation provokes a consequent update of the elastic modulus E through the correlation described in Equation 3.5 (Cory et al., 2010), reported here for sake of completeness

$$E = 8.36\rho_{bmd}^{2.56} \quad (5.2)$$

The value of the attractor state depends on the chosen law of bone adaptation. Generally, the whole range of stimulation is subdivided in four zones: resorption due to disuse, homeostasis, apposition and resorption due to overloading (Figure 5.1b). Numerically, this discretization can be obtained through the definition of three different attractor states, that implies a piecewise linear reformulation of Equation 5.1, reported in Equation 5.3

$$\frac{d\rho_{bmd}}{dt} = \begin{cases} K_r(\psi - \psi_r) & \text{if } \psi < \psi_r \\ 0 & \text{if } \psi_r \leq \psi \leq \psi_a \\ K_a(\psi - \psi_a) & \text{if } \psi_a < \psi \leq \psi_d \\ K_d(\psi - \psi_d) & \text{if } \psi > \psi_d \end{cases} \quad (5.3)$$

where ψ_r , ψ_a , ψ_d are the resorption, apposition and damage attractor states, and K_r , K_a , K_d are the respective adaptation rate constants.

This formulation implies an increase of the elastic modulus if the stimulus belongs to the apposition zone ($\psi_a < \psi \leq \psi_d$). The maximum elastic modulus is considered as specimen-specific, and it is calculated through Equation 5.4

$$E^{j,max} = 8.36(\rho_{bmd}^{j,max})^{2.56} \quad (5.4)$$

where $\rho_{bmd}^{j,max}$ is the maximum BMD value assigned to the bone tissue during segmentation for the specimen j (Section 3.3.2) at the beginning of the adaptation.

Moreover, no variation of the mechanical properties takes place if the stimulus falls within the limits of the Lazy Zone ($\psi_r \leq \psi \leq \psi_a$). Note that this assumption does not entail a lack of biological activity. As a matter of fact, the tissue characterized by a stimulus within the ranges of the LZ is involved in a complex, dynamic interplay between the resorption of damaged bone and the apposition of newer tissue. Nevertheless, this phenomenon does not provoke macroscopic variations of the bone mass and is represented through the maintenance of the existing material properties (i.e. $d\rho_{bmd}/dt = 0$ thus $dE/dt = 0$).

Finally, a reduction of the elastic modulus takes place if the stimulus belongs to the disuse or overloading zones ($\psi < \psi_r$ or $\psi > \psi_a$). Note that the resorption due to disuse or overloading is biologically different. The former occurs through a gradual reduction of the mineralized tissue operated by osteoclasts (Skerry, 2008), while the latter often involves inflammatory reactions and abrupt fatigue cracks that are not accounted in this framework (Kozlovsky et al., 2007). However, in both cases bone is affected by decreased mechanical properties, here represented through a local loss of stiffness. The minimum value for the elastic modulus is fixed to 0.1 MPa to avoid numerical singularities.

Equation 5.3 is iteratively solved through forward Euler integration to update the bone mechanical properties in relation to the loading condition. Basically, a discrete BMD variation $\Delta\rho_{bmd}$ is calculated through Equation 5.5

$$\Delta\rho_{bmd} = \Delta t K(\psi - \psi_{ref}) \quad (5.5)$$

where Δt represent the numerical time step at which the simulation progresses.

To reduce the computational time, an optimized time step calculation is implemented (Van Rietbergen et al., 1993). After each iteration, a maximal BMD variation $\Delta\rho_{bmd}^{max}$ is assigned to the node characterized by the larger adaptive modeling error Ke , within the whole model. Thus, the time step Δt is calculated at each iteration through Equation 5.6

$$\Delta t = \frac{\Delta\rho_{bmd}^{max}}{(K(\psi - \psi_{ref}))_{max}} \quad (5.6)$$

The value $\Delta\rho_{bmd}^{max}$ is specimen specific, and is calculated by Equation 5.7

$$\Delta\rho_{bmd}^{max} = \frac{\rho_{bmd}^{j,max}}{10} \quad (5.7)$$

This procedure allows controlling the simulation during the initial iterations, when the larger density variations occur, and accelerates the convergence when the error of bone adaptation is small.

5.3.2 Algorithm of bone adaptation

The block diagram representation of the implemented algorithm is shown in Figure 5.2. The structure is conceived in order to perform analysis involving several specimens, differ-

ent mechanical signals and multiple loading conditions. In details, the mCT images of a specimen are processed to generate a specimen-specific FE model, as described in Chapter 3. The field of elastic modulus Φ_E preserves the inhomogeneity of bone mechanical properties and establishes the initial reference for the adaptive modeling analysis. Later, the model is subjected to one or two sets of boundary conditions, generating their respective field of stimulus Ψ_1 and Ψ_2 . These fields are blended to produce a unique field of stimulus, representative of both loading conditions, and averaged on a pre-defined zone of influence. The resulting field of mechanical stimulus Ψ is compared with the attractor state Ψ_{ref} to quantify the error of adaptive modeling e . If the error does not fit the convergence criteria, a local tissue response is calculated in relation to the appropriate range of stimuli (i.e. apposition or resorption due to disuse or overloading). Then the iteration time step Δt is calculated through Equation 5.6 and the field of elastic modulus Φ_E is updated. Finally, the FE model with updated material properties is subjected to the loading conditions and a new field of deformation Ψ is obtained. This feedback loop is repeated until convergence is achieved. Then, the post-processing computes the variation of inter-implant strain and BMD in selected ROIs.

Several programs are involved: ITKsnap and *VoxelMesher* generate the FE models that is solved through ABAQUS-Standard^{®1}, while the node data extraction, update and post-processing are treated with on purpose routines in MATLAB^{®2} and Python^{™3}.

5.3.3 Signal blending and Zone of Influence

The presented algorithm is suitable for the analysis of multiple loading conditions, generating different field of deformations on the same FE model. This feature allows combining the stimuli generated on the tibia due to the gait-based loading condition and to the implants activation. The signal blending is based on the assumption that the bone adaptation is driven by the daily stimulus peaks (Frost, 1983) and is computed through Equation 5.8

$$\psi_i = \max(\psi_{i,1}, \psi_{i,2}) \quad (5.8)$$

where $\psi_{i,1}$, $\psi_{i,2}$ are the stimuli at node i during the first and second loading condition.

Then, the resulting field of stimulus Ψ can be homogenized on a pre-defined volume of bone. Note that the algorithm is based on fields of stimuli evaluated at nodes. This feature is of easier implementation with respect to a field at elements, because it allows dealing with organized lists of nodes instead of disorganized element sets. Moreover, ABAQUS[®] performs an interpolation on the node values to characterize the element's integration points,

¹version 6.10, Dassault Systèmes, Vélizy-Villacoublay, France.

²version 2008b, The MathWorks, Natick, Massachusetts, USA.

³version 2.6, www.python.org.

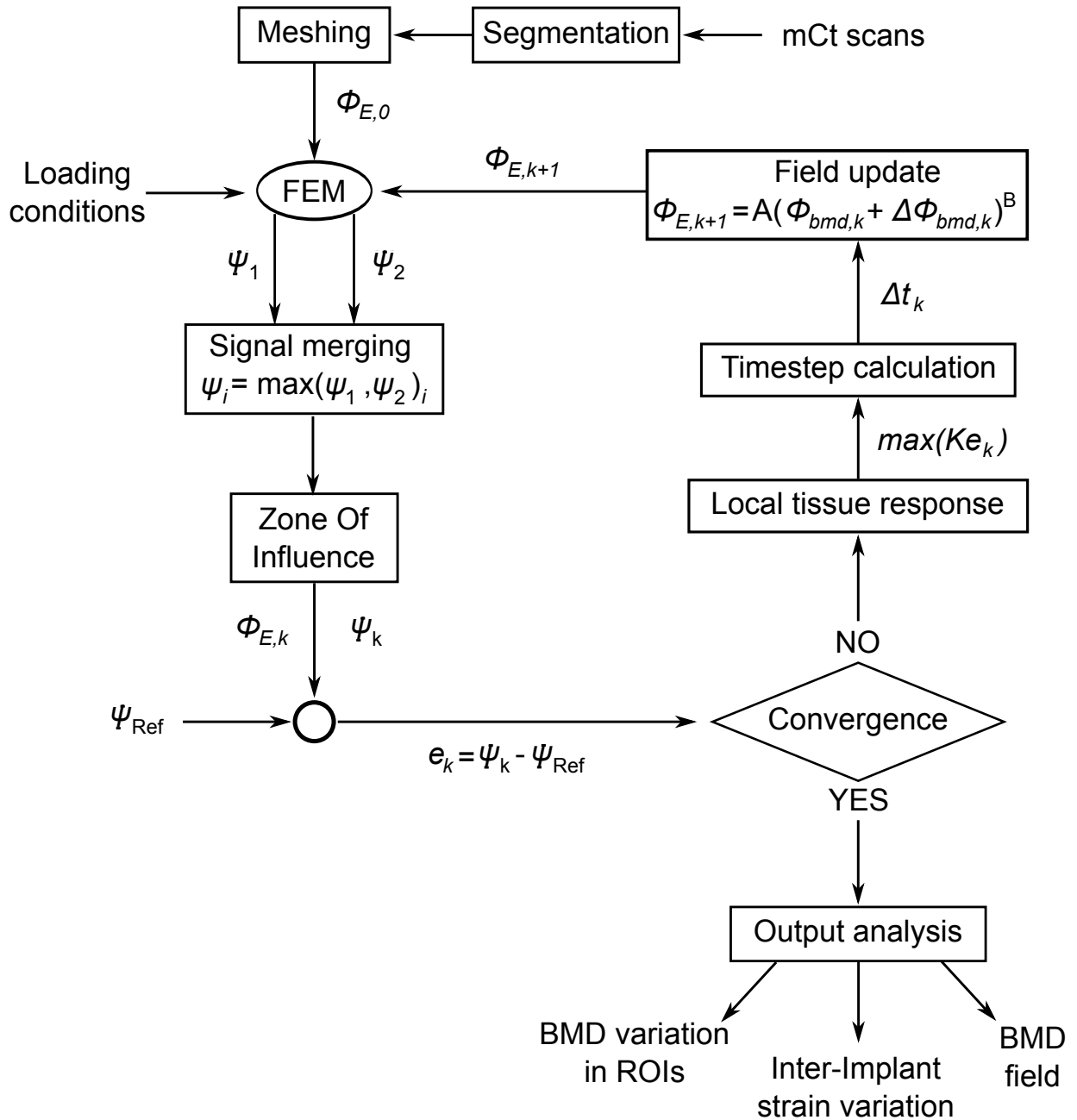


Figure 5.2: Block diagram representation of the algorithm of bone adaptation: i is the node number, k is the iteration number, Ψ , Φ_{bmd} and Φ_E are the stimulus, BMD and elastic modulus fields at nodes, respectively; A and B are the slope and exponent of the conversion law by Cory et al. (2010).

reducing the occurrences of numerical instabilities (e.g. the chessboard effect highlighted by Weinans et al. (1992)). Nevertheless, the node-based algorithm is less representative of the adaptation phenomenon than an element-based one. Indeed, a mechanical signal implies the existence of a discrete volume of bone able to sense a deformation, while a single node is not a representative volume by definition.

To compensate for this drawback while preserving the convenience of node-based fields, the algorithm includes a spatial averaging of the signal over a spherical Zone Of Influence (ZOI). Already adopted in numerical models of bone adaptation to the mechanical stimuli (Mullender and Huiskes, 1995, Schulte et al., 2013), this feature also involves the interesting assumption of a collective contribution to the local stimulation, operated by mechanically sensitive cells interconnected by biological processes (Kumar et al., 2012, 2011). Thus, the size of the ZOI should be chosen to match the size of the Representative Volume Element (RVE) of the bone microstructure and the radius of diffusion of the chemical signals that control bone adaptation. Once the ZOI radius is defined by the user, the signal is averaged as shown in Equation 5.9

$$\psi_i = \frac{\psi_i + \sum_{j=1}^Z f(D_{ji})\psi_j}{1 + \sum_{j=1}^Z f(D_{ji})} \quad (5.9)$$

where Z is the number of nodes included in the defined ZOI and $f(D_{ji})$ is a shape function that weights the signal contribution of the node j with respect to its distance D_{ji} from the current node i . With this formulation the conservation of the integral of ψ is ensured.

The proposed signal averaging generates a node-based, local stimulus that accounts for the volume-based, non-local distribution of the deformation among the defined ZOI. Thus, the dependence of results on the mesh size is reduced and the user is free to define the local impact of the mechanical stimulus by selecting the ZOI radius and weighting function f .

5.3.4 Convergence criteria and output representation

The simulation is automatically stopped when a convergence criteria based on the mechanical stimuli is satisfied, that is when 99.9 % of nodes show null adaptation errors. Moreover, an additional criterion is introduced in analysis involving the inter-implant loading: the calculation is interrupted if the inter-implant strain is equal to 1. This configuration is achieved when the heads of the implants are superimposed, meaning that most of the peri-implant bone is resorbed because of overloading.

Once the convergence is achieved, an automatic post-processing routine extracts the following results, based on the comparison between the initial condition and the converged solution:

Inter-Implant strain variation. Provide information on the enhancement or degradation of the implants' lateral stability.

BMD variation in pre-defined ROIs. Allows numeric results to be quantitatively compared to the experimental observations presented in Chapter 2.

3D mapping of the BMD field variation. Highlights the models' areas where resorption or apposition produce a variation of the bone mineral density field, and can be compared to mCT scans.

In analyses involving groups of specimens, the results are reported in terms of mean and Standard Error of the Mean (SEM). However, the results of each specimen are also reported when the effects of biodiversity are significant.

5.4 External loading

The five Basal specimens belonging to Series 3 (Section 2.4.3.2) are processed to generate specimen-specific FE models and employed as reference group, representative of the initial state of integration. Indeed, these specimens underwent 2 weeks of integration and show a good peri-implant morphology. The analyses of this section are based on this batch of specimens.

A single loading condition is considered: 5 N of inter-implant loading that has shown to induce an improvement of the inter-implant strain and ultimate strength (Figure 2.10b), and an increase of BMD in ROI1 and ROI3 investigated in Series 3 (Figure 2.4b, Section 2.3.1.1). The assumption that the bone mechanical properties are preserved by the rat daily activity is made, and the resorption due to disuse is neglected. This is valid only if the implants are well integrated and is confirmed by the experimental results shown in Table 2.7 (i.e. no differences between Basal and Non-stimulated specimens is observed).

The simulations do not involve the modeling of the bone-implant contact, which is considered perfectly intact. However, this assumption implies an unrealistic transfer of loads to the distal and proximal tissues where the bone-implant interface is subjected to traction. To compensate for this drawback while preserving the computational speed, a small elastic modulus is assigned to the region of the implants in contact with cortical bone in the distal and proximal directions, as shown in Figure 5.3.

5.4.1 Comparison of existing approaches

Two approaches inspired by the works by Li et al. (2007) and Crupi et al. (2004) are implemented in the described framework and compared. They address the bone adaptation around dental implants including resorption because of overloading. The features of these models are presented in the following section.

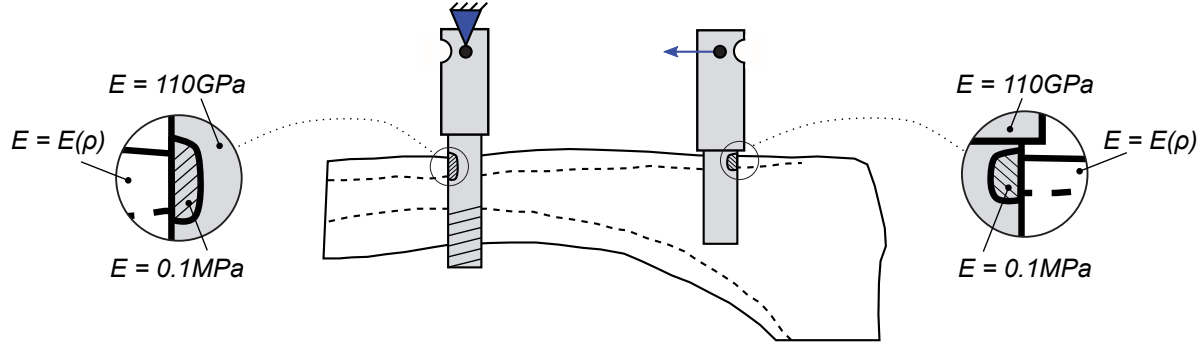


Figure 5.3: Boundary conditions of the FE models for iterative computation. The external load is applied to the proximal implant while the distal one is fixed. The dotted areas are characterized by a small elastic modulus.

5.4.1.1 Models formulation

The approach inspired by Li et al. (2007) adopts the elastic energy density per unit mass as signal (Equation 5.10, Section 4.4.1) and computes the bone density variation through Equation 5.11

$$\psi = \psi_U = \frac{U}{\rho_{bmd}} \quad (5.10)$$

$$\frac{d\rho_{bmd}}{dt} = \begin{cases} 0 & \text{if } \psi \leq \psi_a \\ K_a(\psi - \psi_a) - K_d(\psi - \psi_a)^2 & \text{if } \psi_a < \psi \end{cases} \quad (5.11)$$

This quadratic formulation allows modulating the rate of bone variation from positive to negative values in relation to the adaptive error $(\psi - \psi_a)$ and the coefficients K_a and K_d , as shown in Figure 5.4a. The values assigned by Li et al. (2007) to these variables are reported in Table 5.1.

The approach inspired by Crupi et al. (2004) adopts the daily stress as signal (Equation 5.12, Section 4.4.1), and computes the bone adaptation velocity dr/dt through the formulation in Equation 5.13.

$$\psi = \psi_\sigma = \left(\frac{\rho_{bmd,c}}{\rho_{bmd}} \right)^2 (n\sigma^m)^{1/m} \quad (5.12)$$

$$\frac{dr}{dt} = \begin{cases} 0 & \text{if } \psi \leq \psi_a \\ K_a(\psi - \psi_a) & \text{if } \psi_a < \psi \leq \psi'_a \\ K_a(\psi'_a - \psi_a) + K'_a(\psi - \psi'_a) & \text{if } \psi'_a < \psi \leq \psi''_a \\ K_a(\psi'_a - \psi_a) + K'_a(\psi''_a - \psi'_a) & \text{if } \psi''_a < \psi \leq \psi_d \\ K_a(\psi'_a - \psi_a) + K'_a(\psi''_a - \psi'_a) + K_d(\psi - \psi_d) & \text{if } \psi_d < \psi \end{cases} \quad (5.13)$$

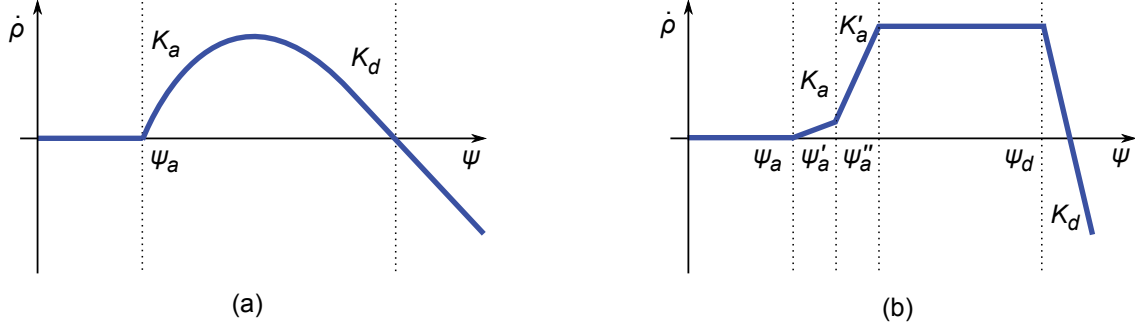


Figure 5.4: Adaptation rate versus mechanical stimulus for (a) Li et al. (2007) and (b) Crupi et al. (2004).

Table 5.1: Adaptation parameters from the literature.

Model	Signal	Cycles	Attractor state				Rate constant		
			ψ_a	ψ'_a	ψ''_a	ψ_d	K_a	K'_a	K_d
Li et al. (2007)	ψ_U	-	0.004 ^a	-	-	-	1 ^b	-	60 ^c
Crupi et al. (2004)	ψ_σ	900*	50 ^d	60 ^d	70 ^d	230 ^d	0.009 ^e	0.18 ^e	-3 ^e

^a J/g; ^b (g/cm³)²/(MPa×time unit); ^c (g/cm³)³/(MPa×time unit)²; ^d MPa; ^e μm/MPa.

* loading cycles of the external stimulation, Section 2.2.4.

where $n = 900$ is the number of loading cycles applied to the implants and $m = 4$ is the cycles-stress weight factor. The adaptation velocity dr/dt allows computing the density adaptation through Equation 5.14.

$$\frac{d\rho_{bmd}}{dt} = \frac{dr}{dt} S_v(\rho_{bmd}) \rho_{bmd,c} \quad (5.14)$$

where $S_v(\rho_{bmd})$ is the surface density of bone tissue proposed by Martin (1984) adapted to BMD values. The apposition is discretized into three zones with different rates and thresholds, generating the piecewise trend shown in Figure 5.4b. The parameters proposed by Crupi et al. (2004) are reported in Table 5.1.

5.4.1.2 Results and discussion

The BMD field variation obtained with both models on the inter-implant plane of a representative specimen is reported in Figure 5.5. Both models involve a reduced volume of bone affected by resorption because of overloading in the apical region of the proximal and distal implant subjected to compression. The model by Li et al. (2007) predicts a limited

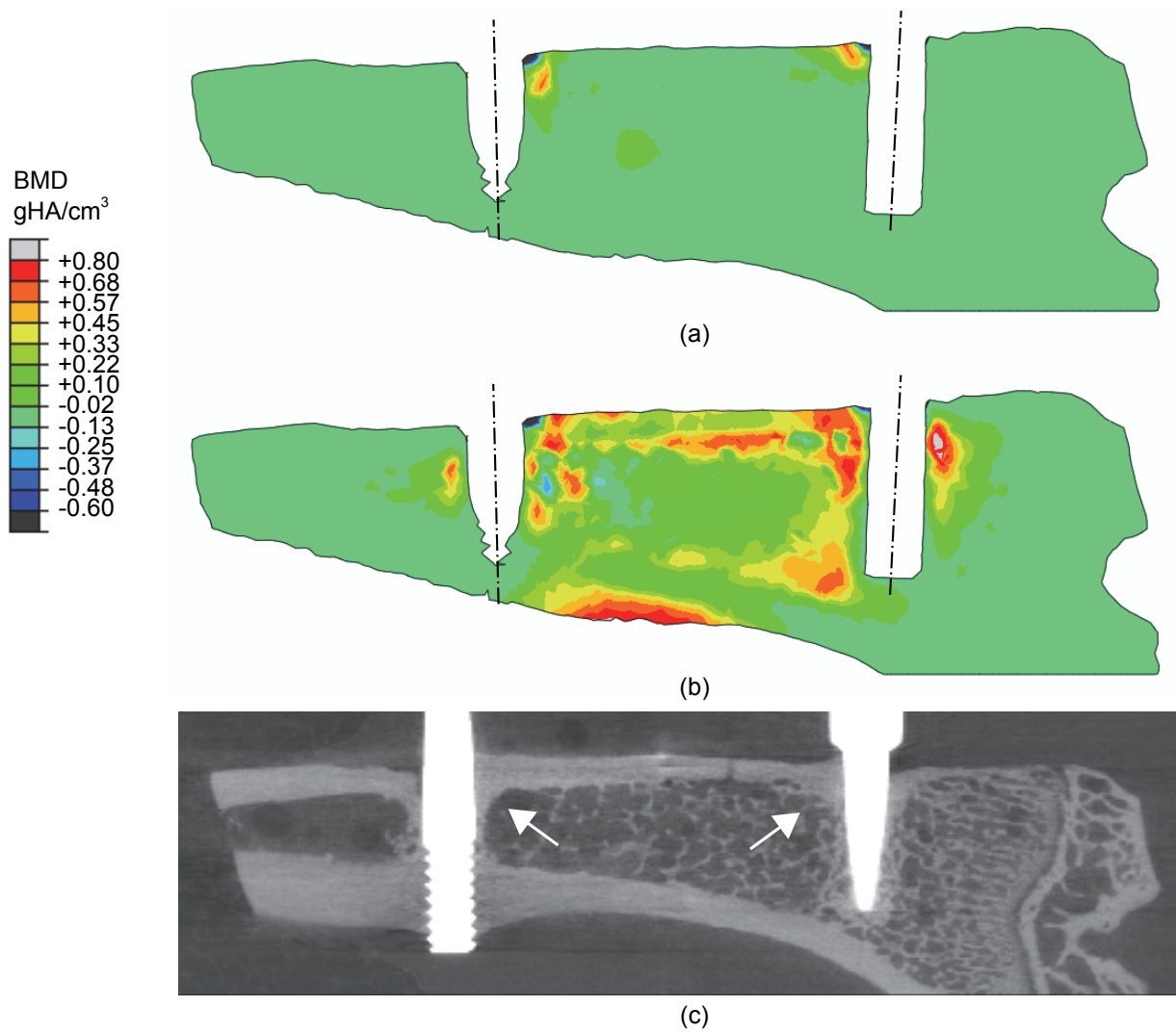


Figure 5.5: Example of BMD field variation on the inter-implant plane calculated through (a) Li et al. (2007) and (b) Crupi et al. (2004). Implants are hidden. (c) mCT of a stimulated specimen.

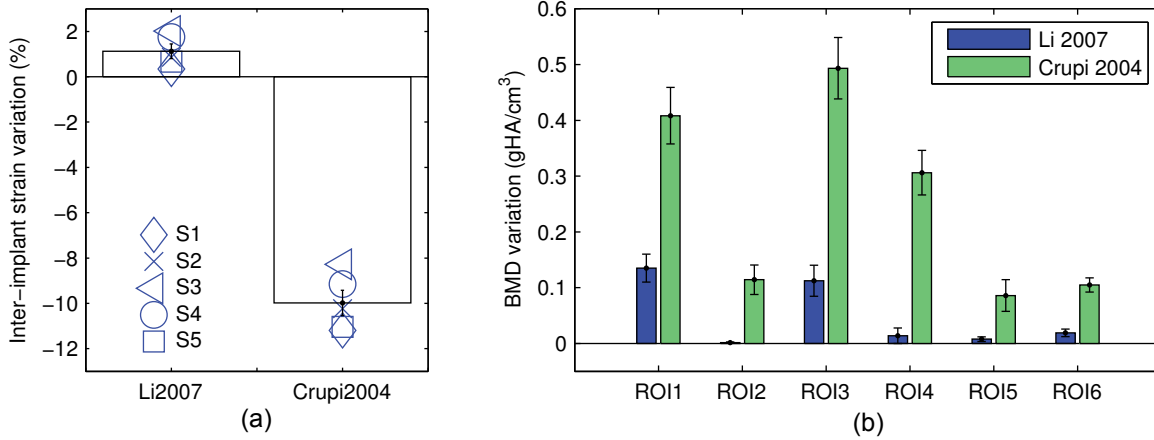


Figure 5.6: (a) Inter-implant strain variation and (b) BMD variation in ROIs predicted through the models by Li et al. (2007) and Crupi et al. (2004).

BMD augmentation involving small areas in the proximity of damaged tissue, while the one by Crupi et al. (2004) produces an important bone apposition scattered between the implants and characterizing both cortical and trabecular bone.

The inter-implant strain variations averaged over the five Basal specimens are reported in Figure 5.6a. The model by Li et al. (2007) predicts a small worsening of the implant lateral stability (+1 %) while the one by Crupi et al. (2004) entails a reduction of the inter-implant strain (-10 %) corresponding to a clear increase of stiffness. Moreover, Figure 5.6b reports the local BMD variation calculated on the six ROIs investigated in Series 3 (Figure 2.4b, Section 2.3.1.1). The model by Li et al. (2007) predicts null variations in all ROIs except a small density increase in ROI1 and ROI3. The model by Crupi et al. (2004) predicts important BMD increments in ROI1, ROI3 and ROI4.

Both approaches capture the general behavior of the investigated phenomenon, but the results are not satisfactory. Indeed, both models overestimate the effects of damage (i.e. all the specimens show peri-implant bone resorption) with respect to the experiments, where only one specimen over five shows apical resorption (Appendix B). The model by Li et al. (2007) predicts nearly no bone augmentation with a consequent negligible increase of stiffness, exactly the opposite of the model by Crupi et al. (2004) where both are overestimated. Moreover, the regions characterized by bone augmentation are not limited to the apical peri-implant areas highlighted by the experiments (Figure 5.5c). These errors are attributed to the parameters which define the attractor states proposed by the authors. As described in Section 1.4.2, the use of parameters of bone adaptation models taken from the literature involves risks of inaccuracies and errors, because of differences in studied species and other experimental conditions. These models may provide better accuracy by

performing an identification of parameters on dedicated experiments corresponding to the rat tibiae.

Finally, it is worth recalling the analysis presented in Section 4.4.3 concerning the signal comparison on the benchmark of the gait-based loading condition. The energy- and stress-based signals, adopted by Li et al. (2007) and Crupi et al. (2004) respectively, show a tissue-dependent behavior: under physiological conditions the signal distribution in cortical and trabecular bone are different (Figure 4.10). This behavior highlights a contrast with the adaptation models that consider a unique Lazy Zone for both tissues. As a matter of fact, if the physiological ranges of signal for cortical and trabecular tissues are different, this variability should be accounted through tissue-dependent LZ thresholds. This feature may affect the accuracy of predictions involving stress- and energy-based signals.

5.4.2 Optimized approach

The results of existing approaches show that the implementation of models from the literature in the proposed framework can generate imprecise results due to inconsistent parameters and stimuli. Thus, a new approach conceived for the adopted numerical strategy is presented.

The theoretical formulation, the choice of the signal and parameters are based on two main concepts: coherence and simplicity. The coherence with the results presented in Chapter 4, concerning the deformations occurring in the rat tibia during gait, is a key factor. Moreover, the model complexity is reduced to the basic necessary to phenomenologically reproduce the observed adaptation processes, limiting the involved unknowns to the essential.

5.4.2.1 Formulation and parameters

As described in Section 4.4.3, the strain-based signal ψ_ϵ shows location and tissue invariant distributions in a physiological environment (i.e. a rat tibia subjected to gait loads), thus ensuring compatibility with a macroscopic adaptation model based on a unique homeostatic range of stimulus. As a consequence, the proposed approach is based on the signal ψ_ϵ , shown in Equation 5.15. The BMD variation $d\rho_{bmd}/dt$ is computed through Equation 5.16, that is inspired by the quadratic form proposed by Li et al. (2007). The trend of $d\rho_{bmd}/dt$ with respect to ψ_ϵ is shown in Figure 5.7a.

$$\psi = \psi_\epsilon = \epsilon_{oct} \quad (5.15)$$

$$\frac{d\rho_{bmd}}{dt} = \begin{cases} K_r(\psi - \psi_r) & \text{if } \psi_r > \psi \\ 0 & \text{if } \psi_r \leq \psi \leq \psi_a \\ K_a(\psi - \psi_a) \left(1 - \frac{\psi - \psi_a}{\psi_d - \psi_a}\right) & \text{if } \psi_a < \psi \end{cases} \quad (5.16)$$

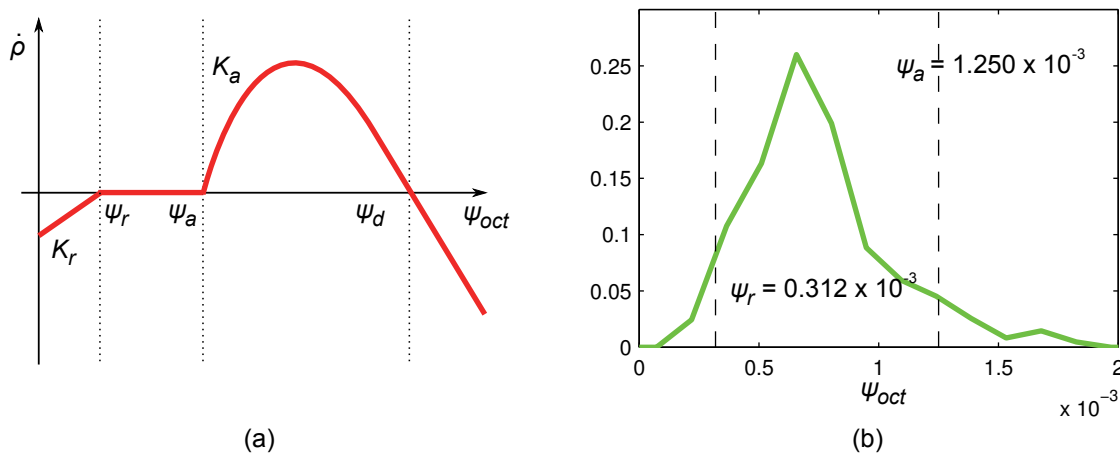


Figure 5.7: (a) Adaptation rate versus ψ_ϵ . (b) fitting of resorption and apposition attractor states as 5th and 95th percentiles of the octahedral shear distribution characterizing both cortical and trabecular tissues between the implants and around the proximal implant (ROI_{II} and ROI_{CY} in Figure 4.9).

Table 5.2: Adaptation parameters of the optimized approach.

Signal	Attractor state			Rate constant		ZOI	
	ψ_r	ψ_a	ψ_d	K_r	K_a	Radius	Function
ψ_ϵ	0.312×10^{-3}	1.250×10^{-3}	4.510×10^{-3}	1	1	0.3	Gaussian

Although this formulation is purely heuristic, it allows describing the whole spectrum of bone mechanical adaptation through two time constants (i.e. K_r and K_a) and three attractor states (i.e. ψ_r , ψ_a and ψ_d for disuse, overloading and damage, respectively).

In the absence of reference longitudinal experiments, the adaptation rates K_r and K_a are taken equal to 1 (gHA/cm³)/(time unit) as proposed by Li et al. (2007). The resorption and apposition attractor states, $\psi_r = 0.312 \times 10^{-3} \epsilon$ and $\psi_a = 1.250 \times 10^{-3} \epsilon$, are fixed by fitting the distribution of deformation occurring in the rat tibia during gait (Section 4.4.3). As shown in Figure 5.7b, these values are quantified as the 5th and 95th percentiles of the octahedral shear strain distribution characterizing both cortical and trabecular tissues between the implants and around the proximal implant (ROI_{II} and ROI_{CY} in Figure 4.9). The damage attractor state $\psi_d = 4.510 \times 10^{-3} \epsilon$ is fixed in agreement with the longitudinal strain threshold of $4 \times 10^{-3} \epsilon$ proposed by Frost (1987) and already adopted by McNamara and Prendergast (2007) for a study concerning bone damage. This value corresponds to the

lower limit of the range of high stimulation where mechanical deformations may become harmful for the bone tissue, thus this threshold is chosen as the beginning of a negative BMD adaptation rate.

A ZOI of 0.3 mm of radius is chosen because it is representative of a trabecular bone volume compatible with the continuum assumption (3 to 5 inter-trabecular lengths, Bouxsein et al., 2010, Harrigan et al., 1988). The decay of the signal with increasing distance from the central node of the ZOI is computed through a gaussian function, which is typical for many natural processes. The adopted parameters are summarized in Table 5.2. In agreement with the previous analysis, the resorption due to disuse is neglected in case of simulations involving only the external loading condition.

5.4.2.2 Validation

The BMD field variation characterizing the inter-implant plane of the five specimens at equilibrium (i.e. once the analyses are converged) is represented in Figure 5.8. Only the first and second specimens from the left show small signs of apical resorption because of overloading (dotted circles), but generally the harmful effects of overloading are less frequent with respect to previous approaches (Crupi et al., 2004, Li et al., 2007). The BMD increments are mostly located in the sub-cortical inter-implant tissue and involve both implants, but the density distribution varies with specimens. The bone tissue external to the implants in the distal direction is not affected by BMD variation, thus confirming the efficiency of the boundary conditions implemented to prevent unrealistic transmission of tension (Figure 5.3). On the contrary, this strategy gives inaccurate results in the proximal area of the proximal implant (dotted squares in Figure 5.8), where density variations occur. As a matter of fact, the trabecular reticulum surrounding the proximal implant relocates the anchorage point along the implant axes, thus introducing an unrealistic bone adaptation in this region. These results highlight the local effects of the external stimulation, mainly focused between the implants and barely involving the trabecular reticulum, despite the floating proximal implant. These findings are supported by the negligible morphometric variation monitored experimentally in the peri-implant trabecular tissue (Section 2.4.1).

The quantification of the BMD increase in ROIs is shown in Figure 5.9a, where both numerical (i.e. specimen-specific and mean value) and experimental results are reported. The experimental BMD variation is calculated as the difference between the statistically representative values measured in the Stimulated (5N) and Basal specimens (Figure 2.11). Note that the ψ_ϵ -based approach correctly captures the local BMD increases and is well correlated with the experiments. The higher average increment is predicted in ROI1 (0.4 gHA/cm³) followed by ROI3 (0.35 gHA/cm³). Other ROIs show negligible BMD variations, while the increment characterizing ROI4 is provoked by the boundary condition discussed previously (Figure 5.3). The biodiversity play an important role, showing

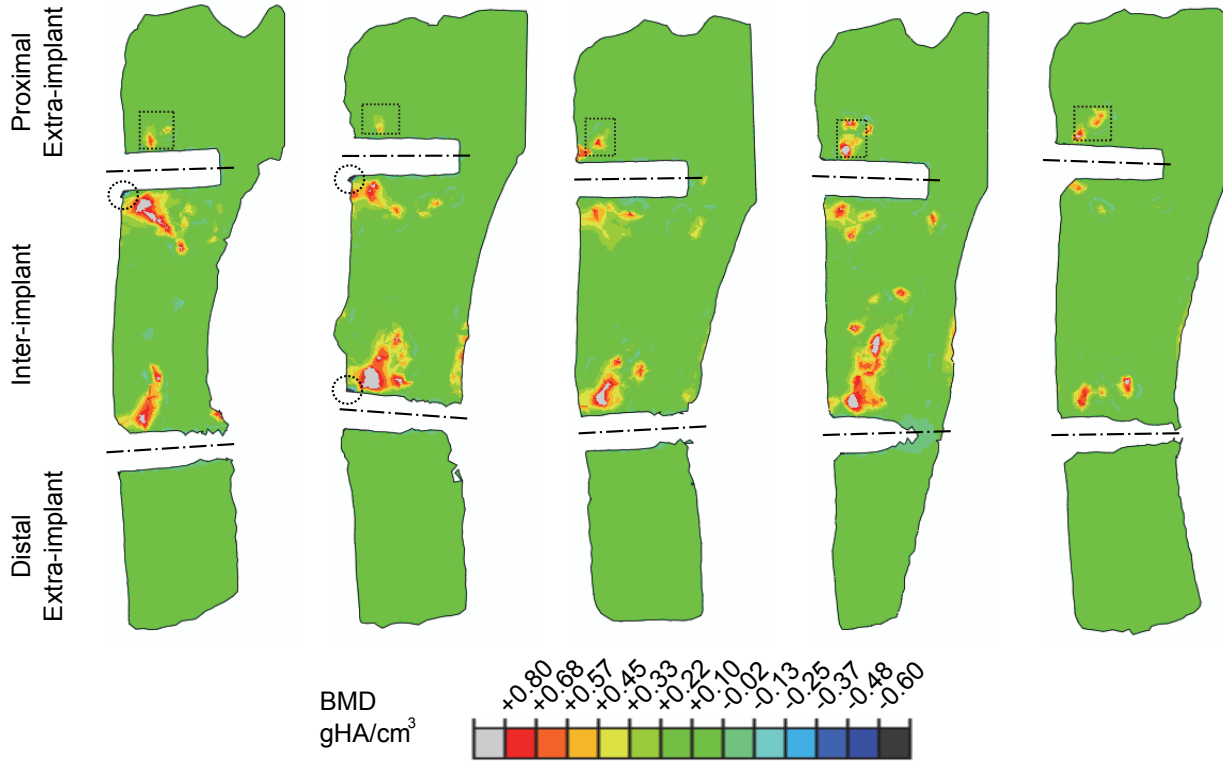


Figure 5.8: BMD field variation on the inter-implant plane of the 5 Basal specimens calculated through the ψ_ϵ -based approach. Implants are hidden.

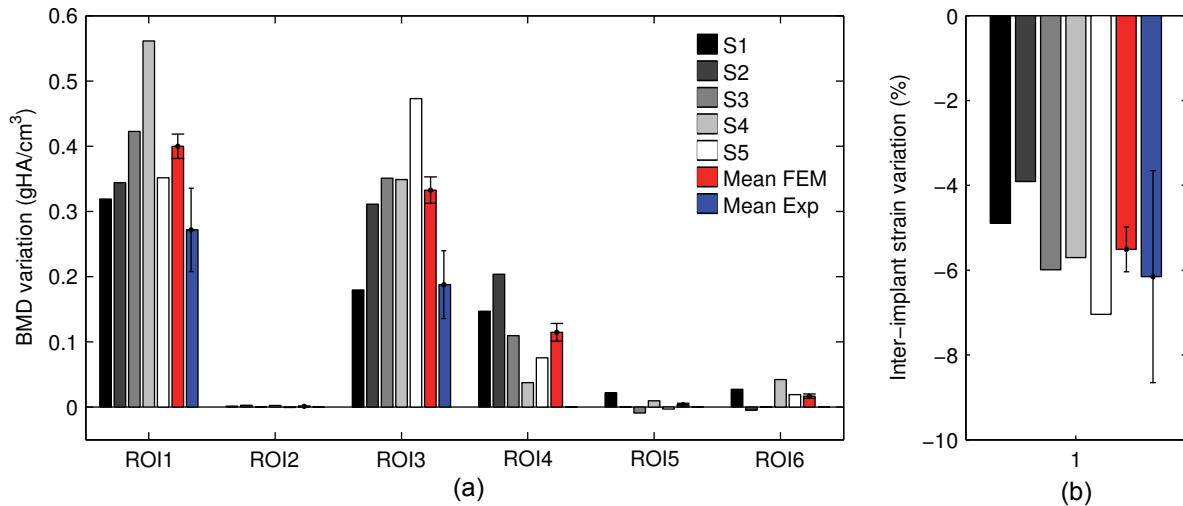


Figure 5.9: (a) BMD variation in ROIs and (b) inter-implant strain variation predicted with the ψ_ϵ -based approach.

non-negligible variances in both ROIs, with values comparable to the measurement itself (i.e. ~ 0.3 gHA/cm³ between S1 and S5 in ROI3).

The comparison with the experiments is satisfactory: this approach predicts the correct hierarchy of ROIs increments and overestimates the mean BMD increase by a maximum of 0.14 gHA/cm³, which is considered as an excellent result considering the relevant influence of biodiversity and the strong assumptions through which this biological phenomenon has been simplified. The reasons of this overestimation are theoretical and experimental. Firstly, the simulations assume a location- and tissue-invariant cap for the material property assignment (Equation 5.4). That is, fully mineralized tissue may appear everywhere in the model if the appropriate stimulation is provided. Although this hypothesis is adopted in the majority of the phenomenological approaches in this research field, no clear experimental confirmation is available. Secondly, the experimental quantification of the BMD variation is related to a defined time-point (i.e. after 4 weeks of stimulation, Section 2.2.4). Although previous studies on the ‘loaded implant’ model show that longer stimulation periods do not significantly affect the peri-implant morphometry (Wiskott et al., 2012), the new tissue generated as a reaction to the external loading lacks mineralization, because this process requires several months. Thus, the BMD measured at four weeks of stimulation may be lower than the equilibrium condition.

Concerning the implants lateral stability, Figure 5.9b shows the predicted variation of inter-implant strain compared to the one measured experimentally (Table 2.7). The bone adaptation to the external stimulation provokes a reduction of inter-implant strain (i.e. increased lateral stiffness) with notable differences between specimens (i.e. minimum -7.0 %, maximum -3.9 %). The average numerical result is in good agreement with the experiments, i.e. overestimated by 0.64 %. Interestingly, this comparison highlights a slightly different trend with respect to the BMD prediction. As a matter of fact, as BMD predictions overestimate the experimental results one should expect to measure a greater reduction of inter-implant strain through the FE models with respect to the mechanical tests, but that is not the case. However, the ambiguity characterizing the implant lateral stability finds two possible reasons. From the experimental point of view, the variance between Basal and Stimulated specimens shown in Table 2.7 is not statistically relevant, thus suggesting a trend rather than a quantitative measurement. From the numerical point of view, the adopted approach does not include variations of the bone geometry (i.e. periosteal reactions). As a consequence, eventual external adaptation phenomena involving variations of the implants insertion depth are not accounted, while they affect the inter-implant stiffness.

Furthermore, it is worth focusing on the results’ spread. The biodiversity affects all the presented outputs: the BMD field and ROIs variations as well as the inter-implant strain, thus pointing out the results sensitivity to the feature of each individual. Considering

that there are no criteria to chose a priori which specimen is representative of the whole population, these results highlight the importance of a strategy that accounts for the differences between individuals through the analysis of several specimen-specific FE models.

Finally, the comparison of BMD distributions between mCT scans and FE models shown in Figure 5.10 highlights the good correlation between experiments and numerical predictions obtained with the proposed approach. In this figure we can observe the cortical thickening by sub-cortical bone growth in the compressive peri-implant regions.

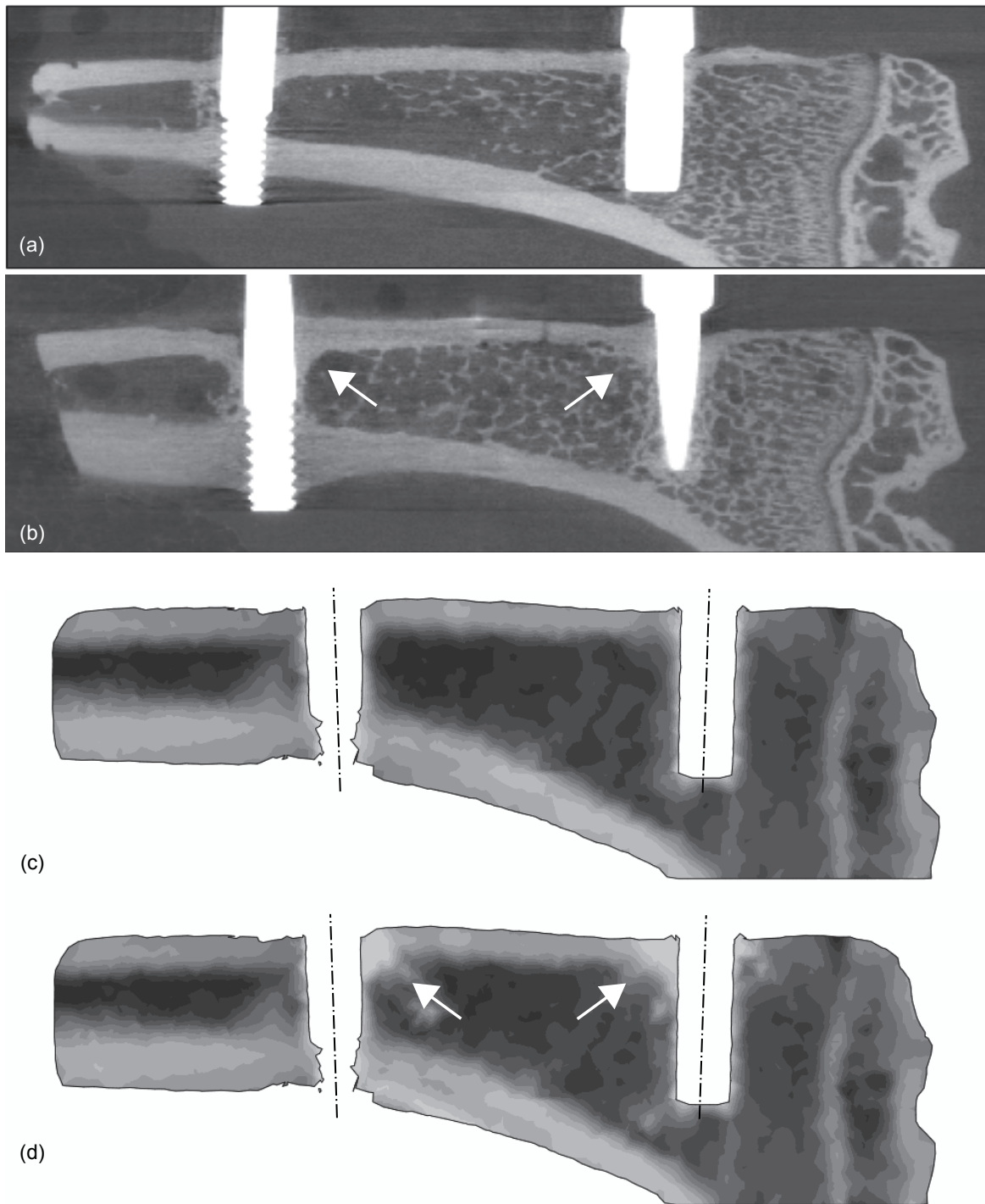


Figure 5.10: Inter-implant sections of mCT scans from (a) a non-stimulated and (b) a stimulated (5N) specimen (Figure 2.12). Inter-implant BMD distribution of FE model: (c) initial state and (d) converged state. A grayscale color map is chosen to facilitate the comparison with mCT images.

5.4.3 Sensitivity studies

As described in Section 1.4.3, the phenomenological approaches are based on several parameters and hypothesis that affect the final results. The sensitivity analysis allows understanding the dependency of outputs on these settings. In the present study the key variables are the following: the biodiversity, the attractor states, the law formulation, the Zone of Influence and the external load. The effects of the former have been extensively discussed in the previous section, while the system response to perturbations of the others is investigated in the following by keeping the five Basal specimens as baseline.

5.4.3.1 Attractor states

The apposition and damage attractor states (ψ_a and ψ_d , respectively) are defined in Section 5.4.2.1 through the results of the analysis on the rats' gait (Section 4.4) and reliable literature data. Nevertheless, the dependency of results on the perturbation of ψ_a and ψ_d is of great interest considering that the equilibrium between the peri-implant bone apposition and the apical resorption because of overloading is a key factor for the implant stability.

To perform this analysis, the spectrum of octahedral shear strain characterizing ψ_a and ψ_d is discretized in four values between 1×10^{-3} and $1.75 \times 10^{-3} \epsilon$, and 4.1×10^{-3} and $5.5 \times 10^{-3} \epsilon$ respectively, thus generating a grid with 16 possible combinations. Then, the bone adaptation is computed for each specimen and each attractor states pair for a total of 80 iterative computations.

The results are shown in Figure 5.11. The trend of the inter-implant strain deviation varies with both parameters (Figure 5.11a), ranging from 0 % to -8 %. Clearly, the maximum and minimum increase of stiffness coincides with the larger and smaller amplitude of the apposition zone (i.e. range of overloading producing a positive BMD rate). Moreover, the effects of ψ_d reaches a plateau after $5 \times 10^{-3} \epsilon$ meaning that none of the nodes is characterized by strain levels higher then this threshold, thus the value assigned to the damage attractor state is negligible above a certain limit. A different trend is shown by the BMD variation in ROI1 and ROI3 (Figure 5.11b and c). The density increment is nearly invariant with respect to ψ_d , while it is definitively reduced with the increase of ψ_a .

These results show that the perturbation of the attractor states within consistent ranges of strain does not affect the robustness of the investigated adaptation process (e.g. no worsening of the implant lateral stability is shown). However, these parameters clearly affect the prediction of both BMD and inter-implant strain variations. This highlight the need of a rigorous way of setting ψ_a , such as the study of daily activity used in this work.

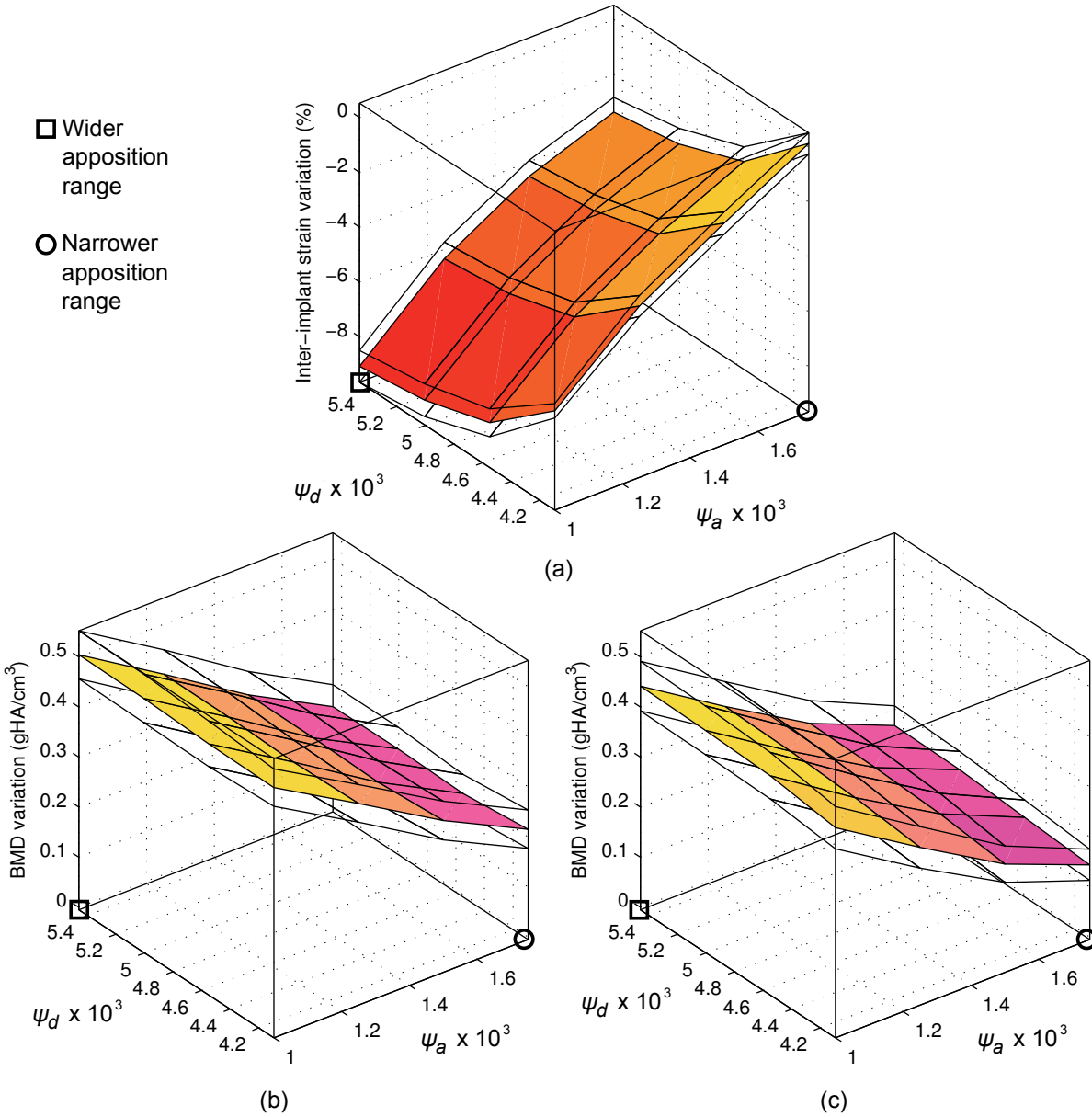


Figure 5.11: Sensitivity of (a) inter-implant strain and BMD in (b) ROI1 and (c) ROI3 with respect to the apposition ψ_a and damage ψ_d attractor states perturbation. The mean values (colored surface) and the SEM (upper and lower grids) are represented.

5.4.3.2 Law formulation

The dependency of the adaptation rate on ψ_ϵ , as formulated in Equation 5.16, consists in a quadratic form that allows describing both apposition and resorption because of overloading with few parameters. Nevertheless, this phenomenological formulation may not be representative of the actual correlation between bone mass variation and mechanical stimulus. As a matter of fact, several formulations have been proposed and discussed in the last years and it is of great interest to study the sensitivity of results to different mathematic forms.

To perform this study, the Basal specimen-specific FE models are processed with three adaptation laws: the optimized approach previously discussed, a linear formulation inspired by McNamara and Prendergast (2007) and a piecewise law with a plateau inspired by Crupi et al. (2004), for a total of 15 iterative computations. The trend of the adaptation rate plotted versus the signal ψ_ϵ is represented in Figure 5.12 for the three approaches, while the adopted parameters are reported in Table 5.3. These parameters are calculated to adapt the laws to the proposed framework and preserve all the other settings: the three formulations are based on ψ_ϵ (octahedral shear strain), the attractor states in common are equal and the models are processed with the standard ZOI (radius: 0.3 mm, shape function: gaussian).

The results of this study in terms of inter-implant strain variation and BMD increment in ROIs are reported in Figure 5.13a and b, respectively. The results of the optimized and linear formulations show a clear agreement, with the latter form slightly underestimating the inter-implant strain and density increments with respect to the former one. Interestingly, the mathematical form including a plateau involves an overestimation of both outputs, highlighting an unrealistic improvement of the lateral stability dependent on overestimated density increments in all ROIs.

This analysis confirms the importance of the mathematical formulation through which the adaptation rate and the mechanical signals are correlated. Moreover, it highlights the necessity to compare the numerical results with the experiments in order to understand the optimal strategy. In the present study, the validation discussed in Section 5.4.2.2 highlights both the optimized and linear formulations as suitable to obtain reliable predictions of the observed phenomenon. Thus, the former is kept for sake of simplicity.

5.4.3.3 Zone of Influence

The implementation of a ZOI first has a numerical justification, because it allows considering the mechanical signal that characterizes a defined volume of bone even if the framework relies on values at nodes. However, the ZOI also introduce the interesting concept of the transmission of local mechanical signal all around the stimulated area, through biologi-

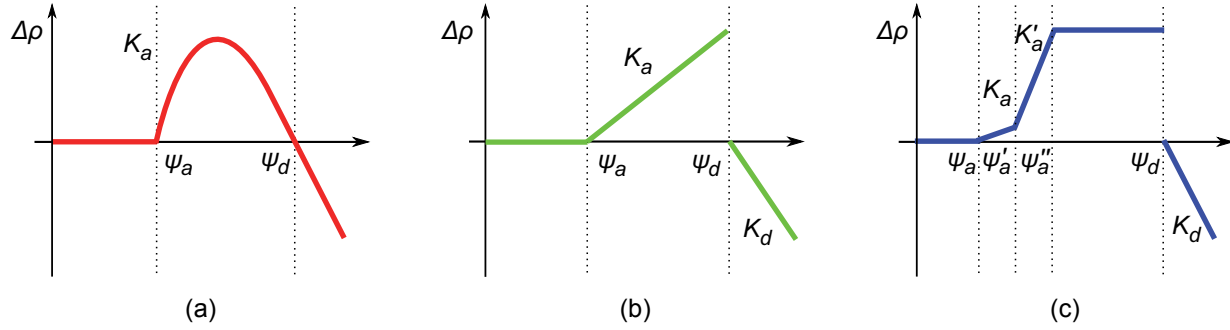


Figure 5.12: Formulations of adaptation rate versus ψ_ϵ : (a) optimized, (b) linear and (c) plateau.

Table 5.3: Adaptation parameters for the comparison of formulations.

Model	Attractor state				Rate constant		
	ψ_a	ψ'_a	ψ''_a	ψ_d	K_a	K'_a	K_d
Optimized	1.25×10^{-3}	-	-	4.51×10^{-3}	1	-	-
Linear	1.25×10^{-3}	-	-	4.51×10^{-3}	1	-	1
Plateau	1.25×10^{-3}	1.5×10^{-3}	1.75×10^{-3}	4.51×10^{-3}	0.05	1	1

Signal: ψ_ϵ . ZOI radius: 0.3 mm, type: gaussian.

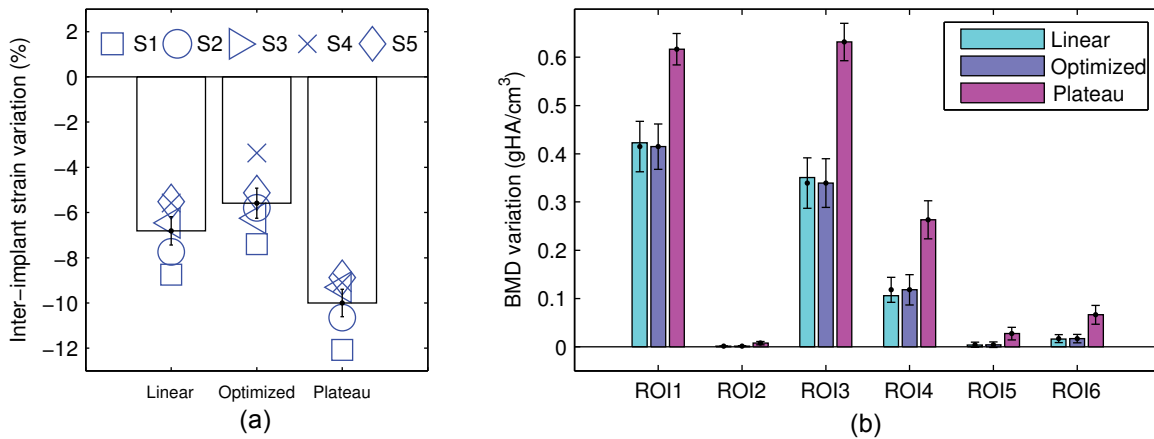


Figure 5.13: Sensitivity of (a) inter-implant strain and (b) BMD in ROIs with respect to the law formulation.

cal processes involving the tissue micro- and cellular-structures. Although the mechanism driving these phenomena are unclear, it is of great interest to investigate the sensitivity of the proposed framework to the ZOI dimensions and decay function (f in Equation 5.9) with a perspective of future multiscale developments.

For this purpose, a parametric study is performed involving a ZOI radius r varying from 0 to 0.9 mm and three weight functions: linear, exponential and gaussian (formulated in Equation 5.17, 5.18 and 5.19 respectively), for a total of 65 iterative computations.

$$f_l = 0.95 \left(1 - \frac{D_{ij}}{r} \right) + 0.05 \quad (5.17)$$

$$f_e = e^{-2.99 \frac{D_{ij}}{r}} \quad (5.18)$$

$$f_g = e^{-\frac{D_{ij}/r}{2\sigma^2}} \quad (5.19)$$

where $\sigma = 0.4085$. These equations compute the decay function f of node j depending on its distance D_{ij} from the main node i . The weight factor ranges from 1 to 0.05 for $D_{ij} = 0$ and $D_{ij} = r$ respectively, while the contribution of nodes outside the ZOI is neglected.

As shown in Figure 5.14, the importance of the ZOI is evident. If the radius is lower than 0.3 mm (i.e. the RVE size is lower than 3 to 5 inter-trabecular lengths) the inter-implant strain increases, notably the models predict a greater resorption because of overloading with respect to apposition. The extreme case of no ZOI (i.e. $r = 0$) provokes a 17 % increase of inter-implant strain. This state corresponds to a reduced inter-implant stiffness which is exactly the opposite of what is found through the experiments. This fact is explained by the sharp stress concentration at nodes in contact with the implants. For radii above the RVE size there is nearly no variation of the inter-implant strain, thus indicating that once the signal is averaged on a consistent volume the solution remains stable. These results are confirmed by the BMD variation shown in Figure 5.14b, where the density increases with the ZOI radius. Interestingly, the effects of different decay formulations on the inter-implant strain are negligible. Small differences affect the BMD predictions in ROIs, but the influence of the radius is predominant.

In summary, the definition of a ZOI is essential to predict results consistent with the experiments. The key factor is the radius, which should at least correspond to the RVE size, while the weight function plays a secondary role. Of course, these results are limited to the treatment of an adaptation signal based on the strain and derived from a macroscale, linear and elastic framework. However, as stress, strain and elastic energy are correlated, a similar trend is expected for these variables.

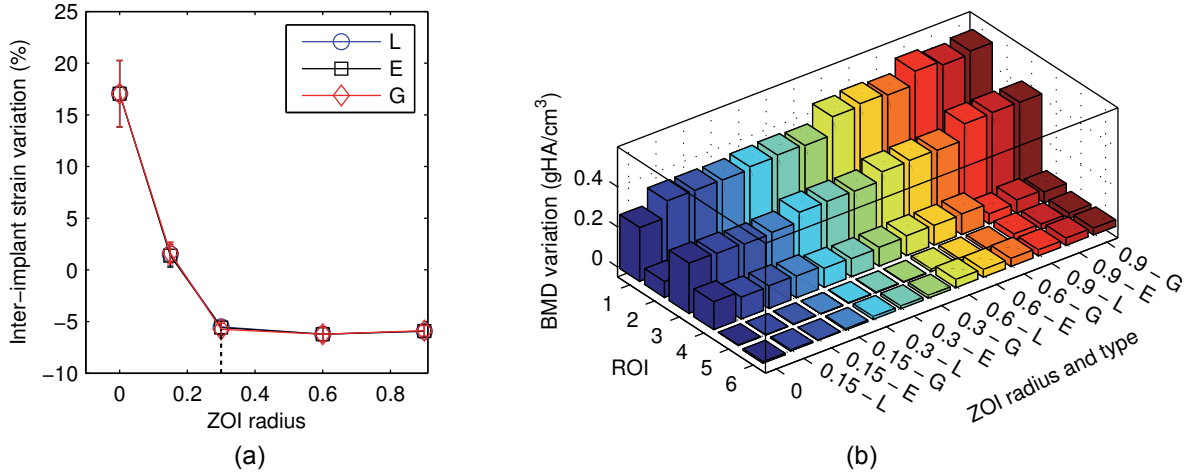


Figure 5.14: Sensitivity of (a) inter-implant strain and (b) BMD in ROIs with respect to the ZOI radius and weight function (i.e. L = linear, E = exponential, G = gaussian).

5.4.3.4 Load level

The external load is the parameter that regulates the mechanical stimulation transferred to the peri-implant bone tissue. In this animal model, characterized by high stress concentrations and risks of local damage, the study of the results' sensitivity to higher loads is interesting in order to investigate the stimulation limits, above which harmful effects are dominant. To explore this dependency, the basal group of specimen-specific FE models is processed with the default adaptive modeling parameters (Section 5.4.2.1) and five load magnitudes, ranging from 3.3 to 10 N, for a total of 25 iterative computations.

The inter-implant strain variation is plotted against the external force in Figure 5.15. The 3.3 N load provokes a weak strain reduction (-3%) nearly doubled by imposing 5 N (-5.5%), that is the results discussed in Section 5.4.2.2 and compared to the experiments. With higher loads, the system stability decreases and the effects of biodiversity are amplified. By applying 6.7 N there is a weak increase of the inter-implant strain ($+3.3\%$) with a result spread that is larger with respect to lower loads. The density variation reported in Figure 5.16 shows an increasing apical resorption because of overloading. At 8.6 N the imbalance between resorption and apposition reaches critical levels for 3 over 5 specimens, that are characterized by the failure of all the tissue surrounding the distal implant (i.e. all analyses where the inter-implant strain deviation overcome $+100\%$ result in complete failures). Nevertheless, two specimens reach a stable converged solution with definitively increased inter-implant strain ($+20\%$). Finally, none of the FE models adapt to the 10 N load: the resorption because of overloading dominates the adaptation mechanism provoking the instability of the distal implant (Figure 5.16).

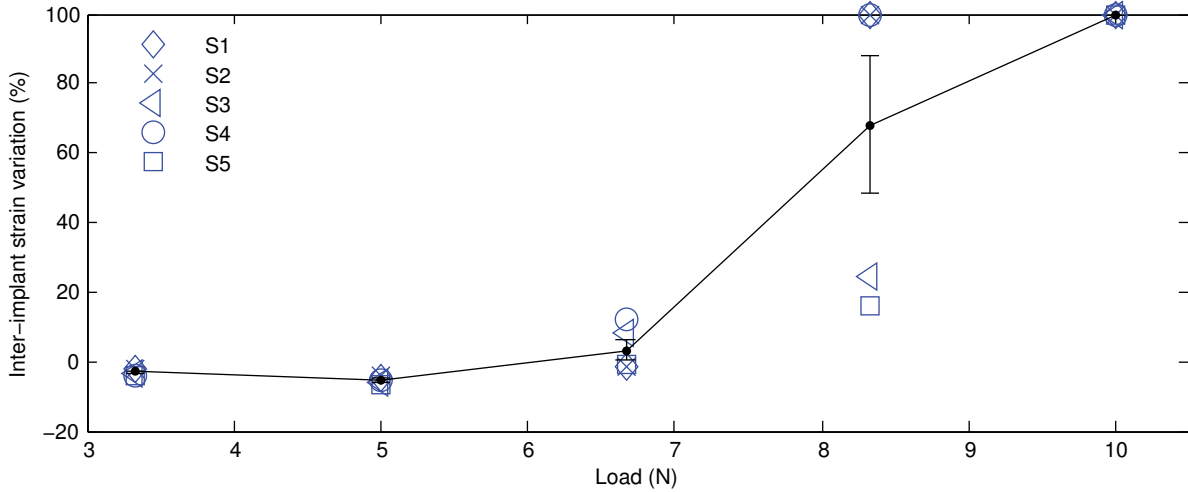


Figure 5.15: Inter-implant strain sensitivity to the external load magnitude.

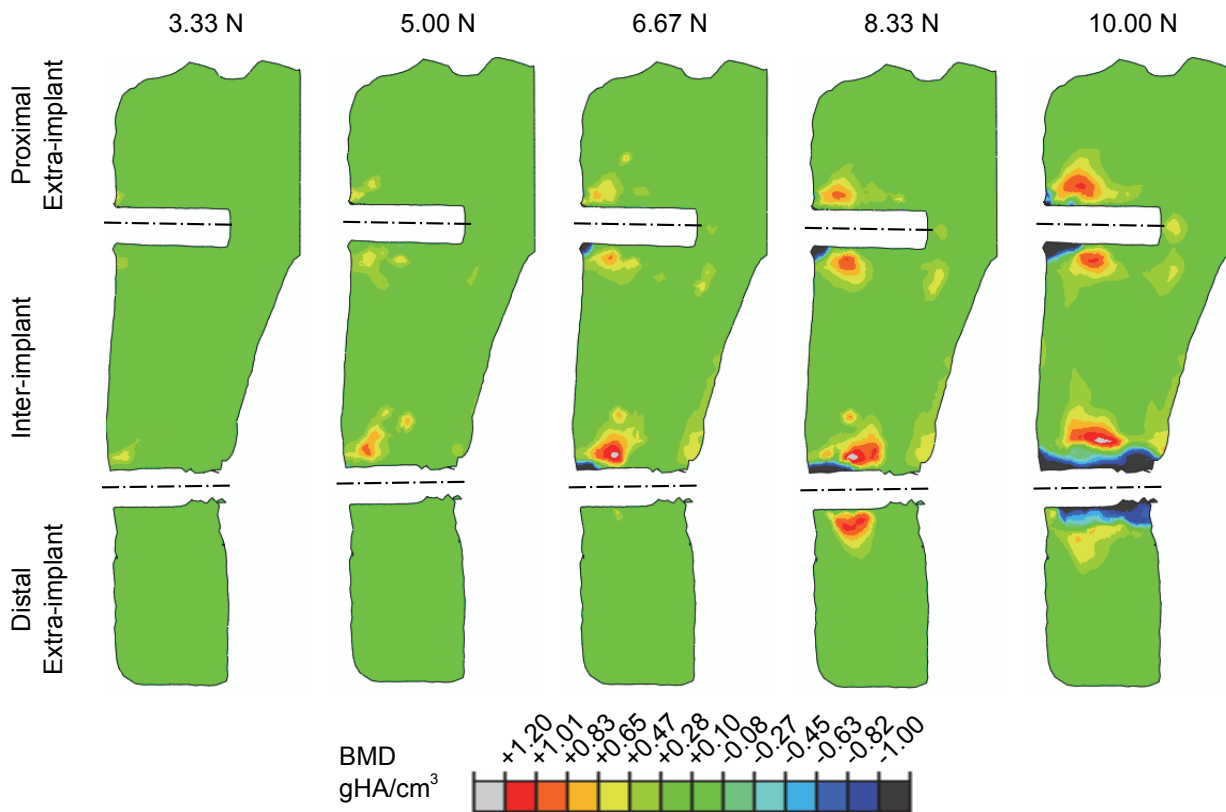


Figure 5.16: BMD field variation with respect to the external load magnitude. Images concern the specimen S3 and increasing loads from left to right. Implants are hidden.

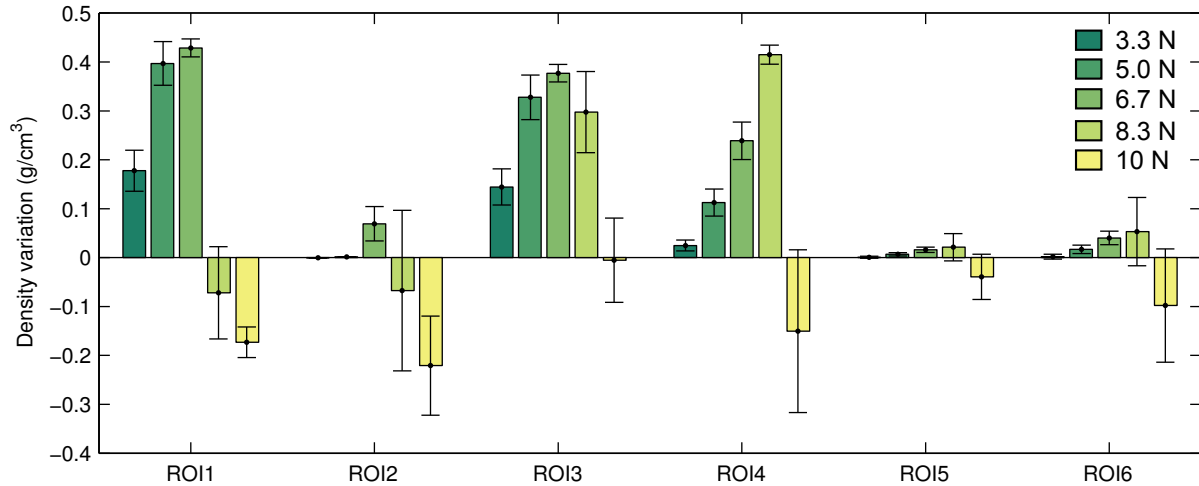


Figure 5.17: *Density in ROIs sensitivity to the external load magnitude.*

The local BMD variation characterizing the ROIs agrees with these results (Figure 5.17), but few differences deserve attention. In case of lower loads (i.e. 3.3 and 5 N) the BMD variation mirror the implants stability showing an increase of density that is correlated to the reduction of inter-implant strain.

Interestingly, the BMD increases also with higher loads (i.e. 6.3 and 8.7 N) while these external stimulations cause harmful effects on the implant lateral stability. This mismatch depends on the zone where the damage propagation occurs, that is not perfectly captured by the selected ROIs, but it depends also on the increase of bone volume affected by bone augmentation. Thus, it is worth noticing that the implants stability and the BMD variation in the selected ROIS are not correlated if high loads are considered.

Although this analysis does not account for eventual fatigue cracks or inflammatory reactions taking place in case of critical overloading (e.g. callus and swelling), several interesting conclusions can be drawn. The proposed approach is really sensitive to the load magnitude and allows investigating the potential of the considered animal model. The range of external forces generating a positive effect on integration (i.e. augmentation of peri-implant density and improved implant stability) is really narrow, indeed with 3.3 N the bone reaction is quite limited while at 5 N the optimum is yet reached. Higher loads provoke larger increases of BMD associated with dangerous peri-implant bone loss because of overloading. This condition is to be avoided in particular because of its possible interaction with the cortical bone loss caused by the animal daily activity discussed in Section 4.3. Moreover, these results highlight the potential of the proposed methodology to predict subject-specific bone adaptation to critical overloading.

5.4.3.5 Summary

The sensitivity studies presented in previous paragraphs underline the influence of the attractor states, the law formulation, the ZOI and the external load on the numerical predictions. Both the implants' lateral stability and bone density are clearly affected by these parameters.

A summary of these analyses is shown in Figure 5.18, where the effects of the perturbed parameters are ordered in relation to their influence on the inter-implant strain and on the maximum BMD variation in ROIs. The reference values for both variables are calculated with the optimized settings (Load = 5 N, Table 5.2). For the sake of clarity, a color code is adopted to differentiate the type of perturbation. Interestingly, the perturbations' rankings on the x-axes of Figure 5.18a and b are different, which means that the inter-implant strain and the BMD predictions react differently. Moreover, a precise color pattern is not visible (i.e. the histograms' bars are not grouped by colors). Indeed, none of the investigated parameter clearly outnumbers the others. However, the higher variations of both the inter-implant strain and BMD in ROIs are generated by an increase of the external load (10 N).

Figure 5.19 blends the results of Figure 5.18a and b, with a color code that differentiates the affected output (i.e. inter-implant strain or maximum BMD in ROIs). The remarkable range of variation on the y-axes, which reach three orders of magnitudes, highlights the different effects provoked by the investigated perturbations. This differentiation allows classifying the considered parameters in three categories:

Critical. This category includes the load overestimation (external load = 10 N, Section 5.4.3.4) and the absence of ZOI (radius = 0 mm, Section 5.4.3.3), which provoke more than 100% variation of both inter-implant strain and BMD in ROIs. If these parameters are not considered or wrongly implemented, the numerical predictions can be totally inconsistent, as shown in Figure 5.16 and Figure 5.14a. The ZOI should be set at least equal to the RVE size.

Important. This typology includes the perturbations provoking variations between 100 % and 10 %, i.e. the attractor states' modulation (Section 5.4.3.1), the piecewise law formulation with a plateau (Section 5.4.3.2), the load underestimation (external load = 3.3 N, Section 5.4.3.4) and the ZOI radius overestimation (radius = 0.9 mm, Section 5.4.3.3). An ambiguous implementation of these parameters does not provoke incoherent solutions, but the results are inaccurate. At least, the attractor states should be identified on experimental data from studies on physiological stimulations.

Negligible. This category involves the linear law formulation (Section 5.4.3.2) and the formulation of the decay function that weights the stimulus of nodes belonging to the ZOI (linear or exponential form, Section 5.4.3.3). These perturbations scarcely

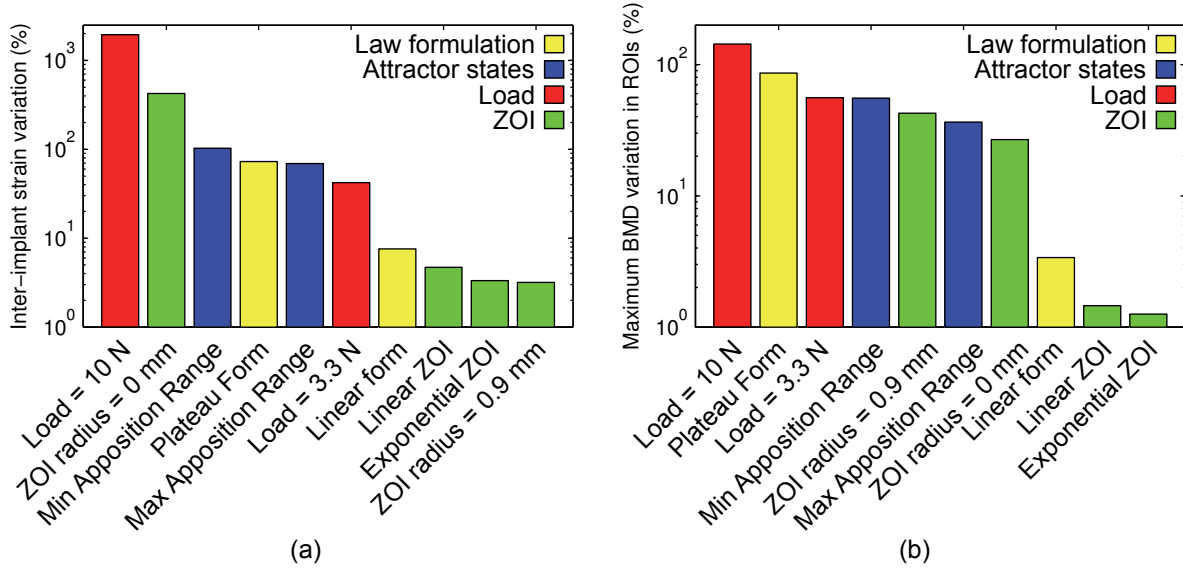


Figure 5.18: Sensitivity of (a) the inter-implant strain and (b) the maximum BMD in ROIs plotted in descending order against the perturbed parameters. The color code groups the perturbations that concern the same parameter. The variations are calculated with respect to the results obtained with optimized settings (Load = 5 N, Table 5.2).

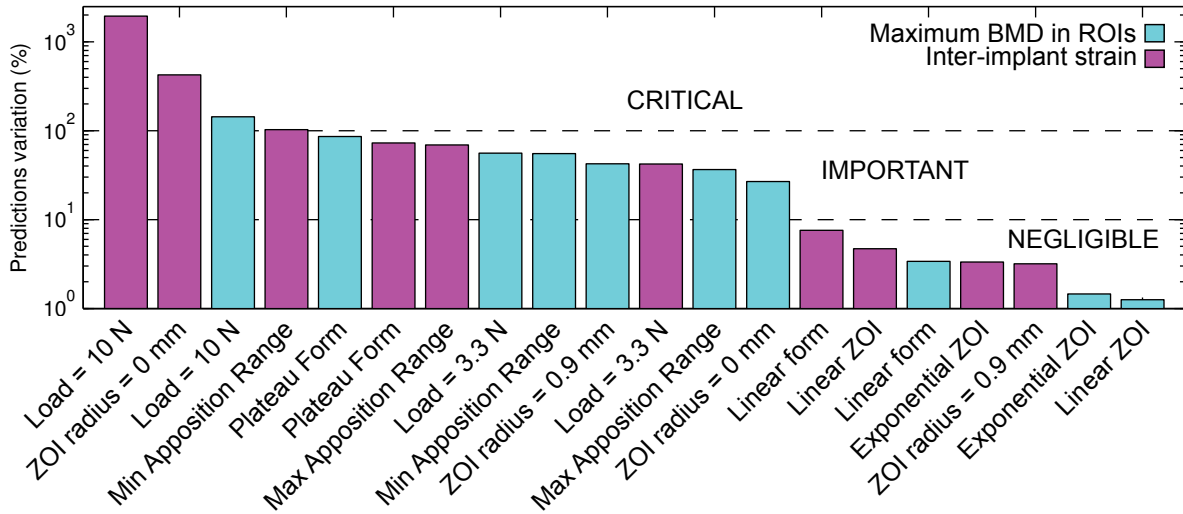


Figure 5.19: Ranking of the effects of perturbations on the numerical predictions. The color code groups the perturbations that concern the same output. The variations are calculated with respect to the results obtained with optimized settings (Load = 5 N, Table 5.2).

affect both the inter-implant strain and the BMD predictions, thus their influence is negligible.

This analysis exhaustively describes the robustness of the proposed numerical framework. Moreover, the classification of the parameter's influence on the numerical predictions is a reference point for the development of similar numerical approaches.

5.5 Musculoskeletal loading

As described in Section 1.4.2, the bone mechanical adaptation theories are employed for various applications. In the previous sections these approaches are adopted to investigate the tissue adaptation to a non-physiological mechanical environment induced by loading the implants. The goal of the analysis is the prediction of the mechanically induced BMD variations assuming that the initial bone structure is not optimized to support the external loads.

This section focuses on the 'internal' loads, which are the musculoskeletal loads characterizing the animal daily activity. The gait based loading condition (Section 4.3.1) is applied to a whole tibia and processed with the proposed adaptation framework to verify an assumption slightly different from the previous one. In details, it is assumed that the tibia structure is optimized to support the proposed gait-loads and the generated strain is sufficient to preserve the initial density field, thus provoking negligible BMD variations due to disuse or overloading.

5.5.1 Methods

The mCT scans of a whole tibia are processed to generate a specimen-specific FE model as described in Chapter 3. The size of this FE model is ~ 4 times larger than the ones processed for the investigations on the external loads, thus requiring a notably increased computational time. For time reasons, only one specimen is investigated in this section in full awareness that the results are affected by the variability discussed in the previous sections.

The nodes belonging to a spherical region of 0.5 mm radius surrounding the anchorage points of the musculoskeletal forces are excluded from the adaptation process to avoid the propagation of effects due to unrealistic stress concentrations. The ψ_ϵ -based approach presented in Equation 5.16 is employed with the parameters discussed in Section 5.4.2.1, here reported for sake of completeness: $K_r = K_a = 1$ (gHA/cm³)/(time unit), $\psi_r = 0.312 \times 10^{-3} \epsilon$, $\psi_a = 1.250 \times 10^{-3} \epsilon$ and $\psi_d = 4.510 \times 10^{-3} \epsilon$.

Two benchmarks are implemented. Firstly, a bare tibia is processed to highlight the model capability to preserve the initial structure. Secondly, the implants are inserted

in~silico and the cortical bone loss due to disuse, identified in Section 4.3.4, is investigated.

5.5.2 Bare tibia

The percentage of nodes showing not-null adaptation error is plotted against the iterations in Figure 5.20a. A relevant amount of nodes are characterized by an octahedral shear strain not compatible with the LZ at the beginning of the simulation (40 %). Nevertheless, the analysis reaches the convergence without problems and the overall tibia density is correctly preserved, as shown in Figure 5.20b. The resorption and apposition occurring in the epiphyses mostly depends on modeling simplifications concerning the loads' attachment points. Indeed, all musculoskeletal loads are represented through punctual forces applied to single nodes. In the proximity of the joints (i.e. ankle and knee), these hypotheses generate inaccurate strain patterns and BMD variations, because in these areas the loads are actually transferred through wide contact areas. On the contrary, the structure of the diaphysis is well preserved, showing only a slight increase of density that characterizes the proximal bone and a small area of the midshaft resorbed because of disuse.

Although this analysis involves only a single physiological loading environment (i.e. others daily activities may provoke different deformation fields), the results confirm the pertinence of both the gait-based loading condition and the proposed adaptation algorithm.

These results can be of great interest in several fields of investigations involving the rat tibia. As a matter of fact, this framework provides a novel representation of the rat tibia's mechanical homeostasis within the range of the Lazy Zone, thus providing an interesting benchmark to analyze the bone daily maintenance process (i.e. remodeling). Moreover, this system can help to quantify the local effect of treatments (e.g. systemic treatments) by identifying the area where the combination of mechanical loads and medicaments generates the best (or worse) results. Furthermore, this framework can be developed to include fracture healing processes and optimize the studies on bone defects.

In conclusion, this benchmark provides a novel reference for investigations on all kinds of perturbations of the tibia homeostasis. In this context, the attention is focused on the perturbation caused by the presence of the implants belonging to the 'loaded implant' model.

5.5.3 Cortical bone loss

The peri-implant bone adaptation to the gait-based loads is investigated to compare numerical predictions with the cortical bone loss due to disuse presented in Section 4.3.4. The optimized adaptation approach is implemented with two resorption attractor states. Firstly, the attractor state $\psi_r = 0.312 \times 10^{-3} \varepsilon$ is considered, thus imposing the LZ width

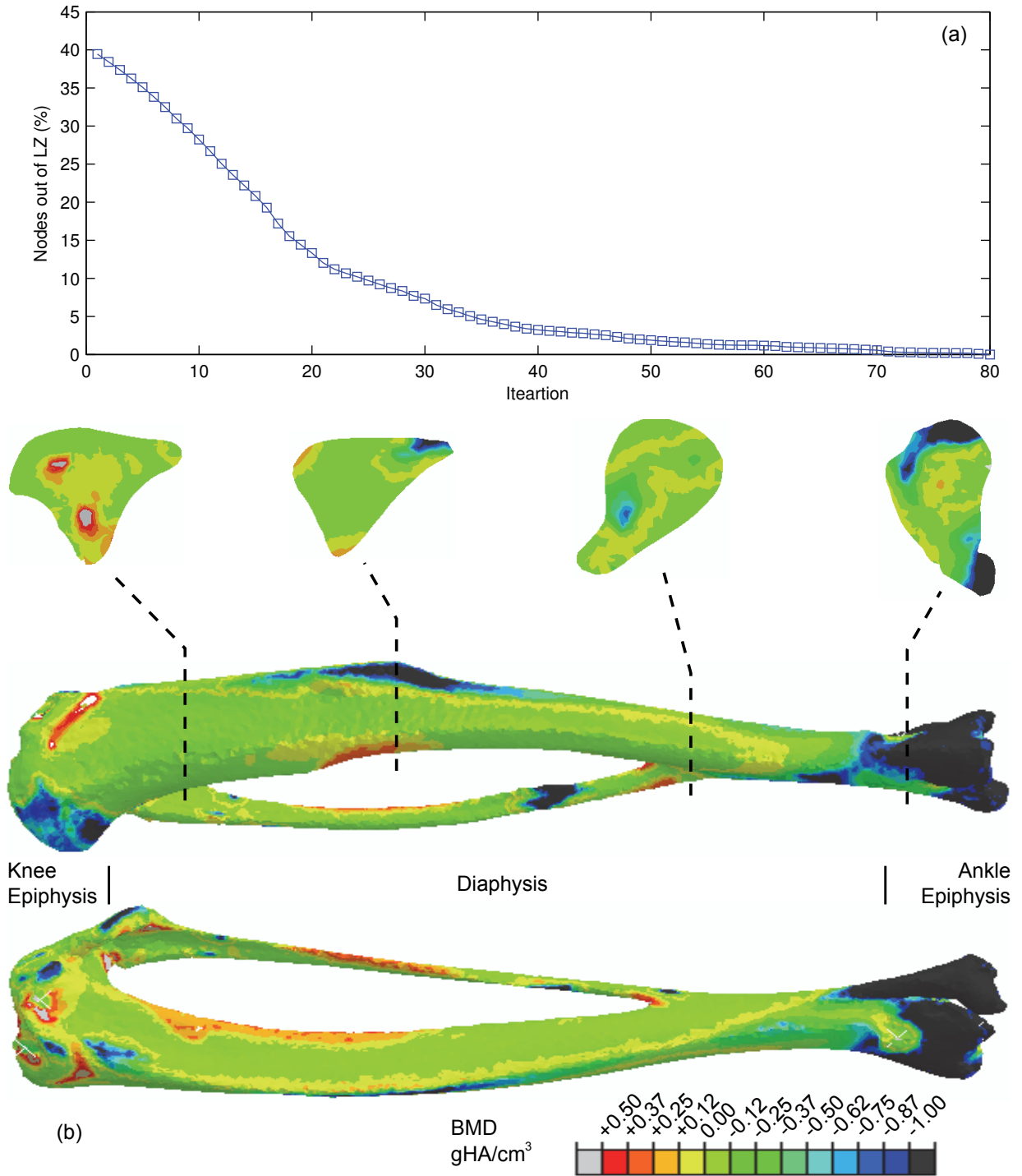


Figure 5.20: Whole tibia subjected to gait-loads and processed with the ψ_e -based adaptation algorithm: (a) percentage of nodes showing not-null adaptation error plotted against the iterations and (b) BMD field variation.

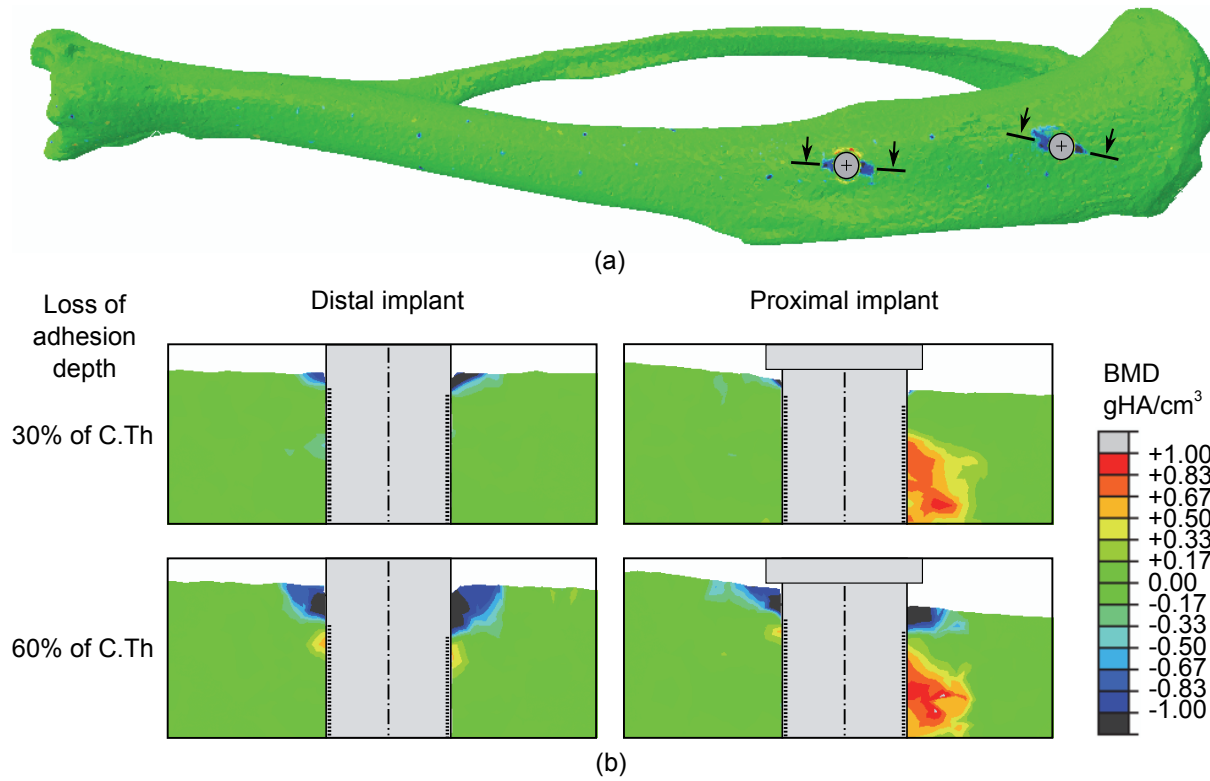


Figure 5.21: Prediction of bone resorption due to the loss of bone-implant adhesion. The BMD variation calculated with $\psi_r = 0.6 \times 10^{-3} \epsilon$ is shown in (a) top view of the whole tibia and (b) cut view along the planes where the resorption is maximized for both implants and both loss of adhesion depths (i.e. 30 and 60 %).

that provides consistent results with the bare tibia. Secondly, a location-dependent attractor state $\psi_r = 0.6 \times 10^{-3} \epsilon$ is implemented, thus assuming that the resorption characterizing the peri-implant cortical tissue is driven by local peak strains. Indeed the assigned value corresponds to the lower peak strain measured in~vivo on the surface of rat tibiae' diaphysis during normal locomotion (Rabkin et al., 2001). In this case the adaptation process is limited to the implants' surrounding to avoid unrealistic resorption and solution divergence.

As described in Section 4.3.2, the implants are inserted in~silico into the whole tibia proximal segment and the distal implant's threaded end is reduced to a cylinder with tied contact to the cortical bone. Since the cortical bone loss depends on the loss of bone-implant adhesion (Section 4.3.4), two FE models are generated with discrete opening depths (i.e. bone-implant opening) corresponding to 30 and 60 % of the cortical thickness, respectively. Despite the simplification of the debonding mechanism, these boundary conditions provide consistent stress fields (Figure 4.7). A perfect adhesion is implemented for

the remaining interfaces.

Interestingly, with $\psi_r = 0.312 \times 10^{-3} \epsilon$ none of the models show apical resorption, thus implying that the peri-implant bone tissue within this area is characterized by an octahedral shear strain sufficiently high to fit into the LZ. On the contrary, the simulations characterized by $\psi_r = 0.6 \times 10^{-3} \epsilon$ show the funnel shaped cortical bone loss observed in the experiments (Figure 5.21). The decrease of BMD follows the loss of adhesion depth confirming the correlation between these phenomena. Moreover, an increase of BMD characterizes the trabecular bone in the proximal direction, thus highlighting an adaptation of the tissue to the variation of strain field due to the presence of the implant, even if no external load is delivered.

These results confirm the assumption that the funnel shaped cortical loss observed experimentally is caused by resorption due to disuse, occurring after a loss of bone-implant adhesion along the longitudinal direction. This configuration is predicted by the presented framework with a location-dependent resorption attractor state that raises interesting observation.

It is worth noticing that this phenomenon characterizes a significant percentage of specimens ($\sim 40\%$ in Series 2 after 6 weeks, Section 2.4.2) but not the majority of the examined population, indicating that the peri-implant mechanical environment is often sufficient to avoid or delay the apical resorption. Moreover, the numerical framework accounts for a single loading condition representative of the gait, while other daily activities generating different deformation patterns are ignored because of the lack of musculoskeletal data. Furthermore, the simulations are based on a discrete loss of bone-implant adhesion, which consists in a drastic simplification of the gradual debonding process actually taking place. Finally, the relative movements between bone and implants are neglected while several studies highlight the importance of the interface's micromotions (e.g. Stadelmann and Pioletti, 2012).

As a consequence, it is worth noticing that the observed phenomenon is probably too complex to be entirely explained through the proposed approach, and a clear discrimination between the results obtained with the resorption attractor state dependent or not on the location is difficult. Nevertheless, this benchmark offers a solid reference for further development of these themes, for example by introducing a contact model for progressive debonding.

5.6 Multi-load model

In previous sections the dependency of integration on two mechanical environments has been discussed: the 'external' stimulation transmitted to the bone tissue through the implants and the 'internal' stimulation mimicking the animal daily activity, in particular the

gait movement. Both analyses provided interesting results validated through comparison with experiments. Nevertheless, they have been investigated separately while they actually influence simultaneously the bone structure. Although these loading conditions are not applied at the same time (i.e. during the external stimulation the rats are anesthetized and muscles are relaxed), the bone structure is stimulated daily through both of them. Indeed, the mechanical adaptation observed experimentally is the result of a biological reaction triggered by a combination of internal and external stimulation.

The interaction between loading environments is discussed in this section by implementing an adaptation analysis based on the FE model of a whole tibia with *in-silico* implants and subjected to the external and internal loading conditions. As shown in Figure 5.3 a small elastic modulus is assigned to the region of the implants in contact with cortical bone in the distal and proximal directions to avoid unrealistic transmission of tensions. To optimize the computational costs, the deformation patterns generated individually by each loading condition are calculated through the *Multiple load case analysis*⁴ of ABAQUS-Standard[®]. Then, the signals generated by the gait-based loading condition and to the implants activation are blended assuming that the bone adaptation is driven by the daily deformation peaks, calculated at each node through Equation 5.8. Finally, the algorithm presented in Figure 5.2 is implemented with the optimized approach of Equation 5.16 and the parameters presented in Table 5.2. The default ZOI of radius $r = 0.3$ mm and gaussian decay function is considered.

The initial and final (i.e. once convergence is achieved) BMD fields are shown in Figure 5.22. The overall BMD variation correspond to the one observed in the bare tibia (Figure 5.20) with pronounced resorption characterizing the epiphyses and a good preservation of the diaphysis. On the contrary, the adaptation to the external loading is clearly visible between the implants, where the bone tissue is subjected to compression. In agreement with the experiments (Figure 2.11), the local increase of BMD mostly characterizes the distal implant and reproduces the shape observed in mCT scans of stimulated specimens (Figure 2.12). In the processed specimen the density variation is less evident near the proximal implant. As a matter of fact, the BMD variations in this region are generally less pronounced and nearly negligible in some specimen (e.g. last specimen to the right in Figure 5.8). Concerning the implants lateral stability, the calculated density adaptation generates a 7.1 % reduction of the inter-implant strain compatible with both experimental and numerical results previously discussed (Section 5.4.2.2).

Although important parameters as the number of cycles or loading frequencies are neglected⁵, these results confirm that the signal blending based on the peak stimulus at nodes is compatible with the proposed animal model investigations. Moreover, the agreement

⁴Abaqus Analysis User's Manual, 6.1.3 Multiple load case analysis

⁵It is assumed that loading at 1 Hz, 900 cycles/day leads to the saturation of cells mechanosensitivity.

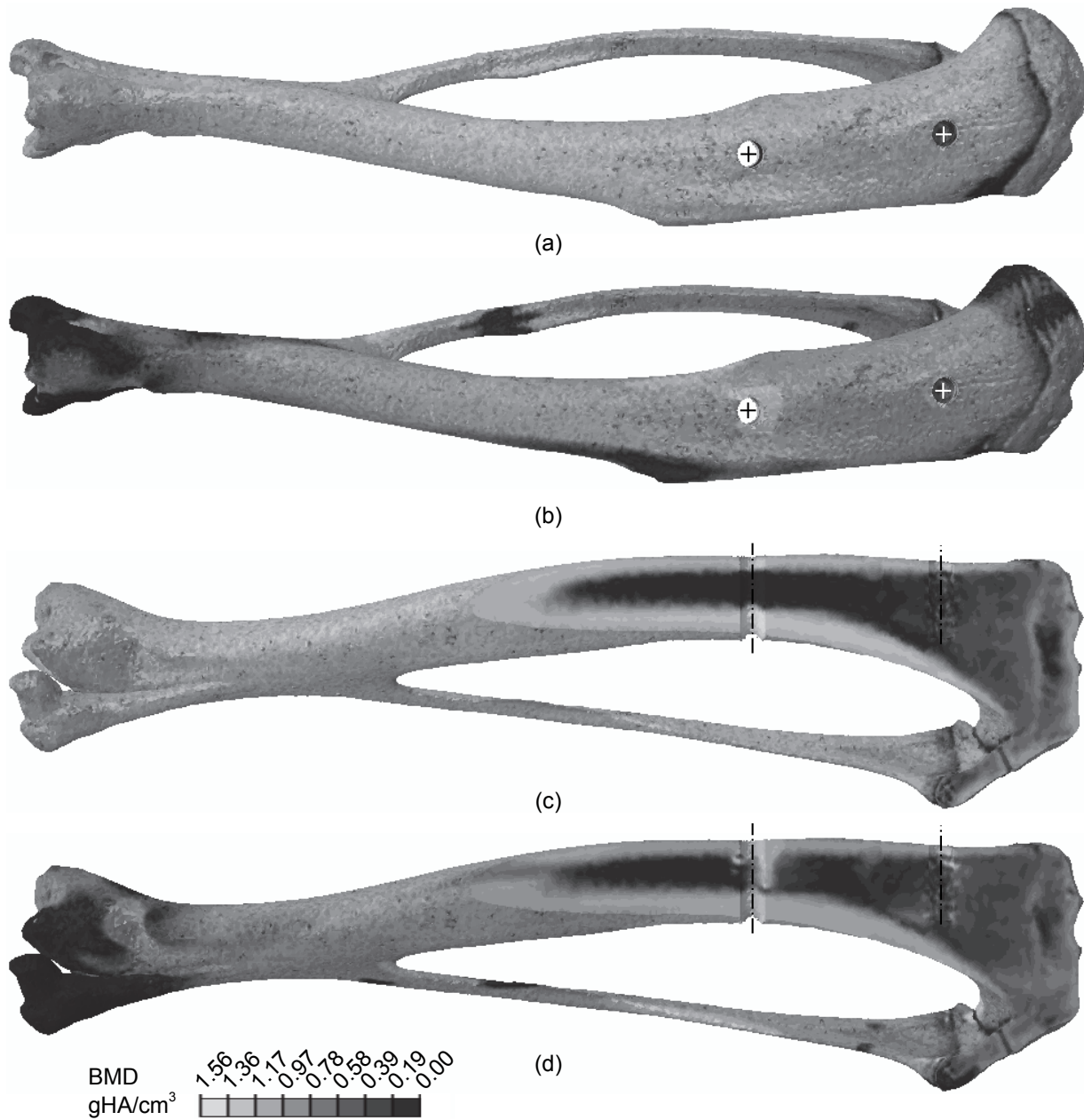


Figure 5.22: BMD field predicted with the multi-load approach. Top view of the whole tibia: (a) initial field and (b) converged field. Inter-implant view cut: (c) initial field and (d) converged field. Implants are hidden. A grayscale color map is chosen to facilitate the comparison with mCT images.

between the outputs of the multi-load approach and the analysis of the single loading conditions confirm the previously adopted modeling assumptions. Finally, the results shown in Figure 5.22 represent the mechanical homeostasis characterizing the ‘loaded implant’ model. As a matter of fact, this model is a rare examples of realistic application of the Mechanostat theory involving an implanted bone, the whole range of signal (i.e. resorption due to both disuse and overloading, homeostasis and apposition because of overload) and both external and internal stimulations (i.e. implants activation and daily activity).

5.7 Conclusions

The proposed bone adaptation framework has been shown to be robust and versatile, it allows processing several specimen-specific FE models with a signal blending and volume averaging that satisfies the continuum hypothesis and the overall dimensions of the observed phenomenon. Although the implemented literature-based theories produce inaccurate outputs, the optimized approaches based on the physiological range of octahedral shear strain (Chapter 4) provides qualitatively and quantitatively accurate results:

- Concerning the external stimulation, the agreement between the numerical and experimental findings is considered excellent. The predictions of both local and overall density variations, as well as the implants' lateral stability, are reliable. The results include verification, validation and sensitivity studies, and the scientific relevance of these findings can lead to interesting improvements in research field involving the effects of overloading on bone defects around dental implants and for the development of therapies for bone augmentation through controlled mechanical stimulation.
- Concerning the internal stimulation, the bone mineral density of a whole tibia is preserved when the gait-based loads are applied, thus supplying a mechanically sound framework to investigate the remodeling process characterizing bare rats' tibiae, which are currently adopted in several studies on implants integration or bone diseases. The results of this approach applied to the 'loaded implant' model confirm the assumption that the funnel shaped cortical loss observed experimentally is caused by resorption due to disuse, occurring after a loss of bone-implant adhesion along the longitudinal direction. This original finding expands the knowledge on clinically relevant peri-implant bone defects, and shows the ability of *in-silico* approaches to predict complex adaptation phenomena. Finally, the multi-load approach combines the contribution of both loading conditions through the assumption that the bone adaptation is driven by the local peak signals.

Chapter 6

Longitudinal study: proof of concept

6.1 Aim

A pilot in~vivo longitudinal study has been carried out at AO Research Institute Davos¹ in collaboration with the Division of Bone Diseases² of the Geneva University Hospitals and Faculty of Medicine. The study involves Ti-coated aluminum implants and stimulated animals monitored through in~vivo, time-lapsed mCT scans.

The main goals of this pilot experiment are the following:

- Upgrade the ‘loaded implant’ model to perform in~vivo longitudinal studies and achieve information on the implants integration history of single specimens.
- Adopt Ti-coated aluminum implants to reduce the x-ray artifacts due to metal components and grant the possibility to investigate the bone-implant interface.

¹CT imaging, Biomedical Services, Clavadelerstrasse 8, 7270 Davos, Switzerland.

²Department of Internal Medicine Specialities, Geneva University Hospitals and Faculty of Medicine, Geneva, Switzerland.

6.2 Introduction

The experiments presented in Chapter 2 are based on validated procedures relying on titanium implants processed with optimized surface treatments. These implants ensure biocompatibility and provide an osteogenic substrate to the bone tissue, thus allowing statistically relevant test campaigns. Nevertheless, the titanium involves strong artifacts when specimens are processed through mCT scanners (Section 3.4.2): this drawback hampers the study of the bone-implant contact, which is a key factor of integration.

Moreover, the analysis of bone adaptation presented in Chapter 5 highlights the dependency of implants integration on the interplay of two loading conditions (i.e. daily activity and external loading). Although it is possible to analyze the effects of each factor separately, the understanding of their interaction in a single individual is limited by the lack of knowledge concerning the integration history of each specimen.

These remarks underline the necessity to upgrade the ‘loaded implant’ model by performing longitudinal mCT studies with radiolucent implants, which allow investigating specimen-specific integration histories and the bone-implant interface. The pilot study presented in the following is a step towards this goal.

6.3 Methods

The study is performed on three female Sprague Dawley rats, 42-weeks old at the onset of the experiment (weight: 382 g, 405 g and 415 g). The *in-vivo* mCT procedure imposes the alignment of the animal limb along the rotation axes of the scanner. As discussed in Section 3.4.2, this alignment entails the generation of strong metal artifacts if titanium implants are employed (Figure 3.5b).

Thus, new implants are produced with aluminum EN AW-7075 T6 coated with a thin layer of pure titanium (thickness: 40-50 nm, RISystem³). The coating is obtained through plasma enhanced chemical vapor deposition and enhances the implants biocompatibility (Li et al., 2012). The lower density of aluminum reduces the x-ray discrepancies characterizing metal components and provides enough mechanical resistance to bear the external load (verified by FE analysis).

The diameter of the cylindrical implant’s surfaces is increased to 1.03 mm to enhance the press fit and improve the primary stability. The implants are placed in the right tibiae of the animals and an injection of antibiotic is administered (Cefovectin 8 mg/kg SC, 2 weeks duration). After surgery, analgesics are administered for three days (Buprenorphin 0.1 mg/kg SC and Paracetamol 210 mg in 100 ml of drinking water). The three animals are subjected to the same schedule as in Series 3: 2 weeks of integration and 4 weeks of

³RISystem AG, Talstrasse 2A, CH-7270 Davos Platz.

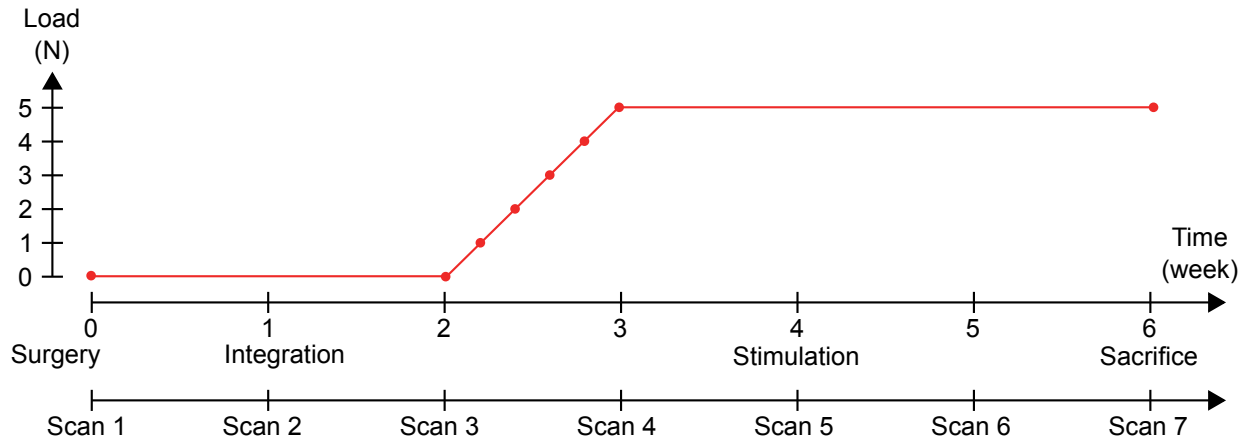


Figure 6.1: Loading and scanning schedule adopted in longitudinal mCT analysis.

stimulation at 5 N (1 Hz sinusoidal cycle, 900 cycles/day, 5 days/week) with a progressive increase of loading during the first week (1 N/day).

The evolution of integration is monitored through weekly scans performed with a high-resolution CT imaging system (VivaCT-40, Scanco Medical AG, Brüttisellen, Switzerland). The stimulation and scanning schedule is reported in Figure 6.1.

6.4 Results

All specimens underwent the entire stimulation period and in~vivo mCT schedule. Post-operative care (i.e. wound cleaning and disinfection) was required during the experiment to heal inflammations and infections. Although this handling led to an additional stress factor for the animals, none of the implants were lost. The implants placement was good and compatible with previous series. The mCT images (Figure 6.2, Figure 6.3 and Figure 6.4 for Specimens 1, 2 and 3 respectively) are excellent: x-ray artifacts are definitively reduced with respect to scans of titanium implants (Figure 3.5b). The specimen-specific integration histories indicate the following:

Specimen 1 (Figure 6.2). Both implants are correctly placed during surgery and the primary stability is granted by the press fit (Figure 6.2a). After the integration period (2 weeks, Figure 6.2b), the proximal implant is well integrated while the bone-implant interface of the distal one is characterized by a gap indicating a not optimal adhesion. This gap persists with the stimulation and a similar debonding affects the apical tissue of the proximal implant after 6 weeks (Figure 6.2c). The BMD variation in ROIs (Figure 6.5) show an increase where the bone tissue is subjected to compression around the distal implant (ROI1) and a decrease elsewhere.

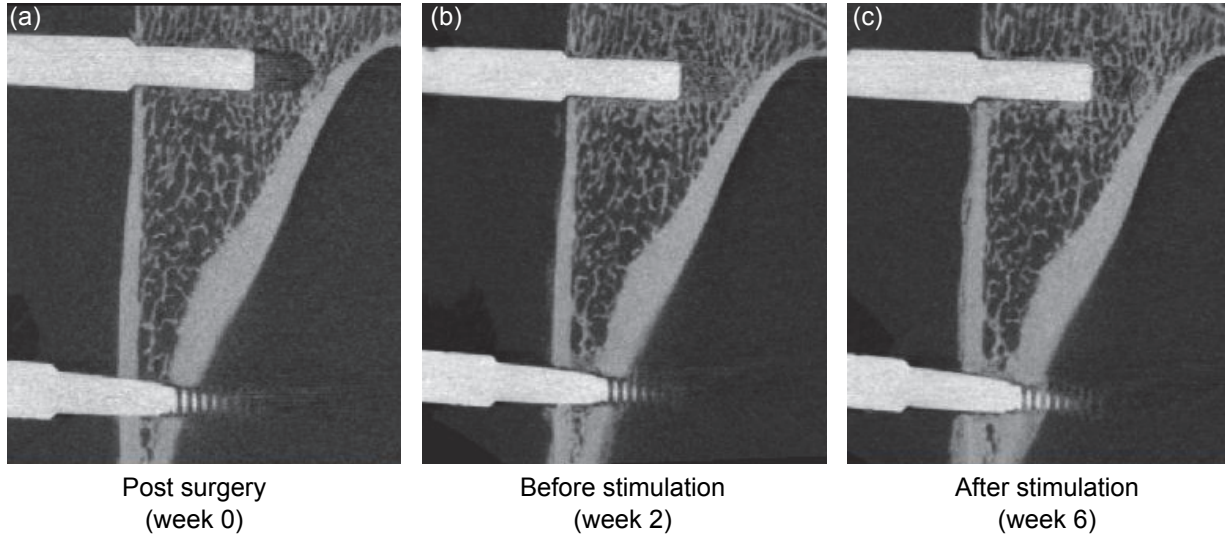


Figure 6.2: Time-lapsed *in-vivo* mCT scans of Specimen 1.

Specimen 2 (Figure 6.3). Both implants are correctly placed during surgery and the primary stability is granted by the press fit (Figure 6.3a). The state of integration before stimulation (Figure 6.3b) is not optimal: an extended area around the proximal implant shows resorption and compromises the implant stability. Moreover, a cortical bone loss occurs around the distal implant. Nevertheless, the specimen supports the stimulation and a strong periosteal reaction is generated around the proximal implant (Figure 6.3c). A loss of adhesion occurs in proximity of the distal implant where the tissue is under traction. BMD increases between the implants, where bone is subjected to compression (ROI1 and ROI3, Figure 6.5)

Specimen 3 (Figure 6.4). The implants are correctly placed during surgery and the primary stability is granted by the press fit (Figure 6.4a). Two weeks after surgery (Figure 6.4b), the proximal implant is well integrated while the initiation of a cortical bone loss is visible around the distal implant. At the end of the stimulation (Figure 6.4c) the distal conic depth is increased and associated with sub-cortical bone apposition. A general increase of BMD is shown in all ROIs around the proximal implant (Figure 6.5) and mostly in ROI1.

The BMD variations in ROIs, calculated as the difference between the end of stimulation (week 6) and the basal state (week 2), are shown in Figure 6.6 and confirm the osteogenic effect of stimulation if applied to well integrated implants. Indeed, Specimen 3 is characterized by a BMD increase in all ROIs and especially the first one. In specimens 1 and 2, which are characterized by a not optimal, pre-stimulation state of integration, the

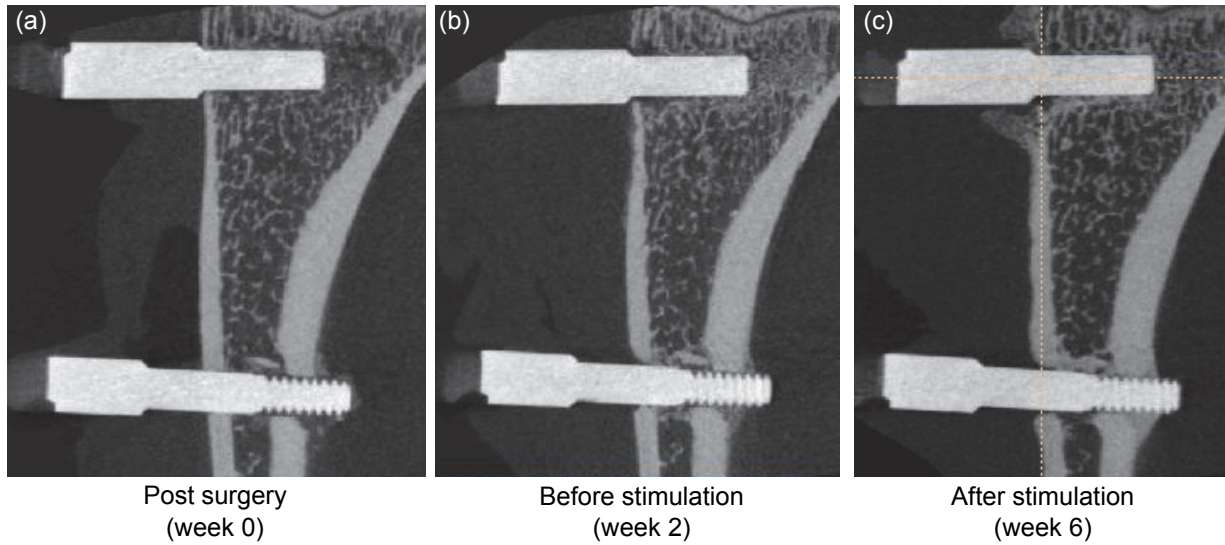


Figure 6.3: Time-lapsed *in-vivo* mCT scans of Specimen 2.

external loading produces an overall BMD reduction, except for ROI1.

6.5 Discussion

The results of this pilot test confirm the compatibility of the ‘loaded implant’ animal model with longitudinal mCT studies. As a matter of fact, the animals well sustain the periodic scanning in addition to the intense stimulation schedule, which implies an increased duration of general anesthesia.

The principal peri-implant features are summarized in Figure 6.7. The gap between bone and implant shown in Figure 6.7b and c underlines a potential lack of adhesion which is probably due to the absence of SLA treatment: with less surface cavities the cell proliferation is reduced. Previous trials highlighted the impossibility to obtain the same roughness of titanium on the surface of Al implants, because the sand-blasting and acid etching protocols (Section 2.2.3) are too aggressive for aluminum. Further investigations could lead to an adequate SLA procedure, which is crucial considering the important role of bone-implant adhesion in this animal model. Despite this drawback, the Ti-coated aluminum implants ensure biocompatibility and that the coating remains intact under loading. This result is an important achievement considering that discontinuities of the coating can expose the aluminum and generate necrosis.

Furthermore, the individual-based longitudinal analysis allows establishing the adaptation history of each specimen, thus providing novel information on the tissue adaptation to the external loading. For example, the periosteal reaction characterizing Specimen 2

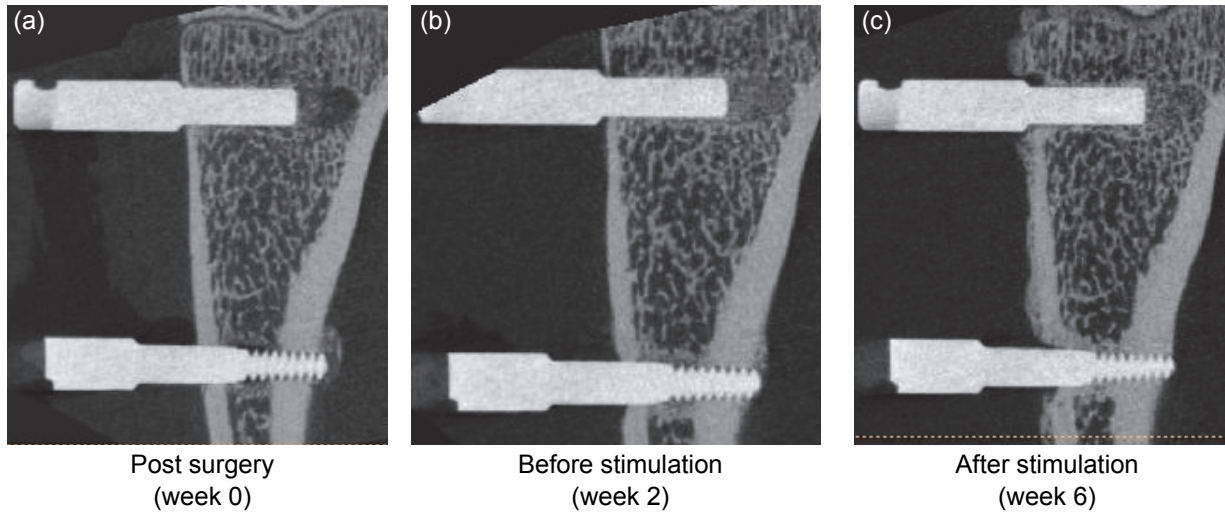


Figure 6.4: Time-lapsed *in-vivo* mCT scans of Specimen 3.

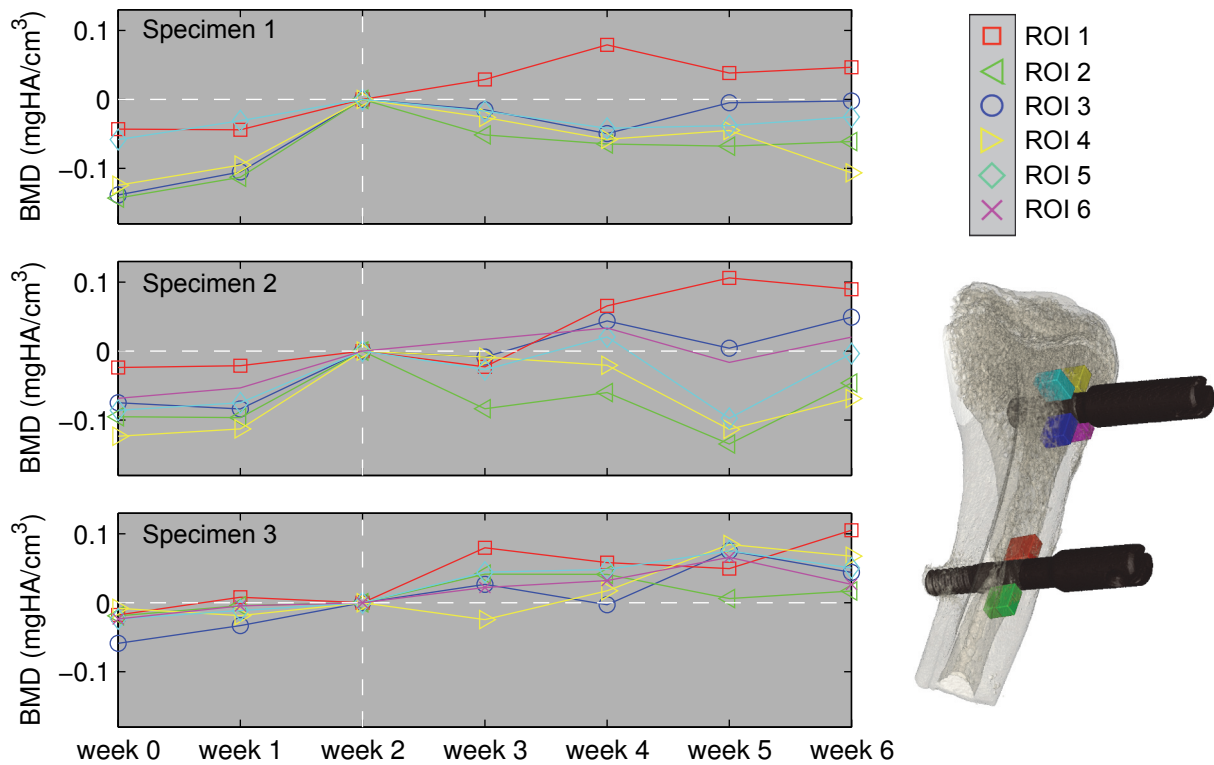


Figure 6.5: BMD variation in ROIs monitored in longitudinal mCT study. Variation is calculated with respect to the basal state (*i.e.* week 2, before stimulation).

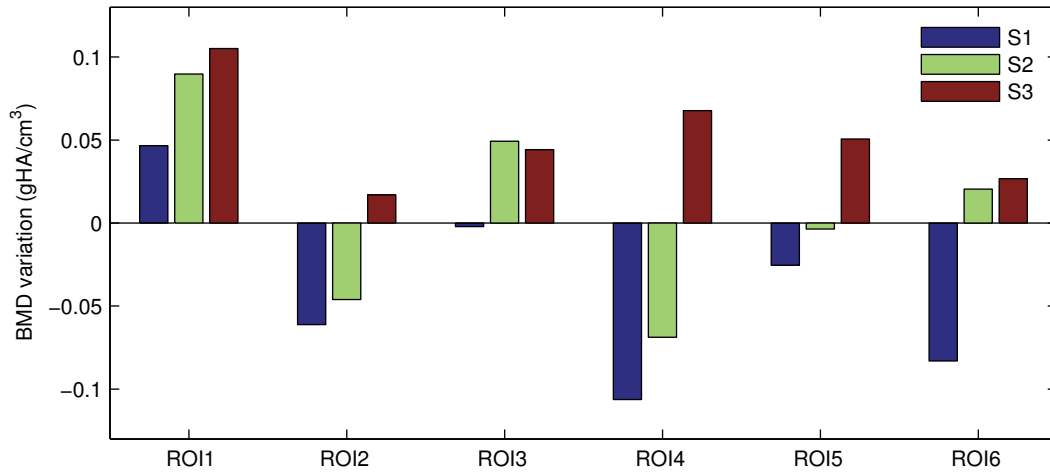


Figure 6.6: *in-vivo* mCT analysis: BMD variation in ROIs calculated as the difference between the end of stimulation and the Basal state.

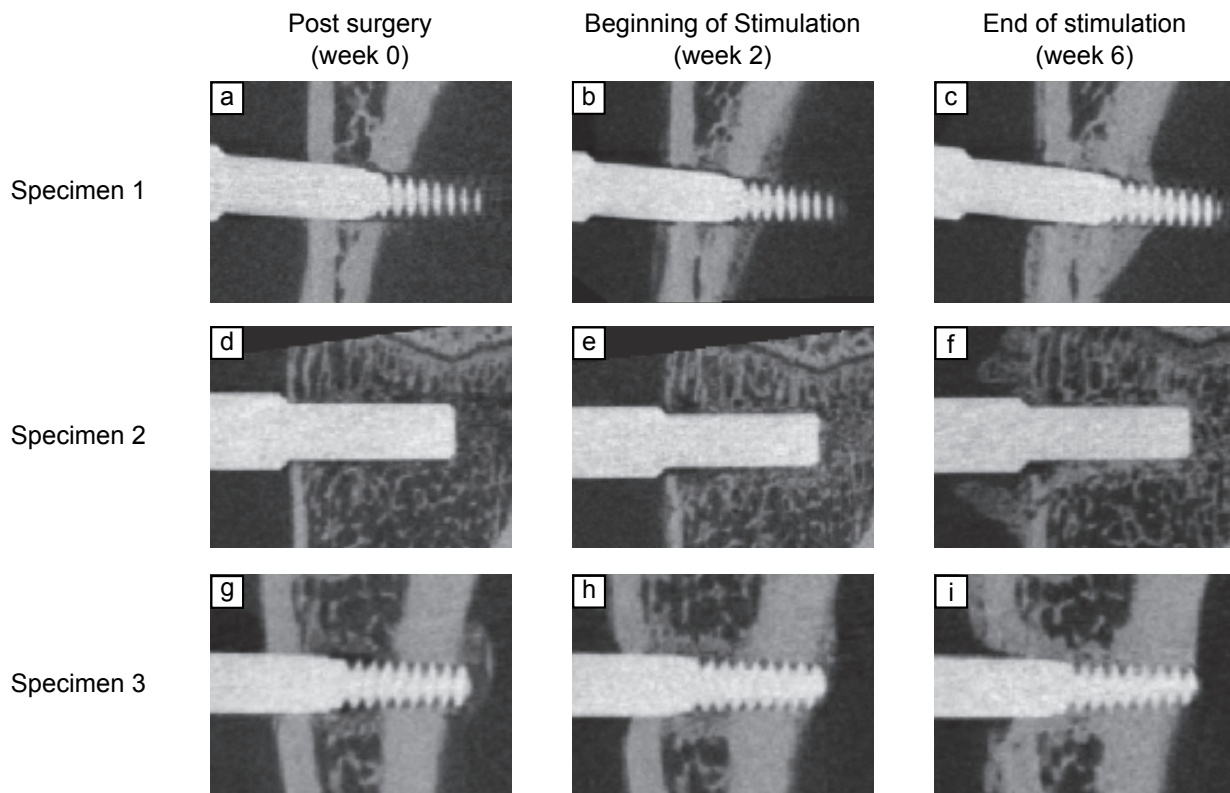


Figure 6.7: *in-vivo* mCT analysis: peri-implant features of specimens implanted with aluminum implants coated with pure titanium. Rows: specimens. Column: time point.

after stimulation (Figure 6.7f) corresponds to the morphologic feature I_A defined in Section 2.3.1.2. The follow up study of this specimen indicates that this strong bony reaction is probably generated because the external loading is applied to a specimen characterized by a weak primary integration (Figure 6.7e). Although this result is derived from a single individual, it provides a logic explanation of a phenomenon already observed in group-based studies.

Moreover, the 2-weeks mCT images of Specimen 3 (Figure 6.4b) are processed with the specimen-specific procedure presented in Chapter 3. Then, the generated FE model is simulated with the optimized algorithm (Section 5.4.2) to predict the adaptation to external loading. The same parameters of group-based simulations are adopted (Table 5.2). Musculoskeletal loads and resorption due to disuse are neglected.

The comparison between the predicted BMD field and time-lapsed mCT scans is shown in Figure 6.8. Numerical analysis predicts an increase of density around the proximal implant and close to the distal implant, mostly where the tissue is subjected to compression (Figure 6.8b). This area is also characterized by resorption due to overloading, which highlights a harmful effect of the external loading on the apical tissue. Due to this bone adaptation, the predicted inter-implant strain increases by 11 %. The predicted BMD field that surrounds the proximal implant matches the mCT scans (Figure 6.8d), while the distal morphology slightly differs from experiments due to the cortical bone loss. Indeed, the tissue around this implant evolves because of the combined effects of the implant loading and the animal's daily activity, while the numerical model does not account for the latter one.

The BMD variations in ROIs are compared to the experimental measurements in Figure 6.9. The trend of numerical predictions match the effects of the *in-vivo* stimulation, which provokes a general increase of peri-implant density, and confirm the efficiency of the previous FE models (i.e. derived from scans of titanium-implanted specimens).

Interestingly, the overestimation of numerical predictions of local BMD variations is increased with respect to Series 3 (Figure 5.9a). This difference may depend on a different reaction to the mechanical stimulation due to the imperfect bone-implant adhesion, which modifies the load's transfer from the implants to the tissue, or the rat age (i.e. this test involves older rats: 42 weeks old versus 27 weeks old in previous series). The investigation of these factors is now possible thanks to the implemented follow-up strategy based on *in-vivo* mCT and Al-implants. With this approach, specimen-specific adaptation parameters (e.g. the attractor states) can be tuned by individual-based analysis of the physiological deformation to improve the accuracy of FE predictions.

Finally, it is worth underlining the most important result of this pilot study: the improved quality of the images obtained with the new implants. Although the specimens' alignment with respect to the scanner axes is not optimal, metal artifacts are absent

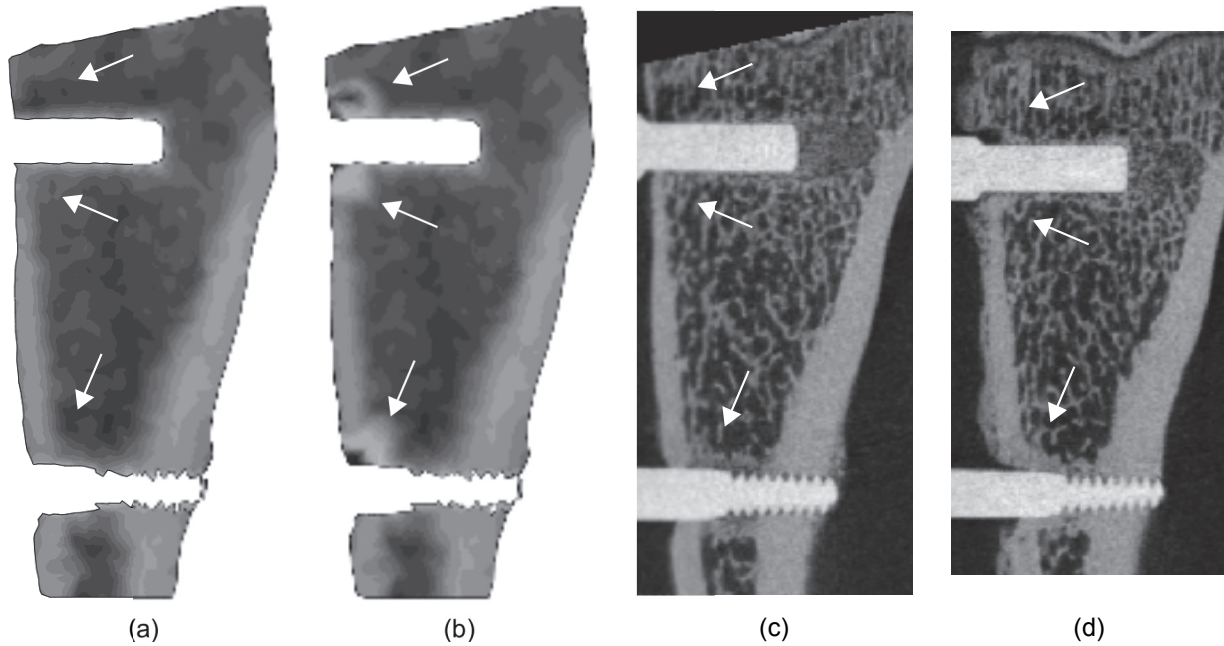


Figure 6.8: Specimen-specific BMD field variation: (a) BMD field derived from the basal state (2 weeks of integration), (b) BMD field adapted to the external load, (c) mCT scan of basal state and (d) mCT scan of the stimulated state (2 weeks of integration and 4 weeks of stimulation). Arrows highlight relevant areas.

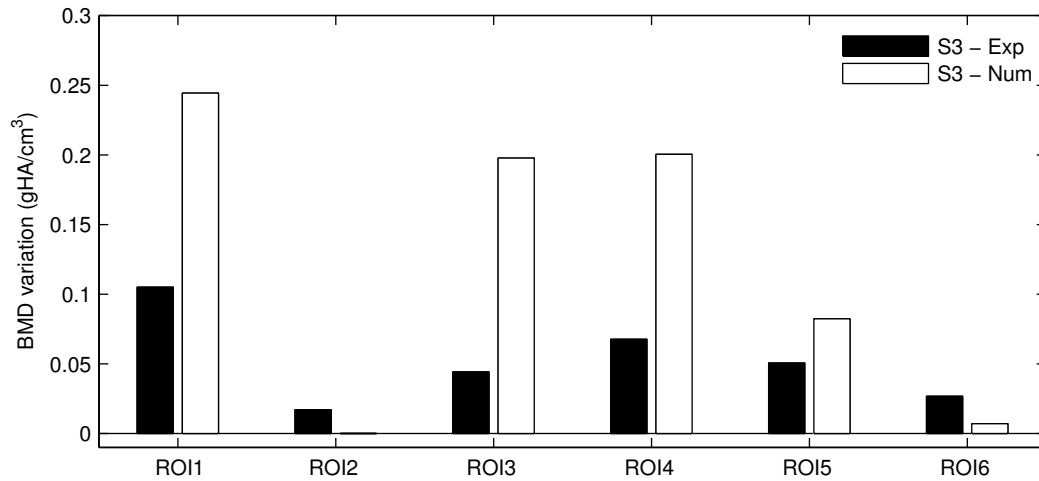


Figure 6.9: BMD variation in ROIs of Specimen 3 predicted with the bone adaptation algorithm presented in Section 5.4.2.1 and compared to experiments.

and the bone-implant interface is properly defined. The absence of x-ray discrepancies is an important step towards the characterization the bone-implant interface and adhesion, which is a key factor affecting integration.

6.6 Conclusions

The proof of concept presented in this chapter focuses on the adaptation of the ‘loaded implant’ model to time-lapse studies based on in~vivo mCT analysis. The results highlight a remarkable step forward, based on two important achievements:

1. The animal model is now compatible with longitudinal studies of single specimens. Statistically relevant analyses performed on groups of animals can be supported by focused investigations aiming at clarifying specific phenomena.
2. Ti-coated Al-implants grant reliable performances and allow investigating the bone-implant interface with accuracy. This improvement opens interesting research themes, as the correlation between pull-out strength and interface adhesion or the study of the effects of surface treatments on implants integration.

Chapter 7

Conclusions and perspectives

7.1 Aim

The themes investigated in this thesis are summarized and highlight the scientific relevance of the results, with a particular attention to the conclusions which allow answering the following research questions:

- Q1.** Is it possible to define a numerical framework to investigate the specimens' mechanical behavior preserving the bio-variability?
- Q2.** Is the peri-implant cortical loss mechanically driven?
- Q3.** Can the density variation generated by external overloading be predicted through an adaptation algorithm?

Furthermore, a brief overview of challenging perspectives is presented with a particular attention to the improvement of the proposed adaptation strategy.

7.2 Summary and conclusions

In this thesis, the results of a complex study, involving both experimental and numerical analyses concerning the peri-implant bone adaptation to the mechanical environment, are presented. The dependency of implants integration on the mechanical stimulation is investigated experimentally through the ‘loaded implant’ model, and numerically by FE analysis involving the animal daily activity and the implants stimulation.

The experiments discussed in Chapter 2 show that the success of implantation depends on the differences between animals, thus highlighting the risks of relying on a numerical approach based on a single individual. This observation leads to the first question: *is it possible to define a numerical framework to investigate the specimens’ mechanical behavior preserving the bio-variability?*

The answer is yes, thanks to the new protocol to generate high fidelity, specimen-specific FE models of bare and implant-fitted rat tibiae from high-resolution CT images, presented in Chapter 3. The characteristics of the animals, such as geometry and material property field, are preserved and the differences between subjects can definitely be captured. Each step of the protocol is evaluated to quantify associated errors. The systematic investigation of the proposed strategy confirms its applicability to studies that account for biodiversity. This protocol provides solid basis for all the numerical analyses presented in this thesis and also for future investigations on bone biomechanics.

Another relevant experimental result regards the peri-implant cortical bone loss observed in implanted specimens not subjected to external loading. The funnel-shaped tissue adaptation appears after a few weeks of implantation and its depth monotonically increases with time, provoking in some cases the complete bone-implant detachment. This phenomenon raises the second question: *is the peri-implant cortical loss mechanically driven?*

Yes, this adaptation process is surely related to the animal unconstrained locomotion. This answer is the result of the analysis of the rat tibia deformation during gait presented in Chapter 4. The analysis is performed using an original loading condition accounting for musculoskeletal forces and different FE boundary conditions mimicking variable integration states.

Firstly, the proposed gait-based analysis agrees with in~vivo deformation measurements and allows describing the deformation pattern characterizing bare rat tibiae during locomotion, thus fixing an interesting reference point according to which implantation studies on rats tibiae are to be evaluated. These findings enhance the knowledge base of the rat tibia biomechanics and allow comparing mechanical signals of bone adaptation under physiological conditions. The analysis highlights the octahedral shear strain as the best candidate for the implementation of the Mechanostat theory at the macroscale. In physiological condition, this signal shows location- and tissue-independent distributions,

confirming the existence of a unique Lazy Zone, driving the bone macroscopic structural adaptation to the mechanical environment.

Furthermore, the investigations on implanted tibiae show that the peri-implant cortical loss observed experimentally is caused by bone disuse atrophy, which is initiated by a loss of bone-implant adhesion and kept ongoing by the cyclic loadings on the interface due to gait cycles. The comparison between implantation strategies highlights that a thick cortical layer has a delaying effect on the occurrence of apical bone loss, while the trabecular bone is crucial in preventing the progressive loss of adhesion and avoid a complete opening. This mechanism clearly affects the implants stability and may provoke clinically relevant consequences on other type of implantation, for example in dentistry, where the cortical bone loss is associated to overloading and pathologies but not to disuse provoked by physiological loads.

Despite this detrimental phenomenon, the experiments show that the specimens not affected by cortical bone loss react to the external loading showing a peri-implant adaptation which involves a significant improvement of the ultimate inter-implant strength. This result raises the third question: *can the density variation generated by external overloading be predicted through an adaptation algorithm?*

Yes, the novel adaptation algorithm based on the octahedral shear strain and relying on the gait-based analysis yields reliable predictions of the observed phenomenon. As discussed in Chapter 5, the numerical quantifications of local and overall density variations, as well as the improved implants lateral stability, show a good agreement with the experiments, confirming that the effects of the external stimulation on well integrated specimens is predictable. The results of such investigations are strengthened by the completeness of the proposed analysis, characterized by an accurate verification and a systematic validation through comparison with experiments. These results open interesting clinical perspectives concerning bone augmentation therapies based on controlled loading and research fields focusing on the effects of overloading.

The proposed adaptation algorithm is also combined with the gait based loading condition, a novelty in this field of research, and leads to the representation of the mechanical homeostasis of the rat tibia. Considering the numerous research applications involving this organ, the proposed strategy can serve as benchmark for further developments, e.g. concerning the harmful effects of fatigue loading due to physical exercise or studies on pathologies involving the alteration of the bone maintenance process. In the present thesis, this framework is successfully employed to confirm that the funnel shaped cortical loss highlighted in Chapter 4 occurs because of resorption of unloaded tissue, thus adding an original contribution to the knowledge base on peri-implant bone defects. Finally, the contribution of both external and gait-based loading conditions are combined in a multi-load adaptation model which confirms the previously obtained results and provides a complete

overview of the mechanical adaptation process characterizing the ‘loaded implant’ model.

This work relies on experiments characterized by limitations: group-based test campaigns provide results extrapolated at limited time-points (i.e. 2 weeks or 6 weeks after implantation) and specimen-specific integration histories cannot be extrapolated. Moreover, the numerical analyses are based on strong assumptions on bone tissue, modeled as an inhomogeneous, continuum, isotropic elastic material without accounting for fluids or actual trabecular microstructures. Furthermore, bone-implant interfaces are assumed to be either tied or open. Despite these limitations, this work leads to a better and sound understanding of the implants integration dependency on mechanical stimulation, and offers the basis for further studies on the important research topics addressed in this thesis.

7.3 Proposed methodologies

The numerical models of bone adaptation around implants presented in this thesis are based on two important concepts:

1. Multiple specimen-specific FE models are adopted as reference to represent a population of individuals.
2. Reliable predictions of bone adaptation to the external stimulation (i.e. the implant activation) are obtained by deriving the parameters of the adaptation law from the animal physiological activity (i.e. the tibia deformation during gait).

A simplified flow chart of this methodology is shown in Figure 7.1a. Multiple, specimen-specific predictions based on averaged parameters produced results in close agreement with group-based experiments. In details, the adaptation stimulus and thresholds are averaged on multiple tibiae subjected to the gait-based loading condition.

Since relevant differences characterize the results of each specimen, the use of a single specimen-specific model hampers to draw conclusions on populations. As a consequence, the proposed procedure is recommended when the goal of the analysis is to numerically predict the behavior of a population.

However, this approach may not be enough accurate to predict the adaptation of single individuals. Since this is the goal to pursue in particular for clinical applications, a fully specimen-specific approach is suggested (Figure 7.1b). Through in-vivo mCT scans, the adaptation parameters can be calculated from the bare tibia subjected to physiological loading before implantation. These specimen-specific parameters can then be used to compute bone adaptation based on a single individual. The result, fully specimen-specific, can improve the accuracy of numerical predictions for single subjects.

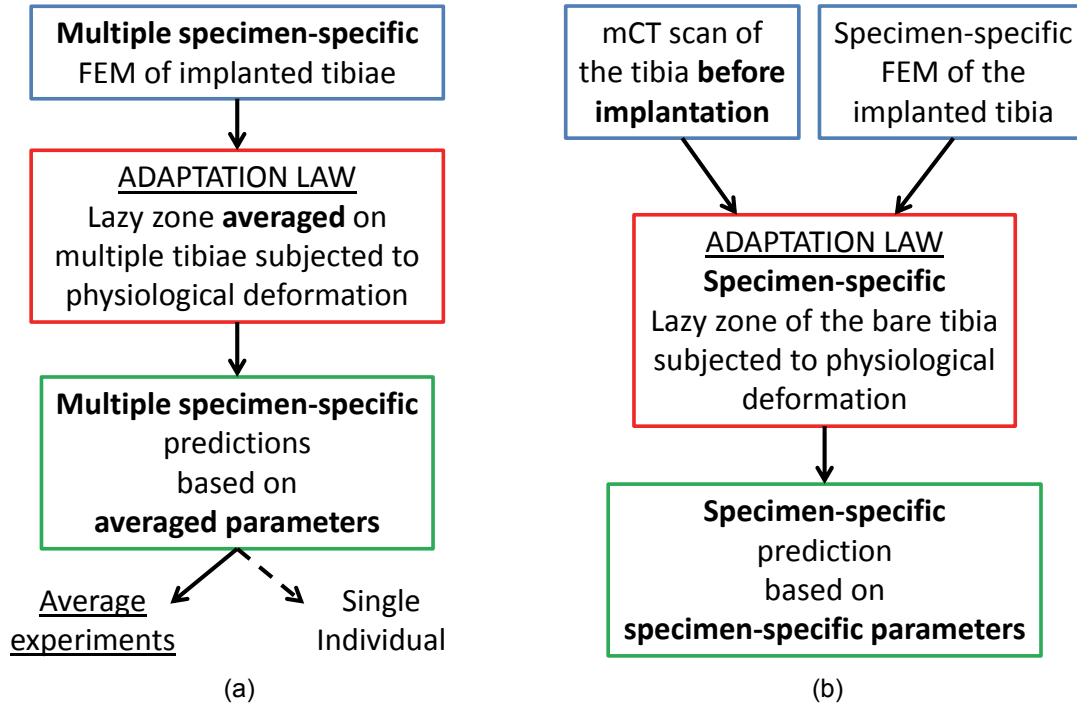


Figure 7.1: Flow charts of the methodologies proposed to predict bone adaptation for (a) a population and (b) single individuals.

7.4 Perspectives

The work developed during this thesis allows answering important questions but it also opens new perspectives. The longitudinal mCT analysis described in Chapter 6 offers a reliable and concrete alternative to group-based studies, and allows investigating the integration history of individuals as well as characterizing the bone-implant adhesion.

Further suggestions for interesting developments are discussed below.

In~vivo monitoring of inter-implant strain. The outcome of in~vivo experiments could be improved by monitoring the inter-implant strain variation during stimulation. This experimental upgrade could provide daily information on the implant stability that can be correlated with in~vivo mCT scans.

Post-exercise bone resorption. Several studies highlight that the bone density quickly increases because of physical exercise but it decreases likewise once the adopted stimulation stops (Terrier et al., 2005). Considering the ‘loaded implant’ model, it could be interesting to add a rest period after the stimulation to verify if this phenomenon occurs, and quantify the time is required to nullify the positive effects

of stimulation on the inter-implant ultimate strength.

Limits of the external stimulation. The parametric study on the force level presented in Section 5.4.3 establishes the first step towards the determination of the damage limits characterizing the peri-implant tissue. An experimental validation of the ranges of forces explored numerically could provide crucial insights on individual-based resistance to critical overloading.

Parallelism with mandible. Both the bone apposition generated by the external activation and the cortical bone loss due to the physiological loading condition are of great interest in clinical applications involving dental implants. A comparison between the results obtained in rats and clinical cases could clarify existing ambiguous results and address further developments.

Bone-implant contact. The bone-implant adhesion plays a key role, in particular concerning the observed cortical bone loss. Thus, the implementation of consistent contact conditions may improve the knowledge on this phenomenon (e.g. cohesive contact). To reach this goal, the pull-out tests presented in this thesis and the mCT images with Ti-coated Al implants are a perfect benchmark for the characterization of the implant adhesion to the bone tissue.

Perturbations of the adaptation law. The mechanical adaptation interacts with other factors affecting the bone metabolism (e.g. age, diseases or medications). These phenomena can be implemented in the Mechanostat-based theory and combined with the proposed framework which allows studying both systemic and local treatments.

The results presented in this thesis clearly highlight the coexistence of different phenomena, positively and negatively influencing the implant stability. Thanks to the present work these phenomena have been quantified, understood and correlated by following an ‘a posteriori’ approach: numerical analyses are performed to investigate phenomena observed experimentally. A great step forward would be the creation of an ‘a priori’ approach, that is capable of highlighting the features that make one specimens more predisposed to cortical loss or apposition, thus reducing the result scatter and amplifying the potential of these methodologies as clinical tools.

During the last months the author had the possibility to make progress on a multi-scale upgrade of the adaptation approach which may help to improve the results of this thesis. Some ideas for further developments concerning this theme are briefly discussed in the following section.

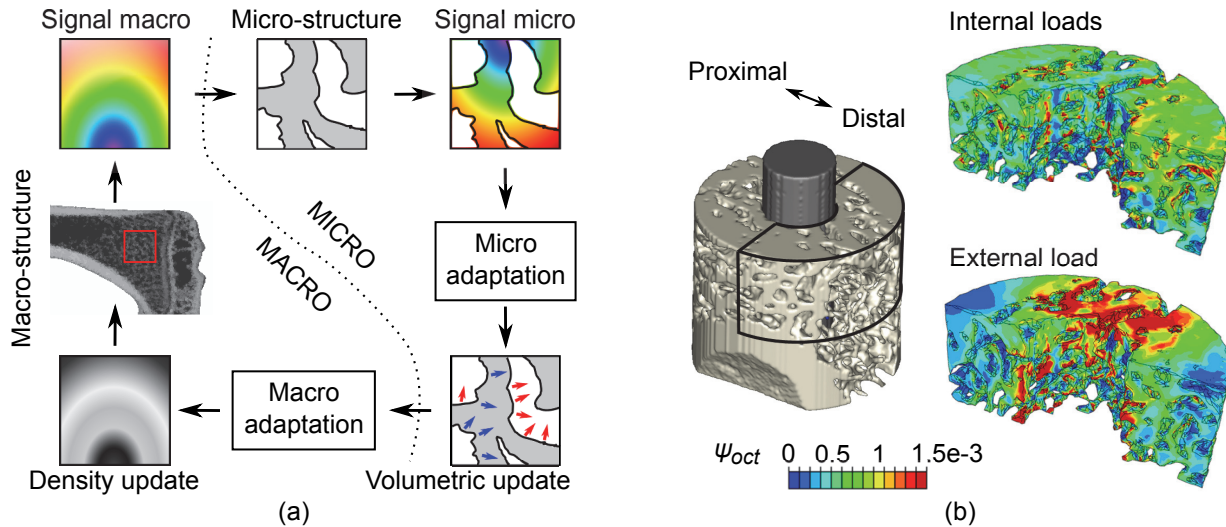


Figure 7.2: (a) flow chart of the multi-scale approach. (b) example of sub-modeling: the highlighted peri-implant trabecular bone is subjected to the boundary displacement field generated by the internal and external loading conditions on the macroscale model.

7.4.1 Multi-scale adaptation

The adaptation analyses presented in this thesis are based on a continuum, isotropic, linear and inhomogeneous representation of the bone tissue which allows obtaining relevant results, but at the same time entails a strong simplification of the osseous structure. As a matter of fact, the density variations previously discussed are actually the consequence of a micro-structural adaptation of both cortical and trabecular bone. These local variations of the bone structure can be predicted with reasonable computational costs by implementing a multi-scale adaptation approach based on the *Submodeling*¹ technique available in ABAQUS-Standard[®]. This technique is used to study a sub-region of a macroscopic model, which is modeled with a refined mesh and subjected to boundary conditions based on the interpolation of the solution from the global model.

A flow chart of the proposed multi-scale approach is represented in Figure 7.2a. Firstly, the macroscopic deformation field characterizing the global model is transferred to the refined subregion, thus generating a microscopic deformation field. Then, this deformation field can be adopted as signal and processed to compute a geometrical adaptation of the refined model (e.g. variation of trabecular or cortical thickness). Furthermore, the calculated local adaptation implies a variation of the global density field, thus provoking an update of the macroscopic material properties.

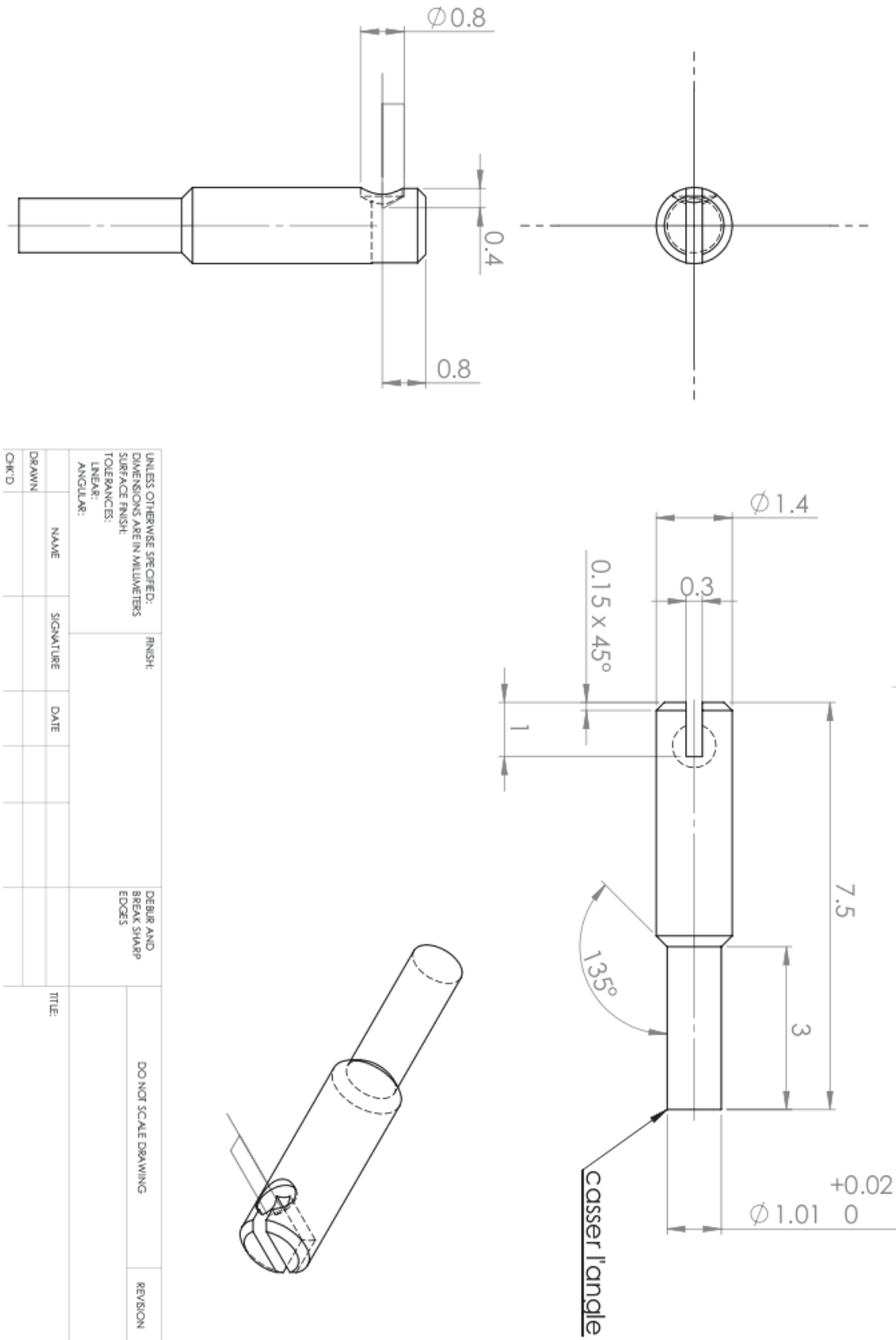
The submodeling technique has been adopted to perform the first part of this ap-

¹Abaqus Analysis User's Manual, 10.2.1 Submodeling: overview.

proach, that is the quantification of the microscopic deformation field characterizing the peri-implant trabecular bone. Figure 7.2b shows the octahedral shear strain in a region of trabecular bone beneath the cortical tissue around the proximal implant, when the gait-based and the external loading conditions are applied to the global FE model. This technique can improve the prediction of bone apposition or resorption around the implants by introducing a local geometrical adaptation and leading to the correlation between macroscopic and microscopic signals of bone adaptation. Moreover, this approach allows implementing proper damage models at microscale, thus offering the basis for the study of destructive tests such as the ultimate inter-implant failure or the pull-out.

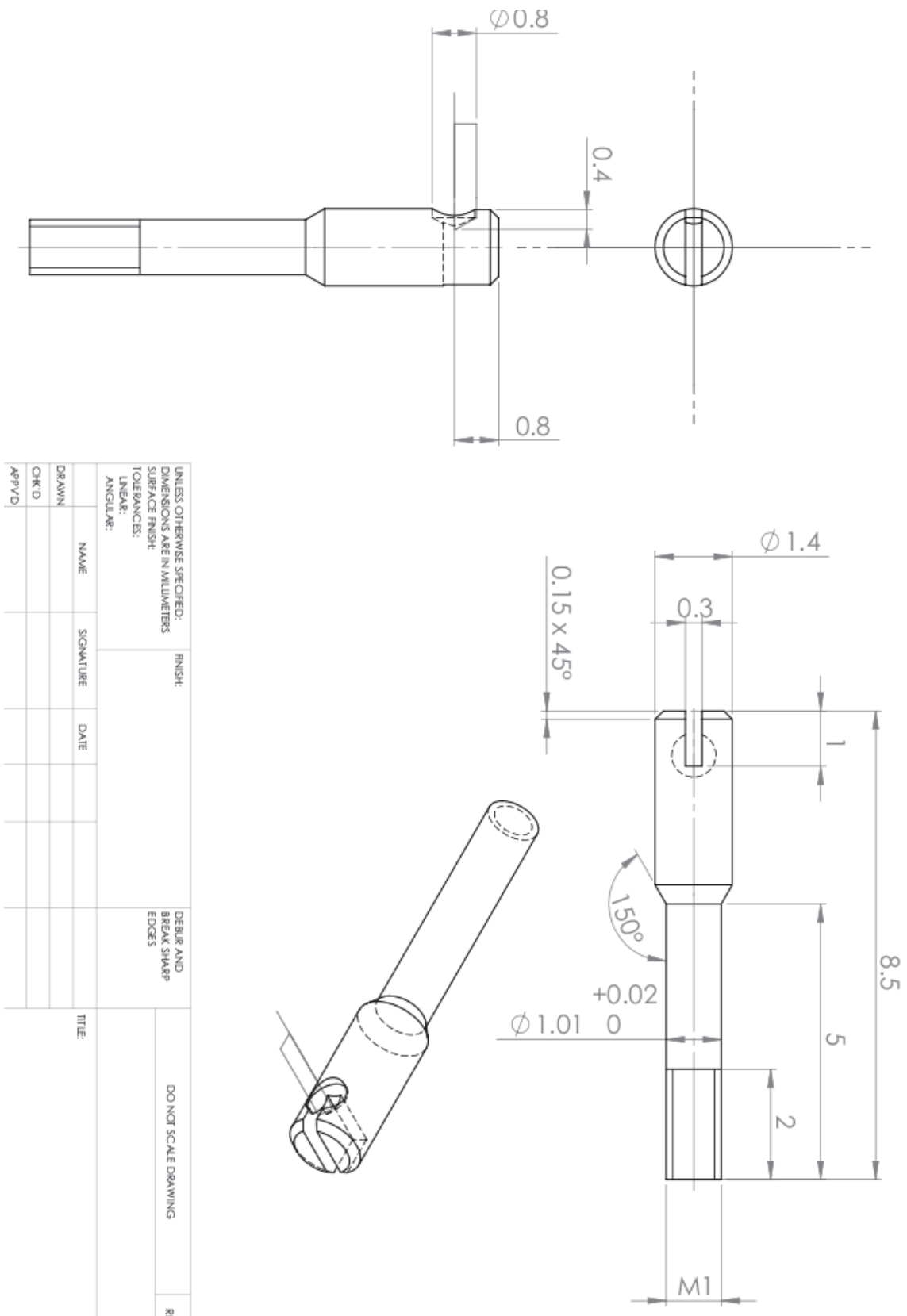
Appendix A

Implants drawings



UNLESS OTHERWISE SPECIFIED: DIMENSIONS ARE IN MILLIMETERS SURFACE FINISH TOLERANCES: LINEAR: ANGULAR:		FINISH:	DEBurr AND BREAK SHARP EDGES		DO NOT SCALE DRAWING	REVISION
DRAWN	NAME	SIGNATURE	DATE			
CHK'D					TITLE:	

Figure A.1: Proximal implant draft.



UNLESS OTHERWISE SPECIFIED: DIMENSIONS ARE IN MILLIMETERS SURFACE FINISH: TOLERANCES: LINEAR: ANGULAR:		FINISH:	DEBUR AND BREAK SHARP EDGES	DO NOT SCALE DRAWING	R1
DRAWN	NAME	SIGNATURE	DATE	TITLE:	
CHK'D					
APP'VD					

Figure A.2: Distal implant draft.

Appendix B

Computed Tomography image

Computed tomography image of a stimulated specimen. Imaging system: mCT-40, Scanco Medical AG (Brüttisellen, Switzerland).

Settings:

- $1022 \times 360^\circ$ slices \times rotation.
- $20 \mu\text{m}$ isotropic voxel size.
- 70 kVp source potential.
- 114 mA tube current.
- $20 \times 26.5 \text{ mm}$ field of view.

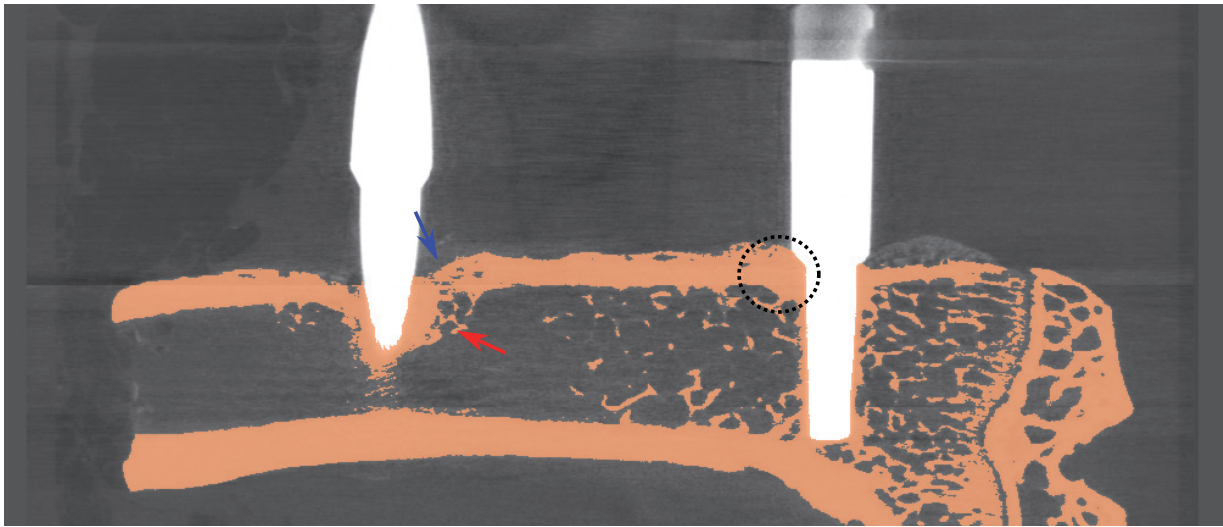


Figure B.1: *Computed tomography image of a stimulated specimen. Both bone augmentation (red arrow) and apical resorption (blue arrow) are visible near the distal implant. Other stimulated specimens show no apical resorption and the thick layer of compact bone surrounding the implant is preserved (dotted circle).*

Bibliography

- Abdul-Kadir, M.R.; Hansen, U.; Klabunde, R.; Lucas, D., and Amis, A. Finite element modelling of primary hip stem stability: The effect of interference fit. *Journal of Biomechanics*, 41(3):587–594, 2008.
- Akhter, M.P.; Raab, D.M.; Turner, C.H.; Kimmel, D.B., and Recker, R.R. Characterization of in vivo strain in the rat tibia during external application of a four-point bending load. *Journal of Biomechanics*, 25(10):1241–1246, 1992.
- Al-Shakhrah, I. and Al-Obaidi, T. Common artifacts in computerized tomography: A review. *Applied Radiology*, 32(8):25–30, 2003.
- Albrektsson, T. Hard tissue implant interface. *Australian Dental Journal*, 53(SUPPL. 1): S34–S38, 2008.
- Ammann, P.; Badoud, I.; Barraud, S.; Dayer, R., and Rizzoli, R. Strontium ranelate treatment improves trabecular and cortical intrinsic bone tissue quality, a determinant of bone strength. *Journal of Bone and Mineral Research*, 22(9):1419–1425, 2007.
- Anderson, A. E.; Peters, C. L.; Tuttle, B. D., and Weiss, J. A. Subject-specific finite element model of the pelvis: Development, validation and sensitivity studies. *Journal of Biomechanical Engineering*, 127(3):364–373, 2005.
- Anderson, A. E.; Ellis, B. J., and Weiss, J. A. Verification, validation and sensitivity studies in computational biomechanics. *Computer methods in biomechanics and biomedical engineering*, 10(3):171–184, 2007.
- Bagge, M. A model of bone adaptation as an optimization process. *Journal of Biomechanics*, 33(11):1349–1357, 2000.
- Barbosa, A.A.; Del Carlo, R.J.; Galva, S.R.; Vilela, M.J.; Louzada, M.J.Q.; Brito, A.F. S., and Natali, A.J. Bone mineral density of rat femurs after hindlimb unloading and different physical rehabilitation programs. *Revista Ceres*, 58:407 – 412, 2011.
- Barrett, J. F. and Keat, N. Artifacts in ct: Recognition and avoidance. *Radiographics*, 24(6):1679–1691+1796, 2004.
- Beaupré, G.S.; Orr, T.E., and Carter, D.R. An approach for time-dependent bone modeling

- and remodeling - theoretical development. *Journal of Orthopaedic Research*, 8(5):651–661, 1990a.
- Beaupré, G.S.; Orr, T.E., and Carter, D.R. An approach for time-dependent bone modeling and remodeling - application: A preliminary remodeling simulation. *Journal of Orthopaedic Research*, 8(5):662–670, 1990b.
- Be’ery-Lipperman, M. and Gefen, A. A method of quantification of stress shielding in the proximal femur using hierarchical computational modeling. *Computer methods in biomechanics and biomedical engineering*, 9(1):35–44, 2006.
- Blum, E.K.; Haun, C., and Ryan, J.E. A musculo-skeletal model of rat ankle motion and its experimental test on rat. *Journal of Biomechanics*, 40(4):891–899, 2007.
- Boas, F. E. and Fleischmann, D. Evaluation of two iterative techniques for reducing metal artifacts in computed tomography. *Radiology*, 259(3):894–902, 2011.
- Bodic, F.; Hamel, L.; Lerouxel, E.; Baslé, M.F., and Chappard, D. Bone loss and teeth. *Joint Bone Spine*, 72(3):215–221, 2005.
- Boissonnat, J. D. and Oudot, S. Provably good sampling and meshing of surfaces. *Graphical Models*, 67(5):405–451, 2005.
- Bona, M.A.; Martin, L.D., and Fischer, K.J. A contact algorithm for density-based load estimation. *Journal of Biomechanics*, 39(4):636–644, 2006.
- Bouxsein, M.L.; Boyd, S.K.; Christiansen, B.A.; Guldberg, R.E.; Jepsen, K.J., and Müller, R. Guidelines for assessment of bone microstructure in rodents using micro-computed tomography. *Journal of Bone and Mineral Research*, 25(7):1468–1486, 2010.
- Brånemark, Per-Ingvar; Zarb, G.A., and Albrektsson, T. *Tissue-integrated prostheses: osseointegration in clinical dentistry*. Quintessence, 1985.
- Burghardt, A. J.; Kazakia, G. J.; Laib, A., and Majumdar, S. Quantitative assessment of bone tissue mineralization with polychromatic micro-computed tomography. *Calcified Tissue International*, 83(2):129–138, 2008.
- Campoli, G.; Weinans, H., and Zadpoor, A.A. Computational load estimation of the femur. *Journal of the Mechanical Behavior of Biomedical Materials*, 10:108–119, 2012.
- Carter, D.R.; Orr, T.E., and Fyhrie, D.P. Relationships between loading history and femoral cancellous bone architecture. *Journal of Biomechanics*, 22(3):231–244, 1989.
- Chambers, T.J.; Evans, M.; Gardner, T.N.; Turner-Smith, A., and Chow, J.W.M. Induction of bone formation in rat tail vertebrae by mechanical loading. *Bone and Mineral*, 20(2):167–178, 1993.
- Chennimalai Kumar, N.; Dantzig, J.A.; Jasiuk, I.M.; Robling, A.G., and Turner, C.H. Numerical modeling of long bone adaptation due to mechanical loading: Correlation with experiments. *Annals of Biomedical Engineering*, 38(3):594–604, 2010.
- Chou, H.-Y.; Jagodnik, J.J., and Müftü, S. Predictions of bone remodeling around dental implant systems. *Journal of Biomechanics*, 41(6):1365–1373, 2008.

- Chui, C. K.; Wang, Z.; Zhang, J.; Ong, J. S. K.; Bian, L.; Teo, J. C. M.; Yan, C. H.; Ong, S. H.; Wang, S. C.; Wong, H. K., and Teoh, S. H. A component-oriented software toolkit for patient-specific finite element model generation. *Advances in Engineering Software*, 40(3):184–192, 2009.
- Clarke, K. A. and Parker, A. J. A quantitative study of normal locomotion in the rat. *Physiology and Behavior*, 38(3):345–351, 1986.
- Clarke, Kenneth A. Swing time changes contribute to stride time adjustment in the walking rat. *Physiology & Behavior*, 50(6):1261–1262, 1991.
- Cochran, D.L.; Nummikoski, P.V.; Higginbottom, F.L.; Hermann, J.S.; Makins, S.R., and Buser, D. Evaluation of an endosseous titanium implant with a sandblasted and acid-etched surface in the canine mandible: Radiographic results. *Clinical Oral Implants Research*, 7(3):240–252, 1996.
- Cory, E.; Nazarian, A.; Entezari, V.; Vartanians, V.; Müller, R., and Snyder, B.D. Compressive axial mechanical properties of rat bone as functions of bone volume fraction, apparent density and micro-ct based mineral density. *Journal of Biomechanics*, 43(5): 953–960, 2010.
- Cowin, Stephen C. The relationship between the elasticity tensor and the fabric tensor. *Mechanics of Materials*, 4(2):137 – 147, 1985.
- Cox, L.G.E.; Van Rietbergen, B.; Van Donkelaar, C.C., and Ito, K. Analysis of bone architecture sensitivity for changes in mechanical loading, cellular activity, mechanotransduction, and tissue properties. *Biomechanics and Modeling in Mechanobiology*, 10(5): 701–712, 2011.
- Crupi, V.; Guglielmino, E.; La Rosa, G.; Vander Sloten, J., and Van Oosterwyck, H. Numerical analysis of bone adaptation around an oral implant due to overload stress. *Proceedings of the Institution of Mechanical Engineers, Part H: Journal of Engineering in Medicine*, 218(6):407–415, 2004.
- Cufí, X.; Muñoz, X.; Freixenet, J., and Martí, J. A review of image segmentation techniques integrating region and boundary information. volume 120, pages 1–39. 2003.
- Cvetkovic, V.J.; Najman, S.J.; Rajkovic, J.S.; Zabar, A.L.J.; Vasiljevic, P.J.; Djordjevic, L.J.B., and Trajanovic, M.D. A comparison of the microarchitecture of lower limb long bones between some animal models and humans: A review. *Veterinarni Medicina*, 58 (7):339–351, 2013.
- Dannemann, C.; Grätz, K.W.; Riener, M.O., and Zwahlen, R.A. Jaw osteonecrosis related to bisphosphonate therapy. a severe secondary disorder. *Bone*, 40(4):828–834, 2007.
- David, V.; Laroche, N.; Boudignon, B.; Lafage-Proust, M.-H.; Alexandre, C.; Ruegsegger, P., and Vico, L. Noninvasive in vivo monitoring of bone architecture alterations in hindlimb-unloaded female rats using novel three-dimensional microcomputed tomography. *Journal of Bone and Mineral Research*, 18(9):1622–1631, 2003.

- Dayer, R.; Rizzoli, R.; Kaelin, A., and Ammann, P. Low protein intake is associated with impaired titanium implant osseointegration. *Journal of Bone and Mineral Research*, 21(2):258–264, 2006.
- De Smet, E.; Jaecques, S.; Vandamme, K.; Vander Sloten, J., and Naert, I. Positive effect of early loading on implant stability in the bi-cortical guinea-pig model. *Clinical Oral Implants Research*, 16(4):402–407, 2005.
- De Smet, E.; Jaecques, S.V.N.; Wevers, M.; Jansen, J.A.; Jacobs, R.; Sloten, J.V., and Naert, I.E. Effect of controlled early implant loading on bone healing and bone mass in guinea pigs, as assessed by micro-ct and histology. *European Journal of Oral Sciences*, 114(3):232–242, 2006.
- Dhert, W.J.A.; Thomsen, P.; Blomgren, A.K.; Esposito, M.; Ericson, L.E., and Verbout, A.J. Integration of press-fit implants in cortical bone: A study on interface kinetics. *Journal of Biomedical Materials Research*, 41(4):574–583, 1998.
- Doblaré, M. and García, J. M. Anisotropic bone remodelling model based on a continuum damage-repair theory. *Journal of Biomechanics*, 35(1):1–17, 2002.
- Durual, S.; Rieder, P.; Garavaglia, G.; Filieri, A.; Cattani-Lorente, M.; Scherrer, S.S., and Wiskott, H.W.A. Tinox coatings on roughened titanium and cocr alloy accelerate early osseointegration of dental implants in minipigs. *Bone*, 52(1):230–237, 2013.
- Duyck, J.; Ronold, H.J.; Van Oosterwyck, H.; Naert, I.; Sloten, J.V., and Ellingsen, J.E. The influence of static and dynamic loading on marginal bone reactions around osseointegrated implants: An animal experimental study. *Clinical Oral Implants Research*, 12(3):207–218, 2001.
- Engh, C. A.; Bobyn, J. D., and Glassman, A. H. Porous-coated hip replacement. the factors governing bone ingrowth, stress shielding, and clinical results. *Journal of Bone and Joint Surgery - Series B*, 69(1):45–55, 1987.
- Fajardo, R.J.; Cory, E.; Patel, N.D.; Nazarian, A.; Laib, A.; Manoharan, R.K.; Schmitz, J.E.; DeSilva, J.M.; MacLatchy, L.M.; Snyder, B.D., and Bouxsein, M.L. Specimen size and porosity can introduce error into ct-based tissue mineral density measurements. *Bone*, 44(1):176–184, 2009.
- Fernandes, P.; Rodrigues, H., and Jacobs, C. A model of bone adaptation using a global optimisation criterion based on the trajectorial theory of wolff. *Computer Methods in Biomechanics and Biomedical Engineering*, 2(2):125–138, 1999.
- Fiorellini, J. P.; Nevins, M. L.; Norkin, A.; Weber, H. P., and Karimbux, N. Y. The effect of insulin therapy on osseointegration in a diabetic rat model. *Clinical Oral Implants Research*, 10(5):362–368, 1999.
- Fredericson, M.; Chew, K.; Ngo, J.; Cleek, T.; Kiratli, J., and Cobb, K. Regional bone mineral density in male athletes: A comparison of soccer players, runners and controls. *British Journal of Sports Medicine*, 41(10):664–668, 2007.

- Frey, P.; Sarter, B., and Gautherie, M. Fully automatic mesh generation for 3-d domains based upon voxel sets. *International Journal for Numerical Methods in Engineering*, 37 (16):2735–2753, 1994.
- Frost, H. M. Skeletal structural adaptations to mechanical usage (satmu): 2. redefining wolff's law: The remodeling problem. *Anatomical Record*, 226(4):414–422, 1990a.
- Frost, H. M. Skeletal structural adaptations to mechanical usage (satmu): 1. redefining wolff's law: The bone modeling problem. *Anatomical Record*, 226(4):403–413, 1990b.
- Frost, H.M. A determinant of bone architecture. the minimum effective strain. *Clinical Orthopaedics and Related Research*, No. 175:286–292, 1983.
- Frost, H.M. Bone 'mass' and the 'mechanostat': A proposal. *Anatomical Record*, 219(1): 1–9, 1987.
- Frost, H.M. The utah paradigm of skeletal physiology: An overview of its insights for bone, cartilage and collagenous tissue organs. *Journal of Bone and Mineral Metabolism*, 18(6):305–316, 2000.
- Frush, D. P. and Applegate, K. Computed tomography and radiation: Understanding the issues. *JACR Journal of the American College of Radiology*, 1(2):113–119, 2004.
- Fujie, H.; Miyagaki, J.; Terrier, A.; Rakotomanana, L.; Leyvraz, P.-F., and Hayashi, K. Detraining effects on the mechanical properties and morphology of rat tibiae. *Bio-Medical Materials and Engineering*, 14(2):219–233, 2004.
- Fyhrie, D.P. and Carter, D.R. A unifying principle relating stress to trabecular bone morphology. *Journal of Orthopaedic Research*, 4(3):304–317, 1986.
- Gillis, G. B. and Biewener, A. A. Hindlimb muscle function in relation to speed and gait: In vivo patterns of strain and activation in a hip and knee extensor of the rat (*rattus norvegicus*). *Journal of Experimental Biology*, 204(15):2717–2731, 2001.
- Globus, R. K.; Bikle, D. D., and Morey-Holton, E. Effects of simulated weightlessness on bone mineral metabolism. *Endocrinology*, 114(6):2264–2270, 1984.
- Glosel, B.; Kuchler, U.; Watzek, G., and Gruber, R. Review of dental implant rat research models simulating osteoporosis or diabetes. *The International journal of oral and maxillofacial implants*, 25(3):516–524, 2010.
- Goodacre, C.J.; Kan, J.Y., and Rungcharassaeng, K. Clinical complications of osseointegrated implants. *The Journal of prosthetic dentistry*, 81(5):537–552, 1999.
- Gross, U.; Roggendorf, W.; Schmitz, H.-J., and Strunz, V. Biomechanical and morphometric testing methods for porous and surface reactive biomaterials. *Quantitative Characterization and Performance of Porous Implants for Hard Tissue Applications*, pages 330–346, 1987.
- Guan, F.; Han, X.; Mao, H.; Wagner, C.; Yeni, Y. N., and Yang, K. H. Application of optimization methodology and specimen-specific finite element models for investigating material properties of rat skull. *Annals of Biomedical Engineering*, 39(1):85–95, 2011.

- Hambli, R. and Rieger, R. Physiologically based mathematical model of transduction of mechanobiological signals by osteocytes. *Biomechanics and Modeling in Mechanobiology*, 11(1-2):83–93, 2012.
- Hara, T.; Hayashi, K.; Nakashima, Y.; Kanemaru, T., and Iwamoto, Y. The effect of hydroxyapatite coating on the bonding of bone to titanium implants in the femora of ovariectomised rats. *Journal of Bone and Joint Surgery - Series B*, 81(4):705–709, 1999.
- Harrigan, T.P. and Hamilton, J.J. Optimality conditions for finite element simulation of adaptive bone remodeling. *International Journal of Solids and Structures*, 29(23):2897–2906, 1992a.
- Harrigan, T.P. and Hamilton, J.J. An analytical and numerical study of the stability of bone remodelling theories: Dependence on microstructural stimulus. *Journal of Biomechanics*, 25(5):477–488, 1992b.
- Harrigan, T.P.; Jasty, M.; Mann, R.W., and Harris, W.H. Limitations of the continuum assumption in cancellous bone. *Journal of Biomechanics*, 21(4):269–275, 1988.
- Helgason, B.; Perilli, E.; Schileo, E.; Taddei, F.; Brynjólfsson, S., and Viceconti, M. Mathematical relationships between bone density and mechanical properties: A literature review. *Clinical Biomechanics*, 23(2):135–146, 2008.
- Hillam, R.A. and Skerry, T.M. Inhibition of bone resorption and stimulation of formation by mechanical loading of the modeling rat ulna in vivo. *Journal of Bone and Mineral Research*, 10(5):683–689, 1995.
- Histing, T.; Garcia, P.; Holstein, J. H.; Klein, M.; Matthys, R.; Nuetzi, R.; Steck, R.; Laschke, M. W.; Wehner, T.; Bindl, R.; Recknagel, S.; Stuermer, E. K.; Vollmar, B.; Wildemann, B.; Lienau, J.; Willie, B.; Peters, A.; Ignatius, A.; Pohlemann, T.; Claes, L., and Menger, M. D. Small animal bone healing models: Standards, tips, and pitfalls results of a consensus meeting. *Bone*, 49(4):591–599, 2011.
- Hodgskinson, R. and Currey, J. D. Young’s modulus, density and material properties in cancellous bone over a large density range. *Journal of Materials Science: Materials in Medicine*, 3(5):377–381, 1992.
- Hoshaw, S.J.; Brunski, J.B., and Cochran, G.V.B. Mechanical loading of branemark implants affects interfacial bone modeling and remodeling. *International Journal of Oral and Maxillofacial Implants*, 9:345360, 1994.
- Huiskes, R.; Weinans, H.; Grootenboer, H.J.; Dalstra, M.; Fudala, B., and Slooff, T.J. Adaptive bone-remodeling theory applied to prosthetic-design analysis. *Journal of Biomechanics*, 20(11-12):1135–1150, 1987.
- Huiskes, R.; Weinans, H., and Dalstra, M. Adaptive bone remodeling and biomechanical design considerations for noncemented total hip arthroplasty. *Orthopedics*, 12(9):1255–1267, 1989.
- Huiskes, R.; Weinans, H., and Van Rietbergen, B. The relationship between stress shielding

- and bone resorption around total hip stems and the effects of flexible materials. *Clinical Orthopaedics and Related Research*, (274):124–134, 1992.
- Isidor, F. Loss of osseointegration caused by occlusal load of oral implants: A clinical and radiographic study in monkeys. *Clinical Oral Implants Research*, 7(4):143–152, 1996.
- Isidor, F. Histological evaluation of peri-implant bone at implants subjected to occlusal overload or plaque accumulation. *Clinical oral implants research*, 8(1):1–9, 1997.
- Jaatinen, J.J.P.; Korhonen, R.K.; Pelttari, A.; Helminen, H.J.; Korhonen, H.; Lappalainen, R., and Krger, H. Early bone growth on the surface of titanium implants in rat femur is enhanced by an amorphous diamond coating. *Acta Orthopaedica*, 82(4):499–503, 2011.
- Jasty, M.; Bragdon, C.; Burke, D.; O'Connor, D.; Lowenstein, J., and Harris, W.H. In vivo skeletal responses to porous-surfaced implants subjected to small induced motions. *Journal of Bone and Joint Surgery - Series A*, 79(5):707–714, 1997.
- Javed, F. and Romanos, G.E. The role of primary stability for successful immediate loading of dental implants. a literature review. *Journal of Dentistry*, 38(8):612–620, 2010.
- Jee, W.S.S. and Li, X.J. Adaptation of cancellous bone to overloading in the adult rat: A single photon absorptiometry and histomorphometry study. *Anatomical Record*, 227(4): 418–426, 1990.
- Johnson, W. L.; Jindrich, D. L.; Roy, R. R., and Reggie Edgerton, V. A three-dimensional model of the rat hindlimb: Musculoskeletal geometry and muscle moment arms. *Journal of Biomechanics*, 41(3):610–619, 2008.
- Kataoka, M.L.; Hochman, M.G.; Rodriguez, E.K.; Lin, P.J.P.; Kubo, S., and Raptopolous, V.D. A review of factors that affect artifact from metallic hardware on multi-row detector computed tomography. *Current Problems in Diagnostic Radiology*, 39(4):125–136, 2010.
- Kenneth, J.F.; Christopher, R.J., and Dennis, R.C. Computational method for determination of bone and joint loads using bone density distributions. *Journal of Biomechanics*, 28(9):1127 – 1135, 1995.
- Kowalczyk, P. Elastic properties of cancellous bone derived from finite element models of parameterized microstructure cells. *Journal of Biomechanics*, 36(7):961–972, 2003.
- Kozlovsky, A.; Tal, H.; Laufer, B.-Z.; Leshem, R.; Rohrer, M.D.; Weinreb, M., and Artzi, Z. Impact of implant overloading on the peri-implant bone in inflamed and non-inflamed peri-implant mucosa. *Clinical Oral Implants Research*, 18(5):601–610, 2007.
- Kumar, N.; Dantzig, J.A., and Jasiuk, I.M. Modeling of cortical bone adaptation in a rat ulna: Effect of frequency. *Bone*, 50(3):792–797, 2012.
- Kumar, N.C.; Jasiuk, I., and Dantzig, J. Dissipation energy as a stimulus for cortical bone adaptation. *Journal of Mechanics of Materials and Structures*, 6(1-4):303–319, 2011.
- Lacroix, D. and Prendergast, P. J. A mechano-regulation model for tissue differentiation during fracture healing: analysis of gap size and loading. *Journal of Biomechanics*, 35 (9):1163 – 1171, 2002a.

- Lacroix, D. and Prendergast, P.J. A mechano-regulation model for tissue differentiation during fracture healing: Analysis of gap size and loading. *Journal of Biomechanics*, 35(9):1163–1171, 2002b.
- Lambers, F.M.; Schulte, F.A.; Kuhn, G.; Webster, D.J., and Müller, R. Mouse tail vertebrae adapt to cyclic mechanical loading by increasing bone formation rate and decreasing bone resorption rate as shown by time-lapsed in vivo imaging of dynamic bone morphometry. *Bone*, 49(6):1340–1350, 2011.
- Lanyon, L.E. and Rubin, C.T. Static vs dynamic loads as an influence on bone remodelling. *Journal of Biomechanics*, 17(12):897–905, 1984.
- Leucht, P.; Kim, J.B.; Wazen, R.; Currey, J.A.; Nanci, A.; Brunski, J.B., and Helms, J.A. Effect of mechanical stimuli on skeletal regeneration around implants. *Bone*, 40(4): 919–930, 2007.
- Li, J.; Li, H.; Shi, L.; Fok, A.S.L.; Ucer, C.; Devlin, H.; Horner, K., and Silikas, N. A mathematical model for simulating the bone remodeling process under mechanical stimulus. *Dental Materials*, 23(9):1073–1078, 2007.
- Li, Z.; Kuhn, G.; Von Salis-Soglio, M.; Weigt, C.; Matthys, R.; Van Lenthe, G.H.; Müller, R., and Ruffoni, D. Three-dimensional in vivo monitoring of bone response to implant insertion. *Journal of Biomechanics*, 45(S341), 2012.
- Lin, D.; Li, Q.; Li, W., and Swain, M. Dental implant induced bone remodeling and associated algorithms. *Journal of the Mechanical Behavior of Biomedical Materials*, 2(5):410–432, 2009.
- Lisková, M. and Hert, J. Reaction of bone to mechanical stimuli. 2. periosteal and endosteal reaction of tibial diaphysis in rabbit to intermittent loading. *Folia Morphologica*, 19(3): 301–317, 1971.
- Machwate, M.; Zerath, E.; Holy, X.; Hott, M.; Modrowski, D.; Malouvier, A., and Marie, P.J. Skeletal unloading in rat decreases proliferation of rat bone and marrow-derived osteoblastic cells. *American Journal of Physiology - Endocrinology and Metabolism*, 264(5 27-5):E790–E799, 1993.
- Maimoun, L.; Brennan, T.C.; Badou, I.; Dubois-Ferriere, V.; Rizzoli, R., and Ammann, P. Strontium ranelate improves implant osseointegration. *Bone*, 46(5):1436 – 1441, 2010.
- Martin, R.Bruce. Porosity and specific surface of bone. *Critical Reviews in Biomedical Engineering*, 10(3):179–222, 1984.
- Martínez, G.; García Aznar, J.M.; Doblaré, M., and Cerrolaza, M. External bone remodeling through boundary elements and damage mechanics. *Mathematics and Computers in Simulation*, 73(1-4 SPEC. ISS.):183–199, 2006.
- McNamara, Laoise M. and Prendergast, Patrick J. Bone remodelling algorithms incorporating both strain and microdamage stimuli. *Journal of Biomechanics*, 40(6):1381 – 1391, 2007.

- Mellal, A.; Wiskott, H.W.A.; Botsis, J.; Scherrer, S.S., and Belser, U.C. Stimulating effect of implant loading on surrounding bone. comparison of three numerical models and validation by in vivo data. *Clinical Oral Implants Research*, 15(2):239–248, 2004.
- Miller, B.F.; O’Toole, M.T., and Keane, C.B. *Miller-Keane Encyclopedia and Dictionary of Medicine, Nursing, and Allied Health*. W. B. Saunders, 2003.
- Mirhadi, S.; Ashwood, N., and Karagkevrekis, B. Factors influencing fracture healing. *Trauma (United Kingdom)*, 15(2):140–155, 2013.
- Mosley, J.R.; March, B.M.; Lynch, J., and Lanyon, L.E. Strain magnitude related changes in whole bone architecture in growing rats. *Bone*, 20(3):191–198, 1997.
- Muir, G.D. and Whishaw, I.Q. Ground reaction forces in locomoting hemi-parkinsonian rats: A definitive test for impairments and compensations. *Experimental Brain Research*, 126(3):307–314, 1999.
- Mullender, M. G. and Huiskes, R. Proposal for the regulatory mechanism of wolff’s law. *Journal of Orthopaedic Research*, 13(4):503–512, 1995.
- Mullender, M.G. A physiological approach to the simulation of bone remodeling as a self-organizational control process. *Journal of Biomechanics*, 27(11):1389–1394, 1994.
- Natali, Arturo N.; Carniel, Emanuele L., and Pavan, Piero G. Dental implants press fit phenomena: Biomechanical analysis considering bone inelastic response. *Dental Materials*, 25(5):573–581, 2009.
- Nazarian, A.; Snyder, B. D.; Zurakowski, D., and Müller, R. Quantitative micro-computed tomography: A non-invasive method to assess equivalent bone mineral density. *Bone*, 43(2):302–311, 2008.
- Oliver, W.C. and Pharr, G.M. An improved technique for determining hardness and elastic modulus using load and displacement sensing indentation experiments. *Journal of Materials Research*, 7:1564–1583, 6 1992. ISSN 2044-5326.
- Ooi, F.K.; Singh, R.; Singh, H.J., and Umemura, Y. Minimum level of jumping exercise required to maintain exercise-induced bone gains in female rats. *Osteoporosis International*, 20(6):963–972, 2009.
- Ozcvici, E.; Luu, Y.K.; Adler, B.; Qin, Y.-X.; Rubin, J.; Judex, S., and Rubin, C.T. Mechanical signals as anabolic agents in bone. *Nature Reviews Rheumatology*, 6(1): 50–59, 2010.
- Pahr, D. H. and Zysset, P. K. From high-resolution ct data to finite element models: development of an integrated modular framework. *Computer methods in biomechanics and biomedical engineering*, 12(1):45–57, 2009.
- Pal, N. R. and Pal, S. K. A review on image segmentation techniques. *Pattern Recognition*, 26(9):1277–1294, 1993.
- Palacci, P. *Optimal implant positioning & soft tissue management for the Brånemark system*. Quintessence Pub. Co., 1995.

- Paoletti, N.; Li, P.; Merelli, E., and Viceconti, M. Multilevel computational modeling and quantitative analysis of bone remodeling. *IEEE/ACM Transactions on Computational Biology and Bioinformatics*, 9(5):1366–1378, 2012.
- Payten, W.M. and Law, M. Generalized shape optimization using stress constraints under multiple load cases. *Structural Optimization*, 15(3-4):269–274, 1998.
- Peter, B.; Pioletti, D. P.; Laïb, S.; Bujoli, B.; Pilet, P.; Janvier, P.; Guicheux, J.; Zambelli, P. Y.; Bouler, J. M., and Gauthier, O. Calcium phosphate drug delivery system: Influence of local zoledronate release on bone implant osteointegration. *Bone*, 36(1):52–60, 2005.
- Peterson, M.C. and Riggs, M.M. A physiologically based mathematical model of integrated calcium homeostasis and bone remodeling. *Bone*, 46(1):49–63, 2010.
- Pham, D. L.; Xu, C., and Prince, J. L. Current methods in medical image segmentation. volume 2, pages 315–337. 2000.
- Phillips, A. T. M. The femur as a musculo-skeletal construct: A free boundary condition modelling approach. *Medical Engineering and Physics*, 31(6):673–680, 2009.
- Phillips, A. T. M.; Pankaj, P.; Howie, C. R.; Usmani, A. S., and Simpson, A. H. R. W. Finite element modelling of the pelvis: Inclusion of muscular and ligamentous boundary conditions. *Medical Engineering and Physics*, 29(7):739–748, 2007.
- Piccinini, M.; Cugnoni, J.; Botsis, J.; Zacchetti, G.; Ammann, P., and Wiskott, A. Factors affecting subject-specific finite element models of implant-fitted rat bone specimens: Critical analysis of a technical protocol. *Computer methods in biomechanics and biomedical engineering*, 2012.
- Pioletti, D.P. and Rakotomanana, L.R. Can the increase of bone mineral density following bisphosphonates treatments be explained by biomechanical considerations? *Clinical Biomechanics*, 19(2):170–174, 2004.
- Pioletti, D.P.; Gauthier, O.; Stadelmann, V.A.; Bujoli, B.; Guicheux, J.; Zambelli, P.-Y., and Bouler, J.-M. Orthopedic implant used as drug delivery system: Clinical situation and state of the research. *Current Drug Delivery*, 5(1):59–63, 2008.
- Prendergast, P.J. and Taylor, D. Prediction of bone adaptation using damage accumulation. *Journal of Biomechanics*, 27(8):1067–1076, 1994.
- Prendergast, P.J.; Huiskes, R., and Sballe, K. Biophysical stimuli on cells during tissue differentiation at implant interfaces. *Journal of Biomechanics*, 30(6):539–548, 1997.
- Qian, J.; Wennerberg, A., and Albrektsson, T. Reasons for marginal bone loss around oral implants. *Clinical Implant Dentistry and Related Research*, 14(6):792–807, 2012.
- Rabkin, B.A.; Szivek, J.A.; Schonfeld, J.E., and Halloran, B.P. Long-term measurement of bone strain in vivo: The rat tibia. *Journal of Biomedical Materials Research*, 58(3): 277–281, 2001.
- Ramaniraka, N.A.; Terrier, A.; Theumann, N., and Siegrist, O. Effects of the posterior

- cruciate ligament reconstruction on the biomechanics of the knee joint: A finite element analysis. *Clinical Biomechanics*, 20(4):434–442, 2005.
- Ramfjord, Sigurd P. and Ash, Major M. *Periodontology and periodontics / Sigurd P. Ramfjord, Major M. Ash, Jr.* Saunders Philadelphia, 1979.
- Ramtani, S.; Garcia, J.M., and Doblaré, M. Computer simulation of an adaptive damage-bone remodeling law applied to three unit-bone bars structure. *Computers in Biology and Medicine*, 34(4):259–273, 2004.
- Reina, J.M.; García-Aznar, J.M.; Domnguez, J., and Doblaré, M. Numerical estimation of bone density and elastic constants distribution in a human mandible. *Journal of Biomechanics*, 40(4):828–836, 2007.
- Ritman, E. L. Micro-computed tomography - current status and developments. volume 6, pages 185–208. 2004.
- Robling, A.G.; Burr, D.B., and Turner, C.H. Recovery periods restore mechanosensitivity to dynamically loaded bone. *Journal of Experimental Biology*, 204(19):3389–3399, 2001.
- Robling, A.G.; Hinant, F.M.; Burr, D.B., and Turner, C.H. Improved bone structure and strength after long-term mechanical loading is greatest if loading is separated into short bouts. *Journal of Bone and Mineral Research*, 17(8):1545–1554, 2002.
- Robling, Alexander G.; Castillo, Alesha B., and Turner, Charles H. Biomechanical and molecular regulation of bone remodeling. *Annual Review of Biomedical Engineering*, 8 (1):455–498, 2006.
- Roshan-Ghias, A.; Lambers, F.M.; Gholam-Rezaee, M.; Müller, R., and Pioletti, D.P. In vivo loading increases mechanical properties of scaffold by affecting bone formation and bone resorption rates. *Bone*, 49(6):1357–1364, 2011.
- Roux, W. *Gesammelte Abhandlungen*. Vol. 1. Leipzig: Engelmann, 1895.
- Rubin, C.T. and Lanyon, L.E. Regulation of bone formation by applied dynamic loads. *Journal of Bone and Joint Surgery - Series A*, 66(3):397–402, 1984.
- Russ, J.C. *Segmentation and Thresholding*, chapter The Image Processing Handbook. CRC Press, 2002.
- Sato, Y.; Fujimatsu, Y.; Kikuyama, M.; Kaji, M., and Oizumic, K. Influence of immobilization on bone mass and bone metabolism in hemiplegic elderly patients with a long-standing stroke. *Journal of the Neurological Sciences*, 156(2):205–210, 1998.
- Schulte, F.A.; Zwahlen, A.; Lambers, F.M.; Kuhn, G.; Ruffoni, D.; Betts, D.; Webster, D.J., and Müller, R. Strain-adaptive in silico modeling of bone adaptation - a computer simulation validated by in vivo micro-computed tomography data. *Bone*, 52(1):485–492, 2013.
- Sema Issever, A.; Vieth, V.; Lotter, A.; Meier, N.; Laib, A.; Newitt, D.; Majumdar, S., and Link, T. M. Local differences in the trabecular bone structure of the proximal femur depicted with high-spatial-resolution mr imaging and multisection ct. *Academic*

- Radiology*, 9(12):1395–1406, 2002.
- Si, H. Adaptive tetrahedral mesh generation by constrained delaunay refinement. *International Journal for Numerical Methods in Engineering*, 75(7):856–880, 2002.
- Sibonga, J.D.; Evans, H.J.; Sung, H.G.; Spector, E.R.; Lang, T.F.; Oganov, V.S.; Bakulin, A.V.; Shackelford, L.C., and LeBlanc, A.D. Recovery of spaceflight-induced bone loss: Bone mineral density after long-duration missions as fitted with an exponential function. *Bone*, 41(6):973–978, 2007.
- Silva, M.J.; Keaveny, T.M., and Hayes, W.C. Computed tomography-based finite element analysis predicts failure loads and fracture patterns for vertebral sections. *Journal of Orthopaedic Research*, 16(3):300–308, 1998.
- Skerry, T.M. The response of bone to mechanical loading and disuse: Fundamental principles and influences on osteoblast/osteocyte homeostasis. *Archives of Biochemistry and Biophysics*, 473(2):117–123, 2008.
- Skinner, H.B.; Kilgus, D.J.; Keyak, J.; Shimaoka, E.E.; Kim, A.S., and Tipton, J.S. Correlation of computed finite element stresses to bone density after remodeling around cementless femoral implants. *Clinical Orthopaedics and Related Research*, (305):178–189, 1994.
- Smit, T.H. and Burger, E.H. Is bmu-coupling a strain-regulated phenomenon? a finite element analysis. *Journal of Bone and Mineral Research*, 15(2):301–307, 2000.
- Srinivasan, S.; Weimer, D.A.; Agans, S.C.; Bain, S.D., and Gross, T.S. Low-magnitude mechanical loading becomes osteogenic when rest is inserted between each load cycle. *Journal of Bone and Mineral Research*, 17(9):1613–1620, 2002.
- Stadelmann, V.A. and Pioletti, D.P. Activation pathways of osteoclasts are up-regulated by micromotions at the bone-implant interface. *Computer Methods in Biomechanics and Biomedical Engineering*, 10(SUPPL. 1):93–94, 2012.
- Stadelmann, V.A.; Gauthier, O.; Terrier, A.; Bouler, J.-M., and Pioletti, D.P. Implants delivering bisphosphonate locally increase periprosthetic bone density in an osteoporotic sheep model. a pilot study. *European Cells and Materials*, 16:10–16, 2008.
- Stadelmann, V.A.; Terrier, A.; Gauthier, O.; Bouler, J.-M., and Pioletti, D.P. Prediction of bone density around orthopedic implants delivering bisphosphonate. *Journal of Biomechanics*, 42(9):1206–1211, 2009.
- Stadelmann, V.A.; Bonnet, N., and Pioletti, D.P. Combined effects of zoledronate and mechanical stimulation on bone adaptation in an axially loaded mouse tibia. *Clinical Biomechanics*, 26(1):101–105, 2011.
- Stadlinger, B.; Pourmand, P.; Locher, M.C., and Schulz, M.C. Systematic review of animal models for the study of implant integration, assessing the influence of material, surface and design. *Journal of Clinical Periodontology*, 39(SUPPL.12):28–36, 2012.
- Stülpner, M.A.; Reddy, B.D.; Starke, G.R., and Spirakis, A. A three-dimensional finite

- analysis of adaptive remodelling in the proximal femur. *Journal of Biomechanics*, 30(10):1063–1066, 1997.
- Taddei, F.; Martelli, S.; Reggiani, B.; Cristofolini, L., and Viceconti, M. Finite-element modeling of bones from ct data: Sensitivity to geometry and material uncertainties. *IEEE Transactions on Biomedical Engineering*, 53(11):2194–2200, 2006.
- Taddei, F.; Schileo, E.; Helgason, B.; Cristofolini, L., and Viceconti, M. The material mapping strategy influences the accuracy of ct-based finite element models of bones: An evaluation against experimental measurements. *Medical Engineering and Physics*, 29(9):973–979, 2007.
- Takatsuka, K.; Yamamuro, T.; Nakamura, T., and Kokubo, T. Bone-bonding behavior of titanium alloy evaluated mechanically with detaching failure load. *Journal of Biomedical Materials Research*, 29(2):157–163, 1995.
- Taubin, G. A signal processing approach to fair surface design. *Proceedings of the 22nd annual conference on Computer graphics and interactive techniques*, 1995.
- Taylor, D.; Hazenberg, J.G., and Lee, T.C. Living with cracks: Damage and repair in human bone. *Nature Materials*, 6(4):263–268, 2007.
- Terrier, A.; Rakotomanana, R.L.; Ramaniraka, A.N., and Leyvraz, P.F. Adaptation models of anisotropic bone. *Computer Methods in Biomechanics and Biomedical Engineering*, 1(1):47–59, 1997.
- Terrier, A.; Miyagaki, J.; Fujie, H.; Hayashi, K., and Rakotomanana, L. Delay of intracortical bone remodelling following a stress change: A theoretical and experimental study. *Clinical Biomechanics*, 20(9):998–1006, 2005.
- Terrier, A.; Reist, A.; Merlini, F., and Farron, A. Simulated joint and muscle forces in reversed and anatomic shoulder prostheses. *Journal of Bone and Joint Surgery - Series B*, 90(6):751–756, 2008.
- Turner, C.H. Three rules for bone adaptation to mechanical stimuli. *Bone*, 23(5):399–407, 1998.
- Turner, C.H. Bone strength: Current concepts. *Annals of the New York Academy of Sciences*, 1068(1):429–446, 2006.
- Turner, C.H.; Akhter, M.P.; Raab, D.M.; Kimmel, D.B., and Recker, R.R. A noninvasive, in vivo model for studying strain adaptive bone modeling. *Bone*, 12(2):73–79, 1991.
- Turner, C.H.; Forwood, M.R., and Otter, M.W. Mechanotransduction in bone: Do bone cells act as sensors of fluid flow? *FASEB Journal*, 8(11):875–878, 1994a.
- Turner, C.H.; Forwood, M.R.; Rho, J.-Y., and Yoshikawa, T. Mechanical loading thresholds for lamellar and woven bone formation. *Journal of Bone and Mineral Research*, 9(1):87–97, 1994b.
- Ulrich, D.; Van Rietbergen, B.; Weinans, H., and R uegsegger, P. Finite element analysis of trabecular bone structure: A comparison of image-based meshing techniques. *Journal*

- of *Biomechanics*, 31(12):1187–1192, 1998.
- Umemura, Y.; Ishiko, T.; Yamauchi, T.; Kurono, M., and Mashiko, S. Five jumps per day increase bone mass and breaking force in rats. *Journal of Bone and Mineral Research*, 12(9):1480–1485, 1997.
- Vahdati, A. and Rouhi, G. A model for mechanical adaptation of trabecular bone incorporating cellular accommodation and effects of microdamage and disuse. *Mechanics Research Communications*, 36(3):284–293, 2009.
- Van Der Linden, J.C.; Homminga, J.; Verhaar, J.A.N., and Weinans, H. Mechanical consequences of bone loss in cancellous bone. *Journal of Bone and Mineral Research*, 16(3):457–465, 2001.
- Van der Meulen, M.C.H.; Morgan, T.G.; Yang, X.; Baldini, T.H.; Myers, E.R.; Wright, T.M., and Bostrom, M.P.G. Cancellous bone adaptation to in vivo loading in a rabbit model. *Bone*, 38(6):871–877, 2006.
- Van Oers, R.F.M.; Ruimerman, R.; Tanck, E.; Hilbers, P.A.J., and Huiskes, R. A unified theory for osteonal and hemi-osteonal remodeling. *Bone*, 42(2):250–259, 2008. cited By (since 1996)48.
- Van Oosterwyck, H.; Duyck, J.; Sloten, J.V.; Van Der Perre, G.; De Cooman, M.; Lievens, S.; Puers, R., and Naert, I. The influence of bone mechanical properties and implant fixation upon bone loading around oral implants. *Clinical Oral Implants Research*, 9(6):407–418, 1998.
- Van Rietbergen, B.; Huiskes, R.; Weinans, H.; Sumner, D.R.; Turner, T.M., and Galante, J.O. The mechanism of bone remodeling and resorption around press-fitted tha stems. *Journal of Biomechanics*, 26(4-5):369–382, 1993.
- Van Rietbergen, B.; Weinans, H.; Huiskes, R., and Odgaard, A. A new method to determine trabecular bone elastic properties and loading using micromechanical finite-element models. *Journal of Biomechanics*, 28(1):69–81, 1995.
- Vanden Bogaerde, L. A proposal for the classification of bony defects adjacent to dental implants. *International Journal of Periodontics and Restorative Dentistry*, 24(3):264–271, 2004.
- Verhulp, E.; van Rietbergen, B.; Müller, R., and Huiskes, R. Indirect determination of trabecular bone effective tissue failure properties using micro-finite element simulations. *Journal of Biomechanics*, 41(7):1479–1485, 2008.
- Viceconti, M. and Taddei, F. Automatic generation of finite element meshes from computed tomography data. *Critical Reviews in Biomedical Engineering*, 31(1-2):27–72, 2003.
- Viceconti, M.; Olsen, S.; Nolte, L.-P., and Burton, K. Extracting clinically relevant data from finite element simulations. *Clinical Biomechanics*, 20(5):451–454, 2005.
- Viera-Negrón, Y.E.; Ruan, W.H.; Winger, J.N.; Hou, X.; Sharawy, M.M., and Borke, J.L. Effect of ovariectomy and alendronate on implant osseointegration in rat maxillary bone.

- The Journal of oral implantology*, 34(2):76–82, 2008.
- Vollmer, J.; Mencl, R., and Müller, H. Improved laplacian smoothing of noisy surface meshes. *Computer Graphics Forum*, 18(3):C137–C138, 1999.
- Webster, D.J.; Morley, P.L.; van Lenthe, G.H., and Müller, R. A novel in vivo mouse model for mechanically stimulated bone adaptation - a combined experimental and computational validation study. *Computer Methods in Biomechanics and Biomedical Engineering*, 11(5):435–441, 2008.
- Wehner, T.; Wolfram, U.; Henzler, T.; Niemeyer, F.; Claes, L., and Simon, U. Internal forces and moments in the femur of the rat during gait. *Journal of Biomechanics*, 43(13):2473–2479, 2010.
- Weinans, H. and Prendergast, P.J. Tissue adaptation as a dynamical process far from equilibrium. *Bone*, 19(2):143–149, 1996.
- Weinans, H.; Huiskes, R., and Grootenboer, H.J. The behavior of adaptive bone-remodeling simulation models. *Journal of Biomechanics*, 25(12):1425–1441, 1992.
- Weinans, H.; R. Sumner, D.; Igloria, R., and Natarajan, R.N. Sensitivity of periprosthetic stress-shielding to load and the bone density-modulus relationship in subject-specific finite element models. *Journal of Biomechanics*, 33(7):809–817, 2000.
- Weinbaum, S.; Cowin, S.C., and Zeng, Y. A model for the excitation of osteocytes by mechanical loading-induced bone fluid shear stresses. *Journal of Biomechanics*, 27(3):339–360, 1994.
- Wiskott, H.W.A.; Cugnoni, J.; Scherrer, S.S.; Ammann, P.; Botsis, J., and Belser, U.C. Bone reactions to controlled loading of endosseous implants: A pilot study. *Clinical Oral Implants Research*, 19(11):1093–1102, 2008.
- Wiskott, H.W.A.; Bonhote, P.; Cugnoni, J.; Durual, S.; Zacchetti, G.; Botsis, J.; Scherrer, S.S., and Ammann, P. Implementation of the "loaded implant" model in the rat using a miniaturized setup - description of the method and first results. *Clinical Oral Implants Research*, 23(12):1352–1359, 2012.
- Witjes, S.; Schrier, J.C.M.; Gardeniers, J.W.M., and Schreurs, B.W. Complications within two years after revision of total hip prostheses. *Nederlands Tijdschrift voor Geneeskunde*, 151(35):1928–1934, 2007.
- Wolff, J. *The Law of Bone Remodeling*. Berlin Heidelberg New York: Springer, 1986.
- Wullschleger, L.; Weisse, B.; Blaser, D., and Fürst, A.E. Parameter study for the finite element modelling of long bones with computed-tomography-imaging-based stiffness distribution. *Proceedings of the Institution of Mechanical Engineers, Part H: Journal of Engineering in Medicine*, 224(9):1095–1107, 2010.
- Yeh, O.C. and Keaveny, T.M. Biomechanical effects of intraspecimen variations in trabecular architecture: A three-dimensional finite element study. *Bone*, 25(2):223–228, 1999.

-
- Yeni, Y.N.; Christopherson, G.T.; Dong, X.N.; Kim, D.-G., and Fyhrie, D.P. Effect of microcomputed tomography voxel size on the finite element model accuracy for human cancellous bone. *Journal of Biomechanical Engineering*, 127(1):1–8, 2005.
- Yu, J. Symmetric gaussian quadrature formulae for tetrahedral regions. *Computer Methods in Applied Mechanics and Engineering*, 43(3):349–353, 1984.
- Yushkevich, P. A.; Piven, J.; Cody, H.; Ho, S.; Gee, J. C., and Gerig, G. User-guided level set segmentation of anatomical structures with ITK-SNAP. *Insight Journal*, 1, 2005. Special Issue on ISC/NA-MIC/MICCAI Workshop on Open-Source Software.
- Zacchetti, G.; Wiskott, A.; Cugnoni, J.; Botsis, J., and Ammann, P. External mechanical microstimuli modulate the osseointegration of titanium implants in rat tibiae. *BioMed Research International*, 2013, 2013.
- Zadpoor, A.A. Open forward and inverse problems in theoretical modeling of bone tissue adaptation. *Journal of the Mechanical Behavior of Biomedical Materials*, 27:249–261, 2013.
- Zhang, L.; Geraets, W.; Zhou, Y.; Wu, W., and Wismeijer, D. A new classification of peri-implant bone morphology: a radiographic study of patients with lower implant-supported mandibular overdentures. *Clinical Oral Implants Research*, 2013.

Curriculum Vitæ

Curriculum Vitæ

Marco Piccinini



Personal Information:

Date of birth: 4th May 1984.
Place of birth: Modena, Italy.
Nationality: Italian
Email: marco.piccinini84@gmail.com

Education:

2010-2014 PhD student at LMAF (Laboratoire de mécanique appliquée et d'analyse de fiabilité), École Polytechnique Fédérale de Lausanne, Switzerland.
2007-2009 Master in Mechanical Engineering at the University of Bologna, Italy. Grade: 110/110 magna cum laude.
2003-2007 Bachelor in Mechanical Engineering at the University of Bologna, Italy. Grade: 98/110.

Research Experience:

2009-2010 Research fellow at DIEM (Mechanical, Nuclear, Aviation and Metallurgical Engineering Department), University of Bologna, Italy. Sector: advanced robotics, anthropomorphic and robotic hand design.

Awards:

2012 IEEE I-RAS Young Author Best Paper Award 2012 (YABP).
Best journal paper published by an Italian author on an IEEE-RAS journal in the previous two years.
Paper title G. Berselli, M. Piccinini, G. Palli and G. Vassura. "Engineering design of fluid-filled soft covers for robotic contact interfaces: guidelines, nonlinear modeling, and experimental validation", IEEE Transactions on Robotics, 27(3), pp.436-449, 2011.

Teaching Experience:

2010-2014 Assistant for the courses:
 “Mechanics of Structures II”. Prof. J. Botsis.
 “Mechanics of continuous media”. Prof. J. Botsis.
 “Introduction to mechanics of structures”. Dr. M. Galli.
 “Finite element modelling and simulation”. Dr. J. Cugnoni.

Scientific Publications:

Piccinini, M.; Cugnoni, J.; Botsis, J.; Ammann, P., and Wiskott, A. Influence of gait loads on cortical osseointegration in rat tibiae: experimental and numerical analysis. Submitted to the *Journal of Biomechanics*, 2014.

Piccinini, M.; Cugnoni, J.; Botsis, J.; Zacchetti, G.; Ammann, P., and Wiskott, A. Factors affecting subject-specific finite element models of implant-fitted rat bone specimens: Critical analysis of a technical protocol. *Computer methods in biomechanics and biomedical engineering*, 2012.

Berselli, G.; Piccinini, M.; Palli, G. and Vassura, G. Engineering design of fluid-filled soft covers for robotic contact interfaces: guidelines, nonlinear modeling, and experimental validation. *IEEE Transactions on Robotics*, 27(3), pp.436-449, 2011.

Oral communications:

M. Piccinini et al. "The 'activated implant' model: establish the animal and numerical models". *Workshop: Animal models in bone regeneration research*, Davos, Switzerland, 2013.

M. Piccinini et al. "A comparison of remodeling approaches applied to an implanted rat tibia". *19th Congress of the European Society of Biomechanics*, Patras, Greece, 2013.

M. Piccinini et al. "Validation of specimen-specific finite element model of implanted rat tibiae". *18th Congress of the European Society of Biomechanics*, Lisbon, Portugal, 2012.

M. Piccinini et al. "Specimen-specific finite element models of implanted bones: methodology and validation". *10th International Symposium Computer Methods in Biomechanics and Biomedical Engineering*, Berlin, Germany, 2012.

M. Piccinini et al. "A Semi-Automatic Procedure to Develop Specimen-Specific Finite Element Models from Micro Computer Tomography Images of Implanted Bones". *17th International Symposium on Computational Biomechanics*, Ulm, Germany, 2011.